UNIVERSITY OF SOUTHAMPTON

FACULTY OF ENGINEERING AND THE ENVIRONMENT

Engineering Sciences

Development of infrared techniques for practical defect identification in bonded joints

by

Rachael C. Waugh

Thesis for the degree of Doctor of Philosophy

May 2014

UNIVERSITY OF SOUTHAMPTON

ABSTRACT

FACULTY OF ENGINEERING AND THE ENVIRONMENT
Thesis for the degree of Doctor of Philosophy

DEVELOPMENT OF INFRARED TECHNIQUES FOR PRACTICAL DEFECT IDENTIFICATION IN BONDED JOINTS

Rachael Caroline Waugh

Identification of kissing defects in adhesive bonds has been reported to be an area of concern across a range of industries. To date the majority of work on this matter has focused on the development of advanced ultrasonic techniques. The current thesis focuses on the use of thermography, specifically pulsed and pulse phase thermography (PT and PPT), for the identification of kissing defects. Initially the thesis focuses on the application of PT and PPT for the identification of a range of defect types in a variety of materials to establish the effect of material properties on identification of defects. A numerical model has been developed to simulate the thermal evolution created during a PT or PPT experiment. After validation through a series of case studies, this model has then been used as a predictive tool to relate defect detectability to the thermal property contrast between defect and bulk materials. Where insufficient thermal property contrast exists defects have a limited effect on heat propagation through a component and therefore are not detected using PT or PPT. A means of producing realistic kissing defects in bonded joints is established. The addition of a small load to bonds containing kissing defects was found to open the defects sufficiently to enable their detection. Initial experiments use the application of a tensile load, via a test machine, to successfully investigate simulated kissing defects in single lap joints. A technique using vacuum loading on one adherend of an adhesive bond while PPT is carried out from the other adherend was successfully trialled. Vacuum loading enables the technique to be taken out of the laboratory. A low cost infrared detector, Flir Tau320, compared to the research based photon detector, Flir SC5000, was demonstrated to be suitable for application in PT, thus enabling a significantly lower cost tool to be developed.

Contents

List of tables

List of figures

DECLARATION OF AUTHORSHIP

I, Rachael Caroline Waugh

declare that the thesis entitled

Development of infrared techniques for practical defect identification in bonded joints

and the work presented in the thesis are both my own, and have been generated by me as the result of my own original research. I confirm that:

- this work was done wholly or mainly while in candidature for a research degree at this University;
- where any part of this thesis has previously been submitted for a degree or any other qualification at this University or any other institution, this has been clearly stated;
- where I have consulted the published work of others, this is always clearly attributed;
- where I have quoted from the work of others, the source is always given. With the exception of such quotations, this thesis is entirely my own work;
- I have acknowledged all main sources of help;
- where the thesis is based on work done by myself jointly with others, I have made clear exactly what was done by others and what I have contributed myself;
- parts of this work have been published as:

Journal papers

Waugh, R. C., Dulieu-Barton, J. M. and Quinn, S., *Infrared thermography to identify low volume defects in adhesive bonds,* in preparation.

Waugh, R. C., Dulieu-Barton, J. M. and Quinn, S., *Modelling and evaluation of pulsed and pulse phase thermography through application of composite and metallic case studies,* NDT&E International, 66: p. 52-66. 2014.

Peer reviewed conference papers

Waugh, R.C., Dulieu-Barton, J.M. and Quinn, S. *Defect detection using pulse phase thermography – repeatability and reliability of data*, Key Engineering Materials Vols. 569 – 570, p. 1164-1169. 2013.

Waugh, R. C., Dulieu-Barton, J. M. and Quinn, S., *Pulse phase thermography and its application to kissing defects in adhesively bonded joints*, Applied Mechanics and Materials, 70, p. 369-374. 2011.

Signed: ……..

Date:……

Acknowledgements

Thank you to Lloyds Register Foundation who financially supported this work. Special thanks to David Howarth at Lloyds Register for providing his knowledge and answering my questions. A massive thank you to my supervisors, Janice and Simon, for their guidance, motivation, and encouragement throughout the PhD. Also thank you to all my friends in the department; from lab buddies, to sporty break friends, to Friday beers attendees – thanks for keeping me sane. Thanks especially to Richard, Duncan and Andy for keeping the tea flowing.

Thank you to all my family and friends for their support. A special thank you to Matt, for keeping me motivated throughout my PhD, supporting me when I needed it and taking me away to play when it was required. A big thank you to Antony who earns the prestigious title of 'chief initial proof reader'. Finally, thank you to my Mum and Dad for giving me the courage to do what I want to do.

Nomenclature

γ	m^2/s	Thermal diffusivity
ϕ	$^\circ$	Phase
ρ	kg/m^2	Material density
ω		Dimensionless time for thickness of material
ω_r		Dimensionless time for defect depth
e	J/m2Ks0.5	Material effusivity
g	m	Small depth in material in which Q is absorbed uniformly
k		Thermal image number
k	W/mK	Thermal conductivity
m	kg	Mass
t	s	Time
t_0	s	Initial time
u		Initial temperature term
x	m	Depth from surface of material
y		Ratio of defect depth to thickness of material
A		Amplitude
C	J/mol.K	Heat capacity
$C(t)$	K	Thermal contrast
L	m	Depth to defect
Lr	m	Depth of material
N		Total number of thermal images
Q	J	Heat
T	K	Temperature
Ti	K	Temperature over area of interest
Ts	K	Temperature over known non-defective material
$T(x,0)$	K	Initial temperature distribution
V		Normalised temperature

Abbreviations

CFRP	Carbon fibre reinforced plastic
CT	X-ray computed tomography
DC	Defect centre
DE	Defect edge
ECT	Eddy current thermography
FEA	Finite element analysis
FFT	Fast Fourier transform
FT	Flexible Triplex
FWHM	Full width at half maximum
GFRP	Glass fibre reinforced plastic
IR	Infrared
LNG	Liquefied natural gas
LT	Lockin thermography
ND	No defect
NDE	Non-destructive evaluation
PPT	Pulse phase thermography
PT	Pulsed thermography
PTFE	Polytetrafluoroethylene
PU	Polyurethane
PUF	Polyurethane foam
RT	Rigid Triplex
SE	Surface energy
TSA	Thermoelastic stress analysis
TSR	Thermal signal reconstruction
UD	Unidirectional
UT	Ultrasound

1. Introduction

1.1 Background and motivation

Advances in manufacturing techniques and the requirement to make structures lighter has led to the increased use of composite materials in a wide range of applications as they can offer significant weight saving advantages over their metallic counterparts. Drilling holes in composite components for joining using traditional mechanical fastenings, such as bolts or rivets, can lead to damage within the material. Mechanically fastened joints are also prone to large stress concentrations around fastenings through which the load is transferred. Adhesive bonds enable a more uniform load transfer through the joint thus removing the stress concentrations associated with mechanical fastenings [1]. The use of adhesive instead of mechanical fastenings also allows weight saving to be maximised, and adhesives provide high levels of corrosion resistance [2]. The advantages of using adhesive over mechanical fastenings have led to the increased use of adhesive joints. To date many of these uses have been in secondary structures. To allow adhesive joints to be used more widely in primary structural roles they must be known to be reliable [3]. A full understanding of the type and likelihood of defects that may affect the joint efficiency must be established. Therefore, non-destructive evaluation (NDE) inspection procedures must be developed that are able to detect all types of defects that can occur in adhesive bonds. Robust NDE approaches must be developed that are suitable for use during the manufacturing and construction stages as well as for through life assessment.

Current NDE for mechanical joints include X-ray radiography and ultrasound (UT). Inspection of composites is primarily carried out using UT, although shearography and thermography are also used [4]. Non-destructive assessment methods for bonded joints have generally followed those used for composites with UT being the most widely used. Current techniques are able to identify defects with a volume associated with them, such as voids, as they create sufficient contrast to the surrounding materials. Such contrast may be a variation in density, thermal properties or other material property differences. Defects with very small or negligible volume are known as kissing defects. Kissing defects are extremely difficult to detect and with current techniques

there is a high potential for them to go undetected. Research has been carried out into new or adapted NDE procedures that could be used to successfully identify kissing defects, e.g. [5]. To date such research has been mainly focused on ultrasonic approaches and several advanced ultrasonic inspection methods have been developed [6-8]. While these approaches have had success for specific applications or materials, none have been shown to be consistent and reliable at detecting low volume defects across a range of materials. Thermographic approaches are full field and so allow large areas to be evaluated efficiently [9]. An infrared detector is used that provides image based results that are easy to interpret. When considering the application of NDE on-site, thermography may be a practical and relatively robust approach. Thermography may also be applied with access to only one side of the joint as may be required in many in service or production situations [10].

The current research focuses on the use of thermography, specifically pulsed thermography (PT) and pulse phase thermography (PPT), for the identification of defects in adhesively bonded joints. Such a technique would be of great benefit in a range of industries including automotive and maritime. In the automotive industry the increased use of composite materials has led to an increase in adhesive bonds [11]. In the maritime industry a particular application has been raised in the construction of adhesive joints in large ship production, namely on the Gaz Transport and Technigaz (GTT) MkIII vessel. Within this sector of the ship building industry a good bond is assumed to be a good bond for life [D. Howarth, Lloyds Register, personal communication 17th November 2010], therefore any defective bonds need to be identified in the construction stages. Currently there is uncertainty in the reliability of the inspection techniques used to assess the adhesive joints sealing the secondary membrane pieces together. The ability to identify defects in the adhesive bonds that require repair in the production stages will decrease the need for the costly process of removing the ship from service for repairs in the future and increase confidence in the secondary membrane. This detection will lead to reduced material consumption and minimise waste, which will lead to an improvement in the sustainability of ship building and a reduction in the environmental impact of future ship repair.

1.2 Aims and objectives

The aim of the current research is to explore the potential of using thermographic methods to develop a reliable method of identifying kissing defects in adhesive bonds. The goal is to define the technology required to make a practical and portable device for NDE of adhesive bonds in the field. To achieve this goal it is necessary to address the following objectives:

1. Define the underlying physics of thermographic techniques with particular reference to pulsed and pulse phase thermography (PT/PPT).
2. Identify the potential and limitations of PT/PPT applied to a range of metallic and polymer materials.
3. Define kissing defects and establish a method of accurately experimentally simulating and introducing kissing defects into structures.
4. Apply PPT to the experimentally simulated kissing defects and assess if they are detectable using the thermographic techniques.
5. Compare and validate PPT with other NDE methods such as water coupled ultrasound.
6. Develop a numerical model of the heat interactions in a structure to understand the physics of PT/PPT and tailor experiments to particular component configurations.
7. Assess how the technique may need to be adapted from the laboratory set-up to become a practical, portable tool for use in the field.
8. Consider the practicalities of applying PPT as a tool for use in a shipyard environment.

1.3 Novelty

The novelty of the current research described in the thesis may be categorised in two sections:

1. The development of a thermographic technique to enable kissing defect identification via the addition of a small load to enhance thermal contrast.

2. The development of a numerical model able to accurately simulate PT and PPT to establish the limits of defect detectability and investigate experimental parameters.

A literature survey has shown that it is not currently possible to consistently and reliably identify kissing defects in adhesively bonded joints [12]. The need for such an inspection technique is of interest to several industries including the marine industry where kissing defects are considered a problem in the adhesive bonded joints found in the MkIII LNG carrier [D. Howarth, Lloyds Register, personal communication 17th November 2010]. In studies that have used thermography to identify defects in adhesive bonds the defects of interest provide sufficient thermal contrast to facilitate their detection i.e. they have a volume associated with them, e.g. [13]. The nature of kissing defects suggests that such low volume defects cannot cause sufficient perturbation to heat propagation for detection using PT or PPT in standard application. A means of creating simulated defects that fit the criteria of real kissing defects so that experiments can be carried out on specimens with kissing defects at known locations to properly verify the methodology.

No published literature is available that investigates the effect of kissing defect visibility using the addition of a load while inspecting using thermographic approaches. A patent application [14] filed in 1999 describes very loosely this idea, without recourse to any experimental verification or numerical simulation. In the present thesis the use of a small load to open defects to enhance contrast has been explored in detail. It is shown in a laboratory based experiment using a test machine that the application of a small load enhanced the thermal contrast of kissing defects and enabled their detection where it was not previously possible. The feasibility of applying the load outside the laboratory was explored using a vacuum applied to one side of a join while PPT inspection was undertaken. Hence a significant contribution to knowledge has been made by the work described in the thesis by demonstrating the feasibility of developing a tool for application of thermographic techniques for onsite inspections.

Previous numerical models developed to simulate PT have attempted to inform experimental data collection parameters, such as the duration of data collection required, or predict defect depth [15, 16]. While some use is made

of these models it is the methods used to simulate defects within components that misses the complexity of a real defect. Previous models tend to model defects as either flat bottom holes, e.g. [16, 17] or areas of perfect insulation, e.g. [15]. Where defect material properties are considered, as in [18], the defect material is used to replace the full thickness of the adhesive layer. All of these approaches of modelling defects will enhance thermal contrast and simplify the thermal interactions. In the current work a new numerical model, is created that more accurately simulates defects, thus enabling the physical understanding of PT to be advanced. The model has enabled PT to be tailored to specific applications. The modelled PT data was then processed to provide a model for PPT. The model can also be used to assess defect detectability by defining the component material and the constituents of the defect and its depth. A further area of novelty is the use of the model to relate defect detectability to the contrast of defect and bulk material properties enabling predictions of potentially detectable / undetectable defects.

1.4 Structure of thesis

The thesis is comprised of ten chapters. Chapter 1 introduces the background and motivation for the work and describes the objectives set to achieve the project aims and the novelty found in the thesis. Chapter 2 begins by giving a general overview of adhesive bonding. The creation and categorisation of defects and specifically kissing defects is introduced and previous methods used to experimentally simulate defects, including flat bottom holes, inserts and liquid layer defects, are reviewed. The manufacturing methodology used to create the Triplex bonds found in the MkIII LNG carriers is then discussed. Current inspection techniques used to assess the quality of the Triplex bonds are then reported. The Triplex joints are discussed at this stage as they underpin some decisions when selecting appropriate NDE techniques.

In Chapter 3 current NDE techniques used for the inspection of composite materials across a range of industries and applications are assessed. A basic description of each technique is given before techniques specifically used for adhesive bonds are covered. The techniques are compared in terms of their suitability for onsite bond inspections before thermography is selected as a promising technique worth investigating further.

An overview of specific thermographic techniques is presented in Chapter 4 before pulsed and pulse phase thermography (PT/PPT) are identified as thermographic techniques of interest for the remainder of the thesis. The underpinning heat transfer physics that enables defect detection is introduced. The experimental setup and data processing associated with PT and PPT are then discussed. Experimental work begins by investigating the data processing variables and their impact on the contrast created between the data directly over the defect and that from a non-defect area. Such contrast is directly related to the detectability of a defect. This study is then used to aid in parameter selection in the remainder of the thesis

In Chapter 5 experimental work to establish the suitability of PT and PPT for a range of materials and defect types is described. An ultrasound (UT) C-scan system is used to enable comparison between the more established UT technique and the thermography methods. Work begins by testing isotropic material with strongly thermally contrasting flat bottom hole style defects before moving to more complex samples. Composite materials with insert style simulated defects are used to test the limits of detectability of PT and PPT and compare the two thermographic techniques. Bonded joints with insert ssimulated defects are then tested, where the advantages of PPT over PT become more obvious as PPT is able to reveal defects that PT cannot.

A numerical model developed using Ansys finite element software is presented in Chapter 6. The purpose of the model is to enable the ability of PT and PPT to identify defects in a range of applications to be investigated. The model is validated using three case studies. The model is then used as a predictive tool to investigate the detectability of defects of various materials in three bulk materials including aluminium and fibre-reinforced composites. Combinations of thermal properties of the bulk material and the defect are considered to define the limits of detectability. Kissing defects are shown as being below the identification thresholds due to the lack of thermal contrast between the bulk and defective materials.

Experimental work focusing on the identification of kissing defects is presented in Chapter 7. The conclusions of the model that kissing defects would not be identified using PT and PPT were confirmed. A methodology using the addition of a load to a sample to enable kissing defect identification

was introduced. Initial experiments focused on the use of a test machine to impart a load into single lap joint samples which showed the technique to be possible.

The success of the laboratory based tests then led to a feasibility study using the application of a vacuum to open simulated kissing defects in Chapter 8. A vacuum was applied onto the rear of a bonded joint to open the defect while the bond was inspected by using PPT on the front surface. A structural model was developed to identify the displacement required to enable defect detection. A further feasibility study into the use of a lower cost bolometer type infrared detector for the application of PT is also presented to give ideas for future work to develop the approach as a more affordable tool for industrial application.

In Chapter 9 a range of industrial applications of PT and PPT are reported to demonstrate the versatility of the technique to a variety of applications. A section covering the development of the technique through applications using the MkIII Triplex joints containing increasingly complex configurations and defect types is included. This section demonstrated the successful identification of an experimentally simulated kissing defect in a representative CFRP – Triplex bond using vacuum loading. The CFRP was used in this case to enhance the stiffness of the bond as it would be adhered to the insulation while maintaining the two sided bond access currently required for the vacuum application. Further studies undertaken into the identification and monitoring of defects in the adhesive bonds of CFRP repair patches in civil engineering structures, the identification of the level of porosity in adhesive bonds and finally the application of PPT to thick composite structures are also presented.

Conclusions are drawn and future work is discussed in Chapter 10. The opportunities for future work include development of a complete tool combining the PPT and vacuum loading to enable single sided access to be enabled, implementation of automation procedures, greatly reducing man hours and the development of a combined thermal and structural model to be coupled with the developed tool.

2. Adhesive bonding

2.1 Introduction

A thorough understanding of the types of defects that frequently occur in adhesively bonded joints is required. Any defect found in an adhesive bond has the potential to affect the strength of that bond. Industry requires a method of not only identifying such defects but also the setting of threshold criteria, to define acceptable / unacceptable defects. The threshold criteria are dependent on where the joint is to be deployed and tailored its application. The first step in this process is to categorise types of defects in adhesive bonds and then to develop reliable methods of NDE that can identify the defect type before tailoring the threshold criteria.

There are two fundamental methods in which an adhesive adheres to a substrate, mechanical interlocking and chemical interaction. Mechanical interlocking is dependent on the adherend surface finish. If a surface is very smooth there is no opportunity for mechanical interlocking, whereas if a surface is too rough air may become trapped in the troughs of the surface [19]. Both situations will reduce bond strength as the area of actual bonding is decreased. If any contamination, such as dust, is present on the adherend surface the adhesive will adhere to it, instead of the adherend, again reducing the total bonded area and weakening the joint. Chemical interactions or chemical bonding is governed by the Van der Waals forces interacting between molecules [20]. The combined strength of these forces varies for different types of materials and affects the surface energy (SE) of the adherend [21]. For a good bond to be produced a high SE is preferable, as this attracts the adhesive and enhances surface wetting [22]. A very low SE repels other materials and so bonding is much more difficult. Typically plastics tend to have low SE and so generally present challenges during bonding [20]. Polypropylene has the lowest surface energy of thermoplastics at 31.2 mN m^{-1}, epoxy resin has a surface energy of 32.9 mN m^{-1}, both very low when compared to metals and glass which have a surface energies of 1000 - 5000 mN m^{-1} and 300 mN m^{-1} respectively [23]. Most issues associated with bonding can be mitigated by appropriate adherend surface preparation and adhesive selection. Unfortunately in large structures perfect surface preparation is

difficult to achieve and there is a risk of contamination so there is a requirement to accurately inspect if defects have formed during the bonding process.

2.2 Defects in adhesive bonds

Several types of defects occur in adhesive bonds [24, 25]. These may be considered to fall into three main categories, see Figure 1. The first type is an inclusion, which is the physical inclusion of a foreign material in the adhesive joint, as in Figure 1a. This could occur, for example, if positioning tape is left on the adherend and has adhesive applied over it. The second type are voids, which is the inclusion of air in the joint, see Figure 1b. This could occur between the adhesive and adherend during joint assembly or be found in the adhesive itself if air is introduced during mixing of a two part adhesive. Voids may also be found in the adherend. The final category of defect are kissing defects, see Figure 1c. Kissing defects are the result of improper adhesion between the adhesive and the adherend where the adhesive / adherend interface is not as strong as expected for that joint configuration [26]. A decreased level of adhesion leads to reduced joint strength and is a significant threat to structural integrity. As all components of the joint are present and in contact, kissing defects are the most difficult type of defect to detect using NDE techniques as very little material property contrast is created.

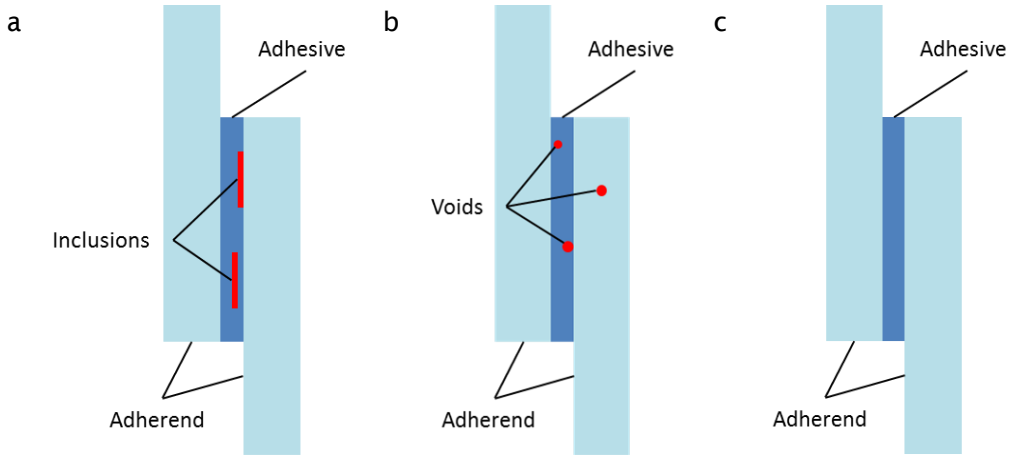

Figure 1 Three categories of defects typically found in adhesive joints; a) inclusions, b) voids and c) kissing defects.

2.2.1 Adhesive bond failure

Adhesive bonds may fail in three ways [27]:

- Adherend failure
- Cohesive failure
- Adhesive failure

If the bond fails via adherend failure the bond has been properly designed and manufactured, as the bond is not the weakest part of the structure and the adherend material has been used to its full potential. This type of failure is not due to problems with the bond. Cohesive failure is failure within the adhesive itself. This may be caused by excessive shear or peel stresses in the bond resulting from a poor joint design and is characterised by the presence of adhesive on both adherend surfaces of a failed joint. Adhesive failure is the failure between the adhesive and adherend, also known as interfacial failure and is caused by the improper preparation or pairing of the adherend and adhesive pairing. Adhesive failure is reported to only occur if there is a problem in the initial joint construction and is not caused through fatigue of the joint [28].

It is noted that for the early failure to be attributed to a kissing defect the failure mode must be adhesive, i.e. at the interface between the adhesive and adherend. As an attempt to quantitatively define a kissing defect a minimum strength reduction of 80% of the shear strength of a perfect joint found during a lap shear test has been suggested to confirm that joints contained kissing defects [29]. It is acknowledged that this criteria is partly arbitrary, although is based on the observed nature of kissing defects.

2.3 Laboratory created defects

In order to develop and understand NDE techniques components or specimens containing defects must be used. There are several methods commonly used for the creation of defects in a laboratory in metallic and composite samples. The most common methods shall be discussed in this section as well as a discussion specifically concerning the simulation of kissing defects.

Flat bottom holes

One of the most common techniques used to simulate defects in metallic materials and ceramics is to mill a flat bottom hole in the rear of the sample thus creating a locally thinned material to simulate a defect [30]. This method originated as a method of simulating corrosion in metals but has been used for other purposes and applied to the study of composites. While this method was appropriate to simulate the loss of material associated with corrosion it is not a realistic means of simulating a commonly occurring defect in composite materials that are not prone to corrosion although due to the strong contrast that flat bottom holes create they are often used when developing techniques in initial studies [31].

Inserts

The most common means of creating an experimentally simulated defect in a fibre reinforced composite material such as carbon fibre reinforced plastic (CFRP) and glass fibre reinforced plastic (GFRP) is the addition of an insert between plies during manufacture. There has been broad use of the addition of PTFE or Teflon inserts typically of circular or square geometry placed at various depths throughout the thickness of the component, e.g. [32-34]. PTFE inserts are typically used to simulate a delamination between plies. This type of experimentally simulated defect is easy to produce and gives an accurately known defect location and geometry.

'Real' damage

Impact damage is frequently introduced in a controlled manner with known impact energies to introduce a controlled experimentally simulated defect that is more realistic of a defect a component may acquire while in service, e.g. [35, 36]. Core crushing has also been introduced when looking at studying sandwich structures [33]. Finally, using composites it is generally possible to manufacture a sample that has an inherent weakness in its layup which is prone to failure in a particular mode and a particular location when subjected to loading. Such contrived samples have been used to produce delaminations in composites or disbonds in adhesive bonds [37]. The nature of creating a 'real' defect is that the precise location and geometry of the defect is not known prior to experiments therefore they can be used to conclusively

parameterise defect comparisons of a developing technique. The technique must then be compared to an established NDE technique or destructive testing undertaken to verify results.

2.3.1 Experimentally simulated kissing defects

Voids and inclusions are of known origin and are therefore relatively easy to recreate in the laboratory, however, the exact cause of kissing defects is unknown. Possible causes are thought to be contamination, abnormality in the adhesive chemistry or curing process, moisture ingress, residual stresses, or a combination of these factors [29, 38]. Several studies have focused on the recreation of kissing defects in the laboratory, e.g. [6]. Most have categorised kissing defects into two types, dry contact and liquid layer [39]. In a dry contact recreation, adhesive is applied to one adherend and cured. The other adherend is put in position and held in place by compressive loading, as shown in Figure 2a. No actual adhesion occurs between the adhesive and adherend. A liquid layer defect is achieved by the introduction of a thin layer of a contaminant such as grease at the adhesive/adherend interface, Figure 2b. The thickness of the contaminant is much thinner than the thickness of the adhesive layer but this thin defect has a detrimental effect on the strength of the joint.

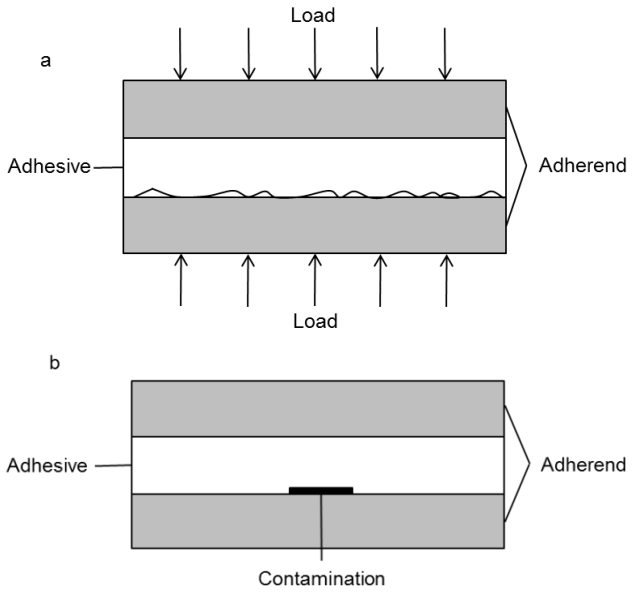

Figure 2 Laboratory created defects, a) a dry contact compressively loaded defect and b) a liquid layer defect with a thin layer of contamination between adhesive and adherend.

2.4 GTT MkIII adhesive bonding and inspection techniques

An application of concern in this work is the adhesively bonded Triplex joints found in the secondary membrane of GTT MkIII LNG carriers. As these joints are enclosed during construction of the vessel and unable to be accessed once completed, it is of paramount importance that they are inspected and found to be defect free, to avoid costly and disruptive remedial repair work having to be carried out during service.

2.4.1 Construction of Triplex adhesive bonds

In the MkIII carriers the liquefied natural gas (LNG) is stored in several tanks; each made using a membrane system. Working inwards from the inner hull of the ship, the system comprises of a secondary layer of insulation that is attached to the inner hull using mastic, a secondary membrane, a primary layer of insulation and a primary membrane which contains the LNG, see Figure 3. The primary membrane is 1.2 mm thick stainless steel, which is corrugated to allow for thermal expansion. The 1 m x 3 m steel sheets are robotically welded together using a TIG (tungsten inert gas) process. The primary and secondary insulation blocks are typically 100 mm and 170 mm thick respectively and are both made of polyurethane foam surrounded by plywood. The secondary membrane is constructed using a specialised Triplex material, which is a 0.7 mm thick sheet of aluminium with a layer of glass cloth on either side attached using a resin system, the specifics of which are confidential.

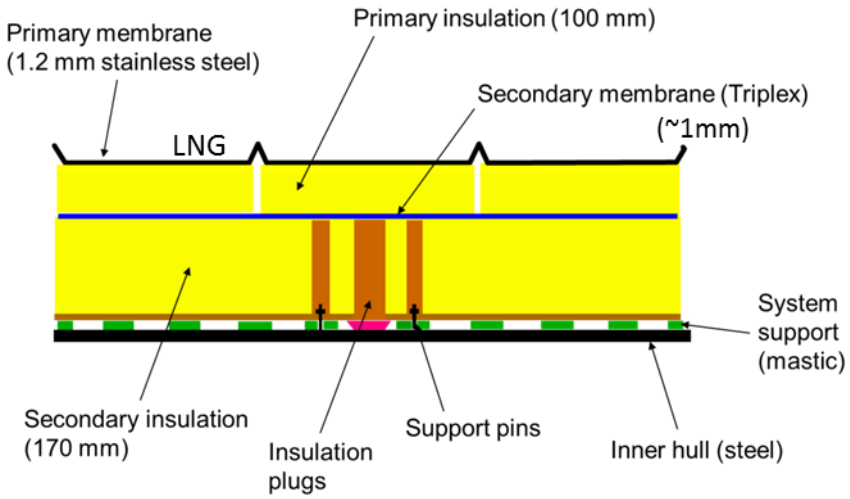

Figure 3 Schematic diagram of the insulation system for the GTT MkIII type LNG carrier membrane system tanks [40].

Prefabricated units comprising both layers of insulation and the secondary membrane measuring 3 m x 1 m are brought into the shipyard where they are attached to the inner hull. A piece of flexible Triplex (FT) is then used to join the rigid Triplex (RT) on the prefabricated boxes to form a continuous secondary membrane, Figure 4. The only difference between the two Triplex materials is the type of resin used to bond the glass fibre to the aluminium, which determines its flexible or rigid nature. In the RT epoxy resin is used and infused into the glass fibre whereas a layer of rubber adhesive is added in the FT. This difference allows the FT to be flexible, enabling easier application. Currently the FT is attached to the RT using either epoxy adhesive, which is applied by hand, or polyurethane (PU) adhesive, which is usually applied by an automated process but only in very small, specific areas of the ship. Due to the improved properties of the PU adhesive at low temperatures compared to the epoxy, there is a push towards using an increased amount of the PU. Epoxy remains the most widely used as manipulation times for the PU are insufficient for the manual application procedures used in most areas of the ships.

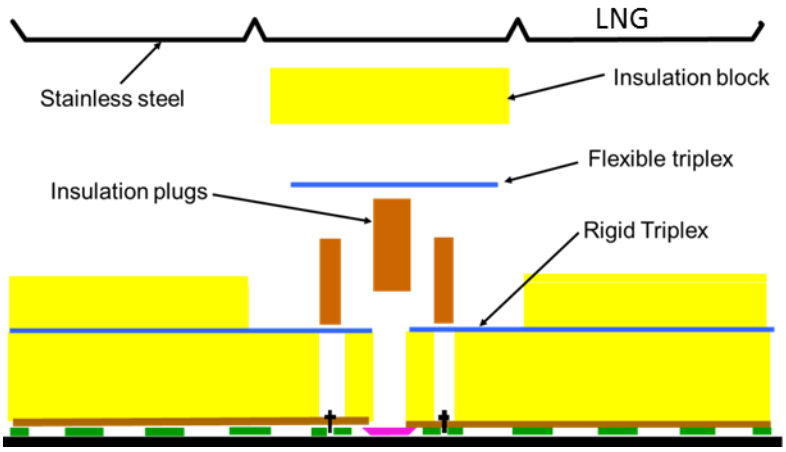

Figure 4 Construction of adhesive Triplex bonds in the secondary membrane of the GTT MkIII insulation system [40].

The vast majority of prefabricated units delivered to the shipyard are 3 m x 1 m, with special pieces being fabricated for the corners and more complex areas. These blocks are adhesively bonded and pinned to the inner hull [41]. Any gap between the prefabricated blocks is filled with more insulation. Adhesive is then applied to the RT and the FT is overlaid. The adhesive is hand spread to a thickness of between 0.2 - 0.8 mm, with an ideal thickness of 0.4 mm. In the epoxy adhesive a thickness of greater than 0.8 mm becomes too brittle when exposed to low temperatures and when the adhesive is less than 0.2 mm thick the strength of bonding is reduced. Although reducing the range of acceptable adhesive thicknesses would improve the quality of the joint while a manual application procedure is employed it is impractical to do so. The amount of adhesive applied is monitored by using a known weight of adhesive for a set area, which is typically a 3 m long bond or 0.3 m width. A pressure bag is then used to apply 150 g/cm^2 of pressure, although pressures in the range 120 – 400 g/cm^2 are acceptable. Pressures above 400 g/cm^2 are not accepted as this leads to the adhesive being squeezed out from the joint and pressures less than 120 g/cm^2 are considered insufficient to adhere the Triplex fully. The pressure is applied for 12 hours as the epoxy cures.

Tank spaces found in the MkIII are 60 m x 33 m x 75 m and in the current fleets there are 5 of these tanks. The total length of adhesive joints to be assessed in a single MkIII carrier is currently 50-60 km. There are plans to increase the size of the carriers to accommodate 12 tanks in the future, more than doubling the length of adhesive joints that require inspection.

2.4.2 Current testing techniques for Triplex bonds

Once the bond has cured and the pressure bag has been removed a series of inspection techniques are carried out. Squeezed out adhesive along the edges of the bonds is visually inspected. The quality of this squeezed out adhesive has been found to be indicative of the quality of the adhesive in the joint. For example, if there are air bubbles in the squeezed out adhesive there are typically air bubbles in the joint, leading to a reduction in the quality of the joint. In another visual test the surface of the FT is illuminated to allow shadows to be cast by any bumps on the surface. These could indicate any defects caused by larger air bubbles or any solid contamination. Another manual test is to take a thin object, such as a coin, and perform a tap test across the surface. Defects that cause a discontinuity below the surface of the material can be heard by the inspector. The effectiveness of this method is dependent on the skill and experience of the inspector. A final test that is carried out on junctions between different pieces of FT is a local tightness test [42]. A vacuum is applied encompassing the full width of the FT and sealed onto the RT. A soap solution is applied to the surface of the joint and as the vacuum is applied the joints are monitored to see if any bubbles form. These bubbles indicate that air is being pulled through the joint from the insulation side by the vacuum and so the joint is not air tight and may allow the LNG to leak through to the inner hull.

Once the construction is complete a total tightness test is carried out [42]. Leaks are detected by sensors between the primary and secondary membranes and the secondary membrane and the inner hull during construction. Nitrogen gas is pumped into the gap between the primary and secondary membrane. The detectors in the space between the secondary membrane and the inner hull monitor for leaks. Whilst this method allows leaks to be detected, it is extremely difficult to locate them accurately and expensive to repair them once they are already sealed into the membrane system.

If a defect or leak is detected by using any of the previously mentioned inspection techniques the joint must be removed and replaced or repaired. This is a costly process due to the nature and size of the joints. For example, if a leak is detected during the total tightness test then the primary membrane and primary insulation must be removed to access the joint. The Triplex joint

must then be disassembled without causing damage to the rigid Triplex or secondary insulation and the joint must be remanufactured. The remaining layers must then be reattached and retested. This is a very time consuming process that should be avoided if at all possible. If a leak is found during the vessel's service then the ship must be taken out of service, costing the ship owners a substantial amount of money in revenue as well as the cost of the repair, which currently totals in the region of $15 million (USD) per incident depending on the extent of the repair required [D. Howarth, Lloyds Register, personal communication 30th March 2010].

As has been described, most current inspection techniques are manual. The practicalities of this lead to only selected 'high risk' areas of the ships being routinely tested, as a full inspection is impractical. Therefore there is demand for an automated inspection method that could quickly collect and process the data, identifying any problem bonds. The total length of the bonds of interest dictates that a time efficient NDE approach must be developed in order for it to be feasible for application in a shipyard.

2.4.3 Current research on Triplex bonds

The main subject of research related to the membrane style LNG carriers is sloshing investigations, e.g. [43, 44]. These studies focus on the effect of sloshing impact of the LNG on the membrane system and mitigation of excessive transfer of impact load to the primary insulation layer via the introduction of composite mats between the primary membrane and the primary insulation. The structural reliability of the membrane containment system under various capacity conditions has been investigated. This research has led to increased awareness of the most dangerous capacities to carry and so has resulted in new loading guidelines being established [45]. Other real scale experimental tests have been carried out focusing on the structural behaviour of the secondary barrier in a MkIII LNG carrier [46]. The structural response was studied for thermal and mechanical loading. Strains were measured via strain gauges and fibre Bragg gratings in the adhesive layer. This experimental work was then correlated with a finite element model. Three adhesive systems were compared: the standard epoxy adhesive used, the PU adhesive previously mentioned and an epoxy adhesive cured using a heat pad. Whilst it was found that the latter two greatly improve the structural properties

of the joint the impracticalities associated with the short work time of the PU and the added cost of the heated cure epoxy meant that currently joints continue to be constructed using the standard epoxy. As the standard epoxy provides a safety factor of more than six [46], a change in adhesive is not necessary to withstand the structural loading imparted on the Triplex joints in service.

A further study has investigated the use of a vibration isolation system to reduce the impact of cavitation caused during LNG boil off transmitted between the primary membrane and the primary insulation [47]. An E-glass/epoxy composite corrugated plate type vibration isolation system to be located beneath the primary membrane was developed, which was found to successfully reduce impact and protect the primary foam insulation with good fatigue resistance.

Research has also been carried out focusing on a slightly varied membrane design where the secondary barrier is simply made of aluminium and the insulation used is polyurethane foam (PUF) [48]. Cracks originating in the aluminium and propagating through the foam at low temperatures were found to be an issue in this construction. The addition of glass fibre in the PUF was found to be a solution. As the aluminium found in the Triplex material is faced with glass fibre the secondary membrane found in the MkIII has not been reported to experience cracking problems.

The main issue reported with the secondary membrane of the MkIII carriers is the detection of leaks, which leads to extremely costly repairs being required. Kim et al [49] have found the primary leakage path through the Triplex barrier to be at the interface between the flexible Triplex and the adhesive. It was shown that this was due to a lack of impregnation of the adhesive into the glass fabric caused by the high viscosity of the epoxy. Adapted curing cycles have been suggested, involving heating of the epoxy for an initial period, while fibre wetting takes place and then a reduced temperature while solidification of the epoxy occurs, thus avoiding introduction of thermal residual stresses. Whilst it was shown that this increased the adhesive impregnation of the fibres and thus reduced leakages it did not mention the cost associated with the heated curing regime and how realistic this is to implement in shipyards. Despite the promising results, to date there has been no application of this

method and as such it can only be assumed that the cost associated with this is too great for ship builders to employ a heated curing cycle along the length of the joints in the MkIII carriers.

The International Code for the Construction and Equipment of Ships carrying Liquefied Natural Gas in Bulk [50] stipulates that the secondary membrane must be periodically checked 'using an appropriate method'. Maguire [50] focuses on the use of global and local acoustic emission techniques to identify leaks through the membrane. To do this, sensors are positioned throughout the region of interest. The insulation space between the secondary membrane and the hull is taken to a partial vacuum, while the insulation between primary and secondary barriers remains at ambient pressure. Any leaks should then be detected by the sensors and their position may then be triangulated using additional sensors. Whilst this process is able to detect leaks, due to the scale of the vessels determining their precise location is relatively difficult and so can be a time consuming process. The application of this technique is also limited to quiet times on the ship as it is very sensitive to external noise. This technique is aimed at through life service monitoring, not for use during construction. For Triplex a good bond is believed to be a good bond for life and as such there is still a great demand for a reliable inspection technique for use during construction after the manufacturing of the Triplex joints and before the primary insulation is overlaid.

To date there has been no published work to the author's knowledge on the application of an advanced NDE technique during construction that is able to assess the integrity of the secondary barrier in the Triplex material. The development of such a technique holds the potential to reduce costly repairs later in the construction stages and through life.

A NDE technique is to be developed that is suitable to provide inspection of the bonded joint between the FT and the RT in the secondary membrane of the MkIII LNG carrier. The inspection should take place during the construction of the vessel after the curing of the bond and before the joints are covered with primary insulation. Due to the length of the joints of interest an efficient, preferably automated, inspection technique is required. This work is concerned with the development of a suitable NDE technique and the on-site automation of the procedure will be a further stage of development.

2.5 Summary

The criteria of identifying kissing defects have been identified. A kissing defect must have an effect on the strength of the bonded joint and must be of approximately zero volume. If a bond is to fail due to the presence of a kissing defect then it must fail via adhesive failure. A review of methods of experimentally simulated defects has been presented, identifying several methods that have been applied to composite materials and adhesive bonds. A problem identifying kissing defects in the MkIII LNG carrier at the bondline between the primary and secondary insulation has been highlighted and it is known that current inspection procedures are unable to identify such defects. Current NDE techniques used across a wider range of industries shall be studied in the following chapter.

3. Non-destructive evaluation

3.1 Introduction

The current chapter introduces a wide range of NDE inspection techniques currently used for the assessment of structures. Such techniques may be broadly classed as either passive or active. In the current work, techniques are considered passive if no additional stimulus or excitation is added to the structure or component for the purpose of the NDE technique. Hence, a NDE approach applied while a system is operational, which uses operational loading to obtain information about the system, is classed as passive. Active NDE techniques are considered as those that require the application of a load or stimulation other than that experienced in operation, to enable inspection of the component.

A literature survey was undertaken to identify current NDE techniques used to assess composite materials. An overview of the basic principles and the mode of operation of each technique is provided. A literature survey covering the application of current NDE techniques used for the inspection of adhesive bonds is also included. Based on the literature survey, judgments are made as to whether specific techniques are suited to the inspection of adhesive bonds for use as an on-site assessment tool with particular reference to Triplex bonds. The primary criteria introduced when considering the on-site inspection of bonded joints, including Triplex joints, include:

- Single sided access
- Efficiency
- Sensitivity
- Portability / practicalities
- Excitation source
- Data interpretation

These factors will aid in the assessment and comparison of the practicalities of implementation of the NDE techniques in a manufacturing environment. The techniques are summarised at the end of the chapter highlighting the

techniques suited to onsite bond line inspections and highlighting the course the remainder of the work shall follow.

3.2 Current non-destructive evaluation techniques

As the use of composite materials in the aerospace industry has increased greatly in recent years, a series of ASTM standards have been developed covering the application of a range of NDE procedures to aerospace composites. These include: ultrasound (ASTM E2580), shearography (ASTM E2581-07), acoustic emission (ASTM E2661/E2661M-10), radiography (ASTM E2662-09) and flash thermography (ASTM E2582-07). The remainder of this section shall focus at looking at the application of these and other techniques to composite materials.

3.2.1 Ultrasonic testing

Methodology

Ultrasonic testing (UT) is a widely used NDE technique [4]. UT relies on the propagation of high frequency sound waves through a medium to reveal information about that structure through measurement of the signals reflected from discontinuities. ASTM 2580 focusses on the application of 'pitch catch' and 'pulse echo' to composite materials using 0.5 to 20 MHz transducers. In a pulse echo test a single piezoelectric transducer is used as pulser and receiver, see Figure 5. The transducer is positioned perpendicular to the material surface and the sound waves penetrate the material in that direction. As the sound waves reach a boundary or area of differing density some of the waves are reflected. The reflected signal will be received by the transducer. Areas of different densities can be mapped through the thickness of the material and hence defects detected. This type of measurement is a point by point process and the lateral resolution is dependent upon the distance between measurements. The depth resolution is dependent on the frequency of the probe used. A higher frequency probe can resolve smaller thicknesses but will be more quickly attenuated, so will be limited to shallower depths. A lower frequency probe can penetrate much deeper but will not resolve features that are thinner than its wavelength. The properties of the material in question

determine what frequency probe is suitable for use to detect defects as increasingly dense or inhomogeneous materials will attenuate the ultrasound signal more quickly. A C-scan may also be taken using a pitch-catch approach where separate pulser and receiver transducers are positioned on opposite sides of the component. This has the advantage of only having to travel through the thickness of material once but cannot then give any information about the depth of the defect; rather it gives shadow style information about the lateral location of defects.

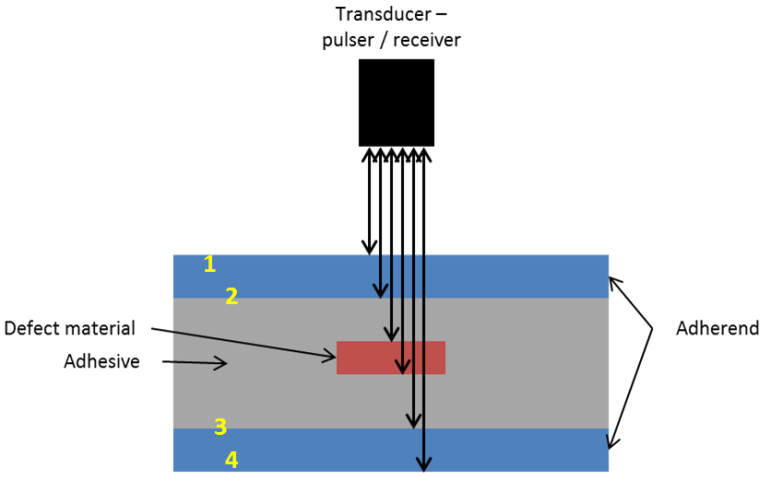

Figure 5 Schematic of ultrasonic C-scan in pulse echo mode inspecting a bonded joint with interfaces numbered to correspond to oscilloscope trace peaks in Figure 6.

A live oscilloscope trace of the signal received, known as an A-scan, shown in Figure 6, may be directly assessed by trained personnel. To produce a C-scan, the magnitude of the peaks of interest are recorded and related to a surface position enabling a 2D map of the sample to be created. Figure 6 shows such a trace and highlights peaks 1 - 4 that correspond to the interfaces in the adhesive bond sample schematically drawn in Figure 5. Peaks may be identified using knowledge of the speed of sound in the medium so an estimate of the time a peak would be expected to occur can be found. This enables the interfaces of interest amongst noise to be studied.

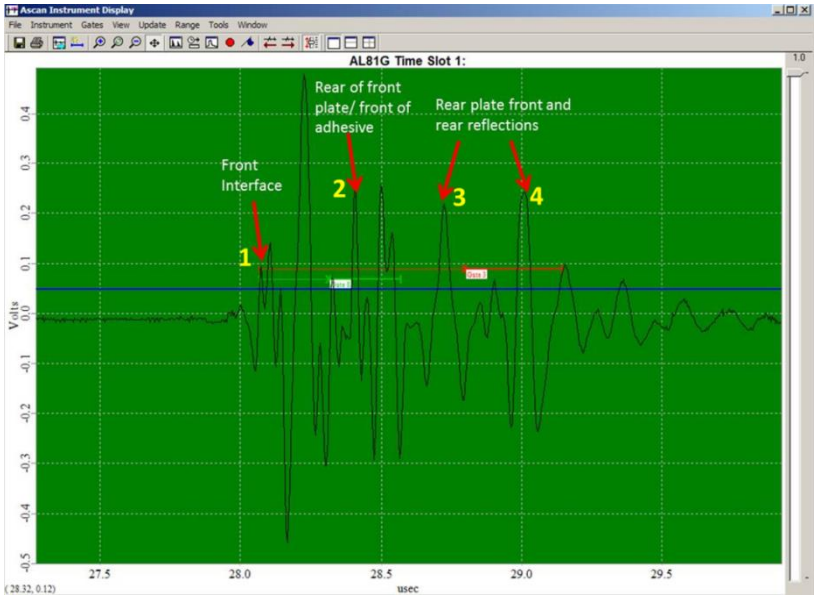

Figure 6 Sample oscilloscope trace with time on the x axis for a 1.2 mm thick CFRP-CFRP single lap joint which is used to identify key areas of the joint and set data collection windows for an ultrasonic C-scan.

Traditionally, UT requires coupling of the transducer to the component. Immersion UT is a well-established technique which submerges a component in a water bath for inspection [51]. This requires the component to be taken out of service to be inspected. Water coupled UT may also be produced using water jets but due to the water use of this tend to be limited to manufacturing lines where a stationary setup may be used [52]. There are more portable techniques, including hand held UT methods, which require only local coupling using a gel coupling agent, however these are less sensitive than immersion UT [53]. Air coupled ultrasound has also been developed, however results have been mixed and it is generally accepted that this method is less sensitive and more difficult to carryout than conventional UT [54, 55]. The point-by-point nature of conventional UT means that scans are reported to be up to 60 times more time consuming [56] than other full field methods such as thermography and shearography [57], which will be discussed in subsequent sections.

Applications

A significant amount of current UT research is focused on the aerospace industry to enhance defect detectability. One such work examines the effect of the angle of incidence of the transducer and receiver on detectability of small (10 x 10 mm and 20 x 5 mm) delaminations in a CFRP laminate [58]. It was

found that by changing the incidence angle of the transducer to 45° it was possible to enhance reflected signals from delamination style defects increasing the chances of their detection using 5 MHz transducer. A finite element approach was also developed, which validated these findings and gave a tool to investigate angle of incidence without the need for costly experiments. A significant amount of research into the application of adaptations of basic C-scan UT to enable enhanced defect detection through various mathematical analysis of the different types of waves, which are found to indicate defects [59]. The most widely used nonstandard UT technique is the use of Lamb waves, also known as plate waves. Lamb waves are produced when a piezoelectric transducer is coupled at 90° to the surface and a receiver is positioned elsewhere on the component surface to allow the material between them to be inspected. The use of Lamb waves gives the ability to investigate a line of material at a time, increasing the rate of inspection compared to a C-scan.

3.2.2 Radiography

Methodology

Radiography uses electromagnetic radiation, typically X-rays, to penetrate components to give information on the sub surface structure. Radiography is carried out in transmission with the X-ray source at one side of the component and a screen of material that reacts with the received radiation on the other side. The level of radiation received is dependent upon the density and thickness of the materials it passes though. Traditionally the screen is a photographic film that would then have to be developed making the process time consuming, however digital approaches where a screen is made of a material that fluoresces when radiation is incident allows for real-time radiography (RTR) [60]. A single image is produced showing variations in density of thickness across a component and so gives no information about the depth of any feature revealed. RTR is used in a range of industries including aerospace and automotive.

Computed tomography (CT) may be used to produce 2D or 3D cross sections of a component [61]. CT uses the same transmission setup as RTR but places the component being inspected on a turntable. The X-ray images obtained are

then related to the position of the turntable and may then be reconstructed into a 3D image, enabling cross sectional data to be obtained through the component.

Applications

A limiting factor in the use of radiography is that it is always carried out in transmission, which requires access to both sides of the component of interest, which is impractical in many cases. The detection of defects using radiography is greatly affected by the orientation of the radiation source to the defect of interest and as such requires a skilled and experienced worker for successful application [62]. The use of ionising radiation has costly health and safety guidelines associated with it [63]. While X-rays have the ability to scan thick materials with better resolution than UT, it is not very sensitive to very shallow defects or delaminations in the material as the penetrating radiation is minimally affected by the thin defects. In order to identify thin defects a penetrant dye must be used to enhance the contrast produced, which adds complexity and risk of contamination as well as additional time to the application of the technique [4]. Microtomographic approaches using X-ray computed tomography (CT) have been developed which have extremely high resolution, able to detect single fibre breaks in composites, however these are laboratory based methods which cannot be taken into the field [61].

An alternative radiation source that has been used is microwave radiation which has the advantage of being able to penetrate insulating materials while having a reduced health and safety protocol [64]. Microwave NDE has shown great promise for inspecting materials that are concealed by an insulating material including the inspection of far side face sheet of composite sandwich panels [65]. Defects including face sheet debonding, impact damage and core cracking in composite sandwich panels were all able to be identified. Use of a technique able to assess through insulation could be very cost effective. Whilst for the case of composite sandwich panels this process shows high potential, due to the inherent nature of microwaves being unable to penetrate metals they are only able to identify surface corrosion on metals although such an inspection could be carried out through insulation materials such as pipe lagging [65]. However, microwave signals are greatly affected by

communications networks and so can only be carried out during 'quiet' times on site.

3.2.3 Eddy current

Methodology

Electrical currents are induced in conducting materials by bring a fluctuating magnetic field, typically created by passing an alternating current through a coil, close to the material. These currents flow in a circular path and are known as eddy currents. Variations in the voltage or impedance identified by a second coil can be used to identify flaws in the material. The depth able to be investigated is proportional to the frequency of the alternating current supplied, as a higher frequency will reduce the depth of the eddy currents created [66].

Applications

Eddy current NDE, traditionally developed for highly conductive metals, may also be applied to less conductive carbon fibre composites [67]. The anisotropy of the electrical conductivity of the fibres allows information such as fibre orientation and distribution to be obtained and indications of flaws may be found. Delamination between CFRP fibres and resin may also be detected [66]. The use of higher frequency alternating currents also allows capacitance effects to be exploited to provide matrix properties [68]. The process relies on features of the material electrical conductivity to identify such characteristics, therefore this technology is only useful when considering electrically conductive materials and so is not more widely applicable [69].

3.2.4 Shearography

Methodology

Shearography involves the production of a laser speckle pattern on the surface of the material under investigation. The speckle pattern is compared for a loaded and unloaded state using a shearing device, such as a Michelson interferometer, to identify any change in the speckle pattern that is caused by deformation of the material surface [70]. Mechanical loading is typically used;

however, thermal loading may also be used in less accessible locations. The main advantage of thermal loading is its non-contact nature, however it is also more difficult to apply a uniform thermal load across an area. A defect detected using shearography produces an interference fringe pattern due to a surface deformation in response to an applied stress. The type of fringe pattern produced depends upon the size, nature, location of the defect as well as the stress at the site of the defect [71]. As such, determination of the true extent of a defect should be carried out by an experienced user.

Applications

Shearography has been found to be an effective non-contact tool to detect near surface damage such as face sheet detachment in sandwich structures, fibre waviness and delaminations [72]. Laser shearography is capable of detecting surface deformations of only a few microns and as such is a highly sensitive tool [73]. Whilst generally shearography is only able to reveal defects in the near surface region a shearographic endoscope has been developed that is able to look at interior surfaces [74], however this device is only useful when considering partially enclosed surfaces.

3.2.5 Thermography

Methodology

Thermographic NDE has the ability to inspect large areas in short periods of time with easily interpretable results [9]. Thermography requires the creation of a temperature gradient between defect and non-defect regions to enable defect detection [33].

Active thermography may be carried out using either transmission or reflection modes [75], see Figure 7a. Transmission mode is when the heat source and detector are on opposite sides of the sample being tested and may be useful where access to both sides of the sample is possible to ensure testing of the full thickness of material is taking place. Reflection mode has both source and detector on the same side of the material, see Figure 7b. The evolution of the temperature of the heated surface is studied. The observed surface temperature will change uniformly as the thermal front travels through material of constant thermal properties. If the thermal front meets a volume of

different thermal properties its rate of propagation will change. If this variation of property is caused by a defect smaller than the observation area, a region of different temperature will appear on the observed surface [76], see Figure 8. For example, for a defect such as a void a region of elevated temperature is produced. The region of elevated temperature is then either conducted laterally around the defect or conducts through the defect depending on the type and geometry of the defect. The time at which the variation in surface temperature occurs is dependent on the depth of the defect theoretically allowing a relationship to be established predicting defect depth. However, this has only had limited success for specific materials or defect geometries [77, 78].

The thickness of the material able to be tested depends upon the sample composition, the heat source and the detector sensitivity. Maximum ranges in different materials must be known for a particular set up to be used confidently on any specific material configuration.

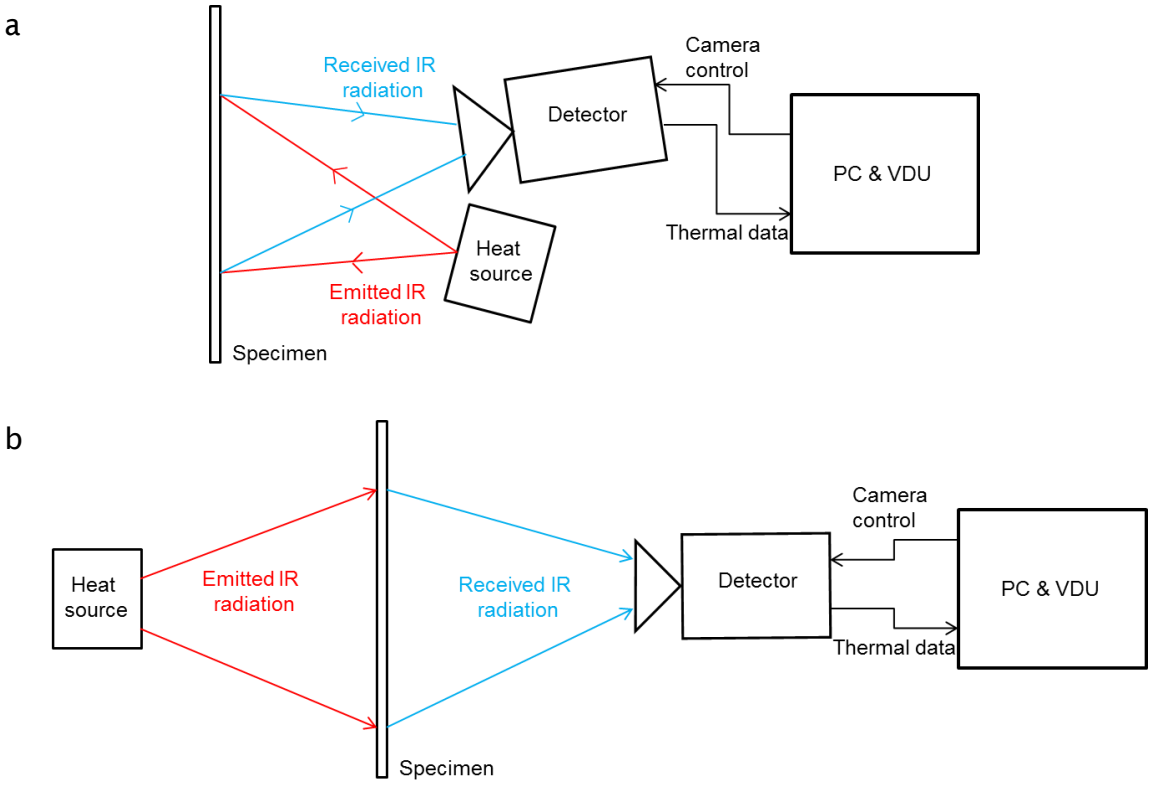

Figure 7 Schematic diagrams of thermographic NDE in transmission and reflection setup.

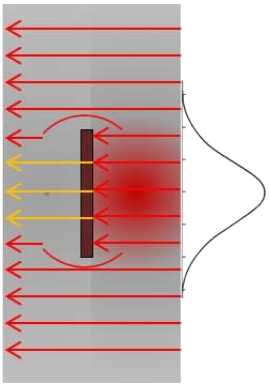

Figure 8 Thermal front propagation (right to left in image) through a material with a defect of lower thermal conductivity than the bulk material, highlighting a non-uniform temperature distribution on the front (right) surface.

Applications

Passive thermography

The most frequently used thermographic methods are passive [4]. Passive thermography may be used to study the integrity of the materials, such as using the natural temperature gradient that occurs as gas passes through pipes to detect wall thinning [79]. The distribution of induction heating applied to cure adhesives or resins may be monitored to ensure activation energy is reached across the whole area of the bond to enable complete curing [80]. Passive thermography has also been used to monitor tensile tests carried out on glass fibre reinforced plastic (GFRP) samples undergoing a range of static tensile loads [81]. The variation of thermoelastic constant with applied stress was established as a damage parameter to evaluate the global damage state of the GFRP specimen which was able to provide damage state information at a range applied of stresses. In an additional study passive thermography has also been used to identify failure initiation in GFRP samples in static tensile tests [82]. Three regions are identified in the tests using thermographic data including the thermoelastic and the elastic regions and finally the plastic region where failure is initiated.

Active thermography

There are numerous variations of active thermography that utilise different means of loading to create a thermal gradient, including mechanical, thermal and electromagnetic excitation. In vibrothermography the structure is subject

to a mechanical vibration load that causes any defect or crack surfaces to vibrate relative to each other causing a localised heating which may then be detected on the surface over the defect [83]. Microwave radiation has been used to stimulate larger concrete structures to detect steel reinforcement when considering the use of thermography in civil engineering applications [84]. The main disadvantage of x-ray stimulation is the health and safety issues associated with the use of such radiation, involving the use of shielding as in [84] or an exclusion zone being enforced, which impacts on other work being carried out. Eddy currents have been used as a heating source that does not rely on just surface heating but rather penetrates to the skin depth, which is dependent on the strength of the eddy current [85], which was found to increase the temperature contrast between defective and defect free regions [86]. Eddy current thermography is restricted to electronically conductive materials. Thermal loading may be implemented using air jets or more typically heat sources such as lights or heat lamps.

In Avdelidis *et al* [87] a thermographic assessment of boron and carbon patches on aircraft was carried out to assess the structural properties of bonded repair patches compared to the original, undamaged structure. They used a portable NDE 'thermoscope' to collect the experimental data, which was then analysed to give defect sizes. It was noted that for composite materials, the highest thermal contrast image was found at notably longer lag times after the heat pulse was applied for the same defect geometry and location. However, a defect size may be obtained after a much shorter period.

Thermoelastic stress analysis

Thermoelastic stress analysis (TSA) is a type of active thermography which uses an infrared detector to monitor the surface temperature of a component while it is undergoing elastic cyclic tensile loading. A change in temperature is observed throughout loading due to the thermoelastic effect [88]. A lock-in process is then used to compare the thermal response detected and the loading cycle, which produces a mean temperature signal, T, and a temperature change response, ΔT. The recorded thermal data may then be related to the change in the sum of the principal stresses, $\Delta\sigma_{11}+\Delta\sigma_{22}$, in an orthotropic material using [89]:

$$\Delta T = -\frac{T}{\rho C_p}\left(\alpha_{11}\Delta\sigma_{11} + \alpha_{22}\Delta\sigma_{22}\right) \quad (3.1)$$

where α_{11} and α_{22} are the coefficients of thermal expansion in the principal material directions, and ρ and C_p are the density and specific heat of the material respectively.

TSA has been widely used on metals to identify crack tip stresses [90, 91]. It has also been applied to composite materials where it was found to be possible to identify delamination [92]. Identification of stress concentrations has been used in the assessment of composite joint design [93]. Previous work has also looked at the categorisation of static damage initiation and progression in single lap bonded joints using TSA [94].

3.2.6 Acoustic emission

Methodology

Acoustic emission (AE) relies on the use of piezoelectric sensors to monitor for signals produced by stress wave propagation as a defect develops [53]. AE can inspect a large area at once and can detect events such as fibre breakage, matrix cracking and delamination; however it relies on the structure being stressed during inspection. While for some applications sensors only need to be sensitive to a narrow range of frequencies, application to composite materials requires the use of broad band sensors which makes the process more susceptible to environmental noise [95].

Applications

AE was used to evaluate the quality of repairs made to GFRP samples and to identify their failure mechanisms [96]. Undamaged, impact damaged, scarf repaired and uniform lap repaired samples were loaded in tension. Lap repaired samples were found to give more predictable damage whereas the scarfed repairs gave more distributed AE signals across the whole repair region making failure modes less predictable. AE has also been used to identify if impact damage affected the serviceability of a lightweight anti-tank gun [95]. Composite cylinders were impacted using energies between 3 and 18 J before

being pressurised to rupture. AE was used to relate the extent of damage to the serviceability of the tubes.

3.3 Non-destructive evaluation of bonded joints

A few standards exist for the NDE inspection of adhesive bonds in composite materials, these include: ASTM E1495/ E1495M (acousto-ultrasonics), ASTM E2582-7 (flash thermography) and ASTM STP1184 (acoustic emission). However, it is widely accepted that conventional NDE techniques are not currently able to identify all types of defects that occur in adhesive bonds, specifically kissing bonds [66]. This section aims to summarise a literature survey of key investigations into the detection of defects in adhesive bonds that go beyond the standardised approaches.

Acousto-ultrasonics (AU) is a combination of acoustic emission and ultrasound as an ultrasonic source is used to 'load' the sample and the ability of a component to transfer strain energy introduced by the small stresses caused by the ultrasonic excitation. A correlation was found between AU measurements and strength of lap shear bonded composites in [97]. However, AU does not allow defects to be visualised, rather gives a measure of their effect on the strength of the bond.

As UT is one of the most commonly used methods for composite inspection most research into the development of a tool for adhesive bonds has focused on advanced forms of UT [3]. Standard C-scan UT is currently used for NDE of bonded joints in the aerospace industry during manufacture [72]. However the time consuming point by point nature and water coupling of this approach make it difficult to implement on site. Application of Lamb waves to for identification of debonds in adhesive bonds is the subject of several investigations as they may be used without direct access to the joints, e.g.[98, 99]. Pitch catch and pulse echo techniques are compared for inspection of bond lines using Lamb waves [98]. Pitch catch inspection undertaken with the pulser on one adherend and receiver on the other, recording the signal that has passed through the bond line. Pulse echo relies on flaws in the bond line to reflect that signal back to a single pulser/receiver. An impedance method was also used in [98] to inspect along the length of the bond line. Bond line

defects in this work were simulated by PTFE patches. In [99] bonds are aged and inspected as their stiffness is reduced. A Fourier transform is applied to Lamb waves sent along the bond to obtain a frequency spectrum, or dispersion curves, which are found to be related to the stiffness of bonded joints as they are aged.

Shearography, has been used for identification of defects in adhesive joints in materials including aluminium and CFRP using flat bottom hole defects in the bond lines [100]. Shearography has been found to be able to identify a range of defects including inserts and adhesive starvation in adhesive bonds in rubber, CFRP and ceramics [101]. The main drawback found with shearography was the interpretation of the fringe pattern results is required to be carried out by trained personnel. There has been some work towards automation of the procedure [102]but this is not wide spread.

As mentioned previously, acoustic emission [103] is currently used to look for bonding defects in the MkIII carrier once the whole tank has been constructed. Acoustic emissions have also been used to assess bonding integrity for a rocket motor case [104]. Finite element analysis (FEA) was incorporated with the acoustic emission data to provide threshold readings to relate an acoustic emission signal rate to a threshold level that correlates to a strain distribution over the bond.

In the literature thermographic techniques have been tested for specific applications of bonded joints. A composite truck box with adhesively bonded joints was tested using PT to identify mechanical damage in the composite panels and disbonds in the adhesive joints [105]. The bond defect found using PT was then identified as a starved bond where insufficient force was applied to fully adhere the bond; this may therefore be considered as a void or delamination of the bond line. As this type of defect has a volume filled with air it is not considered a kissing defect and so is able to be identified. Bonded joints between CFRP reinforcement patches and concrete have been assessed using PT to identify a range of defect types including unbonding, where no adhesive is present, delaminations, where CFRP patches delaminate from each other, and finally debonding, where a defect occurs between the CFRP and concrete [106]. Variations in the pulse duration and heat lamp to sample distance were studied and minimum strength and pulse durations were

suggested to study such composite repairs. Omar *et al* [13] used thermography in transmission mode to study bond integrity of a plastic welded joint between two cups. The technique used boiling water in one of the cups as the heat source and qualitatively identified areas of differing thermal conductivity through the thickness of the joint. The paper then considers pulsed thermography in reflection mode for a more practical NDE approach. Results show this method was able to identify areas of delamination in the bonded region. While this paper classes these defects as kissing defects, it simultaneously classes them as delaminations, which appear to have a volume associated with them. The defects found in this case do not appear to fit within the categorisation of kissing defects defined previously in this work.

3.4 Summary

Criteria required for the practical assessment of bonded joints were suggested in Section 3.1. A summary of the techniques covered is presented in Table 1, which shows the suitability of each assessment method when considering the suggested criteria for robust inspection in a timely manner. Radiography does not allow single sided access and has strong health and safety requirements associated with the use of sources of radiation that make it unsuitable when considering its use in an construction environment where stopping manufacturing is not feasible. Eddy current inspection is limited to use on electrically conductive materials. When considering the development of a technique for application to composites preference is given to an approach that could be used across a wider range of materials. Acoustic emission has been shown to be a powerful technique however, it relies on the whole structure being stressed, therefore application to part of an engineering structure while work is carried out elsewhere on the structure is not feasible. Noise from surrounding work would also be a problem where broadband sensors were used. Ultrasonic methods are varied and hold a lot of potential however they tend to be time consuming and most are reliant on being coupled to the structure. Currently portable techniques do not match the capabilities of immersion UT.

Table 1 The potential for NDE techniques to be used for assessment of composite structures and bonded joints.

NDE Technique	Single sided access	Efficiency	Sensitivity to noise	Portability/ practicalities	Excitation source	Data interpretation
Ultrasonic testing	Yes – pulse-echo or pitch-catch	Point by point or line scan	Minimal	Possible but accuracy decreased compared to immersion UT	Ultrasound	Oscilloscope trace for peak detection but can be visualised
Radiography	No	RTR – live image	Microwaves sensitive to communications	Health and safety requirements	Generally X-ray	Image showing variations in density across plate
Eddy current	Yes	Local	Sensitive to magnetic fields	Yes	Fluctuating magnetic field	Visualised showing local effects on eddycurrents
Shearography	Yes	Local Full field	Sensitive to rigid body motion	Yes	Mechanical or heat	Interference fringe pattern
Thermography	Yes – transmission or reflection mode	Local Full field	Minimal	Yes	Heat – lamps, air, mechanical etc. / passive	Image showing thermal variations across the surface
Acoustic emission	Yes	Whole structure	Broadband sensors are sensitive to noise	Yes	Stress whole structure / passive	Accumulated hits, related to position through triangulation

Both shearography and thermography are relatively efficient full field techniques that may be well suited to a manufacturing environment. The main distinguishing factor between the two in terms of practicalities of use is the interpretation of data. The interference pattern produced in shearography will require an increased level of training for accurate interpretation when compared to the thermal images which shown defects more clearly. Therefore, the technique this work focuses on is infrared thermography, which is discussed in more detail in the following chapter. While the limits of thermographic applications are primarily in the depth of the material able to be investigated, the fast application time, full field nature and portability of the technique highlight thermography as a technique worth exploring.

4. The physics and implementation of thermography

4.1 Introduction

In the previous chapter thermography has been shown to have potential for the identification of defects in adhesive bonds. The current chapter will initially provide an in depth review of the main types of thermography that use the addition of energy from light sources, namely pulsed, lock-in and pulse phase thermography. The types of detectors that may be used for these techniques are then considered. The underpinning physics of heat transfer that enables the detection of defects using thermography are then introduced before interpretation of the thermal data to extract estimated defect size is discussed. The practicalities of experimentation using thermography are then introduced including the experimental setup. Software and data collection and processing methods used in the current work are introduced and the importance of various variables studied. From this investigation knowledge of the importance of the experimental parameters is obtained and used in the remainder of experimental work.

4.2 Types of thermography

While it has been mentioned that a range of forms of heating may be used in active thermography the current work will focus specifically on heating from light sources as this is suitable for applications where the material is not electrically conductive, does not result in the need for health and safety protocols and remains non-contact.

Lock in thermography

In lock in thermography (LT) heating is applied to the surface of the component via a continuous sinusoidal stimulus. The sinusoidal signal from the heat source and the corresponding sinusoidal surface temperature signal from the IR detector are correlated [107]. Typically, a fast Fourier transform (FFT) is used to find magnitude and phase values, although other algorithms

have been investigated [108-110]. The phase values collected reveal information about the variation between the heating signal and the component's thermal response. The attenuation of the signal is dependent upon the frequency of the input wave. A high frequency signal is quickly attenuated and so is only able to probe shallow depths. Lower frequencies are able to probe deeper but with reduced resolution due to the increased wavelength. The depth to which a specific frequency is able to interrogate is dependent on the component material. The LT experiment is repeated using various frequency heat sources to probe different depths throughout the thickness of a component. Phase values produced by the FFT are less affected by surface characteristics of the material or uneven heating and so allow deeper probing than the IR data taken directly from the detector. The range of phase values produced between defect and defect-free areas is dependent on the size and depth of the defect [111].

Pulsed thermography

Pulsed thermography (PT) involves the application of a pulse of thermal stimulation to the surface of a material. Where as in LT a single frequency is applied to the surface of the component of interest, in pulsed thermography (PT) a pulse of heat containing many frequencies is deposited on the surface. This negates the need for repeated experiments at different frequencies thus being very time efficient. In the current work pulsed thermography is considered to include the direct assessment of the thermal data collected or some basic processing such as contrast images and background subtractions.

Pulse phase thermography

Pulse phase thermography (PPT) combines the single experiment approach of PT with the data processing of LT. The pulsed signal is then processed using the FFT to obtain phase values as in LT. The extraction of phase values enables deeper probing than is possible using PT due to the reduced influence of reflections, optical surface effects and uneven heating [33]. Further discussion into the processing of the IR data is discussed in detail in section 04.6.3.

Applications

The following section focuses on the introduction to a range of applications of PT, LT and PPT within the literature to give a background of previous applications that have been assessed. The distinctions between different variations of thermography vary between authors, however in the current thesis the understanding of PT, LT and PPT shall remain as detailed in the previous section.

Ibarra-Castanedo *et al* [112], assessed the application of infrared thermography techniques to aircraft materials and their ability to detect typical aircraft defects which included: delaminations, moisture ingress, impact sites and failure at the interface between the aluminium honeycomb and a CFRP face sheet. The active infrared techniques that were assessed include PPT, LT, vibrothermography (ultrasound excited thermography) and eddy current thermography (ECT). It was found that in general the optical techniques, PPT and LT, performed well and were able to detect most defects with acceptable resolution. The use of thermal signal reconstruction (TSR) enabled deeper probing down to depths of 2.5 mm in CFRP. A threshold depth-to-size ratio of approximately 2 was found, which was higher than that of earlier work [9]. The PPT was able to detect all the different types of defect, apart from failure at the honeycomb/face sheet interface, which was only detected by the ECT. The ECT was able to detect the defect as use of eddy currents heats the site of the defect due to its resistance to the electrical current.

PT and square pulsed thermography (SPT), where a longer heating pulse is used, has been applied to natural fibre laminates with static impact damage [36]. It was found that PT was able to identify different types of defects whereas SPT was reported to give information about the shape of the impact while undergoing the same post processing. The difference in these two experimental approaches is the duration over which energy is added to the system and that during the SPT experiments a detector designed to record longer wavelengths was used compared to the short wavelength spectrum of detectors used for the PT and typically used in thermography studies as discussed in Section 4.3. The different types of features observed may be due to the different observation frequencies studied. SPT has also been used to

compare impact damage between laminates made of glass fibres and basalt fibres [35].

A study to assess bonded repairs using graphite epoxy composite patches on aircraft has also been carried out using PT and PPT [37]. The bond line was inspected for signs of delamination and disbonds. The system was first trialled for the identification of artificial Teflon defects inserted into the bond line before samples were manufactured, which were known to fail in particular locations, thus allowing identification of real disbonds. PPT was again found to give clearer images of disbonded regions, providing a less subjective result than PT.

To date, PPT has been successfully tested on its ability to detect defects in a range of different materials including aluminium (maximum resolved defect depth of 5 mm) [30], acrylic (8 mm), copper (2 mm) and ceramic (5 mm) [30], steel (4.5 mm) [113] and CFRP (2.5 mm) [77].

A range of active thermographic methods and associated equipment and theory have been reported in more detail. The main techniques of interest for the current work were found to be PT and PPT as they allow more efficient testing when compared to LT. PPT was reported to offer improved defect detection due to the reduction in the effect of surface optical variations and increased penetration depth compared to PT although data processing was increased.

While the focus of the work is on the use of PPT, this will be compared throughout using more established methods to corroborate PPT results. TSA will be used so comparisons may be made with a more established thermographic techniques and C-scan UT is used to compare PPT with an industry standard.

4.3 IR detectors

Infrared detectors can be categorised as either thermal detectors or photon detectors [114, 115]. Photon detectors are cooled to enable higher detector performance and a fast response speed. These sensitive detectors identify the incident radiation of a set range of wavelengths that is dependent on the type

of sensor material used. Typically a detector will be sensitive to wavelengths between 2-5 μm or 8-12 μm [116]. Photon detectors produce a photovoltaic response when radiation is incident on the sensor array. Thermal detectors on the other hand are not dependent on the wavelength of incident radiation but measure the change in resistance of the sensor material used. As they are not cooled, resistance method thermal detectors are less sensitive and have a longer response time than the photon detectors. Due to the lack of a cooling system and less costly detector system, thermal detectors are far cheaper than photon detectors. The laboratory based work in this project focuses on the use of a photon detector, detailed in Section 4.6.1. However, when considering the design of a portable tool to take into a construction environment a cheaper thermal detector would be preferable. The practicalities of using a less sensitive detector for the experimental technique presented in this work should be considered once the technique has been fully developed. A higher resolution photon detector is therefore used to develop the technique while a feasibility study using a very lost cost bolometer has been carried out in Section 8.3.

4.4 Heat transfer

Thermographic approaches are based on the principles of heat transfer [117]. An application of this theory is given in [78], where an overview of depth prediction methods using thermographic data are given. All of these methods are based upon the 1D heat transfer solution given in Parker *et al* [118] which is derived in [117]. A study of diffusion through composite media based on the original work by Carslaw and Jaeger has also been carried out [119]. Work in this section begins by covering the derivation carried out in [117] to enable a fuller understanding of the physics behind thermography and then continue to summarise more recent work.

The work in [117] begins with derivation of the temperature distribution in a uniform material of depth, L, with the temperature distribution changing through the thickness, $0 < x < L$, through time. The initial input temperature function $f(x)$ varies through time and position and the surface temperatures are kept at zero.

$$\frac{\partial T}{\partial t} = \gamma \frac{\partial^2 T}{\partial x^2} \quad 0 < x < L \tag{4.1}$$

where γ is the thermal diffusivity,

$$\gamma = \frac{k}{\rho C} \tag{4.2}$$

Where k is conductivity, ρ is density, and C is specific heat.

The following boundary conditions are satisfied;

$$T = 0 \qquad x = 0,\ x = L$$
$$T = f(x) \qquad t = 0$$

Dirichlet [120] found a set of conditions where, if satisfied, a real-valued periodic function *f(x)* is equal to the sum of its Fourier series at each point where *f* is continuous. Fourier series behaviour at points of discontinuity can also be determined. These conditions, known as Dirichlet's conditions, are:

1) A finite number of discontinuities, maxima and minima exist for the function *f(x)* in a period.

2) The integral of the function is convergent and the Fourier series of that function is also convergent as the number of terms goes to infinity.

If these conditions are satisfied for the function of initial temperature *f(x)* in interval *(0, L)* it can be expanded in the sine series:

$$\sum_{n=1}^{\infty} a_n \sin \frac{n\pi x}{L} \tag{4.3}$$

where,

$$a_n = \frac{2}{L} \int_0^L f(x) \sin \frac{n\pi x}{L} dx$$

So, *T(x,t)* is defined by the following infinite series

$$T(x,t) = \sum_{n=1}^{\infty} a_n \sin \frac{n\pi x}{L} \exp\left(-\frac{n^2 \pi^2}{L} \gamma t \right) \tag{4.4}$$

where,

$$\frac{\partial T}{\partial t} = -\sum_{n=1}^{\infty} \frac{\gamma n^2 \pi^2}{L^2} a_n \sin\frac{n\pi x}{L} \exp\left(-\frac{n^2\pi^2}{L^2}\gamma t\right)$$
$$\gamma \frac{\partial^2 T}{\partial x^2} = -\sum_{n=1}^{\infty} \frac{\gamma n^2 \pi^2}{L^2} a_n \sin\frac{n\pi x}{L} \exp\left(-\frac{n^2\pi^2}{L^2}\gamma t\right) \quad (4.5)$$

Hence, $\frac{\partial T}{\partial t} = \gamma \frac{\partial^2 T}{\partial x^2}$ is satisfied.

A material with initial temperature *f(x)* and both ends thermally insulated is then considered. Using an initial cosine function an expression may be obtained with an additional initial temperature term, *u*, as the surfaces are no longer kept at *T = 0* so that

$$T(x,t) = u + \sum_{n=1}^{\infty} a_n \cos\frac{n\pi x}{L} \exp\left(-\frac{n^2\pi^2}{L}\gamma t\right) \quad (4.6)$$

It follows that,

$$a_n = \frac{2}{L}\int_0^L f(x)\cos\frac{n\pi x}{L}dx \quad (4.7)$$

and

$$u = \frac{1}{L}\int_0^L f(x)dx \quad (4.8)$$

Combining Equations (4.6), (4.7) and (4.8) gives:

$$T(x,t) = \frac{1}{L}\int_0^L T(x,0)dx + \frac{2}{L}\sum_{n=1}^{\infty} \exp\left(-\frac{n^2\pi^2\gamma t}{L^2}\right)\cos\frac{n\pi x}{L}\int_0^L T(x,0)\cos\frac{n\pi x}{L}dx \quad (4.9)$$

which represents the temperature distribution within a thermally isolated solid of uniform thickness *L*, at any time *t*, with respect to the initial temperature distribution, *T(x,0)* at depth *x*. Parker *et al* [118] used this expression as a starting point for their 1D heat transfer solution.

Considering the application of a pulse of heat, *Q*, on the front surface *(x = 0)* of a component which is instantaneously and uniformly absorbed in a small

depth, g, then the temperature distribution for that instant may be given using the material density, ρ, and heat capacity, C as follows:

$$T(x,0) = \frac{Q}{\rho C g} \qquad for \quad 0 < x < g$$
$$T(x,0) = 0 \qquad for \quad g < x < L$$

Using these initial conditions Equation (4.9) may be rewritten as:

$$T(x,t) = \frac{Q}{\rho C L}\left[1 + 2\sum_{n=1}^{\infty} \exp\left(-\frac{n^2\pi^2}{L^2}\gamma t\right)\cos\left(\frac{n\pi x}{L}\right)\frac{\sin\left(n\pi g/L\right)}{n\pi g/L}\right] \tag{4.10}$$

For insulating materials g is very small and so a small angle approximation can be used, i.e.

$$T(x,t) = \frac{Q}{\rho C L}\left[1 + 2\sum_{n=1}^{\infty} \exp\left(-\frac{n^2\pi^2}{L^2}\gamma t\right)\cos\frac{n\pi x}{L}\right] \tag{4.11}$$

For the case where $x = L$, the thermal decay on the rear surface of the plate is provided:

$$T(t) = \frac{Q}{\rho C L}\left[1 + 2\sum_{n=1}^{\infty} \exp\left(-\frac{n^2\pi^2}{L^2}\gamma t\right)\right] \tag{4.12}$$

The thermography data may then be compared in terms of the surface temperature evolution over an undamaged area compared to that over a defect. The decay of surface temperature, T, over time, t, after a known amount of heat is deposited, Q, is found as given by Equation (4.12). This equation is the exact solution of the 1D heat conduction with a plate of uniform thickness and instantaneous uniform heating across the surface.

A typical comparison of surface temperature decay over non-defective and defective areas is shown in Figure 9. It can be seen that the surface temperature over the undamaged area decreases exponentially and approaches the background temperature as time evolves. The surface temperature over the defect initially decreases at the same rate as the undamaged area. The cooling rate slows and then increases again as the material tries to approach ambient temperature. The initial slow temperature reduction rate occurs when the thermal front travelling through the material reaches the subsurface defect

causing, in this case, a reduction in the rate of heat conduction through the material and, as for any wave meeting a boundary, some reflection of the heat will occur. The acceleration in temperature reduction is caused by 3D conduction around the defect starting to play a more important role than the typically slower conduction through the defect. The extent of the importance of 3D conduction around the defect on the thermography data is proportional to the lateral extent of the defect, the specifics of how this data was collected shall be discussed in Section 4.6.1.

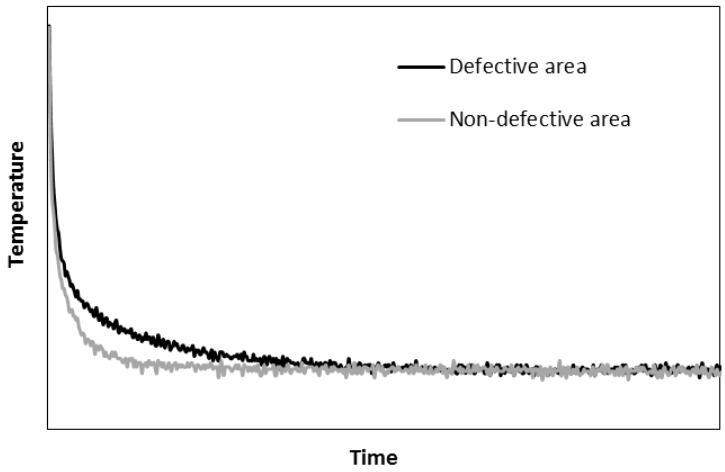

Figure 9 Thermal decay of surface temperature after application of a heat pulse over defective and non-defective material.

If the areas over defective and non-defective material are treated as two separate plates of different thickness then equation (4.12) still holds and the temperature contrast may be found as follows:

$$\Delta T = \frac{Q}{\rho C L}\left[1 + 2\sum_{n=1}^{\infty} e^{-n^2\omega}\right] - \frac{Q}{\rho C L_r}\left[1 + 2\sum_{n=1}^{\infty} e^{-n^2\omega_r}\right] \tag{4.13}$$

where a dimensionless time expression, ω, related to defective material thickness, L (see Figure 10).

$$\omega = \frac{\pi^2 \gamma t}{L^2} \tag{4.14}$$

has been substituted into Equation (4.13). A dimensionless time expression, ω_r, related to the reference non-defective material thickness, L_r, (see Figure 10) may be found in the same way.

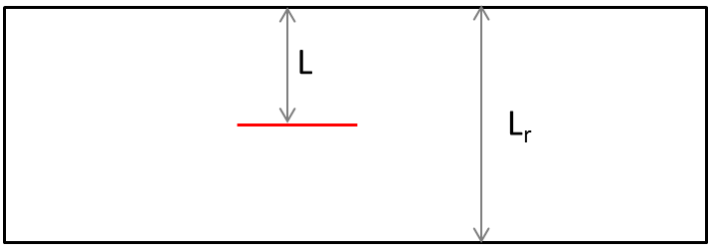

Figure 10 Schematic showing defect depth, L, and reference or full material depth, L_r, where the front surface of this sample is the top surface in the diagram.

A normalised temperature, *V*, may be introduced. This is a function of material properties, input heat, *Q*, and non-defective material thickness, L_r, giving normalised temperature contrast Δ*V*.

$$V = \frac{T\rho C L_r}{Q} \tag{4.15}$$

$$\Delta V = \frac{L_r}{L} + 2\sum_{n=1}^{\infty} e^{-n^2\omega} - 1 - 2\sum_{n=1}^{\infty} e^{-n^2\omega_r} \tag{4.16}$$

Then using y as the ratio between defect depth and non-defect material thickness $y = L/L_r$, this becomes

$$\Delta V = y^{-1} - 1 + 2\sum_{n=1}^{\infty}\left(y^{-1} e^{-n^2\omega/y^2} - e^{-n^2\omega_r} \right) \tag{4.17}$$

As is seen from Equation (4.17), as time increases the change in normalised temperature, *ΔV,* approaches $(y^{-1}-1)$. For each value of *y* after a period, a constant *ΔV* value may be found, as illustrated in Figure 11 where the lines increase and then plateau at constant values for each *y* value. As the defect depth approaches the reference depth of the material the contrast between defect and non-defect areas is reduced and the path the heat takes becomes comparable.

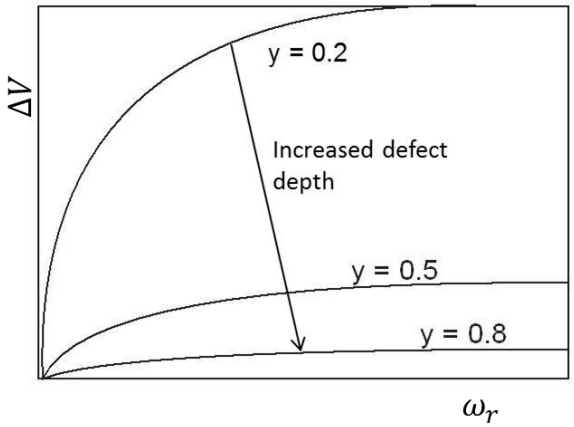

Figure 11 Temperature contrast ΔV against dimensionless time ω_r for different values of thickness ratio, y [78].

The method of considering the defective and non-defective areas as two plates does not take into account any 3D conduction that will take place. The difference in temperature will peak and then decrease again to eventually meet ambient temperature due to the presence of 3D conduction resulting in reducing ΔV values after a time, not a constant temperature difference as in Figure 11. Other processes use thermography data to define maximum temperature contrast, which has been found to be proportional to L^2. However, using this method it has also been found that the proportionality constant is proportional to the size of the defect. Smaller defects produce lower thermal contrast and a shorter peak contrast time due to the increased effect of lateral conduction around the defect. A defect with a smaller area allows the heat to be transferred around the defect faster than a larger defect thus making smaller defects harder to detect as the surface temperature hotspot magnitude decreases more quickly. Temperature contrast methods have been successfully used to show the sensitivity of systems for; minimum detectable defect size [121], the thermal resistance of a delamination air gap of various thickness [122] and insert thickness [123]. Generally, depth predictions from thermal contrast methods give good results for very large defects where 3D effects are small but for use on unknown sized defects results are not consistent or reliable. The effect of using flat bottom holes on the depth estimations has been studied [124], revealing that the sample-defect interface has a large effect on depth estimations due to the effect on heat transfer through the defective region.

4.5 Defect size prediction

Several studies have focused on being able to measure the lateral extent of defects. In Avdelidis *et al* [87] defect sizes were found using the maximum contrast thermal image and maximum contrast phase image. Maximum contrast images are the images where the variation between defective and non-defective material peaks. Line profiles are created across defective areas and the defects are sized using a full width at half maximum (FWHM) approach, shown in Figure 12. FWHM has no scientific basis and is purely an image analysis technique. It involves extracting the temperature or phase values across a defect in the maximum contrast image and then plotting the profile of these values. The edges of the defects are defined to be the point at which the temperature or phase contrast is at half its maximum value. It was found that whilst both image types produced good defect size measurements, the maximum contrast phase image was slightly more accurate.

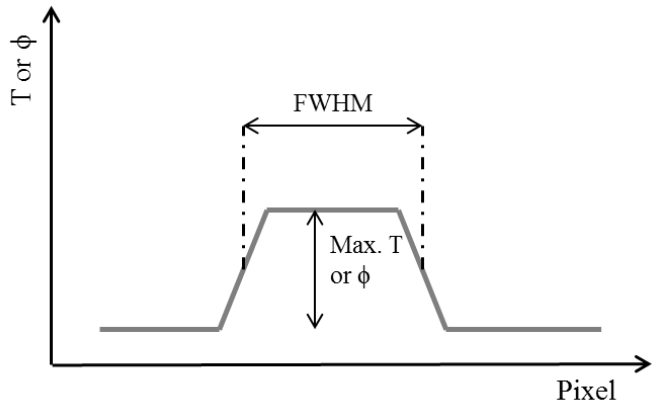

Figure 12 FWHM approach to sizing defects.

In Ibarra-Castanedo *et al* [125] it is suggested that defect sizing should take place either at the peak contrast slope, where the definition of edges is clearest, the maximum contrast where the contrast between defective and non-defective areas is greatest (as suggested in [87]), or as early as possible once the anomaly is detected in the thermal data. It is likely that the size of the defect will be over predicted as lateral thermal diffusion, i.e. 3D conductivity, takes place if defect sizing is not made from the correct thermal or phase image. Wysocka-Fotek *et al* [126] plot the time derivative data of the temperature data and apply the FWHM approach to this data to predict defect

size for a series of flat bottom holes in austenitic steel, which were then used to provide calibration for defect depth predictions in the same material.

A different method of enhancing the images to allow sizing of detects was suggested by Omar *et al* [127] which, contrary to other methods, does not require any knowledge of a non-defective area response. This technique uses the mean of the surrounding pixels of the pixel in question as the 'defect free' region subtraction for each pixel to calculate the thermal contrast image. It was highlighted that the observation area selected should be larger than the defect but small enough to not be influenced by uneven surface characteristics or uneven thermal excitation. This method can also be used when using phase images.

The current work described in the thesis focuses on the development and application of PPT to a series of samples with defects. Samples initially comprise of a single material with a foreign insert and progress to more complex multi-material bonded joints, with defects. The PPT results for detection of such defects are compared with more established NDE approaches including UT and TSA. Defect detection and location is assessed for the techniques used.

4.6 Pulsed/pulse phase thermography

In general the experimental setup has remained consistent throughout tests although some variations have occurred where necessary. The basic experimental setup and equipment used are described, with any amendments or alterations to the setup reported when such experimental data is discussed.

4.6.1 Experimental set up and data collection

The infrared (IR) detector used in this work is a FLIR Silver SC5000. This is a photon detector with an indium antimonide (InSb) sensor array of 256 x 320 pixels. This type of sensor enables the detector to be sensitive in the spectral range of 2.5-5.5 μm. A photovoltaic response to radiated photons incident on the array produces a voltage proportional to the amount of radiation which is then recorded. The detector is cooled using a Stirling pump, which maintains the operating temperature of the detector at approximately 77 K. This is a

high specification detector capable of producing a maximum, full frame, frame rate of up to 383 Hz and a thermal sensitivity of 20 mK.

Typical heat sources previously used in PPT experiments in the literature were specialist high power flash systems [77]; however in the preliminary experiments a simple inexpensive photographic flash unit was used. The use of such a flash unit greatly decreases the price of the heat source from in the order of £1500 to £150 as well reducing the cost of consumables such as replacing flash tubes. It is noted that the heat source should be tailored to the application but in some cases a cheaper and more durable unit may be suitable. The flash unit used was a Nikon Speedlight SB-600. The flash was a standalone part of the set-up run on four 1.5 V batteries and triggered manually. The flash unit had the option of varying the duration of the flash from 1/900 seconds, which is the full output, to 1/25000 seconds. The majority of experiments described in the thesis were carried out with the flash on the full power setting because it was found that the lower output settings provided insufficient heating across a sufficiently large area to detect a defect.

The experiments comprised of a pulse of heat being deposited on the surface of the specimen, the detector then received the IR radiation emitted from the surface after the pulse, as shown in Figure 13. The data is saved at defined intervals over a selected duration; the selection of these parameters is discussed in the following software section. A typical stand-off distance between detector and specimen was 250 mm and between flash and sample was 180 mm. The detector distance was selected as appropriate to view a single manufactured defect and the flash distance was tailored to the IR detector observation window size. The flash distance should ensure uniform illumination across the observation area as well as suitable strength without the flash becoming visible in the observation window. The detector always observed a flat surface and the flash and detector were always at an angle as close to normal as possible to the specimen surface, typically <10°. The shallow angle of incidence of the flash enables more uniform illumination across the sample using a single flash and the detector should be just off normal to the surface to avoid viewing its own reflection, known as the narcissus effect. The flash was aligned to point at the centre of the detector observation area. A single flash was sufficient to provide uniform heating over

this area. If a much larger region was to be observed several flashes could be connected and triggered simultaneously for more widespread uniform heating [9].

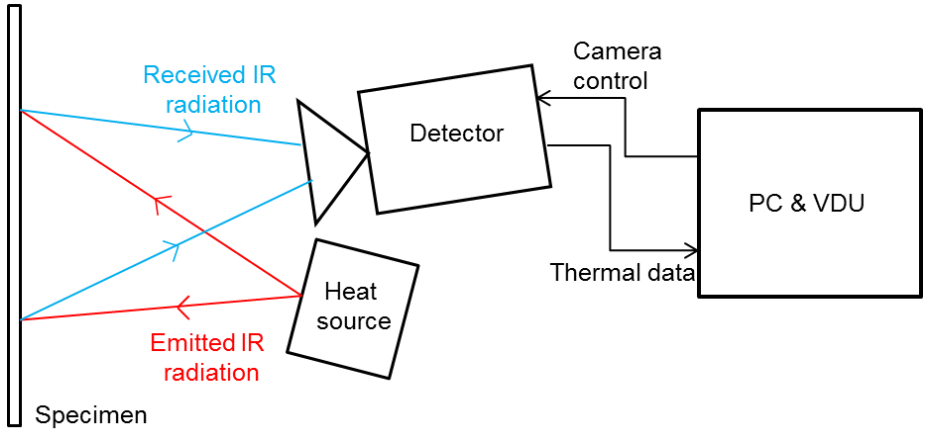

Figure 13 Schematic of PT/PPT experimental set-up.

4.6.2 Software

Three pieces of software are used to collect and process the data. These are firstly introduced and then their specific application discussed in the following section.

The Cirrus software embedded in the infrared system was used to set up the detector at the beginning of measurements. It enabled focusing of the detector and selection of an integration time. The integration time is similar to exposure time in photography, i.e. a longer integration time leads to increased sensitivity to smaller variations. A frame rate, or frequency at which data is collected, was selected and a non-uniformity correction was carried out that corrects for variations in sensitivity across the array of detector elements.

Software developed by FLIR called Altair, was used to record the IR thermography data. Frames were recorded at the sampling rate that was set in either the Cirrus software or in Altair and then saved as a sequence.

Another piece of software from FLIR, Altair LI, was used to process the data after collection. To carry out the FFT on the thermal data, without the use of a lock-in signal, the s-mode (sweep mode) in the software was used. S-mode allows the user to define the range and interval of frequencies to be sampled. The software then sweeps through these frequencies, generating sine waves to

be used as reference signals. As defects at different depths will appear at different frequencies, appropriate values for the material and thickness being tested must be selected which will be limited by the experimental sampling frequency. The Nyquist criteria states that the sampling frequency must be 5-10 times the highest frequency of interest [128]. Using the s-mode a FFT was carried out at each frequency defined.

4.6.3 Data processing

The data collected experimentally was in the form of digital level (DL) data in a sequence of images through time. A calibration is carried out using Altair to convert these DL readings to thermal data. If carrying out PT, the data was observed at this point and some basic processing undertaken, such as background temperature subtraction, to enhance the raw IR data. If carrying out PPT, Altair LI was used to process the data as shown in Figure 14. Firstly the data was converted into a series of vectors through time where each vector represents the temporal evolution of temperature for a particular pixel. A FFT was then carried out on each vector to produce real and imaginary components for the n frequencies selected. Phase and modulus values for each pixel at each frequency were then calculated and a set of phase, amplitude and average temperature images were then produced for each frequency sampled. It is the phase images that are of most interest in PPT. Each frequency selected views defects in a different depth range. It is important that the frequencies selected for the FFT are appropriate to view the material at the depths of interest. The method for frequency selection is discussed later in the current section.

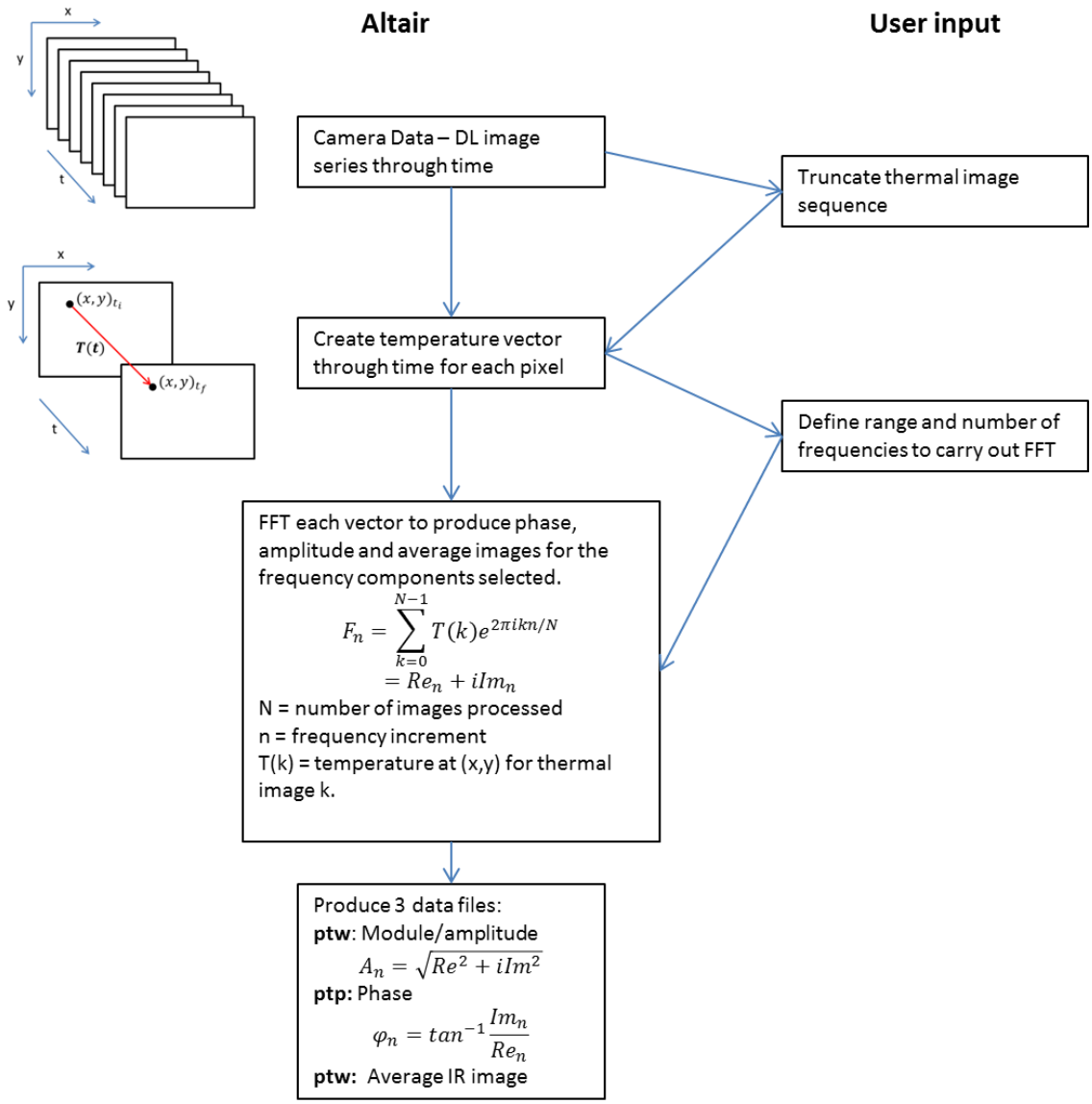

Figure 14 Flow diagram illustrating data processing routine using Altair and Altair LI.

There are several variables to be considered at this stage including; the start point of the data over which the FFT is calculated, the number of frames that are included in the FFT, i.e. the end point of the data, and the range and interval of frequencies used in the FFT. An example PTFE defect in a CFRP panel has been used to study the effect of these processing parameters on the phase contrast results between defect and non-defect areas indicated by boxes 1 and 2 in Figure 15.

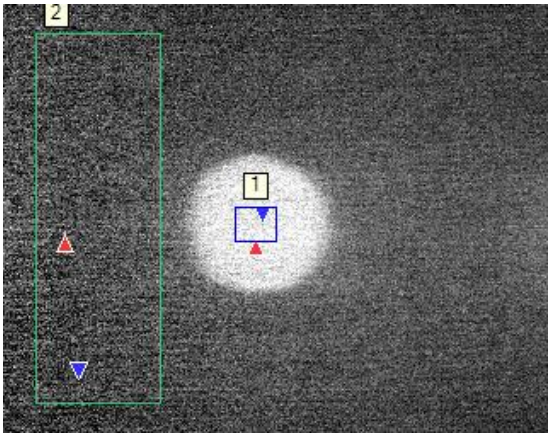

Figure 15 Phase image of CFRP panel showing defect (1) and non-defect (2) areas used for calculation of effect of processing parameters on phase contrast.

Firstly the start point of the FFT relative to the heat pulse must be chosen. The effect of variation of the start point on the phase contrast produced is shown in Figure 16 where zero time represents the frame the flash appears in and positive time is then after the flash. The error bars displayed illustrate the standard deviation for areas used to calculate the phase contrast. It is clearly shown that if the data is processed from greater than 0.2 s before or after the flash the phase contrast are greatly reduced and hence the likelihood of defect detection is decreased. From this outcome it was decided that the optimum frame for use as the first frame of the data to be processed should be the frame immediately after the flash as this was easily and consistently identifiable in experimental data either via manual or automated selection. The flash frame itself is disregarded due to the high levels of reflected IR radiation that are present, often exceeding the calibrated range of the detector. The frame immediately after the flash has been defined as the start point for the FFT in the current work. This has been defined manually, however, it would be possible to automate this.

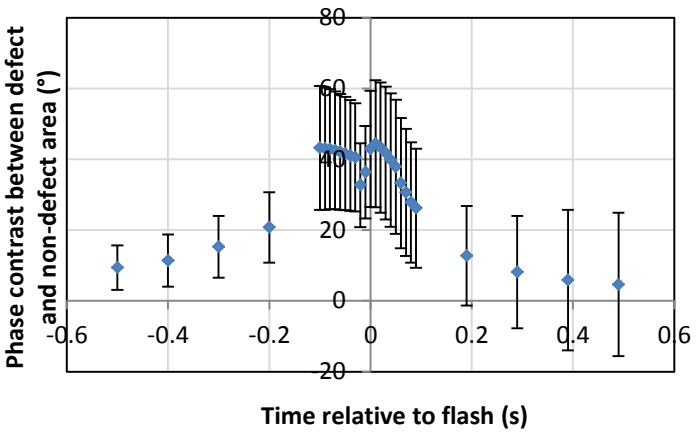

Figure 16 Effect of varying FFT start position relative to heat pulse on phase contrast.

The number of frames processed using the FFT can also be varied. The number of frames has been truncated to different lengths to find the effect of data collection duration from the frame after the pulse for the same experimental data previously considered, Figure 17. While there appears to be a peak in contrast at around 400 frames this is just for this specific defect so it should not be applied for all depths in the material. Overall there is a general decrease in phase contrast with a decrease in the number of frames or observation time after the pulse. The shorter recording periods may not capture the full thermal decay back to ambient temperature, which then leads to a reduction in phase contrast. A recording period that covers the full decay back to ambient is preferable, where there is no longer thermal contrast between defect and non-defect regions. The observation time is dependent on the material thermal properties and heat pulse and must be selected accordingly for different samples. A thermal decay plot may be used to give guidance of how long it takes for thermal equilibrium to be restored (at the front surface).

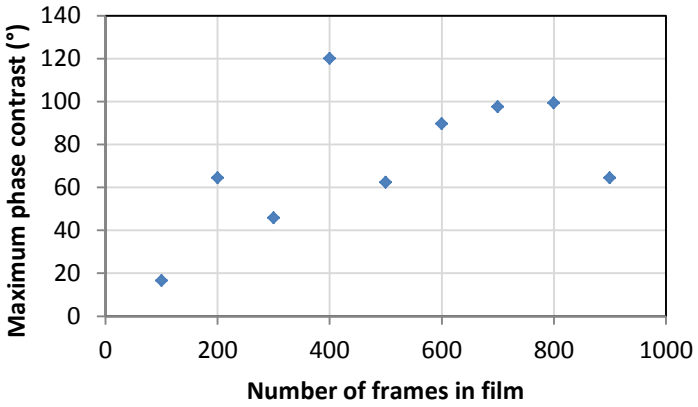

Figure 17 Variation of recording duration after heat pulse on phase contrast between defect and non-defect areas.

A final factor for consideration in the data processing is the range and interval over which the FFT is applied. The range of frequencies available, f_n, are found using

$$f_n = \frac{n}{N\Delta t} \tag{4.18}$$

where N is the number of images recorded, n = 0,1,...N/2 and Δt is the time interval between images. The maximum frequency is limited by the data collection frequency, i.e. the frame rate, and the minimum frequency is limited by the number of frames collected. Equation ((4.18) provides a large number of available frequencies. It is only the lower frequencies that are of interest as this is where the majority of the energy is contained. As an example the range and interval of frequencies have been varied to investigate how incorrect or untailored frequency selection may affect the phase contrast produced.

Figure 18 shows the effect of narrowing the range and decreasing the interval of the frequencies sampled. Each line shows the phase contrast for one frequency range and each is plotted on a scale of 0 - 100˚ between each gridline. Lines are separated for clarity. For each frequency range 11 frequency values were sampled so 11 phase images were produced. As the range was narrowed the interval between the sampled frequencies was narrowed, thus allowing the capture of the maximum phase contrast. At the largest frequency range between 0.0001 and 1 Hz the interval was 0.1 Hz whereas at the narrowest frequency range 0.5 – 0.6 Hz the interval was just

0.01 Hz. The narrower interval allows peaks to be captured more accurately, however, the time taken to process the data across the same frequency range greatly increases as the interval decreases. While at the widest interval the phase contrast does not appear to capture the peak at about 0.55 Hz this peak becomes much clearer and in the correct position in the frequency range of 0.2 – 0.8 Hz, where the frequency interval is 0.06 Hz. This means that while the maximum contrast may sometimes still be missed, using a frequency interval of 0.06 Hz is sufficient to capture the phase contrast peak for such a defect and the current experimental setup without unnecessarily increasing the data processing time. While in this case the frequency range has been focused around the frequency peak that has become visible it is important to maintain the range wide enough to sweep the whole depth of the material of interest. The frequencies used in this section are specific to the current samples however the principles of the range and interval of frequencies are the same for all cases.

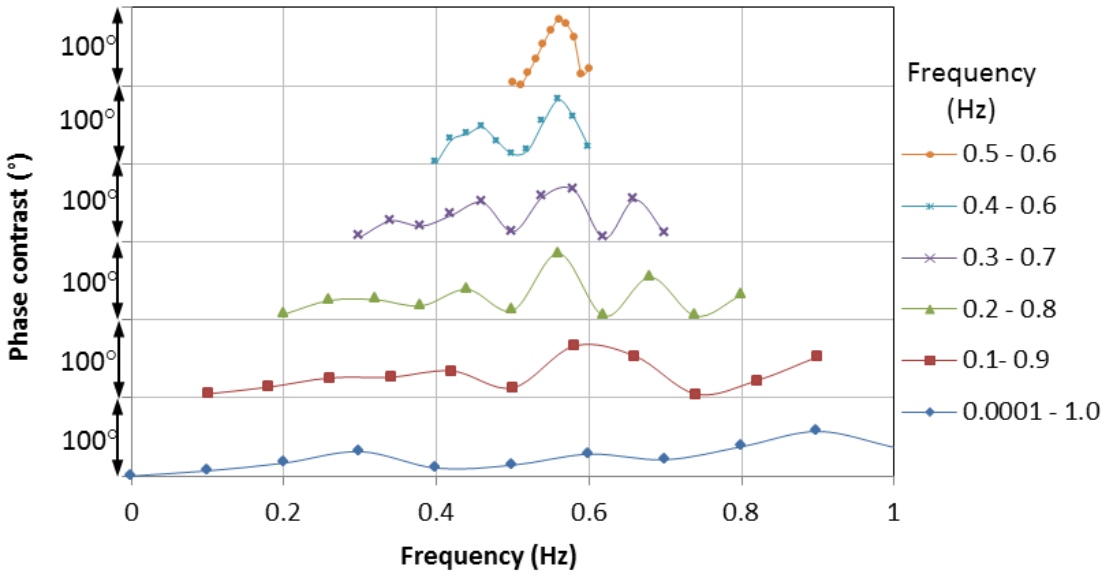

Figure 18 Phase contrast between defect and non-defect areas for a variety of frequency ranges and intervals.

Repeatability of PPT was investigated to show that the phase contrast produced between defect and non-defect areas is repeatable over several tests. The same experiment was repeated nine times for the CFRP panel with PTFE insert. The data was then processed using exactly the same parameters for all tests. Figure 19 shows that for the tests the data correlates well for each sampling

frequency, with a low amount of scatter. Generally the standard deviation of phase difference for each frequency is around 3˚ however this range is increased for the peak frequency (0.601 Hz in this case) to around 6˚. Despite this increase in spread at the peak phase contrast frequency the peak is still clear in all data sets.

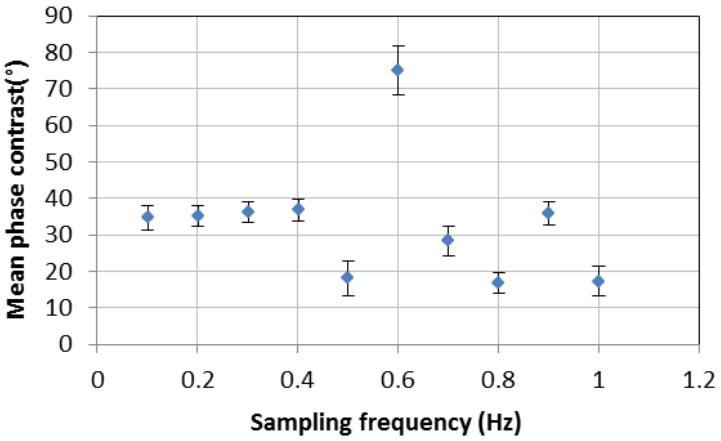

Figure 19 Frequency value used in FFT against the mean phase contrast for each sampling frequency found between defective and non-defective areas showing repeatability of phase data.

4.7 Summary

This chapter has shown the introduction of PT and PPT which are the thermographic techniques to be used throughout the remainder of this work. The principles of heat transfer which enable defect detection have been covered and IR detector types have been introduced. The work shall focus on the use of a photon type detector however may consider the use of a lower cost bolometer in its later stages.

Various aspects of the experimental setup and data collection and processing for PT and PPT have been investigated to give indications of the importance of accurate selection for future data processing. A PTFE insert in a CFRP panel was used as an example in this investigation. It was found that the selection of the start and end points of the data to be Fourier transformed had a large influence on the phase contrast produced. The frame immediately after the pulse should be selected as the initial frame to process and the sequence should be truncated once the surface temperature has returned to ambient temperature. This maximises the phase contrast while minimising the amount

of data to process. The importance of the correct selection of processing frequencies has also been highlighted for the example data. The processing of PPT data has been shown to be consistent and repeatable.

5. Preliminary results

5.1 Introduction

The current chapter covers the preliminary work that was undertaken to investigate the range of defect identification possible with PT and PPT. Preliminary tests were carried out on simple geometry samples containing thermally contrasting simulated defects, i.e. not kissing defects. A variety of test specimens have been manufactured starting with single isotropic materials to orthotropic materials to adhesive bonds incrementally building the complexity of the heat transfer. A base line study using aluminium with flat bottom hole style defects was initially carried out as an introduction to the technique in an isotropic material. Initial samples using orthotropic composite materials focused on manufacturing materials with insert style defects. Bonded samples were then created with the addition of insert style defects to develop experience in testing bonded joint configurations. In all samples experimentally simulated defects were spaced sufficiently so that they could be studied individually, without interference from surrounding defects.

To allow comparison of thermography findings to a more standard approach UT C-scans were produced for a range of samples. An Ultrasonic Sciences Limited custom built immersion ultrasound machine has been used. The system comprised of an immersion bath filled with distilled water, a 200 MHz analogue to digital converter, a computer system and a pulser-receiver unit. The transducer was driven across the sample by stepper motors mounted on the immersion tank with minimum step size 0.02 mm. A selection of transducers ranging from 2.25 to 50 MHz was available. Some UT scans were carried out at AWE Aldermaston. Unless stated otherwise all C-scans in the current work were carried out using a single transducer in the pulse echo setup.

5.2 Simulated defects in aluminium alloy

5.2.1 Test specimen

Flat bottom holes were milled into the back surface of a thin aluminium plate to provide an isotropic sample with known material properties. The plate was 1.5 mm thick and flat bottom holes were milled to a maximum depth of 1.2 mm, giving a shallowest defect depth of 0.3 mm down to a maximum of 1.3 mm in 0.2 mm intervals, detailed in Table 2 and Figure 20. Defects were made with 5, 10 and 16 mm diameters.

Table 2 Aluminium sample and defect descriptions.

Bulk material	Configuration	Defect material	Defect size	Defect depths	Total thickness
Aluminium	Flat plate with flat bottom holes milled into back surface	Air	5, 10 & 16 mm diameter milled holes	0.3 – 1.3 mm in 0.2 mm increments	1.5 mm

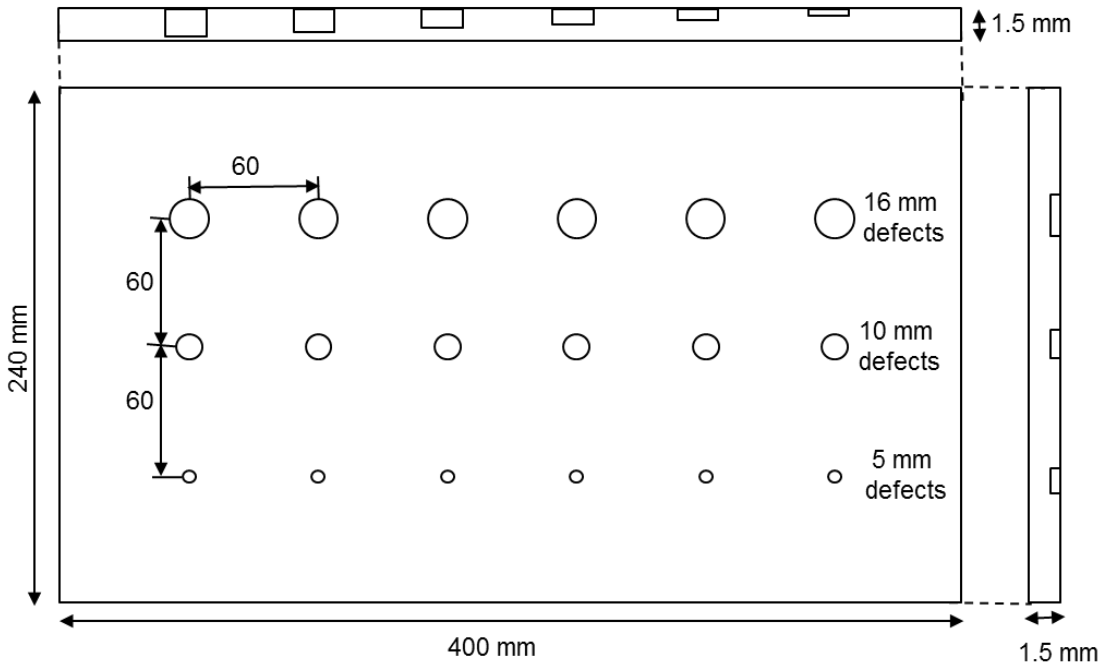

Figure 20 Aluminium with flat bottom hole simulated defects.

5.2.2 Test arrangements

The front surface of the plate was painted using RS matt black spray paint to reduce reflections from the surface by increasing the uniformity and emissivity to 0.92 [129]. Without painting the surface thermography on the aluminium plate would be extremely difficult. Defect depth was taken with respect to the painted surface, i.e. a deeper hole produces a shallower defect. Data was collected with the recording frequency at 100 Hz and heat was added using the Nikon Speedlight SB600 flash in reflection mode. A UT C-scan of the aluminium sample was performed using a 15 MHz transducer.

5.2.3 Results

The thermal PT data, PPT phase data and a UT C-scan image of the 0.3 mm deep 10 mm diameter flat bottom hole defect are presented in Figure 21. All three of the experimental techniques presented are able to clearly identify the defect shown. The thermal PT data, in Figure 21a, clearly reveals the circular defect. Some scratches on the surface of the aluminium, beneath the paint, were also apparent in the PT data. Whilst in this particular case these surface features are small compared to the defect they are still visible and have the potential to lead to inaccurate identification of defects. Surface features are significantly reduced in the PPT phase data in Figure 21b, potentially leading to clearer defect identification where surrounding features could obstruct the defect in the PT data. The UT data in Figure 21c, clearly shows the defect. The edges of the defect in this case are particularly clear as more of the UT signal is scattered at vertical boundaries as found at the edge of the milled hole. The main advantage of the thermography techniques over the UT is the time taken to collect the data and practicalities of application of UT in a construction environment. Whereas PT takes approximately 3 seconds, PPT approximately 20 seconds, the time taken just to scan the same area in UT is approximately 5 minutes. These times do not include set-up of equipment which were assumed to be equal. The practicalities of UT require the ultrasound transducer to be coupled with the sample, which is typically done using water or an agar jelly. While portable UT techniques are available they tend to only be used on regions of interest rather than used to provide complete inspection.

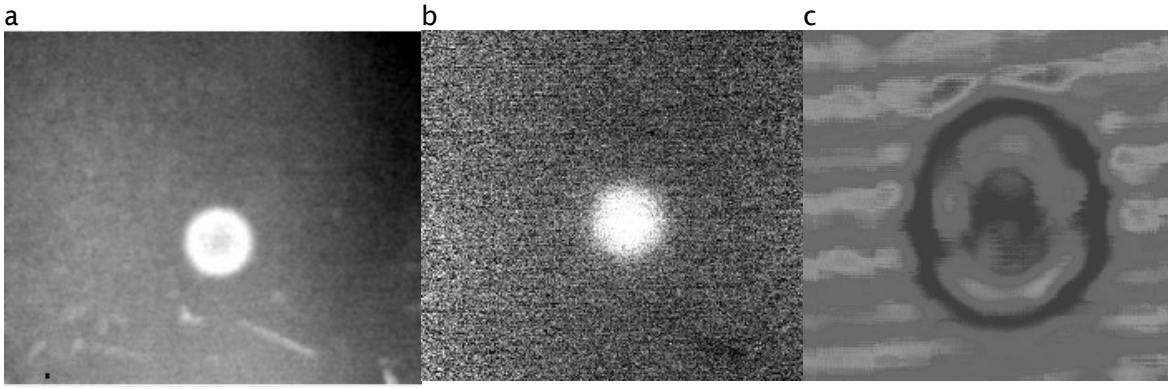

Figure 21 Experimental data for 10 mm diameter, 0.3 mm deep defect a) thermal PT image, b) PPT phase image and c) UT image (spatial scale different to thermal data).

The PPT data collected for the 16 mm diameter defects across the full range of depths is presented in Figure 22. The shallower defects, Figure 22c, are clearly defined and easily resolved whereas the deeper defects, Figure 22a, are much fainter with less well defined edges. The phase contrast, $\Delta\phi$, taken as the difference in phase between the defect and defect free regions, is proportional to the depth and size of the defect and was found to vary from over 100° for the shallowest defect to approximately 2° for the deepest defect. The phase contrast achieved is reduced with increasing depth. The ability to resolve deeper defects is also dependent on the rate of the diffusion of heat within the material. For highly diffusive mediums, such as aluminium, this will limit the resolution of deeper defects as demonstrated.

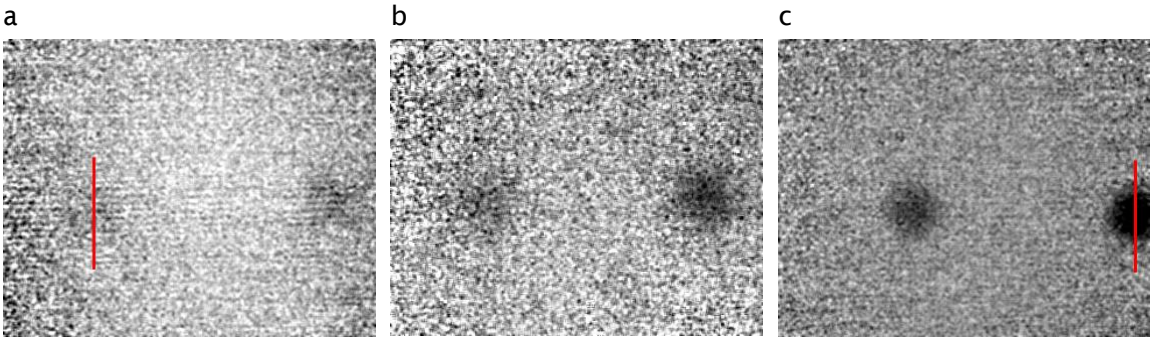

Figure 22 Phase difference images for aluminium plate with flat bottom holes drilled to simulate defects of depths (left to right in each image) a) 1.3 and 1.1 mm, b) 0.9 and 0.7 mm and c) 0.5 and 0.3 mm from the front surface.

Figure 23 shows profiles of the phase values plotted across the diameter of the deepest and shallowest 16 mm diameter defects, indicated by the red lines in Figure 22. The shape of the profiles clearly reflects how the visibility of the

defect in the phase images changes. The shallow defect which is very clear in the phase image produces a well-defined rise and plateau across the defect region in the phase profile. The deeper defect is much more difficult to locate in both the phase image and in the profile. The inability to accurately locate the defect in the profile data will make defect size estimation practically impossible.

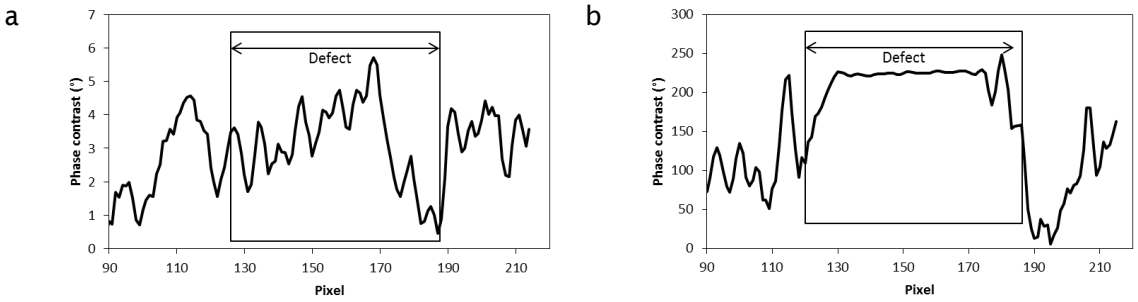

Figure 23 Profile plots taken across a) the deepest, 1.3 mm and b) the shallowest, 0.3 mm, 16 mm diameter defects in the aluminium plate (estimated defect locations shown as a guide).

A full width at half maximum (FWHM) approach, introduced in Section 4.5, has been carried out to give a size estimation of the 16 mm diameter defect, at 0.3 mm and 1.3 mm deep. A comparison of this approach applied to PT and PPT data is provided in Table 3. Defect size estimations via direct visual evaluation of the PT and PPT images have also been performed. Direct visual estimation was taken as a manual approach to visually extract defect size estimations from the phase images. For the shallowest 0.3 mm deep defect the FWHM approach has performed better than the visual estimation. Both sizing techniques have underestimated the defect size when applied to the PT data by 7% for the FWHM and 11% using visual evaluation. The application of the same techniques to the PPT data resulted in a large over estimation of defect size by 47% using FWHM and 53% using visual evaluation. The 1.3 mm deep defect was not able to be identified in the PT data. PPT was able to resolve this defect however the defect size was over predicted using both FWHM by 44% and visual estimation by 33%. While the use of PT thermal data appears to yield more accurate results predicting the shallower defect size, when considering in field use the underestimation of defect size could result in important defects being missed. The inability of PT to reveal deeper defects is also a limiting factor that will hinder its application. The ability to reveal deeper defects using

PPT should enable this technique to be more widely used however, improved methods of defect sizing must be developed, particularly when considering its application to such highly thermally diffusive mediums, such as aluminium.

Table 3 Defect size predictions of 16 mm diameter 0.3 mm and 1.3 mm deep defects in aluminium using FWHM and visual estimates from PT thermal and PPT phase data.

Defect depth (mm)	**Data**	**FWHM (mm)**	FWHM error (%)	**Visual (mm)**	Visual error (%)
0.3	PT – thermal	14.9	- 7	14.3	- 11
	PPT – phase	23.5	+ 47	24.5	+ 53
1.3	PT – thermal	-	-	-	-
	PPT - phase	23.1	+ 44	21.4	+33

5.2.4 Discussion

Comparison of PT, PPT and UT has been undertaken when applied to an aluminium plate with flat bottom hole style defects. PPT was able to reveal deeper defects than PT. UT was able to clearly reveal such defects. Deeper defects were found to be difficult to reveal in such a highly diffusive material. Defect size prediction using FWHM and visual estimation was carried out on PT and PPT data. Such basic image analysis methods were found to have limitations in their accuracy but FWHM results were found to be comparable with visual identification.

5.3 Simulated defects in carbon fibre reinforced composites

5.3.1 Test specimens

The materials used to construct the carbon fibre reinforced composite specimens are detailed in Table 4 and were all prepreg materials that were cured in an autoclave. Carbon fibre composites were the focus of many of the samples in this study as it is an inhomogeneous material but has reasonable heat conduction properties and a naturally high and uniform emissivity. CFRP is widely used in the aerospace and automotive industries and as such is relevant to any developing NDE technique. Initial samples were manufactured with PTFE inserts between the plies of the laminate. PTFE has contrasting

thermal properties to CFRP and will not mix or move during curing and so was used as an initial control defect. PTFE defects in the CFRP were placed between plies from a depth of 0.375 mm down to 2 mm with an interval of 0.125 mm between defect depths (the ply thickness). The defects were circular discs of diameter 5, 10 and 20 mm, shown in Figure 25 and Figure 25.

Table 4 CFRP sample and defect descriptions. *Polytetrafluoroethylene (PTFE)

Bulk material	**Configuration**	**Defect material**	**Defect size**	**Defect depths**	**Total sample thickness**
Carbon fibre – epoxy (Gurit HSC -SE84LV)	CFRP laminate with PTFE inserts between plies, $[(0,90)_4]_s$	PTFE*	5, 10 & 20 mm diameter circles	0.375 – 2 mm in 0.125 mm increments	2.25 mm
Carbon fibre – epoxy (Gurit HSC -SE84LV)	CFRP laminate with PFTE and aluminium inserts between plies, $[0,90]_s$	PTFE and aluminium foil	20 mm diameter circles	0.25 mm	0.5 mm

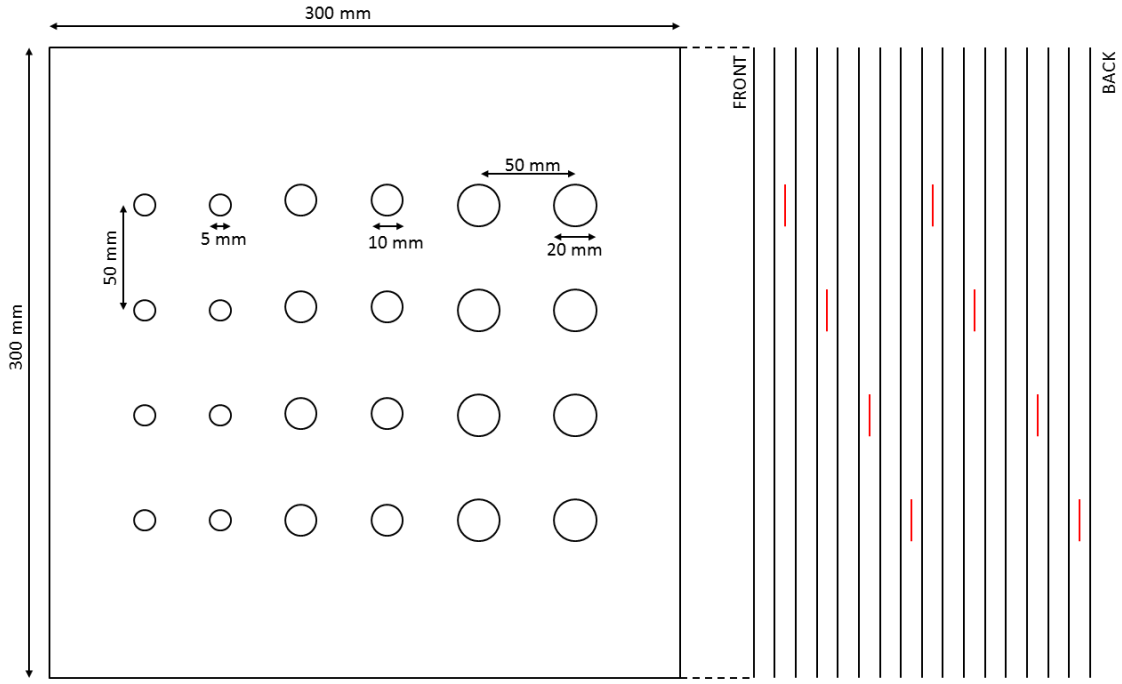

Figure 24 CFRP panel with PTFE inserts.

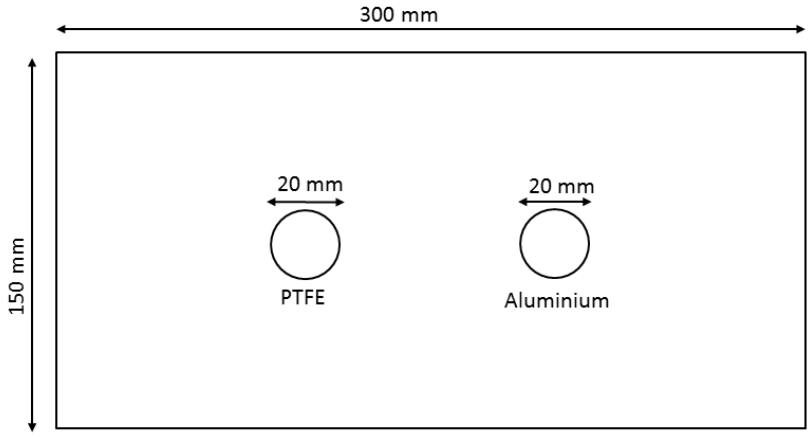

Figure 25 CFRP panel with aluminium and PTFE inserts.

5.3.2 Test arrangements

The observed surface of the CFRP is textured, created by covering the material with peel ply, a nylon fabric. This is used during composite consolidation and curing to prevent the composite from attaching to the mould and keep the surface clean. This textured surface reduces strong reflections as would occur from a very smooth surface and so the CFRP does not require any surface preparation before PPT. A recording frequency of 383 Hz was used for PT / PPT data collection with the Nikon Speedlight SB 600 flash for shallower defects. For deeper defects (>1 mm) a 1500 W quartz heater with a manual shutter was used to provide heating while data was collected at 25 Hz. All experiments were carried out in reflection mode. A UT scan of the CFRP panel with PTFE inserts was taken using a 20 MHz transducer.

5.3.3 Results

PT, PPT and UT data are presented for the 20 mm diameter defect at a depth of 0.375 mm, see Figure 26. All three techniques reliably identify the defect. The results using PT and PPT for such shallow defects are comparable. This highlights that for such strongly contrasting, shallow defects the additional processing of PPT may not be necessary, or beneficial. The UT image contains a rippled effect which may be caused by the sample being slightly tilted, causing spurious reflections in the recorded signal. This data, while still detecting the defect demonstrates the need for accurate set up of the UT.

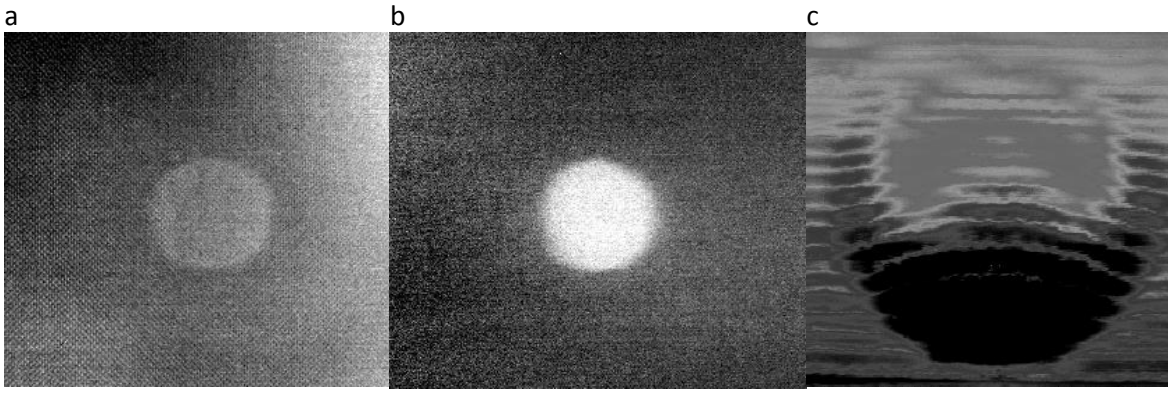

Figure 26 Experimental data for CFRP with PTFE insert at 0.375 mm deep: a) thermal PT image, b) PPT phase image and c) UT image.

Figure 27a shows a phase image of the CFRP panel for 10 and 20 mm diameter defects at depths of 0.375 and 0.625 mm. A profile plot taken over two defects allows comparison of the phase difference obtained for the same size defect at two different depths, see Figure 27b. It is noted that there is a significant decrease in the variation in phase over defect and non-defect areas as the defect depth increases by two plies in the CFRP. This reduced phase contrast initially results in the edges of the deeper defects being less sharp in the phase images, but as the depth increases further will lead to the defect becoming no longer visible. Defect size estimates have been calculated using the profile data for the FWHM approach and the phase image for the visual estimation, see Table 5. The majority of results over estimate defect size. The 20 mm defect at 0.375 mm is predicted within 5% of the actual size using visual estimation and 10% using FWHM. The deeper 20 mm diameter defect is over estimated further using visual estimation, roughly doubling the error to 8%. The underestimation of this defect by FWHM is due to the increased noise in the signal as the defect becomes deeper causing an early intersection of the profile across the half maximum value resulting in false edge detection. Using visual estimation is based on consideration of the whole data set, rather than a single line plot and therefor is less likely to be thrown off be spurious data points. The 10 mm defects are consistently and significantly over predicted using both approaches by up to 52%. As discussed for the aluminium case, uncertainty in defect sizing is caused by lateral diffusion of the heat concentration caused by the defect.

a b

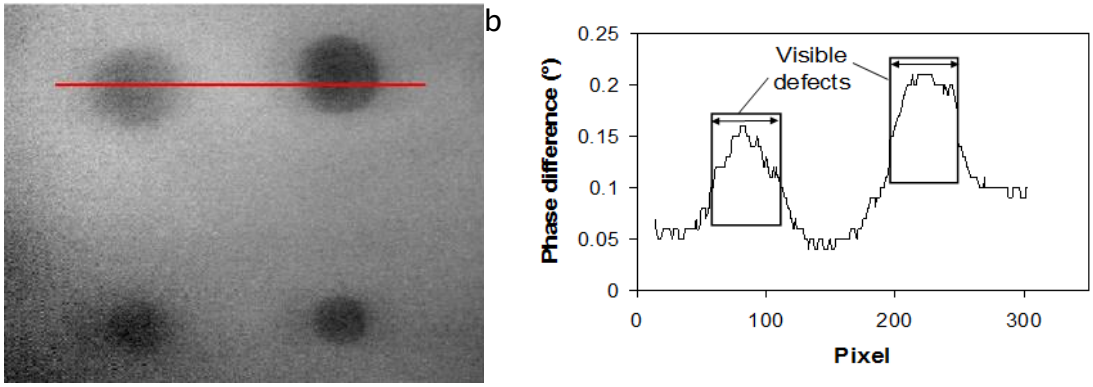

Figure 27 a) Phase image for CFRP plate with PTFE inserts of diameters 20 mm (top row) and 10 mm (bottom row) where the left defect of each size has depth 0.625 mm and the right 0.375 mm, b) Phase difference profile across all four defects in a).

Table 5 Defect size predictions of 20 and 10 mm diameter PTFE inserts at 0.325 and 0.675 mm deep in the CFRP panel using PPT phase data via FWHM and visual estimates.

Defect diameter (mm)	**Defect depth (mm)**	**FWHM (mm)**	FWHM error (%)	**Visual (mm)**	Visual error (%)
20	0.625	16.3	- 18	21.7	+8
	0.375	22.0	+ 10	20.9	+ 5
10	0.625	12.9	+29	14.1	+41
	0.375	15.2	+ 52	13.7	+37

The Nikon Speedlight flash used on previous tests was found to provide insufficient energy to assess depths greater than approximately 1 mm in CFRP. Trials were undertaken using a 1500 W quartz heater with a manual shutter. Defects down to the maximum tested depth of 2 mm were revealed using a 5 second exposure to the IR lamp, see Figure 28. In the figure a total of 6 defects are present in the image, although the image is optimised to highlight the central, deepest defects at 1.875 and 2.0 mm, which are indicated with red arrows. For such a long pulse duration and larger thickness of material the data collection period had to be extended to ~30 seconds. It was not necessary to collect data at such a high frequency as had been previously used as the defect detection occurred later. Data sizes must be kept to a minimum whilst maintaining representative recorded data. The recording frequency found to be adequate in this instance was 25 Hz. The recording period included the illumination period in order to ensure uniform heating, however,

in a fixed set up, where equipment is accurately aligned, this would not be necessary. Data was processed in the same way as the flash heating; taking the frame after the heat was removed as the initial frame for PPT processing. This data demonstrates that variation of heat sources can have a great effect on defect visibility. As the overall thesis is tailored towards thinner bonded joints the Nikon flash remains the heat source typically used throughout the rest of the work.

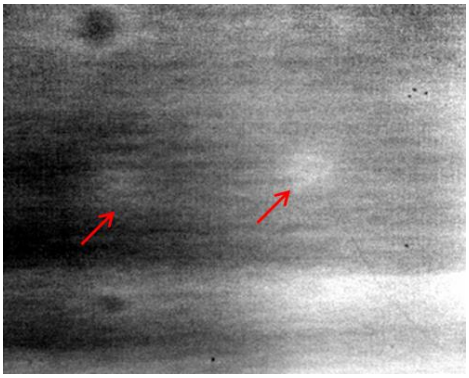

Figure 28 PPT phase image showing the deeper PTFE defects detected using a 5 second heating from an IR lamp. Defects indicated by red arrows are found at depths of 1.75 mm (right) and the maximum tested depth of 2.00 mm (left).

The signature created by defects of differing thermal properties has been studied using a CFRP panel containing PTFE and aluminium foil inserts of 20 mm diameter. The PT data was unable to reveal the aluminium insert and as such only the PPT phase data is shown in Figure 29a and b. Profile data is taken across the defect locations indicated in Figure 29, shown in Figure 30. While the magnitude of the maximum phase contrast is found to be similar for the two defects, the mean phase contrast created across the defects is found to be different for the PTFE and aluminium inserts at 43.4 $\pm$ 13.3° and 29.9 + 20.7 ° respectively. The high conduction of the aluminium leads to a lower mean phase contrast with a higher standard deviation, as illustrated in the phase images.

a b

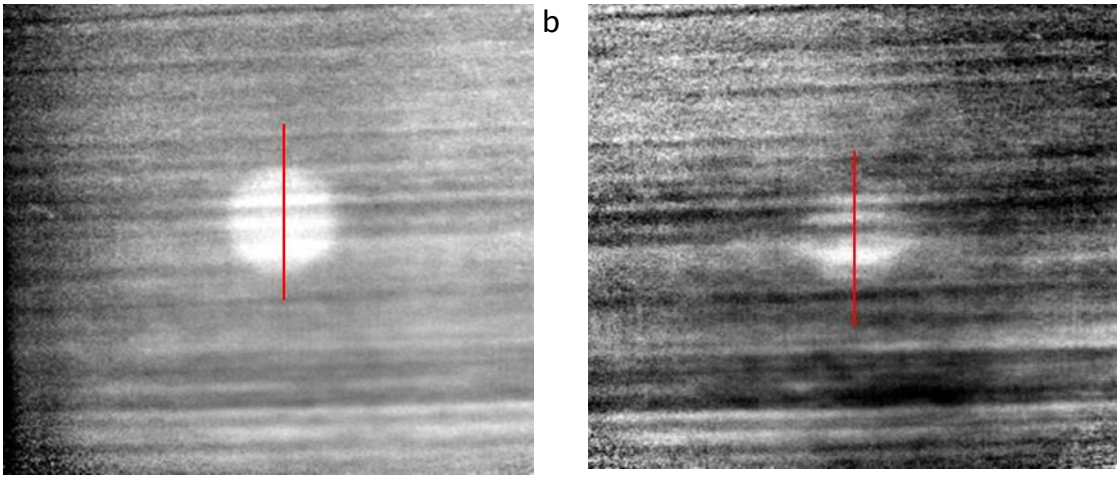

Figure 29 PPT phase data of a CFRP panel containing a) PTFE and b) aluminium inserts.

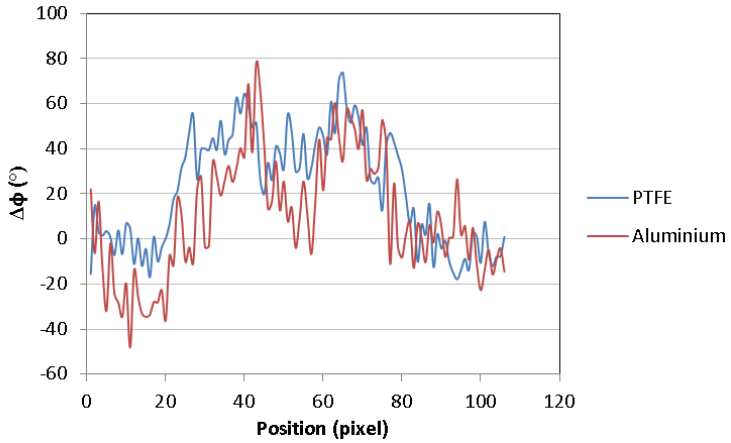

Figure 30 PPT phase contrast data taken across PTFE and aluminium defect in CFRP panel.

5.3.4 Discussion

A series of composite panels were manufactured with insert style defects. CFRP panels with PTFE inserts were tested to a maximum depth of 2 mm. It was possible to identify all defects when the heat source was tailored to the application, i.e. the flash for the shallower defects and the IR lamp for the deeper defects (>1 mm). The role of the contrast of thermal properties between defect and surrounding material was highlighted. UT was found to reveal insert style defects easily especially using high frequency probes, however the relatively long testing times for such scans was a disadvantage. Defect size estimates using FWHM and visual estimates were undertaken for various sized PTFE inserts in CFRP at two depths. It was found that such approaches performed well for the shallowest defect but the lateral diffusion of

the defect signature associated with the increase in depth resulted in a decrease in accuracy.

5.4 Simulated defects in glass fibre reinforced composites

5.4.1 Test specimens

A GFRP sample was also manufactured with PTFE inserts, detailed in Table 6. The PTFE and GFRP have much closer thermal properties than the CFRP and PTFE. The PTFE defects were 10 mm squares and were positioned at depths of 0.2 and 0.4 mm sample schematic shown in Figure 31.

Table 6 GFRP sample description.

Bulk material	Configuration	Defect material	Defect size	Defect depths	Total sample thickness
GFRP – epoxy (E-glass - MTM28)	GFRP laminate with PTFE inserts between plies, $[0, 90]_s$	PTFE	10 mm squares	0.2 & 0.4 mm	0.8 mm

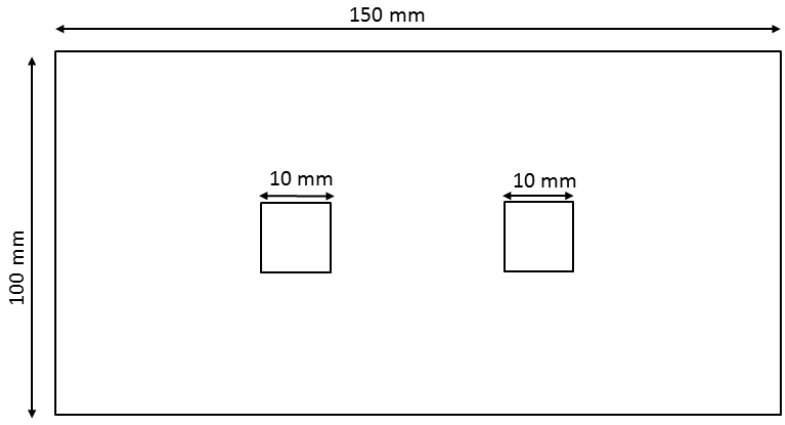

Figure 31 GFRP sample with 10 mm PTFE inserts at 0.2 and 0.4 mm.

5.4.2 Test arrangements

It was necessary to paint the surface of the GFRP sample with matt black paint as the sample was translucent so a uniform and high emissivity coating was necessary. The Nikon Speedlight SB 600 flash light was used in reflection

mode to provide heating in PPT tests where data was collected at 383 Hz. A UT C-scan was produced in pitch catch mode using a very high frequency 50 MHz transducer.

5.4.3 Results

It was possible to identify the PTFE inserts in the GFRP, see Figure 32a, however they provided a lower thermal and phase contrast than the PTFE in the CFRP at similar depths previously studied. The reduction in contrast is due to the similarity of PTFE and GFRP properties when compared to the strongly contrasting PTFE and CFRP. When a profile is taken across such a defect, as in Figure 32b, it is impossible to identify the edges of the defect and so it is impossible to perform FWHM. Other features are identified in the PPT image; these are voids within the GFRP caused by the introduction of air during the infusion manufacturing process. The voids appear clearer than the PTFE inserts as the contrast of thermal properties between GFRP and air is more than that between GFRP and PTFE.

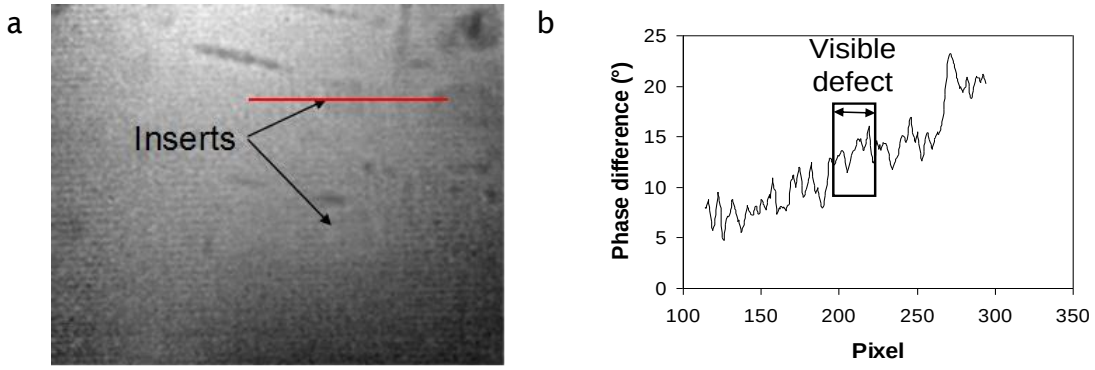

Figure 32 a) Phase difference image showing PTFE inserts in GFRP at 0.2 mm (upper defect) and 0.4 mm deep (lower defect) and b) phase profile across the upper defect with defect location estimated from a).

A UT C-scan was taken over the two defects in the GFRP panel and the PTFE defects were clearly located, see Figure 33a. When this UT scan is compared to the PPT phase data it is obvious that for identification of the defect the results are far superior. When considering the voids that are present in the GFRP, circled in the PPT image in Figure 33b these real defects are much easier to identify in the PPT data and do not appear to be visible in the C-scan. The time taken to produce the images differs significantly as the PPT took approximately 20 seconds whereas the UT scan with a step size of 0.2 mm took

approximately 15 minutes (although the step size could be made larger to speed up the process, depending on the required resolution). A very high frequency transducer of 50 MHz was used that enabled greatly enhanced UT results for defect detection of these shallow defects when compared to the previous CFRP scan. The use of such a high frequency probe in the pitch catch approach may be why the voids were not identified, particularly if they are located deeper in the component, where the signal has become attenuated. While there is an improvement of results in terms of defect resolution, initial set up costs of the UT system using higher frequency probes are also increased.

a b

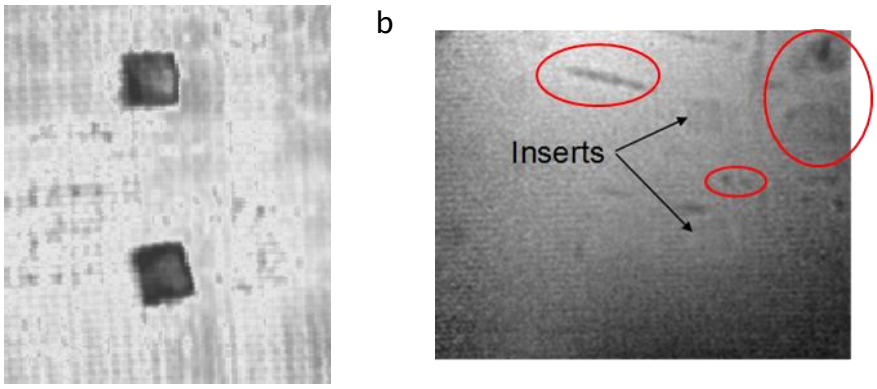

Figure 33 a) UT image of GFRP with PTFE at 0.2 and 0.4 mm deep using a very high frequency probe (50 Hz) and b) PPT phase image of the same sample with voids highlighted in the red ovals.

5.4.4 Discussion

It was found that when the thermal properties of the defect approach those of the bulk material the visibility of the defect using PT and PPT was decreased. For example the PTFE inserts were easier to identify in CFRP than GFRP. The voids found in the GFRP were easier to identify than the PTFE due to the strong contrast in the thermal properties of air and GFRP. UT was able to identify the defects very clearly when using a very high frequency transducer.

5.5 Simulated defects in bonded joints

5.5.1 Test specimen

The following work investigates the identification of inserts in adhesively bonded joints, detailed in Table 7 to find the effect of increasing the complexity in the layers of materials. Two CFRP panels were bonded with an adhesive area of 200 x 150 mm, see Figure 34a. Due to the large bond area an epoxy adhesive film, SA80 from Gurit, was used initially to control the adhesive thickness across the bond. Square PTFE inserts of 5, 10 and 20 mm were added to the bond line. CFRP-CFRP adhesively bonded lap joints were made using Araldite Rapid epoxy adhesive. A 10 mm square PTFE insert style defect was added to the bond line, see Figure 34b. Each piece of CFRP is a 4 ply panel with a layup of $[0, 90]_s$ resulting in a defect depth of 0.5 mm.

Table 7 Bonded samples with inserts descriptions.

Bulk material	**Configuration**	**Defect material**	**Defect size**	**Defect depths**	**Total sample thickness**
CFRP – film adhesive (Gurit HSC -SE84LV)	CFRP panels adhered using epoxy film adhesive (SA80) 2 x $[0,90]_s$	PTFE	5, 10 & 20 mm squares	0.5 mm	1.4 mm
CFRP lap – epoxy (Gurit HSC -SE84LV)	CFRP - CFRP single lap joint adhered using epoxy adhesive (Aradlite rapid) 2 x $[0,90]_s$	PTFE	10 mm squares	0.5 mm	1.2 mm

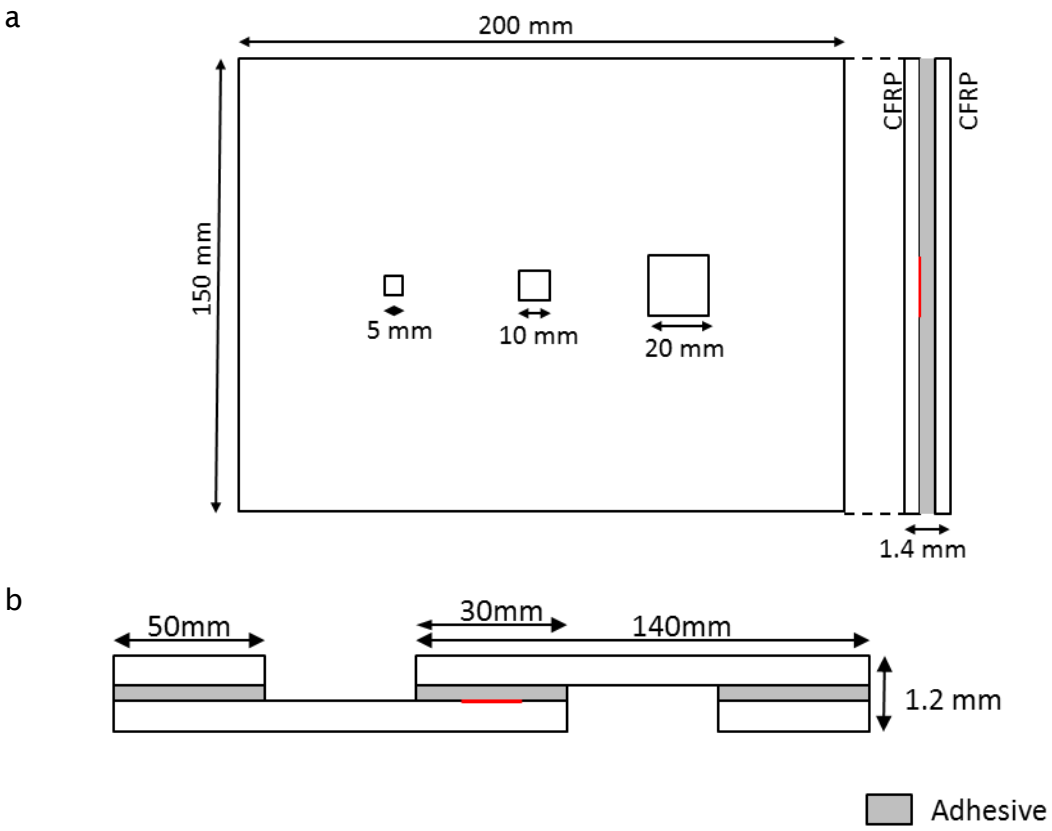

Figure 34 sample diagrams for a) CFRP bonded panel with PFTE inserts and b) CFRP single lap joint with PTFE insert.

5.5.2 Test arrangements

The Nikon Speedlight SB600 was used as the heat source in bonded joint PT and PPT investigations which were carried out in reflection mode. As CFRP was used it was not necessary to paint the surface of the samples. A recording frequency of 383 Hz was used for PT / PPT data collection. A UT pitch catch C-scan was carried out using a very high frequency 50 MHz transducer on the CFRP lap specimen.

5.5.3 Results

The PTFE inserts were able to be clearly detected in this configuration in both the PPT phase data and the profile plot taken across the phase image, see Figure 35a and b. Defect sizes have been estimated using the FWHM and visual estimation approaches for the three defects, see Table 8. These defects are sized far more accurately than previous examples. This may be caused by the change in shape of the defect resulting in enhanced contrast due to the

increased defect area and sharper edges, i.e. comparing a 10 mm wide square and a 10 mm diameter circle, although it should be noted that circular defects are used in [78] where the FWHM is introduced.

a

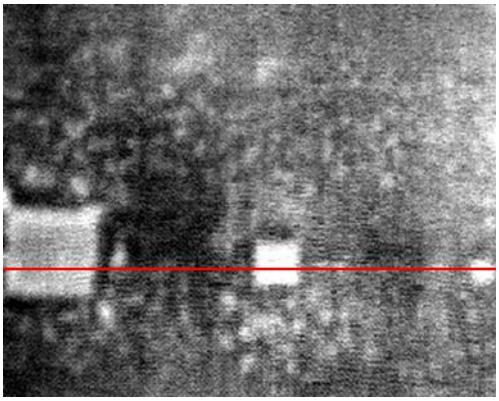

b

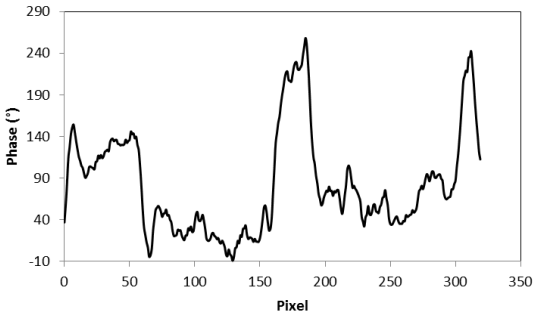

Figure 35 a) PPT phase image of PTFE defects with epoxy film adhesive in CFRP (4 ply) bonded joint. b) Profile plot taken across full image width through the three defects. Defect sizes 20, 10 and 5 mm.

Table 8 Defect size predictions of 20, 10 and 5 mm PTFE inserts at 0.5 mm deep in the CFRP-CFRP bonded panels using epoxy film adhesive found using FWHM and visual estimates.

Defect size (mm)	**Defect depth (mm)**	**FWHM (mm)**	FWHM error (%)	**Visual (mm)**	Visual error (%)
20	0.5	19.3	- 3	20.0	0
10	0.5	9.5	-5	10.2	+ 2
5	0.5	4.9	-2	5.3	+5

The thermal PT data for the lap joint, Figure 36a, does not clearly reveal the PTFE defect in the lap joint, however, when this data is processed the defect becomes visible in the PPT phase data, see Figure 36b. Whilst defects that are detected using PT are also detected by PPT, the reverse is not true, as is demonstrated in this case. The UT data for this sample, Figure 36c, was taken using the very high frequency probe of 50 MHz to allow the very thin features in the adhesive layer to be resolved in the double through transmission method. This results in a very clear image with a lot of detail but is a time consuming process taking approximately 15 minutes for this 20 x 20 mm scan where this detail is not required for the identification of the defect. PPT was significantly quicker and simpler to carry out and gives sufficient information for the extent and position of the defect to be identified. The relative visibility

of the defect in PT and PPT data is highlighted in the profile data shown in Figure 37. As the thermal contrast is low, the PT ΔT profile does not clearly identify a defect within the joint. However, the PPT $\Delta\phi$ data is able to indicate the presence of the defect. Where the defect is not visible in the PT data the usefulness of the phase data becomes apparent as the defect becomes identifiable.

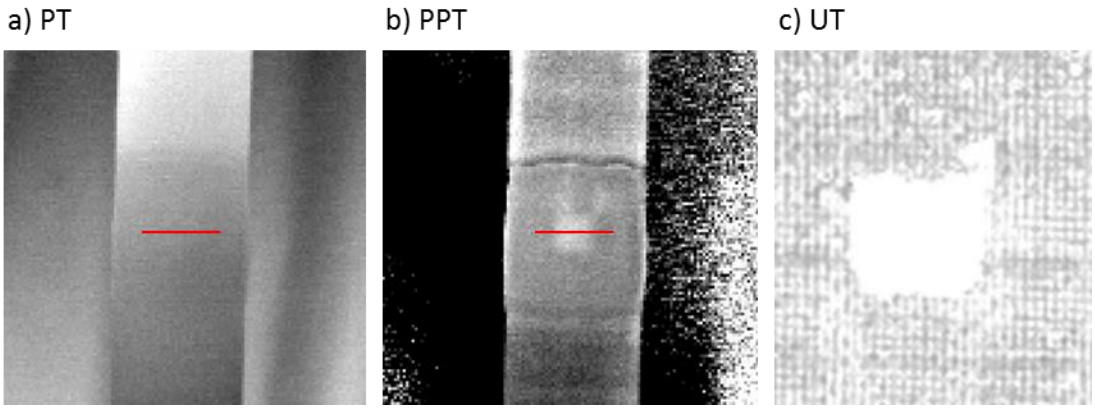

Figure 36 Experimental data for sample 3: a) PT thermal image at 0.514 s, b) PPT phase image at 0.053 Hz and c) UT image.

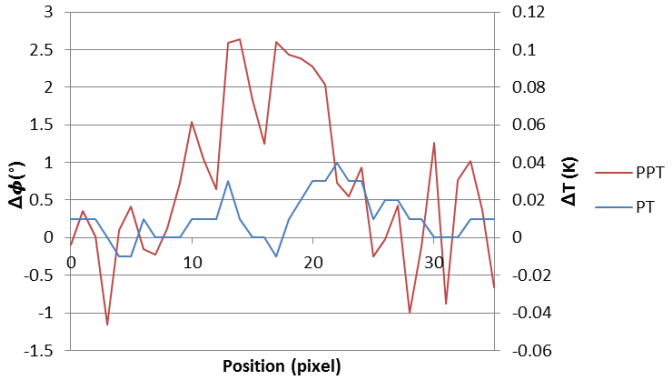

Figure 37 Profile plots taken across the width of the defect visible in the PPT data shown in Figure 36a & b.

5.5.4 Discussion

Bonds with PTFE inserts have been inspected. PT was unable to identify PTFE in such cases where a reduced thermal property contrast existed between adhesives and the PTFE. PPT and UT were able to clearly identify such defects. Defect sizing approaches were found to perform well on the square inserts used, showing their dependence on the geometry of the defect.

5.6 Summary

A comparison between PT, PPT and UT has been undertaken. It was demonstrated that where a defect is shallow and strongly contrasting it is identifiable using PT. However, where defects become deeper or thermal property contrast is reduced the thermal property contrast is also reduced and hence becomes no longer identifiable using PT. Through processing of the data into PPT phase data such defects can be revealed, as demonstrated in the adhesive bond data. If only shallow defects that have a large effect on the heat front propagation through the component are of interest, e.g. voids, then it may be appropriate to reduce computation time and use PT for identification. To reveal defects with reduced contrast it has been demonstrated to be advantageous to process the data into PPT phase data. The effect of different heat transfer properties of the materials being tested has been highlighted showing that more diffusive materials, such as metals, lead to more blurring in defect imaging as the thermal concentration over the defect is quickly reduced. UT C-scans have been shown to give a high level of capability in defect detection when carried out using high frequency probes. The main disadvantage of C-scanning is its time consuming nature as it is a point by point process.

The work in the present chapter has highlighted there are limitations to PT and PPT. The contrast between defect and surrounding bulk material properties has been highlighted as having an impact on the thermal/phase contrast produced using PT/PPT. The heating required to reveal defect must be tailored to the application, as must the duration of recording. These parameters must be investigated to establish what types of defects can and cannot be detected using a particular experimental setup. The next stage of work is the development of a finite element model of the PT/PPT technique that enables experimental parameters, e.g. flash strength, to be tailored to the component of interest. The same model can be used to predict the detectability of defects in terms of the contrast of defect and bulk thermal material properties.

6. Numerical modelling

6.1 Introduction

There has been a limited amount of work carried out into the development and application of finite element analysis (FEA) to thermography for the detection of defects. Chu *et al* [15] use FEA to investigate the start point of data collection in their experiments to ensure the thermal contrast produced by the presence of a defect in a composite panel was not missed. The defects in this case are modelled by disconnecting nodes between elements in the model, producing an area of perfect insulation, which is not realistic for delaminations in materials; however the main goal of this model was to study the effect of heat flux strength on defect detectability. It was found that the stronger the heat flux the greater the contrast between defect and non-defect areas and that the peak thermal contrast between these areas occurs later. This result was then successfully experimentally validated.

Krishnapillai *et al* [17] developed a FEA model of PT to determine if the thermal diffusion length or inflection time of thermal contrast curves could be used to predict defect depth. A correlation was found for the defect depths used, however, all defects, both experimental and modelled, were flat bottom holes. Flat bottom holes are known to greatly enhance thermal contrast between defect and non-defect regions. The model did not incorporate convection or radiation and as such is comparing conduction through two thicknesses of the material. From these basic plate models it was stated that more complex geometries could be studied but no work was presented. A later paper by Krishnapillai *et al* [16] has shown that 2D FEA modelling of subsurface defects is inaccurate for contoured surfaces or complex geometries but may be suitable for flat plates. The present work described in the thesis focuses on flat plates or bonds and as such a 2D model is deemed suitable.

A 3D model has been developed by Dumoulin *et al* [18] to compare the effect of two types of flash on the detection of four types of defect material in an epoxy adhesive bond between a CFRP panel and concrete block. Both the epoxy adhesive layer and the defect materials are modelled as 1 mm thick. As this is the case it can be assumed that the through thickness layers of the

model are either CFRP/epoxy/concrete or CFRP/defect/concrete, which is not a realistic configuration of a bonded joint with a defect. This method of modelling the defects would be expected to enhance the detectability of the defects as the thermal difference in the linear path of the heat, through the thickness of the model, is maximised. The model developed in the current thesis aims to create a more realistic model of adhesive bonds with defects incorporating true defect thicknesses and adhesive/defect interfaces.

In the present chapter a description of a finite element model of the heat transfer processes has been created using Ansys. The model is aimed at determining the heat transfer process through a realistic defect, understanding the effect of the sytem and material parameters as well as being a predictive tool. The aim of the predictive tool is to determine the thresholds of defect detection, as well as optimising the experimental parameters, such as pulse duration, for a particular joint of interest. A description of the development of the model has been published by the author in [130].

The experimental procedures for PT and PPT are identical so the modelling approach is to recreate the experimental conditions and parameters used for both. The results obtained from the model are then compared to the PT results in each case. PPT phase result may then be created by processing the modelled PT results.

To successfully identify kissing defects PPT must operate towards the limits of the technique. The results shown in Chapter 5 demonstrate different levels of success when identifying defects using PPT. It was shown that the ability to identify a defect is not only dependent on the depth and geometry of the defect but also on the thermal property contrast between defect and surrounding bulk material. There is a need to identify what types of defects may or may not be detectable. Section 6.5 focuses on the application of the model to propose relationships between thermal property contrasts and defect detectability to enable prediction of the types of defects that may be detected using PT and PPT.

6.2 Model development

A 2D model was developed as the advantages of a 3D model at this stage are not considered to outweigh the extra computational expense. Each sample is modelled as a cross section through the area where a defect exists, see Figure 38. Animated results are produced that enable visualisation of the thermal front propagation through the sample whilst giving the comparative results of surface temperature values over defect and non-defect areas. The surface temperature values are equivalent to the PT data, which is then processed using a FFT to obtain the phase values equivalent to PPT data.

The model was developed using Ansys 12.1. The element type used is Plane55 which is a 4 node 2-D thermal solid element. A 4 node element was selected to limit the computational expense required to run the model. The mesh size chosen was 0.2 mm which was kept consistent for all models developed in this work. The results generated using the 0.2 mm mesh were found to be convergent within 10 mK of the results given by smaller meshes so there was no loss of accuracy by selecting such a mesh size. The physics of the model is based on the fundamental heat transfer equation

$$\frac{\partial T}{\partial t} = \gamma\left(\frac{\partial^2 T}{\partial x^2} + \frac{\partial^2 T}{\partial y^2}\right) \tag{6.1}$$

where the thermal diffusivity, γ, is given as,

$$\gamma = \frac{k}{\rho C} \tag{6.2}$$

Parameters such as specific heat, C, density, ρ and thermal conductivity, k, for each material are inputted into the model. For orthotropic materials thermal conductivity values parallel, $k_{\parallel}$, and perpendicular, $k_{\perp}$, to fibres are included in Equation (6.2) which becomes

$$\gamma = \frac{1}{\rho C}\left(k_{\parallel} + k_{\perp}\right) \tag{6.3}$$

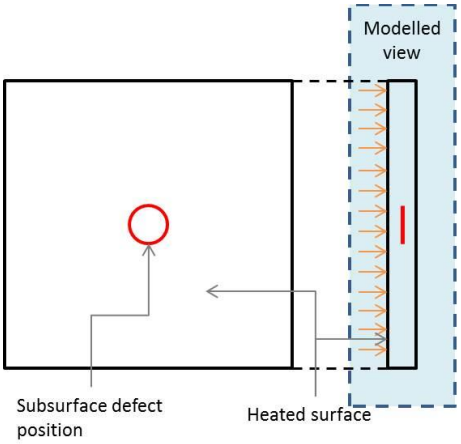

Figure 38 Modelled view of example sample with defect in 2D model.

The modelled and experimental PT thermal data was then processed into PPT phase data, which has been carried out using a routine developed in Matlab, described in Section 6.4.

6.2.1 Constructing the model

When considering modelling PT there are several factors to be considered and included. Firstly, the heat being added to the component as the pulse incident on the surface must be of realistic strength and duration. Secondly, the conduction of the heat through the material and the transfer of the heat across material boundaries must be considered. Finally, the interaction of the sample with the surrounding environment must be included. Convection of the heat away from the surfaces of the component must be possible in a realistic manner.

The parameters required to establish such a model include the conductivity, specific heat and density of each material. The surface heat transfer coefficients for any material open to the surrounding air must also be known. Experimental parameters must also be added, such as the ambient air temperature, pulse duration and strength, and data collection/sampling rate.

The initial condition of the model assumes the sample and surroundings are in thermal equilibrium. All free surfaces of the sample were set so that convection could occur controlled by appropriate heat transfer coefficients found in the literature [116, 131]. To maintain consistency between experimental and numerical tests the pulse was modelled by applying a

uniform temperature across the front surface of the sample. The temperature value was determined using IR detector data from the experiments. The heat input was then removed and the component allowed to return to ambient temperature. The model was processed in three load steps to simulate PT. Load step one was the initial condition with the sample and surroundings in equilibrium. Load step two was the duration of the thermal pulse. The third load step was taken from the end of the pulse for a duration appropriate to the component, which captured the thermal decay of the component back to ambient temperature. The duration of each load step was varied according to the sample of interest. The interval between recorded data points, analogous to the recording frequency in the experiments, was selected to be appropriate to capture the details of the heat transfer in that component. The increase of the sampling frequency results in a more computationally expensive model, just as the increase of recording frequency would result in a very data intensive experiment. The minimum recording / sampling frequency should be used while still being able to capture the details of the thermal decay of a component.

6.2.2 Assumptions and limitations

There are some assumptions and limitations to the current model. The first restriction in its use is that knowledge of several material properties is required. This knowledge of properties includes those of the defect, hence identification of the defect material is necessary, which is not always practical. In this situation the model could be used to find the limiting values of properties of a defect material that would allow it to be detectable. Another assumption of the model is that there is perfect contact conduction between the surfaces of different materials within the component. As bonded joints are the main area of interest, where contact is assumed to be 100% for a good bond, then this assumption is considered reasonable. Finally, the model applies a uniform illumination across the surface of the samples. However, in experiments, while this is the ideal case there may be a thermal gradient on the surface that may lead to discrepancies in results between the model and experimental work, particularly towards the edges of observed areas in experiments. This thermal gradient should be considered when processing experimental results and efforts should be made to remove this error.

There are some more minor effects that have not been included in the model that are present in the experimental data. For all case studies the experimental peak pulse temperature recorded is consistently higher than that modelled. This elevated peak in the experimental data is caused by the reflection from the sample as the thermal pulse is incident on the surface; this is not replicated by the model. The modelled pulse temperature was taken from the experimental data using the frame after the pulse, to avoid reflections.

6.2.3 Case studies

Three case studies are studied (CS1, CS2 and CS3), covering various materials and bonded/non-bonded configurations detailed in Table 9 with schematics of the samples shown in Figure 39. Both experimental and modelled data is presented for all cases. Models have used literature values of heat transfer properties which are presented in Table 10.

Table 9 Case study specimen information.

Case study	Description	Material	Defect material	Defect depth	Full sample thickness	Defect thickness
1	Aluminium with flat bottom hole	Al95 Dural Aluminium alloy	Air	0.3 mm	1.5 mm	-
2	CFRP	UD CFRP [UD]	PTFE	0.375 mm	1.0 mm	0.2 mm
3	CFRP-CFRP adhesive lap	UD CFRP [0, 90]	PTFE	0.7 mm	2.0 mm	0.2 mm

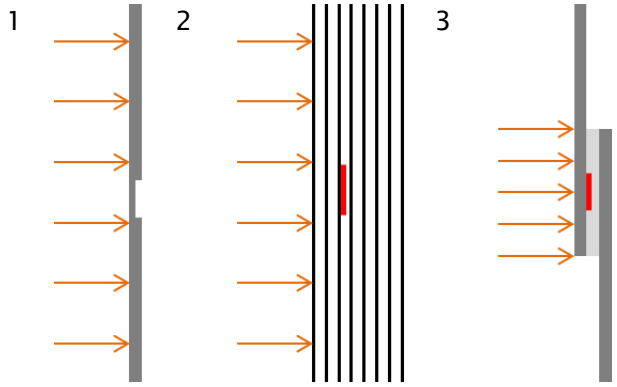

Figure 39 Schematics of the four case study samples with heated surface indicated by orange arrows. 1) flat bottom hole milled into aluminium, 2) CFRP with PTFE inserted between plies 3 and 4 from the front, 3) a CFRP single lap joint made with epoxy adhesive with a PTFE insert in the bond line between front adherend and adhesive.

Table 10 Material properties used in the model, taken from literature [116, 132].

Material	**Conductivity (W/m K)**		**Specific heat (J/kg K)**	**Density (kg/m^3)**	**Diffusivity (m^2/s)**
Aluminium	230		880	2700	9.7×10^{-5}
CFRP	$\perp$ 0.8	$\parallel$ 7	970	1290	$\perp$ 6.4×10^{-7} $\parallel$ 5.6×10^{-6}
GFRP	$\perp$ 0.3	$\parallel$ 0.38	1200	1900	$\perp$ 1.3×10^{-7} $\parallel$ 1.7×10^{-7}
PTFE	0.32		1100	2400	1.2×10^{-7}
Air	0.14		500	460	6.1×10^{-7}

6.3 Pulsed thermography model results

The modelled and experimental data comparison is based on three key points on the surface. The first point is taken as the surface data directly above the defect centre (DC). The second point is taken from above the defect edge (DE) while still being over the defect. The final point is taken from a non-defect (ND) area away from the edge of the defect and the edge of the sample, this point is assumed to be unaffected by any lateral conduction. A schematic of

the data point locations is given in Figure 40, and the equivalent data was taken from both modelled and experimental results.

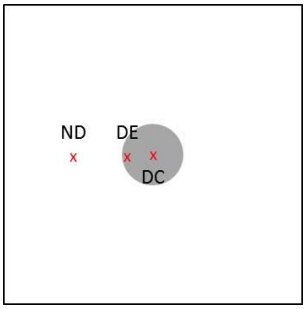

Figure 40 Data point positions for comparisons between modelled and experimental data.

The ΔT thermal decay data is presented initially to allow comparison of the modelled and experimental data, this data is presented as ΔT data as a background subtraction of ambient temperature has been removed to observe the change in temperature on the surface over time caused by the external heating. A thermal contrast plot is also produced measuring the ΔT between the defect and non-defect areas over time. The information in the ΔT plot identifies the time at which a defect is most clearly visible. Hence, informing the experiments of the duration that a surface must be monitored for, to capture the maximum contrast between surface temperatures over defect and non-defect regions.

6.3.1 Case study 1: Aluminium with flat bottom hole

A comparison of modelled and experimental data for CS1is shown in Figure 41a-d, where the trends present in the modelled data match those found in the experimental data for the three points considered. The initial decay section, prior to 1.5 s, shows the surface temperature at ND decaying fastest after the pulse. This occurs because the component is thicker here and so the heat can be conducted through the thickness of the aluminium for longer, decreasing the surface temperature by a larger amount. At DC the aluminium is much thinner so the propagation of the thermal front through the material via conduction is stopped in the through thickness direction. The elevated temperature in that region is dissipated by either lateral conduction or convection from the surfaces. In the DC position there is less opportunity for lateral conduction as it is in the centre of the 'hot spot'. More lateral conduction occurs at the edge of the defect allowing DE to cool faster than DC.

As convection becomes more dominant, at 1.5 s, there is an inversion in the relative temperatures of the three points in the model. Where there is less material in location DC, a faster decrease in temperature is observed than where the material is thicker in location ND. This is caused by the ratio of surface area to volume of material being decreased for the thicker region. This effect is only visible in the model although could be present in the experimental data but, as it is a relatively small variation in the thermal decay, it cannot be distinguished from the experimental noise. The modelled and experimental PT data correlate within $\pm$ 0.03 K.

The thermal contrast between the defect centre and non-defect areas is shown in Figure 42. Due to the shallow depth of the defect and the high thermal conductivity of aluminium the peak in thermal contrast (ΔT_{peak}), at 0.2 s, occurs very soon after the heating stimulus. The timing of this peak is predicted well by the model. The ΔT_{peak} value is underestimated by the model at 0.06 K as opposed to the experimental value of approximately 0.09 K. The discrepancy between modelled and experimental data is possibly caused by differences between the literature values of the material thermal properties and the true values of the sample used.

a

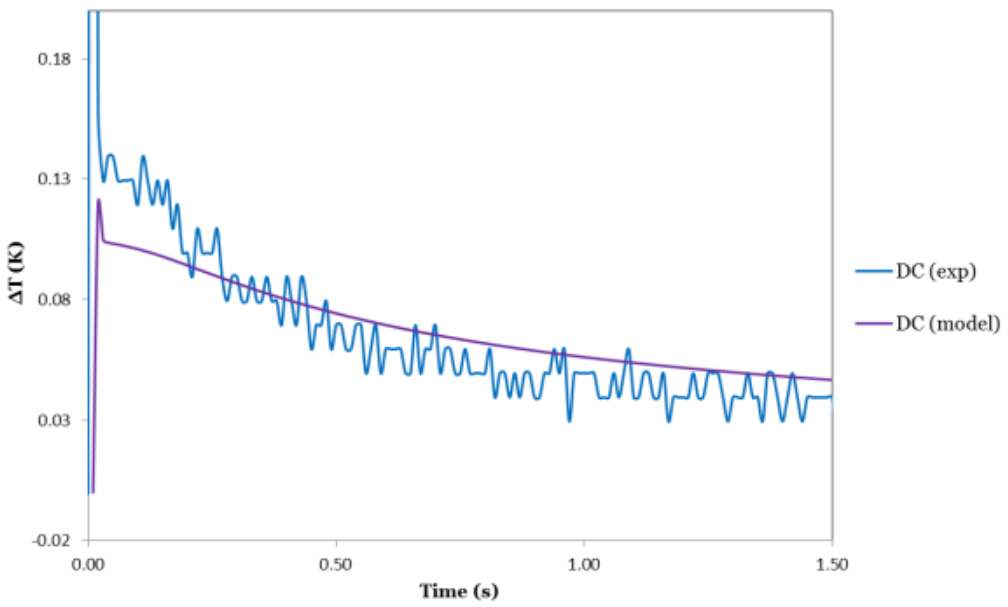

b

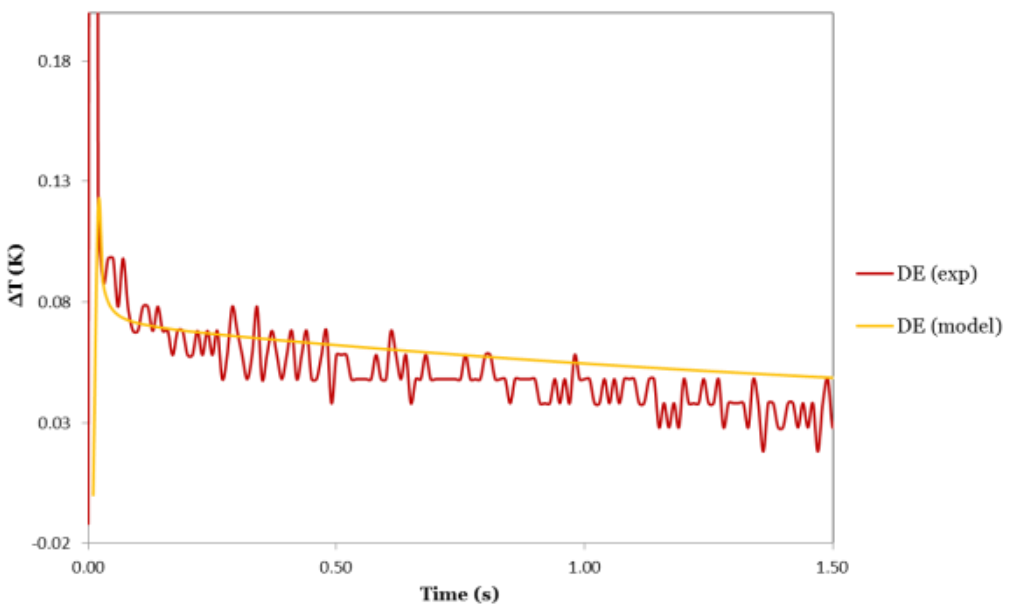
0.18
0.13
0.08
0.03
-0.02
ΔT (K)
0.00
0.50
1.00
1.50
Time (s)
DE (exp)
DE (model)

c

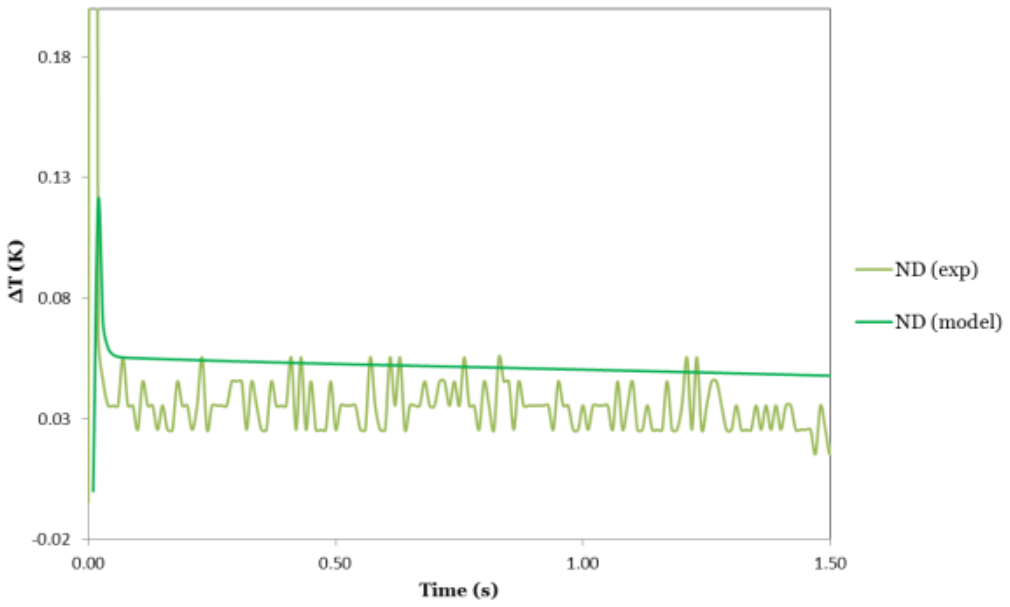
0.18
0.13
0.08
0.03
-0.02
ΔT (K)
0.00
0.50
1.00
1.50
Time (s)
ND (exp)
ND (model)

d

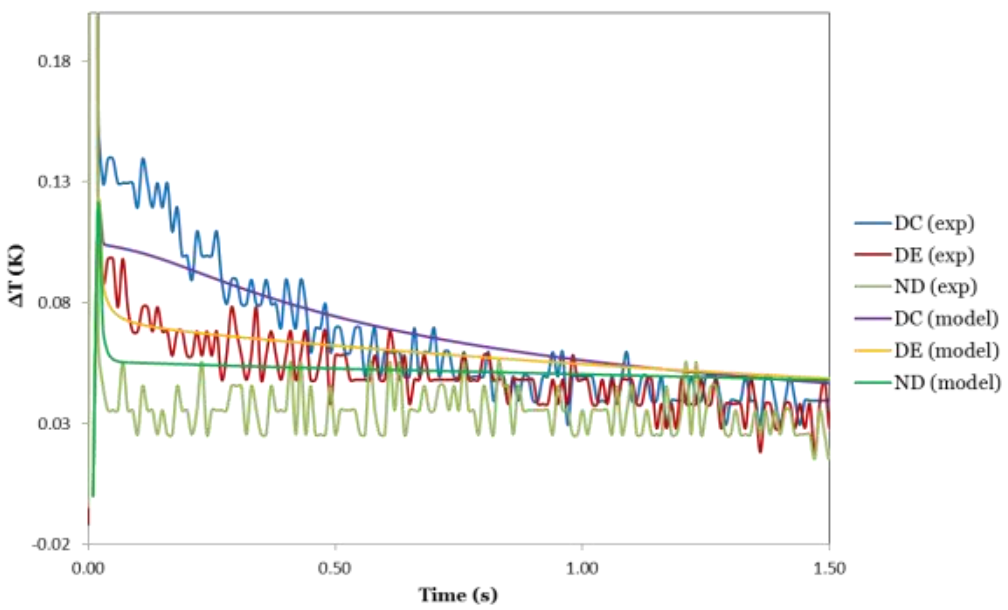

Figure 41 Surface temperature data comparison of PT data for CS1 showing modelled and experimental data for a) DC, b) DE, c) ND and d) all three data points.

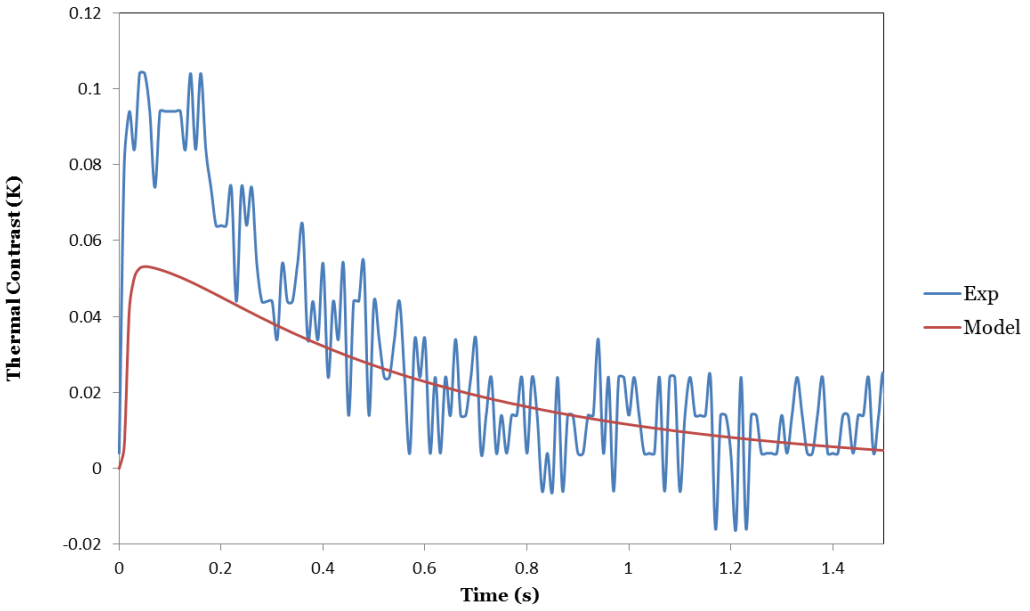

Figure 42 Modelled and experimental surface thermal contrast data between defect and non-defect regions.

The aluminium model has also been compared to another model recently published [133], which uses virtual heat sources (VHS) at defect locations to model surface temperature data. In [133] flat bottom hole style defects in steel are considered; as such it was possible to reproduce the VHS model

applied to aluminium to make comparisons between the VHS model, the 'Southampton model' of the current thesis and experimental data. The aluminium case study is a 1.5 mm thick aluminium plate with a 10 mm diameter defect at a depth of 0.5 mm. A comparison of the thermal contrast between DC and ND were compared between the two models and experimental data, see Figure 43. It was found that while both models performed with a similar degree of accuracy when predicting the experimental data the VHS model over predicted the peak contrast whereas, the current model under predicted the peak contrast. It is suggested that the VHS model over predicts the peak contrast in this case as the pulse strength used in the current work is lower than in [133] and as such lateral heat conduction may have an increasingly visible effect relative to the lower strength signal.

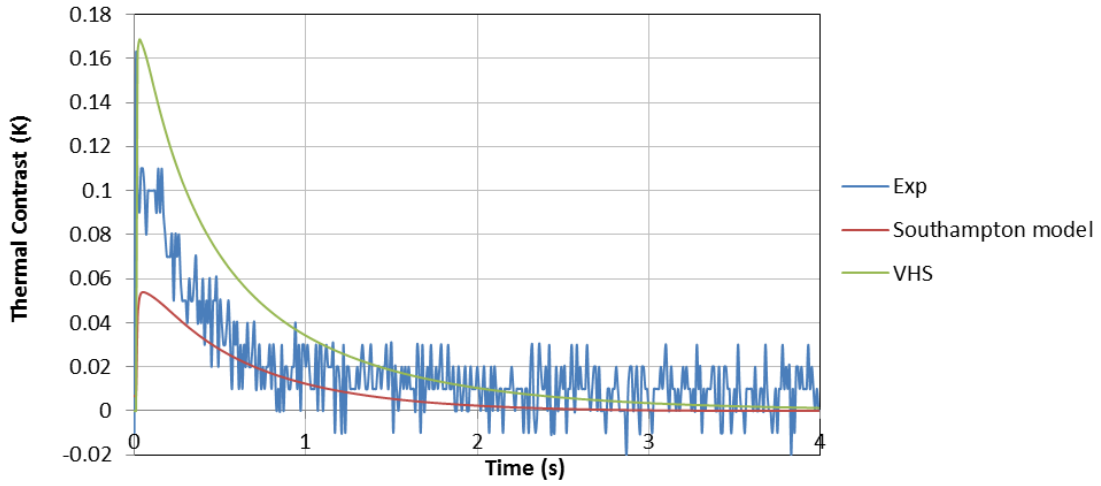

Figure 43 Comparison between current 'Southampton model', virtual heat source (VHS) model and experimental data for aluminium sample.

6.3.2 Case study 2: CFRP

For CS2 the model data is in good agreement with the experimental PT results within ± 0.04 K, see Figure 44a-d. The DC position is slowest to decay as the thermal front meets the PTFE defect as it propagates in this area. PTFE has a lower thermal conductivity than the surrounding CFRP. The DC stays at a higher temperature than the DE due to the increased limitations of lateral conduction, as previously discussed for CS1. The inversion of decay rates seen in CS1 is not present as the total component thickness is consistent, so cooling by convection will be more uniform than in the previous example as the ratio of volume of material to surface area is continuous across the sample.

Figure 45 shows thermal contrast between defect and non-defect areas for the modelled and experimental results. The time of ΔT_{peak} in the model occurs at 0.2 s whereas in experiments it occurs slightly earlier at approximately 0.13 s. The decay of thermal contrast between DC and ND is faster in the model than in the experiment which may be attributed to the literature based material properties entered in the model.

a

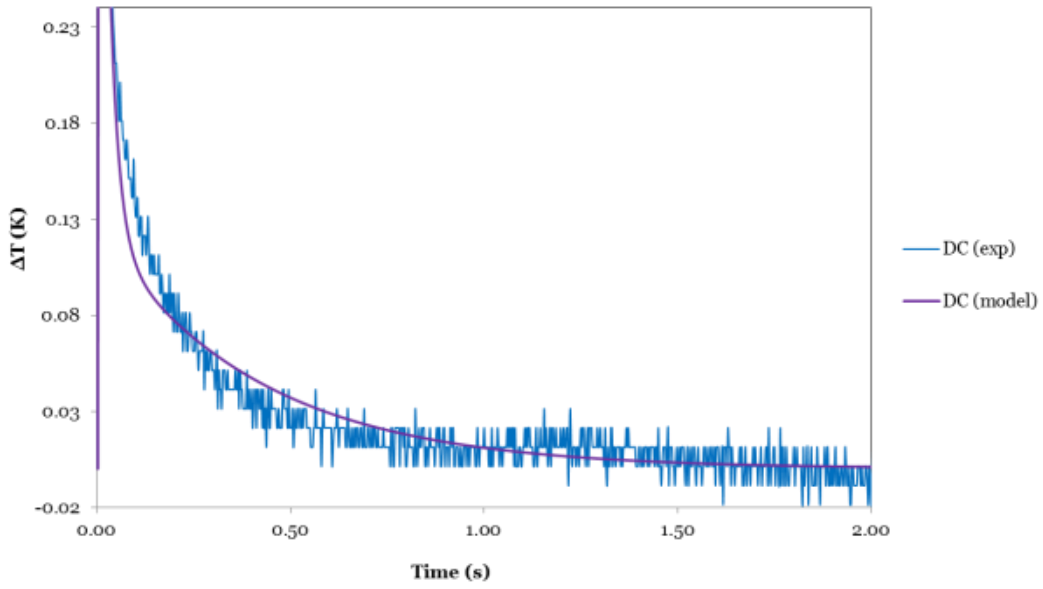

b

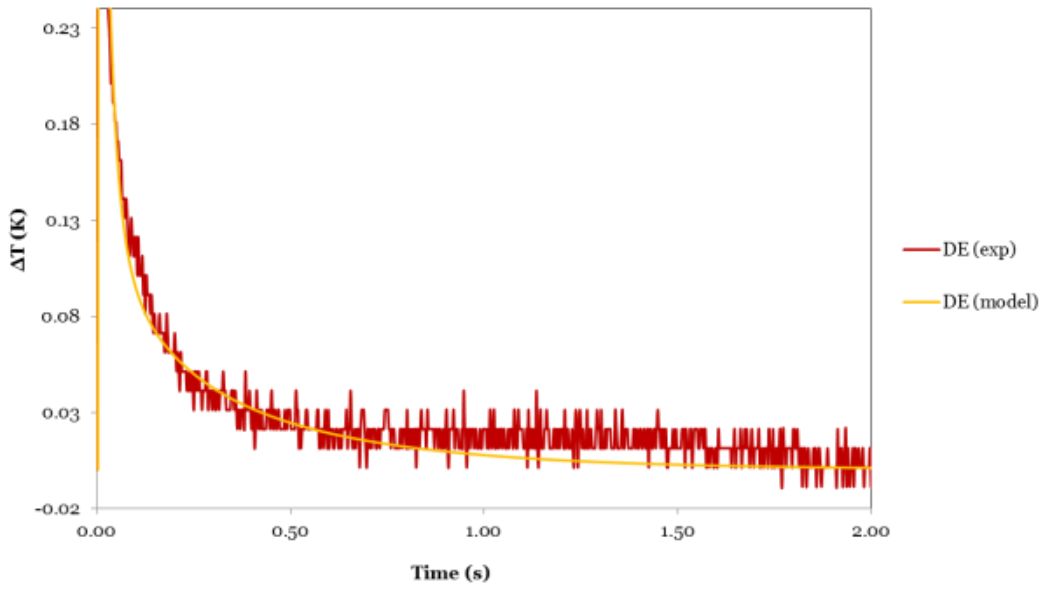

c

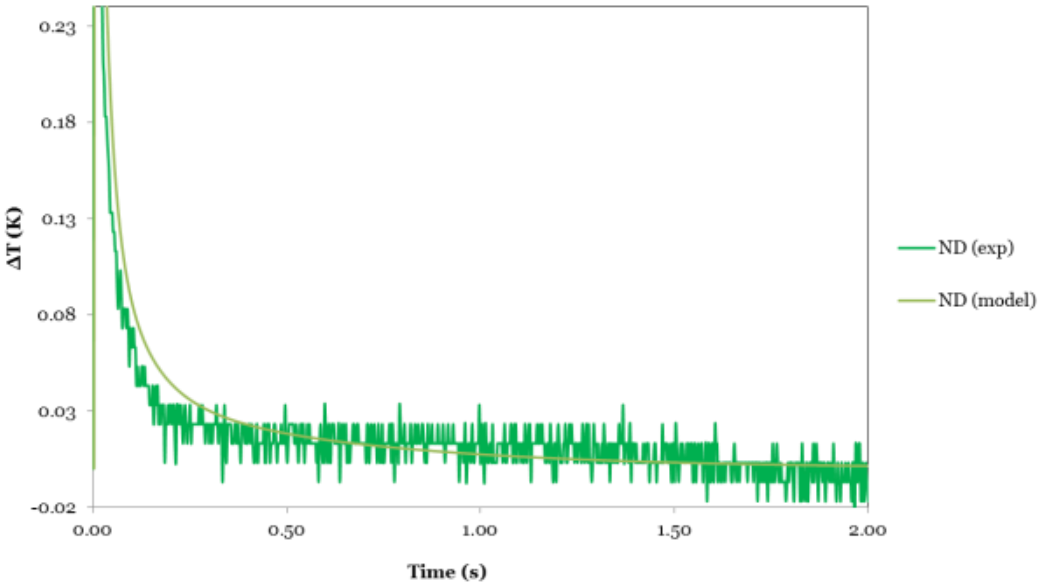

d

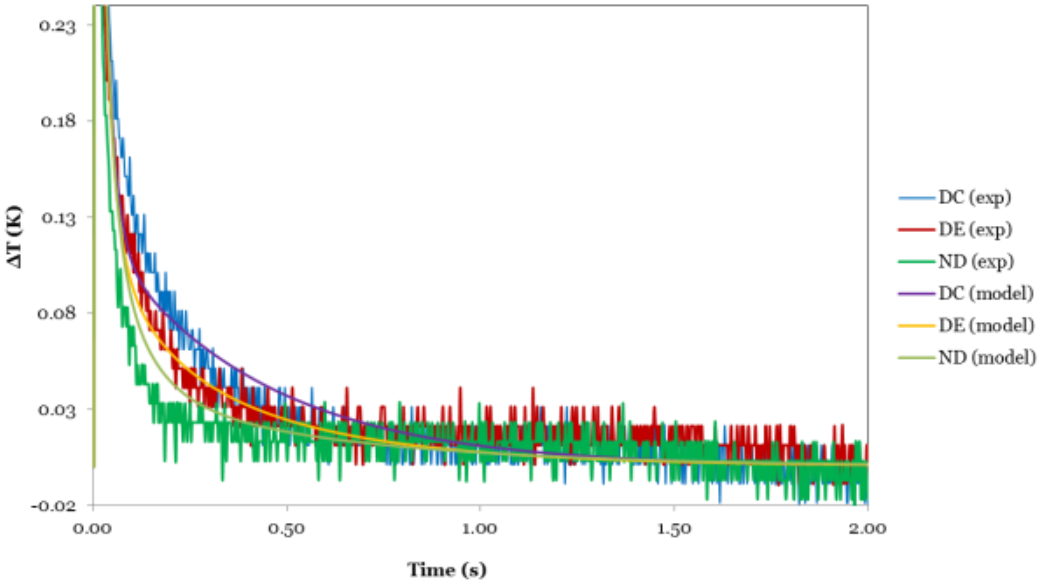

Figure 44 Surface temperature data comparison of PT data for CS2 showing modelled and experimental data for a) DC, b) DE, c) ND and d) all three data points.

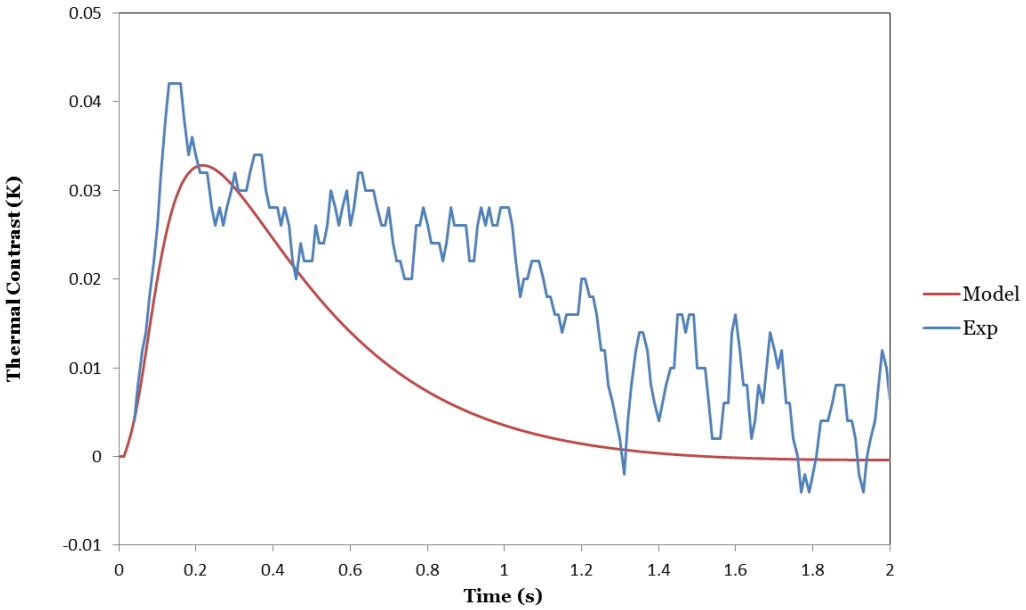

Figure 45 Modelled and experimental surface thermal contrast data between defect and non-defect regions.

6.3.3 Case study 3: CFRP-CFRP adhesive lap joint

The modelled data for CS3 is also in good agreement with the experimental results within $\pm$ 0.05 K, Figure 46a-d. The error has slightly increased as the component geometry has increased in complexity, however, a strong correlation remains.

Where very low thermal contrast is obtained as for the lap joint sample the experimental noise becomes significant. The profile plot in Figure 47 shows that the magnitude of ΔT_{peak} is accurately predicted at 0.03 K however the peak occurs later at 0.3 s in the model compared to approximately 0.2 s in the experimental data.

a

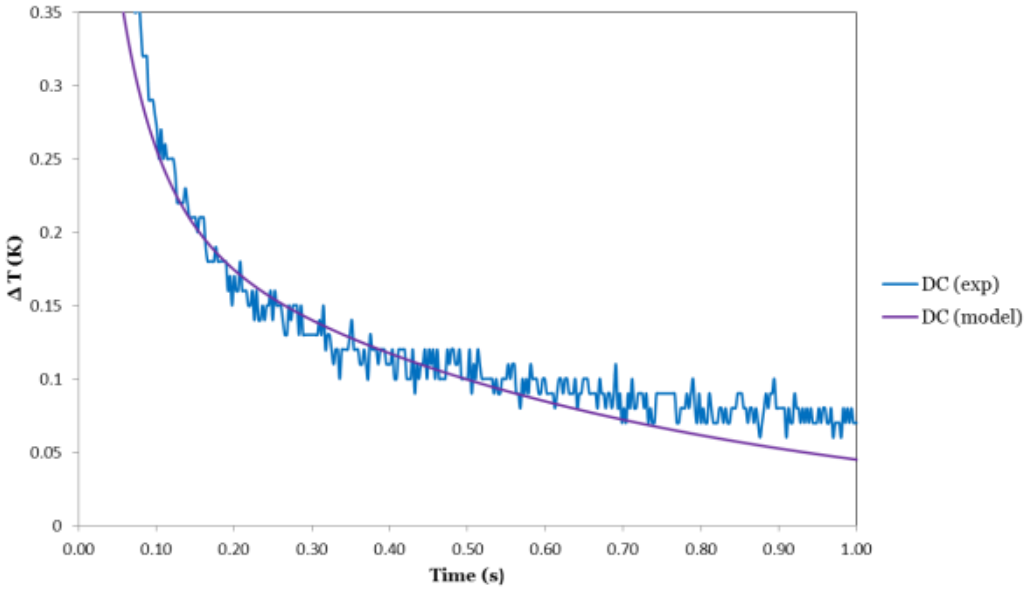
0.35
0.3
0.25
0.2
0.15
0.1
0.05
0
ΔT (K)
0.00
0.10
0.20
0.30
0.40
0.50
0.60
0.70
0.80
0.90
1.00
Time (s)
DC (exp)
DC (model)

b

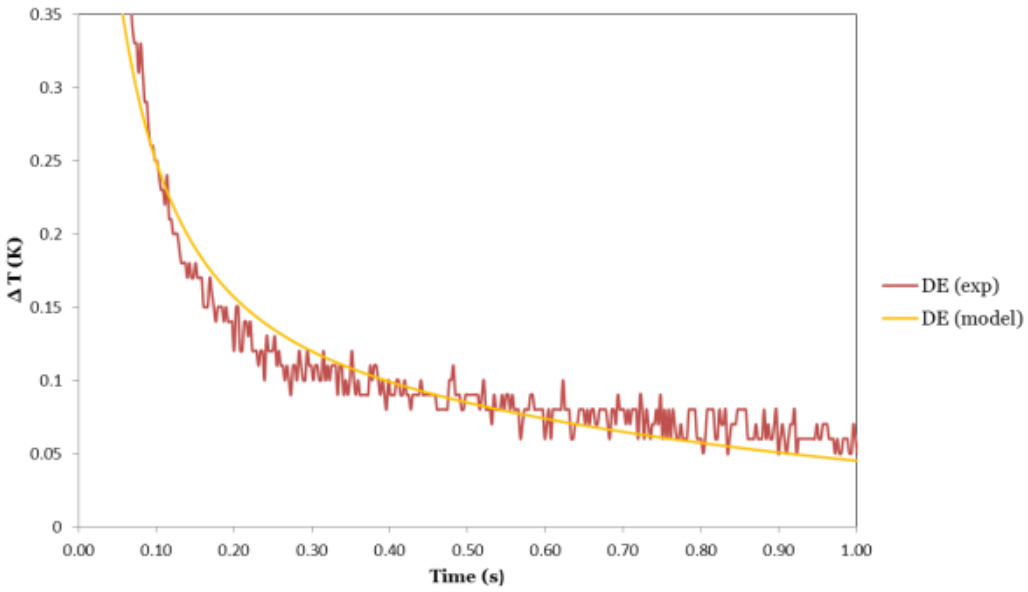
0.35
0.3
0.25
0.2
0.15
0.1
0.05
0
ΔT (K)
0.00
0.10
0.20
0.30
0.40
0.50
0.60
0.70
0.80
0.90
1.00
Time (s)
DE (exp)
DE (model)

c

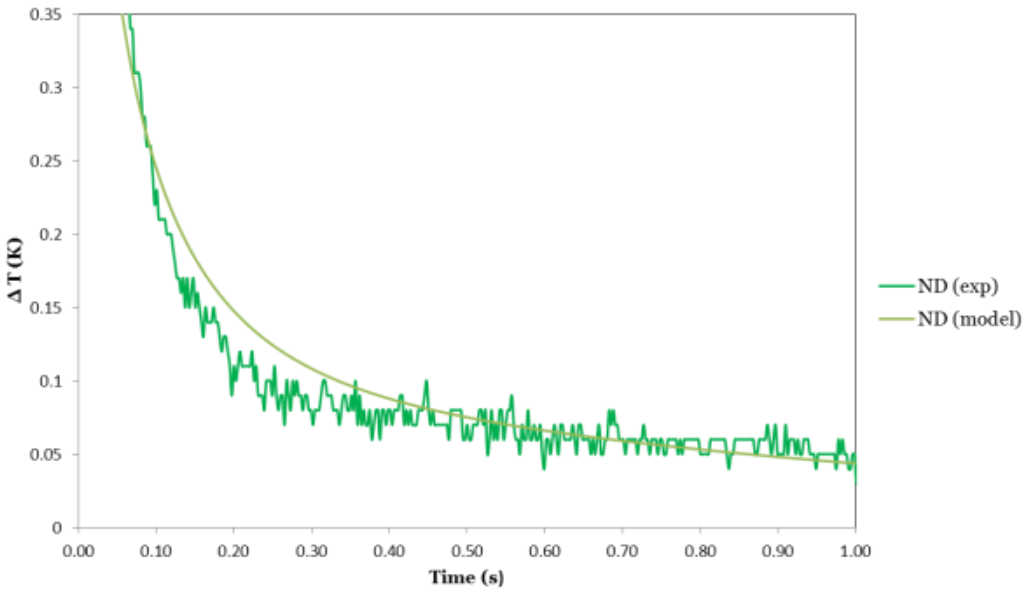

d

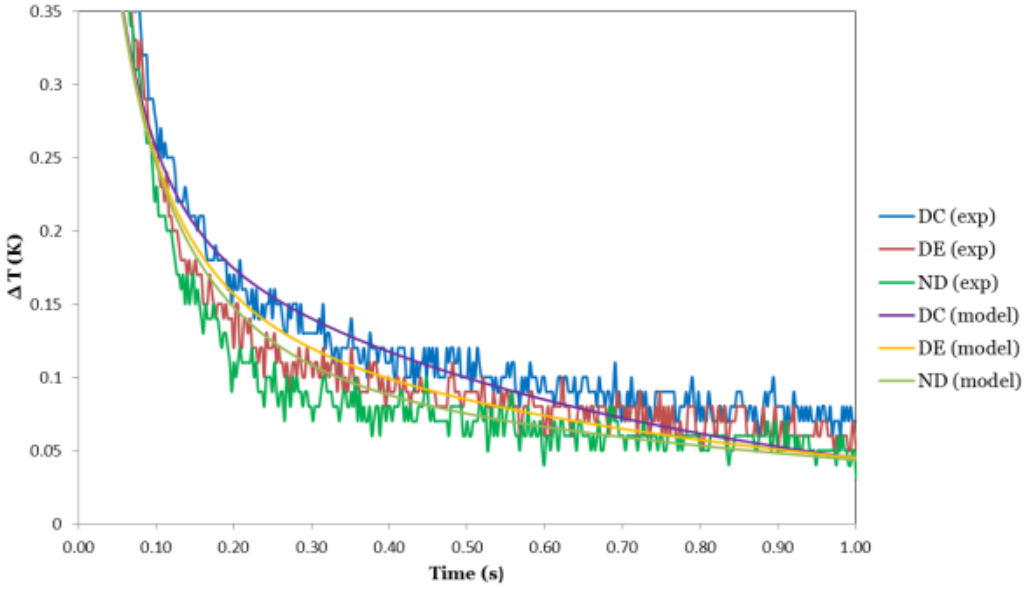

Figure 46 Surface temperature data comparison of PT data for CS3 showing modelled and experimental data for a) DC, b) DE, c) ND and d) all three data points.

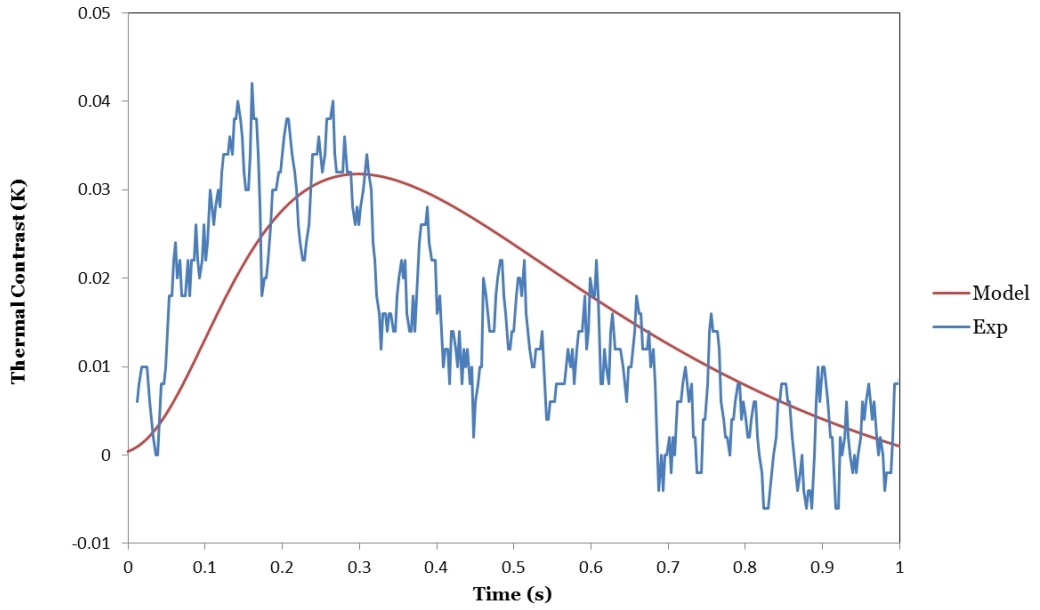

Figure 47 Modelled and experimental surface thermal contrast data between defect and non-defect regions.

6.4 Pulse phase thermography model results

The real and imaginary components of the FFT have then been used to produce phase data for the DC and ND regions. Phase contrast values, $\Delta\phi$, have been produced over a range of sampling frequencies for both the experimental and modelled data, see Figure 48a-c. The absence of noise in the experimental phase data is because the processed data is presented as the mean thermal decay for the defect and non-defect areas. The FFT sampled frequency at which the maximum $\Delta\phi$ occurs and the magnitude of this peak are recorded and the ratio between the modelled and experimental results was found, see Table 11. The magnitude of the peak $\Delta\phi$ is consistently under predicted by the model. The FFT sweeps for a particular frequency component in the thermal decay signal for each pixel through time. As the FFT in PPT is identifying the frequency components of the thermal decay signal from the PT, any differences between the modelled and experimental PT data will be amplified by the algorithm that provides the phase data. The FFT has been carried out using

$$F_n = \sum_{k=0}^{N-1} T(k) e^{2\pi i k n / N} = \mathrm{Re}_n + i\,\mathrm{Im}_n \tag{6.4}$$

where n is the frequency increment, $T(k)$ is the temperature at a pixel for thermal image k and N is the total number of thermal images processed.

The phase data is calculated using

$$\phi_n = arc\tan\left(\frac{\mathrm{Im}_n}{\mathrm{Re}_n}\right) \tag{6.5}$$

Equation (6.5) shows that the *arc*tan function of Im/Re calculates the phase which provides the amplification in contrast seen in Figure 36 that reveals the PTFE defect in the lap joint when comparing PT and PPT. However in devising a model for PPT it should be noted that the *arc*tan operation will also magnify any difference caused by assumed material properties etc.

The FFT frequency at which the maximum $\Delta\phi$ occurs is accurately predicted for the lap joint case study. The frequency at which the peak phase contrast occurs in the aluminium case study is slightly over predicted at 1.111 Hz in the model compared to the experimental result of 0.871 Hz. For the CFRP-PTFE case study the modelled frequency for the peak phase contrast is found at three times the experimental frequency of 0.281 Hz compared to the experimental value of 0.091 Hz. The ability to predict the frequency at which the peak will occur may allow reduced data processing as the range of frequencies required to be processed will be decreased. These results show that the data processing routine used shows promise, however, improvements are required in the thermal model to allow the $\Delta\phi$ magnitude data to be accurately predicted as currently differences between the thermal datasets are emphasised by processing into phase data.

a

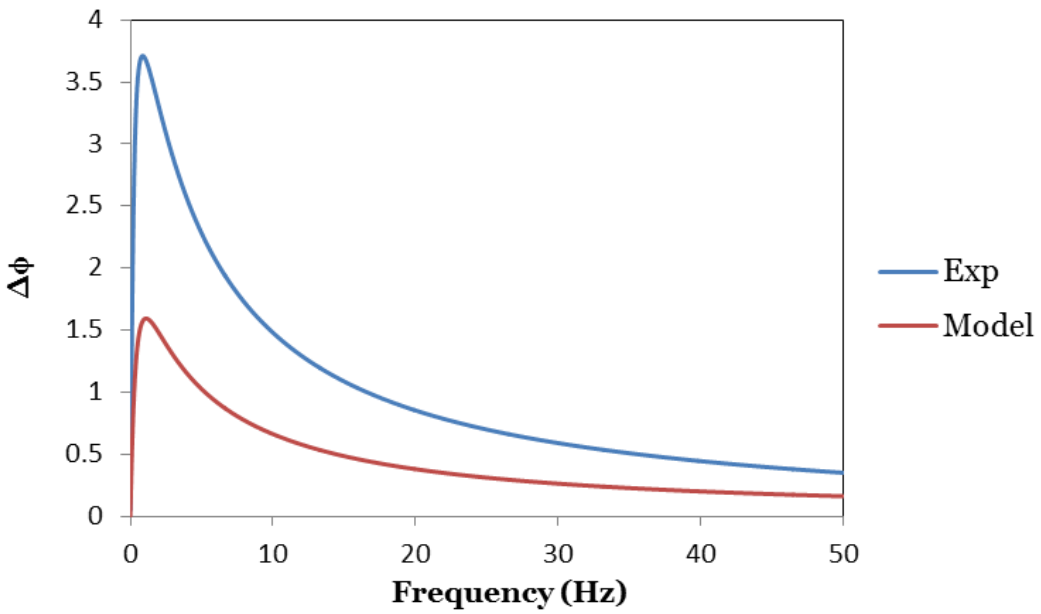
4
3.5
3
2.5
2
1.5
1
0.5
0
Δϕ
0
10
20
30
40
50
Frequency (Hz)
Exp
Model

b

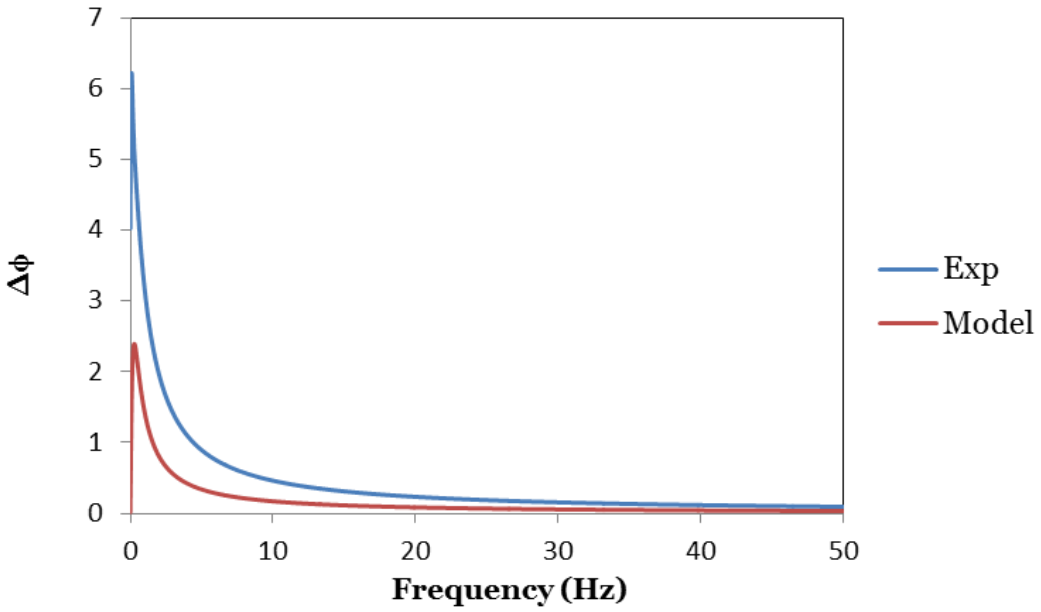
7
6
5
4
3
2
1
0
Δϕ
0
10
20
30
40
50
Frequency (Hz)
Exp
Model

c

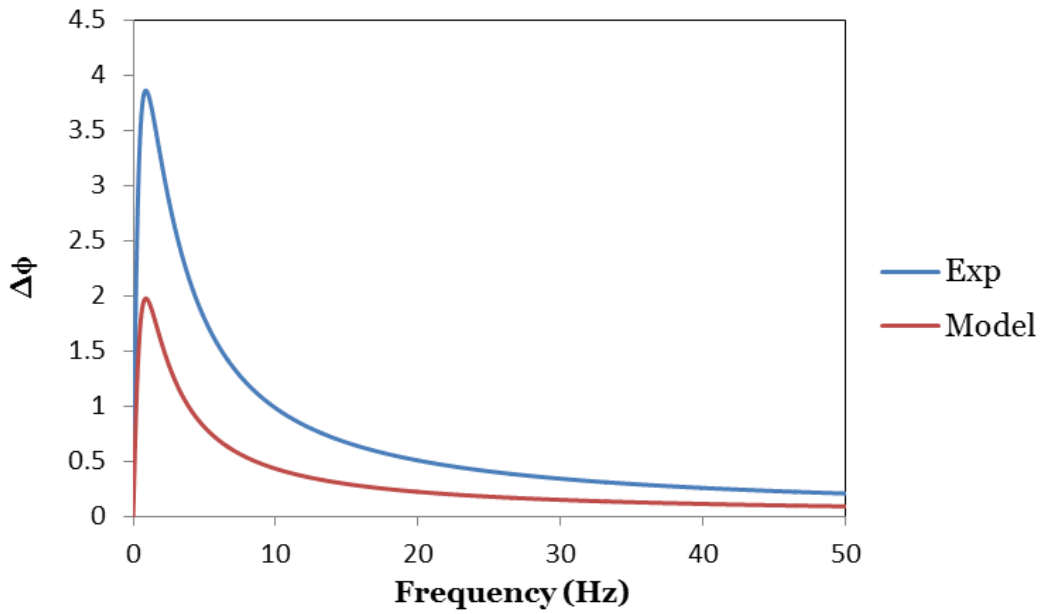

Figure 48 Phase contrast between DC and ND for experimental and modelled data for a) CS1: Aluminium, b) CS2: CFRP with PTFE, c) CS3: CFRP-CFRP adhesive lap.

Table 11 Ratio of modelled and experimental frequency at which the peak phase contrast occurs and ratio of magnitude of maximum phase contrast peak for each case study.

Case study	Frequency Ratio	Phase Contrast Ratio
CS1 - Aluminium	1.28	0.43
CS2 - CFRP	3.08	0.38
CS3 - CFRP-CFRP Lap	1.00	0.51

6.5 Modelling of defect detectability

PT and PPT rely on an underlying detectable thermal contrast of surface temperatures over defective and non-defective regions. Where this contrast is low the detectability of defects is greatly reduced. The previous case studies highlight examples where there is a strong contrast in thermal properties between defect and bulk material properties, such as CS1 and 2, and weak contrast, as in CS3. The current section aims to identify relationships between bulk and defect heat transfer properties relating to the detectability of the defect. Three common bulk materials that have been investigated are; aluminium, CFRP and GFRP. The geometry of all of these samples has been

defined as 1 mm thick and 100 mm long with a 0.2 mm thick 10 mm long defect at a depth of 0.4 mm.

The effect of variation of the defect material diffusivity, relative to that of the bulk material, on the temperature contrast produced between defective and non-defective regions was investigated. Figure 49a shows the ratio of defect to bulk material diffusivity plotted against the temperature contrast produced, ΔT. There is no temperature contrast when the defect and bulk material properties are the same, i.e. $\gamma_D/\gamma_0 = 1$. As the difference between defect and bulk properties is increased then $|\Delta T|$ also increases, which enables defect identification. Where the defect has a higher diffusivity than the bulk material, $\gamma_D/\gamma_0 > 1$, ΔT is negative as the heat is transferred through the defect region, away from the surface, quicker than the surrounding defect free regions, resulting in a cool spot on the surface over the defect. When $\gamma_D/\gamma_0 < 1$, ΔT is positive as when a defect has a lower thermal diffusivity it hinders the propagation of heat causing an increased amount of reflection from the defect boundary which results in a hotspot on the surface over the defect. The heat must then either propagate through the defect of lower diffusivity or laterally around the defect, both of which will result in a distinctive perturbation in propagation of heat through the component. It is noted that defects with a diffusivity ratio less than 1 produce a much greater absolute temperature contrast than those where the ratio is greater than 1 due to the variation in heat propagation as discussed. Figure 49a illustrates that in the region surrounding $\gamma_D/\gamma_0 = 1$, the $|\Delta T|$ produced is insufficient to be reliably identified by the detector which has a thermal resolution of 20 mK. Within these regions there is no visible contrast using PT between the defective and defect free regions of the material. The size of these regions is proportional to the diffusivity of the bulk material. Threshold values of the diffusivity ratio outside of which the detection of defects is possible using PT are suggested in Table 12. As an example, the diffusivity contrast between CFRP and PTFE is 0.3 whereas the ratio between GFRP and PTFE is 0.9. These ratios are indicated with the dashed lines in Figure 49a. This correlates with the results from the experimental work found in Chapter 5 where it was found to be more difficult to detect PTFE in GFRP compared to detecting the same defect in CFRP as the ratio of diffusivities becomes closer to 1.

The modelled ΔT data has then been processed into PPT $\Delta\phi$ data to show how the visibility of defects may be affected when presented as phase data, shown in Figure 49b. The magnitude of the $\Delta\phi$ data shows a similar asymmetric relationship as the original ΔT data where a defect of lower diffusivity than the surrounding bulk material remains easier to identify than one of higher diffusivity. For all three materials processing the data into $\Delta\phi$ has the greatest effect on the visibility of defects with lower diffusivity than the bulk material while having a relatively small effect on defects of higher diffusivity. The visibility of the defects remains clearest in the aluminium however, the CFRP and GFRP show much closer results in terms of magnitude of $\Delta\phi$. The FFT approach used for producing the phase data has had the greatest effect on the defect visibility in the GFRP, i.e. the material with the lowest diffusivity. This is clearly a beneficial effect of the signal processing. In Figure 49b the maximum value of $\Delta\phi$ for has been plotted, hence accounting for the great improvement in identifying defects in the GFRP when using PPT instead of PT. This demonstrates that when ΔT values are low it is most crucial that the FFT operates over the correct frequency range for the particular material.

The key feature of the data shown in Figure 49b is the effect of the phase processing on the extent of the central plateau region around $\gamma_D/\gamma_0 = 1$. It is shown in Table 12 that, while the extent of the $\Delta\phi$ plateau in the aluminium remains similar to that found in the ΔT data, the plateaus for the composite materials of lower diffusivity are reduced. The reduction in the extent of the plateau regions enables defects of reduced contrast in diffusivity compared to the bulk material to become identifiable using PPT. Defects with diffusivity ratios within the remaining plateaus will remain undetected using PPT.

a

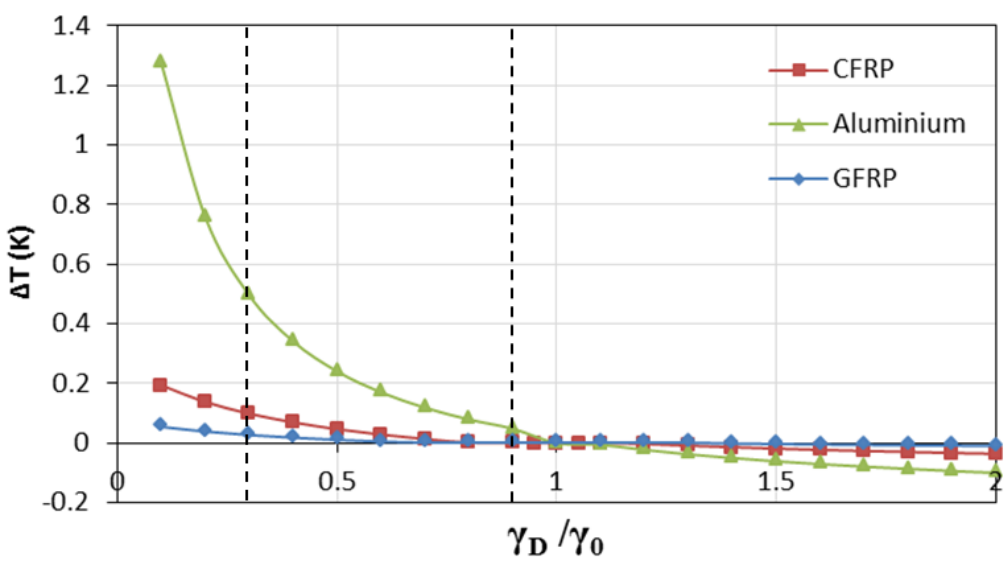

b

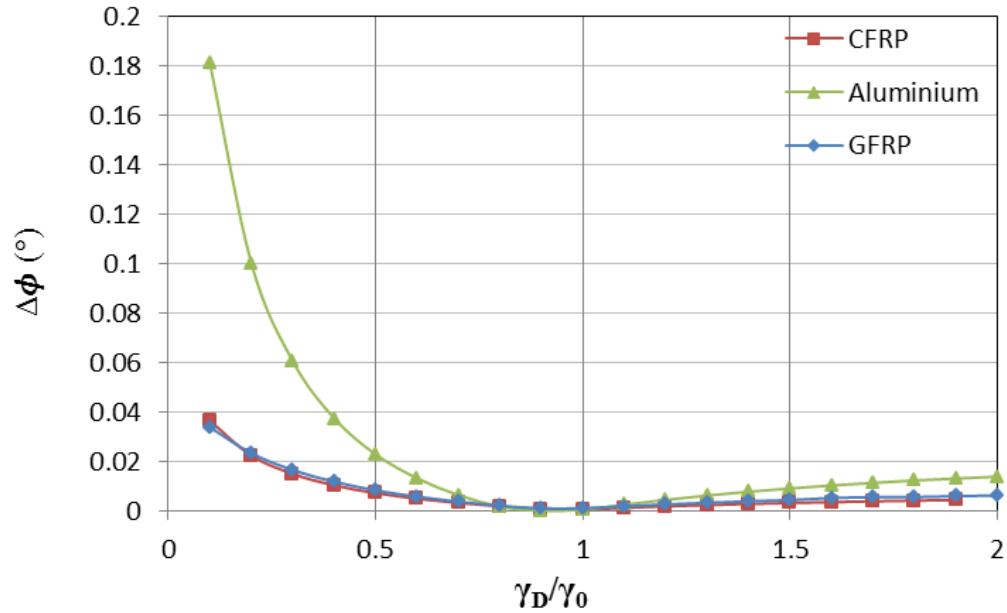

Figure 49 a) ΔT values and b) $\Delta\phi$ values as ratio between defect and bulk thermal diffusivity, γ_D/γ_0, is varied.

Table 12 Threshold values within which defects are no longer visible using PT ΔT values and PPT $\Delta\phi$ values as a percentage of bulk material property.

Material	**γ_D/γ_0 threshold for PT**	**γ_D/γ_0 threshold for PPT**
Aluminium	$\leq \pm$ 0.1	$\pm$ 0.1
CFRP	$\pm$ 0.2	$\pm$ 0.1
GFRP	$\pm$ 0.3	$\pm$ 0.1

It is noted that the three case studies previously presented have a diffusivity ratio of defect to immediately surrounding material of less than one and so are all visible. The geometry and presence of any additional materials of the samples has not been taken into account in the calculation of ratios. It is identified that if sufficient thermal excitation is applied to the components that the current defect materials have sufficient contrast of thermal diffusivity compared to the immediately surrounding material, i.e. adhesive for CS3, for defects to be detectable. The overall detectability of defects in a component will also be dependent on the geometries of the surrounding material and the thermal pulse applied.

Another quantity that has been used in studies of defect visibility is 'effusivity', e.g. [116, 134]. Effusivity, *e*, is the measure of the ease with which heat is able to transfer between two materials and is given by [135]

$$e = \sqrt{k\rho C_p} \tag{6.6}$$

Clearly this is important as the thermal contrast detected in thermography must be related to the heat transfer between one media and another. However, the model that has been developed in the present work does not include the effect of effusivity but is based entirely on the Fourier diffusion relationship given by Equation (6.1). A further point to note is the very good agreement between the experimental and modelled data for the pulsed thermography. Notwithstanding this, for completeness a study of the thermal and phase contrast in terms of relative effusivities was carried out and is shown in Figure 50 with threshold values also presented in Table 13. The trends are almost identical to those given in Figure 49 for the thermal contrast but with larger values of contrast. For the phase contrast, comparing effusivities provides different trends to the diffusivity comparison with more contrast. It is the square root in Equation (6.6) that drives the more optimistic contrast values whereas in Equation (6.2), there is a linear relationship between the material properties. The purpose of this section of work is to provide a means of determining if a specific defect type will be detectable. Hence comparing diffusivities provides the most conservative prediction as to whether a defect is detectable. The diffusion model has been validated with experimental data and is therefore considered to be reliable.

a

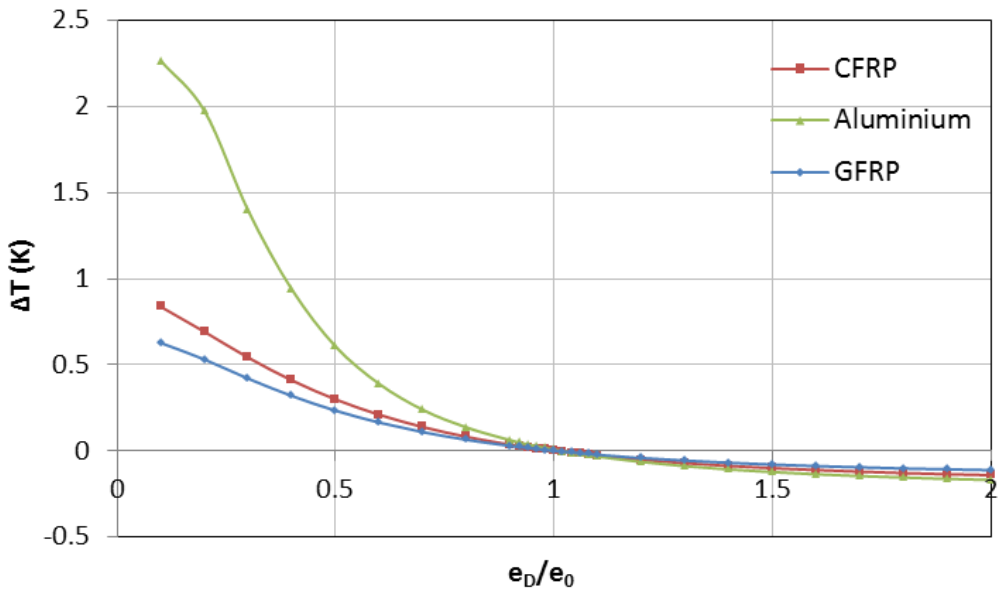

b

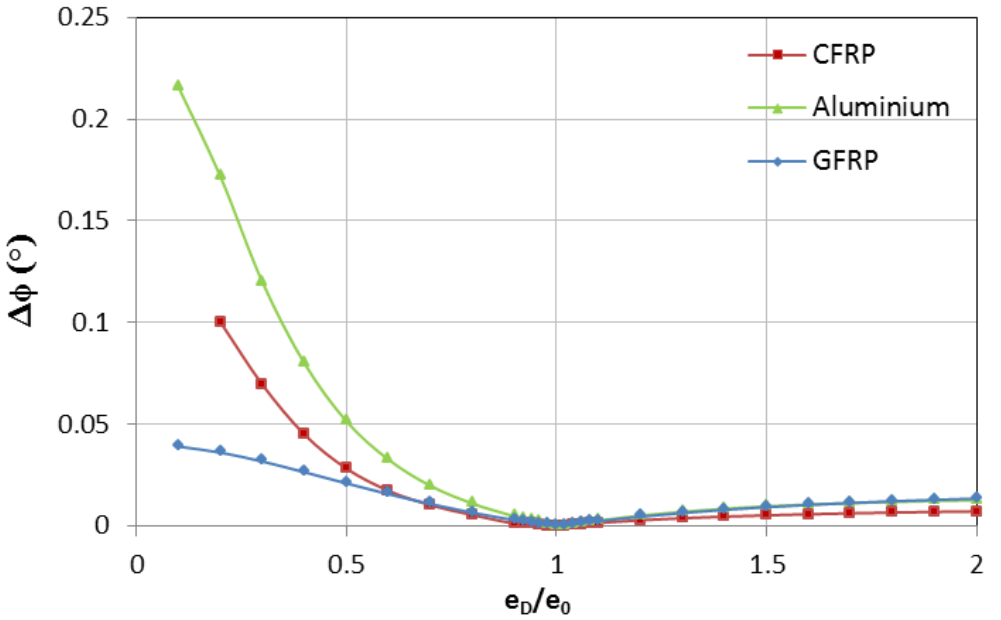

Figure 50 a) ΔT values and b) $\Delta\phi$ values as ratio between defect and bulk thermal effusivity, e_D/e_0, is varied.

Table 13 Threshold values within which defects are no longer visible using PT ΔT values and PPT $\Delta\phi$ values with relation to thermal effusivity ratios.

Material	**e_D/e_0 threshold for PT**		**e_D/e_0 threshold for PPT**	
	Min limit	Max limit	Min limit	Max limit
Aluminium	0.98	1.06	0.98	1.02
CFRP	0.96	1.06	0.98	1.04
GFRP	0.94	1.08	0.98	1.02

6.6 Summary

Three case studies (CS) were used to compare the thermal experimental PT data with the modelled PT results, both of which were then converted into PPT phase data. CS1 was an aluminium sheet with a flat bottom defect milled into the rear of the sample. CS2 was a CFRP panel with a PTFE defect added between plies during manufacture. CS3 was a CFRP single lap joint made using a standard epoxy adhesive with a PTFE defect introduced at the adhesive/adherend interface.

The model and PT data comparison focused on three key points on the surface above the defect centre (DC), defect edge (DE) and a non-defect area (ND) and the thermal contrast between DC and ND. The data for corresponding points in the modelled and PT data was taken for comparison. In CS1 the data compared well although an additional effect was revealed in the model, the inversion of the decay curves which was not identified in the PT data. Whilst this may be present in the experimental decay it was found that this effect would be likely to be hidden by experimental noise. In CS2 and 3 the modelled and experimental data compared very well. The thermal contrast data for CS2 and 3 demonstrates that the model is capturing the thermal contrast evolution produced in the experiments.

PPT phase contrast data has been presented for the modelled and experimental results. The processing routine used under predicted the magnitude of the phase contrast but had some success the frequency at which the peak $\Delta\phi$ occurred. The discrepancies are caused by the inverse tan processing involved in the production of the phase data as this emphasises small differences in data, which is why the phase data reveals defects that were not visible in the thermal data.

A defect detectability study was carried out. It was found that the presence of ΔT and $\Delta\phi$ regions surrounding $\gamma_D/\gamma_0 = 1$ where defects are not identifiable may be related to defect detectability and threshold values where defects are able to be identified have been suggested. Generally processing of the PT thermal data into PPT phase data has been found to reduce the extent of plateau regions surrounding $\gamma_D/\gamma_0 = 1$ and hence enhance detectability of defects with lower thermal contrast. Neither PT nor PPT is able to detect kissing defects

that would occur within the region around $\gamma_D/\gamma_0 = 1$ so the following work now focuses on the adaptation of the experimental approach to reveal kissing defects.

7. Kissing defects

7.1 Introduction

The work described in the preceding chapters has demonstrated PT and PPT cannot detect kissing defects as they provide insufficient thermal contrast for the defects to be resolved. If thermography is to be used for kissing defect identification the process must be adapted to create a thermal contrast. An investigation is undertaken to find if a small air gap could create sufficient contrast for defect detection. Initial work focuses on the use of the model, developed in Chapter 6, to identify the thickness of the minimum detectable air gap. Results showed it would be possible to identify a very thin air gap, therefore, a means of opening such defects was then considered. Kissing defects were simulated via the addition of silicon grease to the bond line. Initially work focussed on the use of the bending moment created through loading single lap joints to open experimentally simulated kissing defects. TSA was also carried out during these tests to give information about the stress state in the lap joints to assess the effect the defects were having when joints were loaded. Comparison of TSA and PPT defect detection was undertaken. While the addition of load using a test machine was found to enable defect detection using PPT it was not practical for onsite use. However the findings of this chapter enabled the development of a portable device, described in Chapter 8.

7.2 Model of the presence of the effect of a small air gap

The finite element model (FEM) of PT and PPT previously developed was used to investigate the minimum detectable gap using the current experimental set up. In the previous chapter the model was validated using a series of three case studies, one of these case studies is the lap joint of focus in the current section. The model does not include the addition of load. To model the opening of the defect the defect material is taken as air, the thickness of the defect is incrementally changed and the model rerun, simulating a new PT experiment each time. The air gap thickness is modelled as 50, 100, 150 and 200 μm.

Surface thermal contrast (ΔT) between defect and defect-free regions was calculated through time, as shown in Figure 51a. The value of maximum ΔT increases with increasing defect thickness as the heat transfer through the defect region is significantly altered compared to the non-defect, as shown in Figure 51b. Using the detector sensitivity as a detectability threshold, shown as the dashed horizontal line at 20 mK in Figure 51a and b, a minimum thickness of an identifiable air gap can be identified. The model suggests that a minimum air gap thickness of approximately 75 μm is required for a 10 mm wide defect within the CFRP lap joint to be detected above the detector threshold. Air gaps below 75 μm are deemed undetectable. The temporal duration of ΔT remaining above the detector threshold is also proportional to the thickness of the air gap making the detection of thinner defects also dependant on suitable recording frequency for the detector being used. A variation of the lateral extent of a defect would also have an impact on the ΔT obtained and the duration it would be visible for, however, currently only this specific lap joint case has been considered.

a

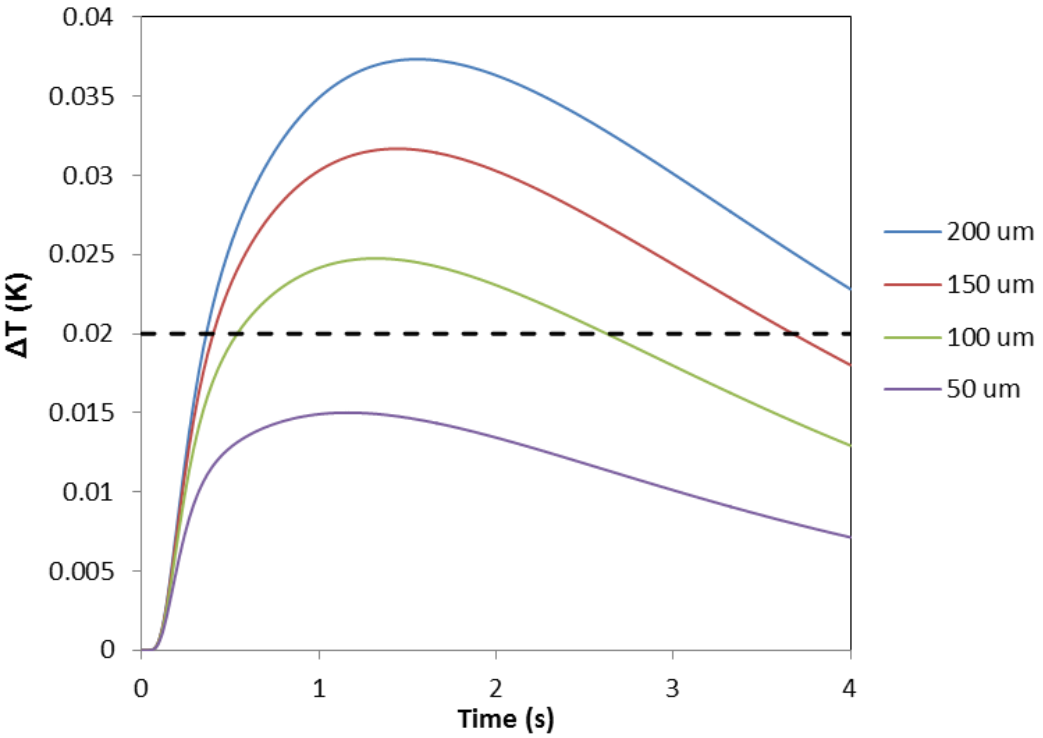

b

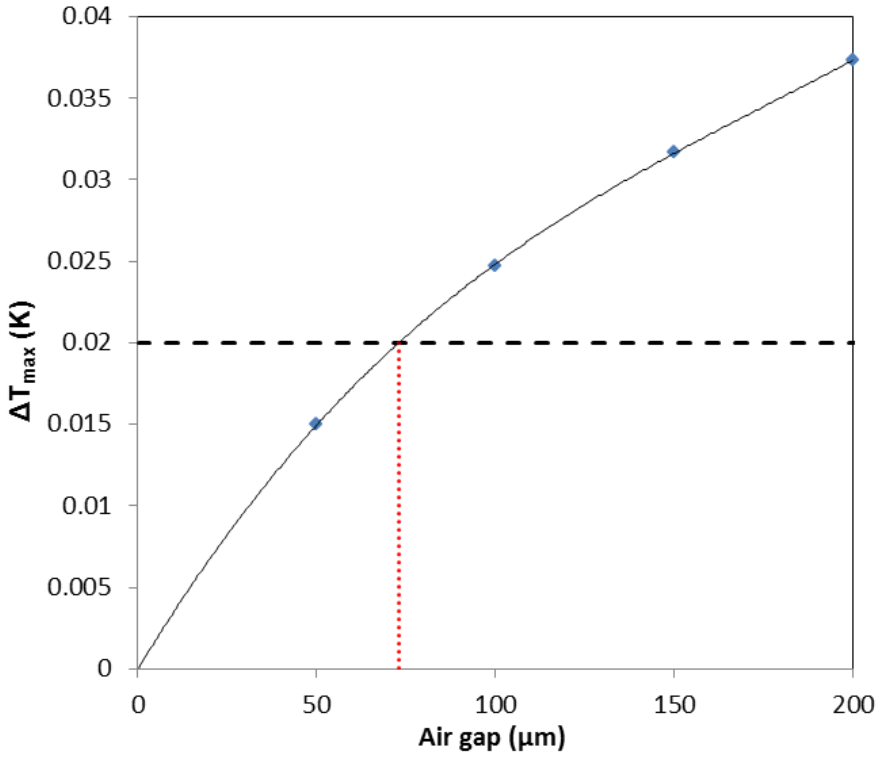

Figure 51 a) Thermal contrast through time between the surface temperature over the defect centre and a non-defect region for air gaps of 50 – 200 µm, b) maximum thermal contrast produced for varied air gap defects.

The FEM results presented highlight that only a small opening is required for a defect to be detected. This then suggests that it may be possible to use a non-destructive load to open defect a sufficient amount to enable defect detection.

7.3 Test specimens with kissing defects

7.3.1 Lap joint configuration

A series of single lap joints were made using 4 plies of Gurit UD CFRP $[0, 90]_s$ with SE84LV epoxy matrix. Bonds were adhered using Araldite rapid epoxy adhesive. Specimens were 30 mm wide and 270 mm long with a bonded area of 30 x 30 mm, shown in Figure 52. Defect materials were added to the bond line covering an area of 10 x 10 mm in the centre of the bonded area.

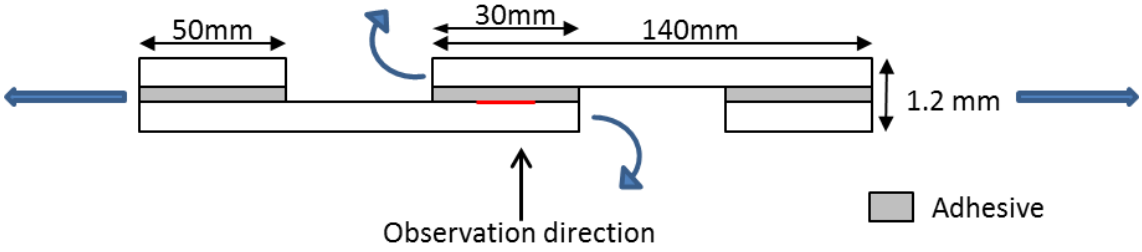

Figure 52 Lap joint specimen diagram giving sample geometry and tensile load and resulting bending moment illustrated by the blue arrows.

7.3.2 Defects

Silicon grease and Frekote mould release agent were used to simulate kissing defects. These materials were chosen as they are likely to be present in construction or composite manufacturing environments. A 10 x 10 mm square a contaminant was added to the centre of the bonding area on one adherend of the bond, the adhesive was applied to the other adherend and the bond created. Lap joints containing PTFE inserts were also created to give a baseline defect for detection using the NDE techniques.

Tensile tests were carried out to find the effect of the simulated kissing defects created on the ultimate tensile failure load and shear strength of the lap joints. Inspection of the bonded surfaces after failure enables the effect of contaminants can be qualified, see Figure 53, as well as quantified via the

failure loads, see Table 14. The failure loads in Table 14 are obtained from experimental stress/strain graphs produced for a series of 5 samples of each joint configuration and their respective shear strength calculated. As expected the addition of the silicon and Frekote contaminations significantly reduce the failure load and shear strength of the joints by about 50%. Both contaminants have reduced the adhesion and hence the failure loads of the joints by approximately the same amount. Generally a reduction of adhesion area of about 12% resulted in a reduction of failure load by about 50%. The contaminated joints adhere to the criteria set out by Marty *et al* [29] with a shear strength of below 80% when the whole joint was contaminated compared to a non-defect lap and failed via the required adhesive failure mode. As such according to this criterion the silicon grease and Frekote contaminations produce kissing defects. However the introduction of the Frekote and the silicon grease had visibly different effects on the adhesive. The silicon grease was still present in the joint when it failed, in the location it was applied and had prevented adhesion between the adherend and adhesive in the defined area. The Frekote appears to have had a chemical reaction with the adhesive and prevented adhesion of the adhesive on both adherends. As Frekote has very low viscosity there was some bleeding from the application area, which led to a larger area of the bond being affected by the contaminant. The chemical effect of Frekote on the adhesive is not known and is not expected to be caused by a kissing defect. Therefore, kissing defects in the current work are simulated via the addition of silicon grease, where only the adhesion of the bond is affected.

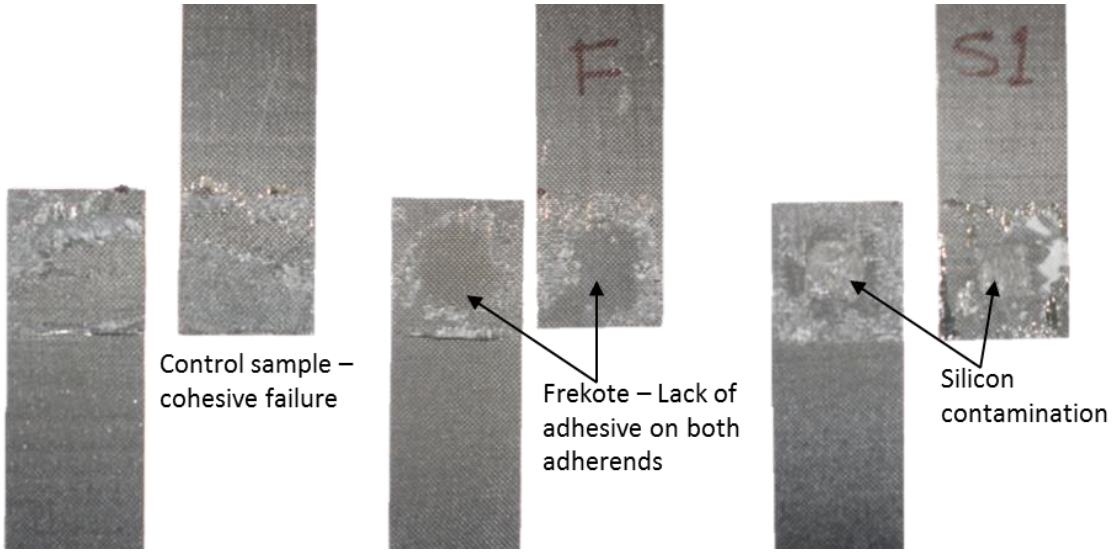

No defect **Frekote mould release** **Silicon grease**

Figure 53 Failed lap joints containing no defect, Frekote mould release agent and silicon grease.

Table 14 Failure load and effective adhesive area for failed lap joints containing no defect, Frekote and silicon grease.

Contamination	Failure load (kN)	Shear strength (kN/m^2)	Adhesive area (mm^2)
Control (no defect)	11.9	13222	900
Silicon grease	6.6	7333	800
Frekote mould release	6.0	6666	<800

7.3.3 Test setup

TSA required the joints to be loaded in an elastic cyclic routine where as a static load was required for PPT. The elastic loading range for TSA was found using the failure test data previously discussed and the PPT data was collected in reflection mode at the mean of the cyclic load. PPT was also carried out before and after the tests without applied load. The experimental routine for these tests is presented in Table 15. The aim of the tensile load was to create a bending moment in the sample that was sufficient to open the defects, illustrated in Figure 52. Defects are found on the neutral axis of bending for the sample as is typical for lap joint configurations. Therefore, a relatively large tensile load at 50% of the failure load was selected for the tests to give the best chance of defect detection.

Table 15 Testing and loading regime for TSA and loaded PPT experiments.

Test	Load (kN)
PPT	0
PPT	3
TSA	3 ± 1 at 5 Hz
PPT	3
PPT	0

The test setup is shown in Figure 54. The equipment was positioned around a servo hydraulic test machine. The same infrared detector was used to collect TSA, PT and PPT data. The Nikon Speedlight SB600 flash was used for heating the samples for PT and PPT. All experiments were carried out without moving the sample from the test machine. The detector standoff distance was maintained at 250 mm and the flash standoff distance was 150 mm.

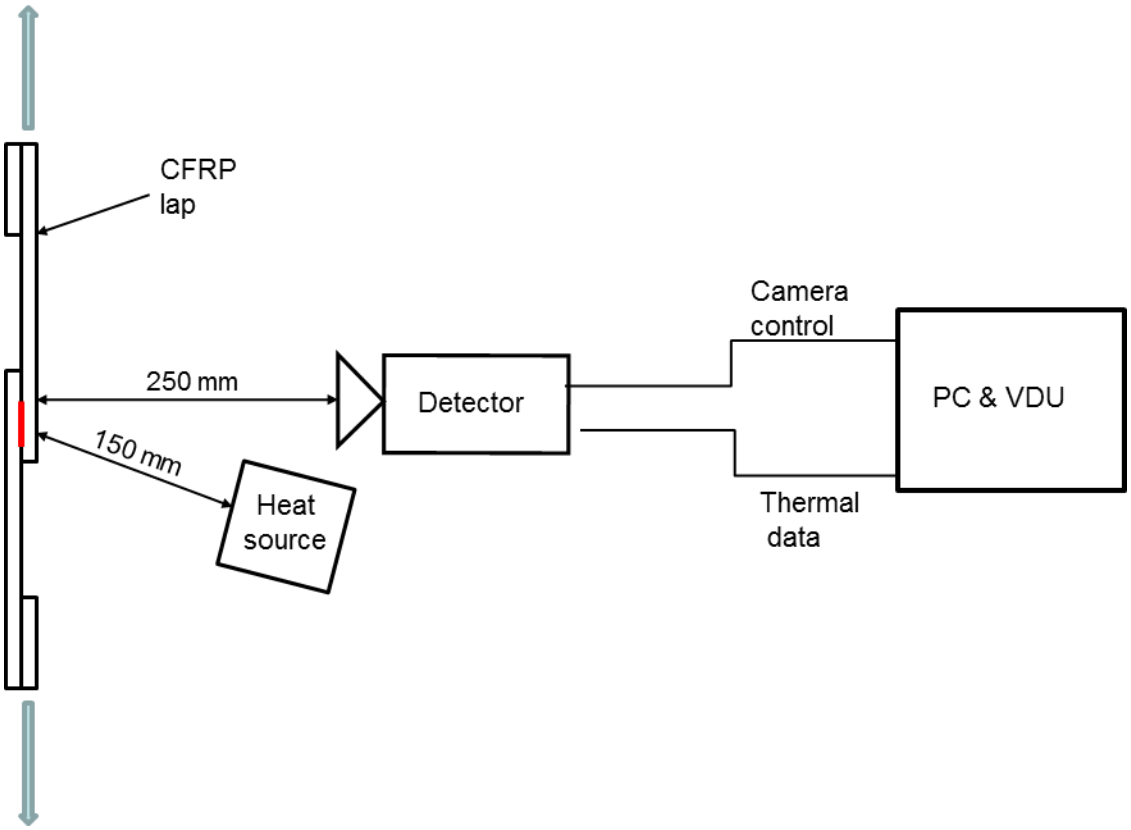

Figure 54 Schematic for TSA and PPT with the addition of static tensile load for PPT and cyclic tensile load for TSA.

7.4 Results

7.4.1 PTFE

The TSA ΔT data for the lap joints containing PTFE, shown in Figure 55a, shows a thermal gradient increasing from the upper edge of the bond to the lower edge of the bond. The gradient occurs due to the bending of the lap joint which is caused by the geometry of the samples. This bending means that a region of tension will occur at the upper edge of the lap and a region of compression at the lower edge when observed as presented with the nearest free edge at the top. The TSA data collected for the lap joint with the PTFE insert demonstrates that under the cyclic loading of the TSA the PTFE insert has had no effect on the ΔT data collected, see Figure 55a. As ΔT is directly related to the change in the sum of the principal stresses it is shown that the stress distribution is not affected by the presence of such an insert. The TSA phase data in Figure 55b shows no departure from the uniform phase distribution apart from at the upper and lower edges of the lap where the stress magnitude is at a maximum due to the bending. There is no indication of the presence of the PTFE insert in either of the TSA data sets. The TSA data therefore suggests that the PTFE insert may not be classed as a defect as it has no effect on the stress distribution through the joint.

PPT $\Delta\phi$ in Figure 55c is able to identify the PTFE insert prior to the application of load within the CFRP and epoxy adhesive joint as expected. The thermal diffusivities of the PTFE and the surrounding material are significantly different enough that the heat transfer through this region is sufficiently altered to identify the PTFE using PPT. The results of the PPT taken with the sample at a load of 3 kN also revealed the PTFE insert, see Figure 55d. Profile PPT $\Delta\phi$ data was taken across the width of the defect region for both the unloaded and loaded results, see Figure 56a and b. Figure 56b shows that the magnitude of $\Delta\phi$ between the surrounding well bonded area and the bonded area containing the PTFE was not altered by the addition of load. The artificial defect is not being opened under this load and the heat transfer path is not being altered. The PTFE is being identified due to its contrast of thermal properties compared to the surrounding materials equally for both cases. The lack of change in $\Delta\phi$ confirms the conclusion drawn from TSA that it may be inappropriate to

classify the PTFE insert as a defect as the load applied is unable to open the defect and the PTFE defect is having no effect on the joint mechanism.

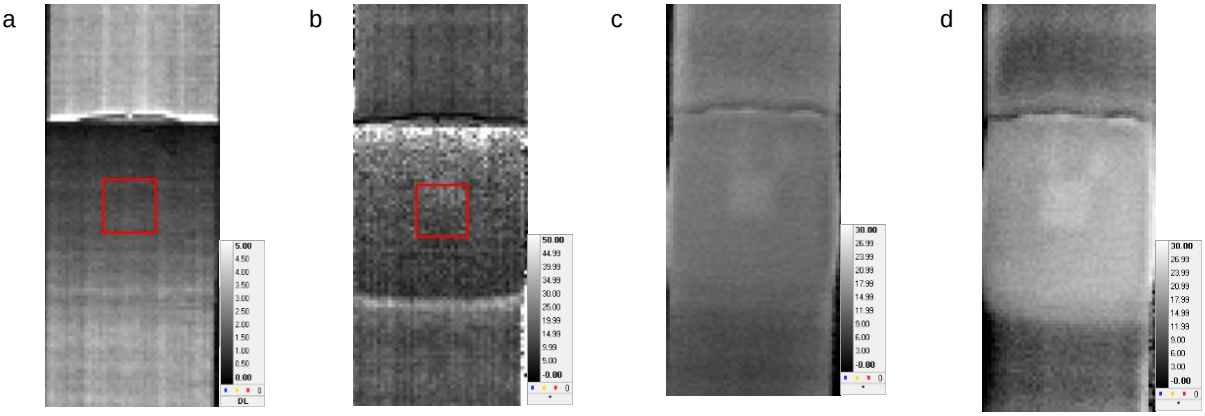

Figure 55 PTFE insert results a) TSA ΔT (3+1kN), b) TSA phase data, c) PPT phase data (0 kN) and d) PPT phase data (3 kN).

It is important to acknowledge that false positives may be caused by identification of regions of differing thermal diffusivity using PPT, as in the case of PTFE inserts. If the level of loading is sufficient to open a defect then a comparison of $\Delta\phi$ profiles, as shown in Figure 56b for the PTFE insert, may be used to clarify if identified defects are real defects or just a change in thermal properties that is not affecting the stress through the bond.

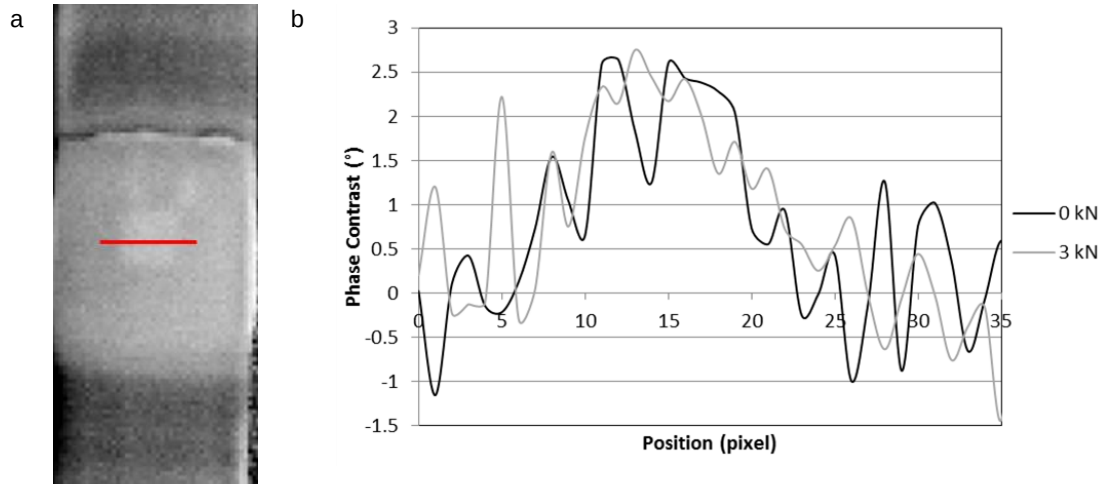

Figure 56 a) Position of profile data and b) PPT phase contrast data taken along the profile line across the PTFE insert for both the unloaded and 3 kN static loaded PPT results.

7.4.2 Silicon grease

As is the case for the PTFE insert lap joint the silicon grease contaminated joint TSA ΔT data shows a gradient across the joint where the bending occurring is creating local tension and compression regions in the joint at the upper and lower edges, see Figure 57a and b. The TSA ΔT data is unable to identify any clear anomalies in the stress distribution through the joint with the silicon contamination, however, the TSA phase data does identify a discontinuity in the joint. Variation in TSA phase data shows areas where the stress change and ΔT do not occur simultaneously i.e. where thermoelastic equation, Equation (3.1) given in Section 3.2.5, is no longer valid. Such out of phase data may be the result of a range of factors including non-adiabatic conditions, localised plasticity or localised heating. The out of phase data of the silicon grease contaminated lap joint is at the edges of the lap, where largest amounts of compression and tension are found, but then also at the upper and lower edges of the defect. If it is considered that the defect is not bonded then these areas must be localised areas of tension and compression due to the bending that occurs when the joint is under a tensile load. The out of phase data suggests that the loading of the lap is opening the bond where the silicon grease was placed.

PPT is unable to identify the silicon grease when the joint is unloaded, see Figure 57c. This implies that the contamination is having minimal effect on the heat transfer through the defect region compared to the non-defect region which is as expected with a kissing defect. When the joint is loaded to 3 kN sufficient load is applied to open the defect due to the lack of bonding between the adhesive and adherend where the silicon grease is present. A thin gap is created in the defect region which creates sufficient thermal contrast for the previously undetectable defect to be detected using PPT, see Figure 57d.

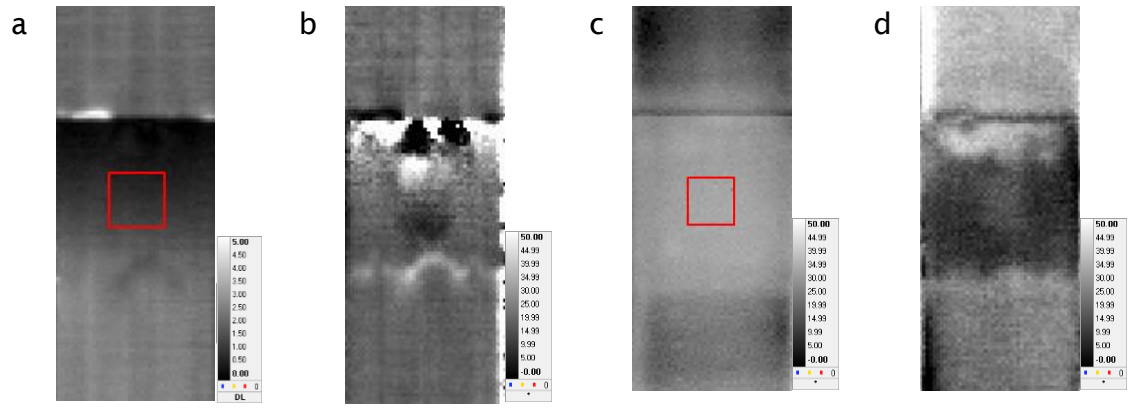

Figure 57 Silicon grease contamination results a) TSA ΔT (3+1kN), b) TSA phase data, c) PPT phase data (0 kN) and d) PPT phase data (3 kN).

The detection of a defect using PPT relies upon sufficient thermal contrast being introduced to cause a detectable variation in the PPT $\Delta\phi$ data. The profile plot data taken horizontally through the central region of the silicon grease defect, see Figure 58a, shows that the phase contrast is greatly increased when the joint is under load, see Figure 58b.

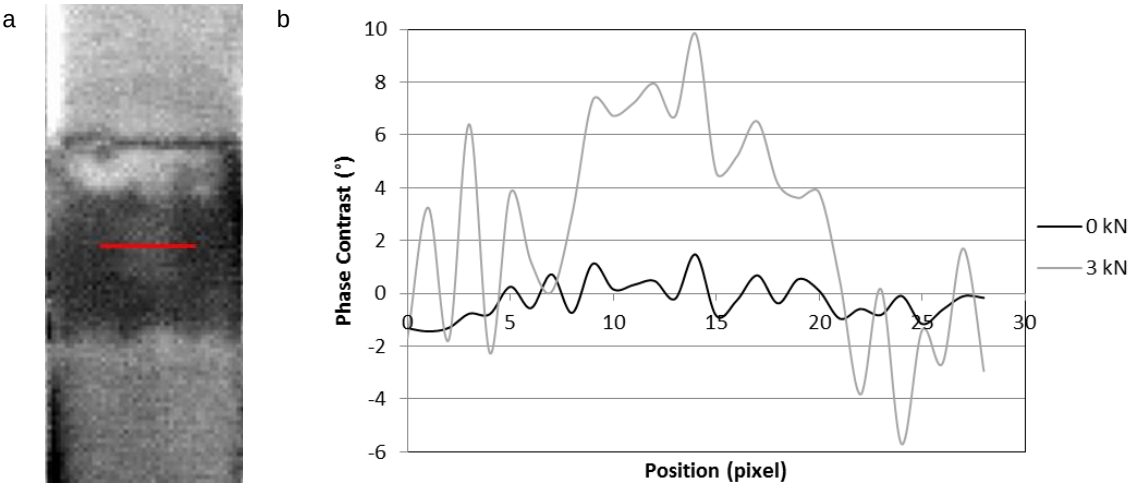

Figure 58 a) Position of profile data and b) PPT phase contrast data taken along the profile line across the silicon grease contamination for both the unloaded and 3 kN static loaded PPT results.

7.5 Summary

A common method for the artificial creation of defects, particularly in composite materials is the addition of a piece of PTFE in the layup of the material. Through the use of both PPT and TSA it has been found that the addition of a PTFE insert may not be classed as a defect. TSA has shown that

the presence of such a PTFE insert to have no effect on the stress distribution across the joint. PPT with and without a load applied found that the PTFE insert defect region was not opened by load as the phase contrast produced for both loaded and unloaded tests remained unchanged. It is concluded that the PTFE insert is only detected using PPT due to its thermal contrast to the surrounding materials rather than due to it having any effect on the adhesive bonding. It is possible that this occurs if the PTFE insert has been encapsulated by adhesive and a good bond formed.

The addition of silicon grease to a bond appears to create a more realistic defect than the PTFE insert. The silicon grease contamination has caused the bond to fail via adhesive failure, is not identifiable through material thermal contrasts and has caused a lack of adhesion in that region of the bond. Therefore there is confidence that an experimentally simulated kissing defect has been produced. TSA phase data is able to identify the upper and lower edges of such a defect where assumptions such as non-adiabatic conditions no longer hold. PPT without loading is unable to identify the silicon grease as the contamination has a minimal effect on the overall heat transfer through the defect region compared to the non-defect regions. Upon application of the tensile load the defect is opened to create an air gap of sufficient thickness that a measurable change in the heat transfer path is created and thus the PPT is able to identify the previously unidentifiable defect.

The bending moment that is created when loading a single lap joint in tension has resulted in the opening of the experimentally simulated kissing defect and hence the detection of such defects using PPT. It is acknowledged that the amount of load required will be material and geometry dependent and should be tailored to the component of interest. While this technique was successful it is a laboratory based technique. The following chapter shall focus on the application of load that enables the technique to be taken out of the laboratory and into the field.

8. Practical application of PT/PPT

8.1 Introduction

It has been shown that application of a load can enable a kissing defect to open sufficiently to enable its detection. So far the technique is laboratory based; using a test machine to impart load, and a high specification IR detector to measure the thermal response. The current chapter focusses on the adaption of the technique to allow it to become more practical and accessible to industry. Firstly the use of a vacuum load to open experimentally simulated defects with the aim to provide a more portable means of loading is studied. Then a feasibility study is carried out showing the potential use of a lower cost bolometer for PT. At this stage only PT has been considered as the data transfer from the low cost bolometer used is not suitable for the current processing into PPT data however, it is shown that PT is possible using a very low specification detector.

8.2 Vacuum loading

A feasibility study of the application of a vacuum load to one side of a component has been carried out. An aluminium and CFRP bonded sample containing a 20 mm square silicon grease contamination was manufactured using Araldite epoxy adhesive. The aluminium was 0.125 mm thick and the CFRP was 0.5 mm thick. The bonded area was 82 x 180 mm, shown in Figure 59. These materials were selected to have a mismatch in stiffness so the application of a vacuum to the aluminium side of the bond may elastically deform the aluminium adherend before deformation of the CFRP would occur. This was desired to simulate the adhesion of a secondary component to a larger fixed structure, although generally the current case provides an exaggerated stiffness mismatch.

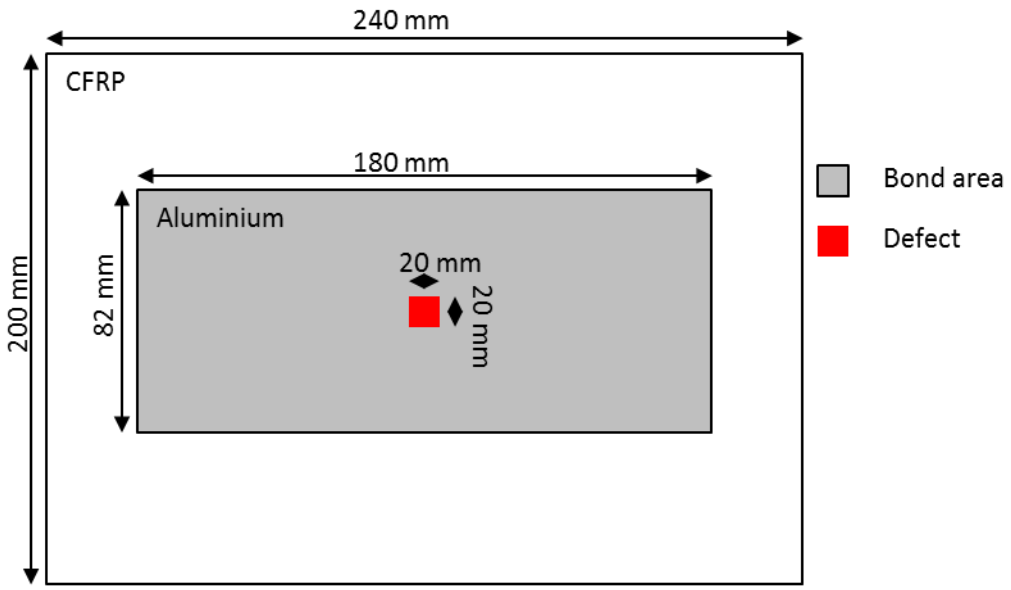

Figure 59 Schematic of CFRP – Aluminium bonded joint with silicon grease kissing defect for vacuum loading.

Initial tests were undertaken collecting the PPT data in reflection mode from the CFRP side of the bond and applying the vacuum to the aluminium side. The experimental configuration is shown in Figure 60. The initial setup required two sided access to the bond which would limit the application of the technique in its current form, however this enabled a proof of concept to be investigated. It would be anticipated that should the design be taken into industry the PPT setup should be incorporated into the vacuum design creating a tool requiring only single sided access.

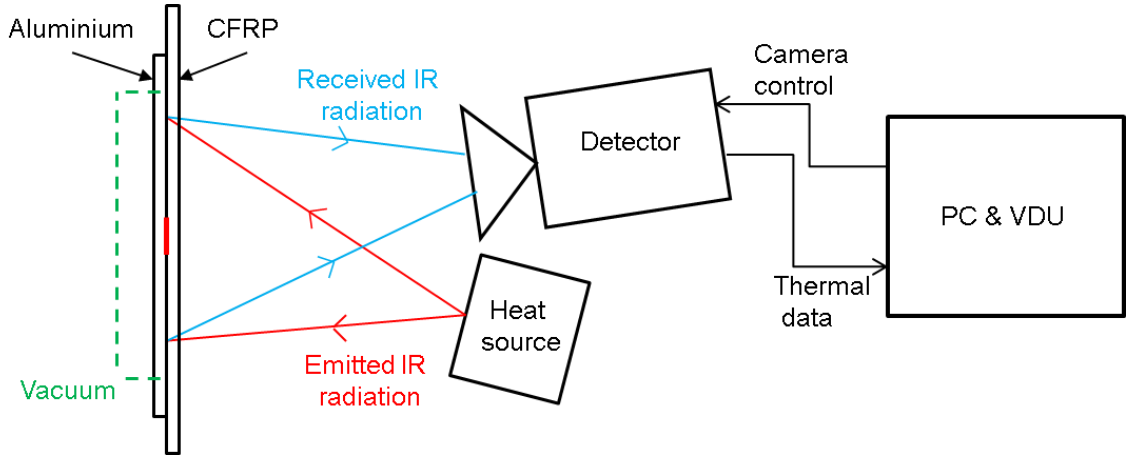

Figure 60 PPT and vacuum loading schematic with two sided access for feasibility study.

The PPT phase data was found to be unable to reveal the experimentally simulated kissing defect without the application of load, see Figure 61a. When a vacuum was applied to the rear of the sample the defect was opened and became clearly identifiable as shown in Figure 61b. The circular shape in the phase data images is the vacuum chamber attached to the rear of the sample and the rectangular shape across the images is the strip of aluminium adhered to the rear of the CFRP as viewed.

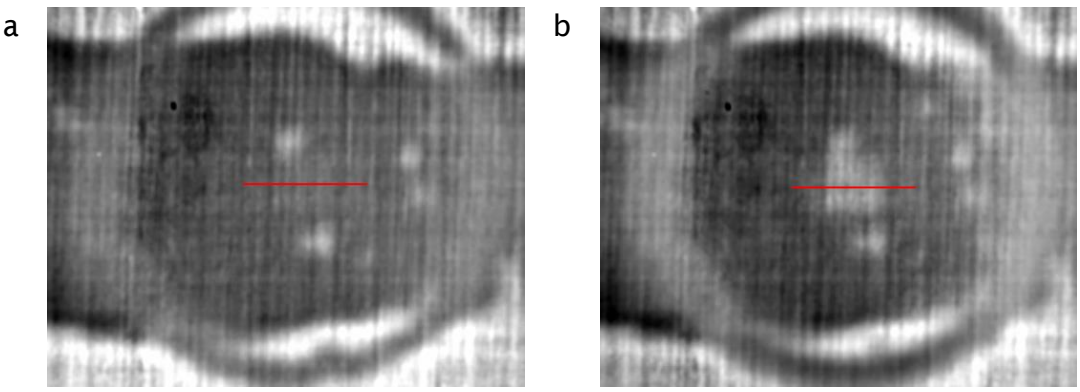

Figure 61 PPT phase data for the CFRP/Aluminium bonded sample a) unloaded and b) full vacuum applied to the rear of the sample.

The percentage vacuum was varied between zero and 100% vacuum to identify the level of vacuum required to open such a defect sufficiently for successful identification. Profiles were taken across the defect location, as indicated in Figure 61, for each level of vacuum applied, shown in Figure 62a. The phase contrast is shown to increase with increased percentage vacuum as the defect is opened further and the heat path is altered. Figure 62b shows the mean $\Delta\phi$ obtained over the defect for each percentage vacuum. The error bars are taken as the standard deviation of the phase values taken over the defect. There is an increase in the phase contrast obtained as the vacuum is increased from 0 % to 60 %, as the defect is opened. It appears that at 60 % the defect is as open as it can be, under vacuum loading as insufficient load is applied to propagate the defect. Phase contrast does not increase further as the vacuum is increased to 100 %. Upon unloading of the sample the defect closed again and became undetectable, hence the application of the vacuum did not occur. As the non-defect sections of the profile data are closely correlated, Figure 62a, the defect was not propagated into 'well bonded' areas and so the loading remain non-destructive. The amount of vacuum pressure required is dependent on the adherend material and the size of the defect to be identified.

a

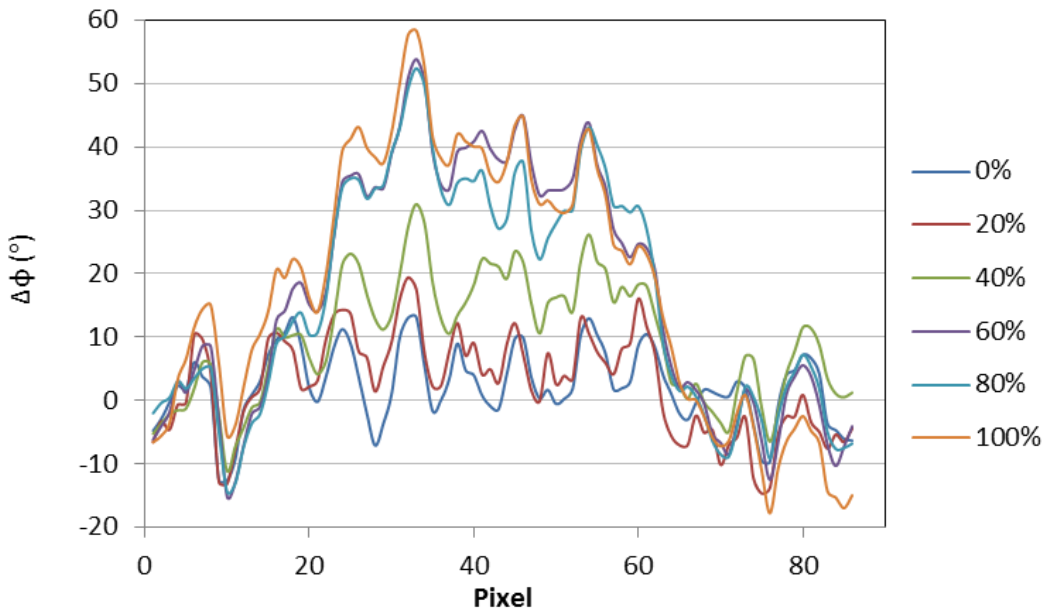

b

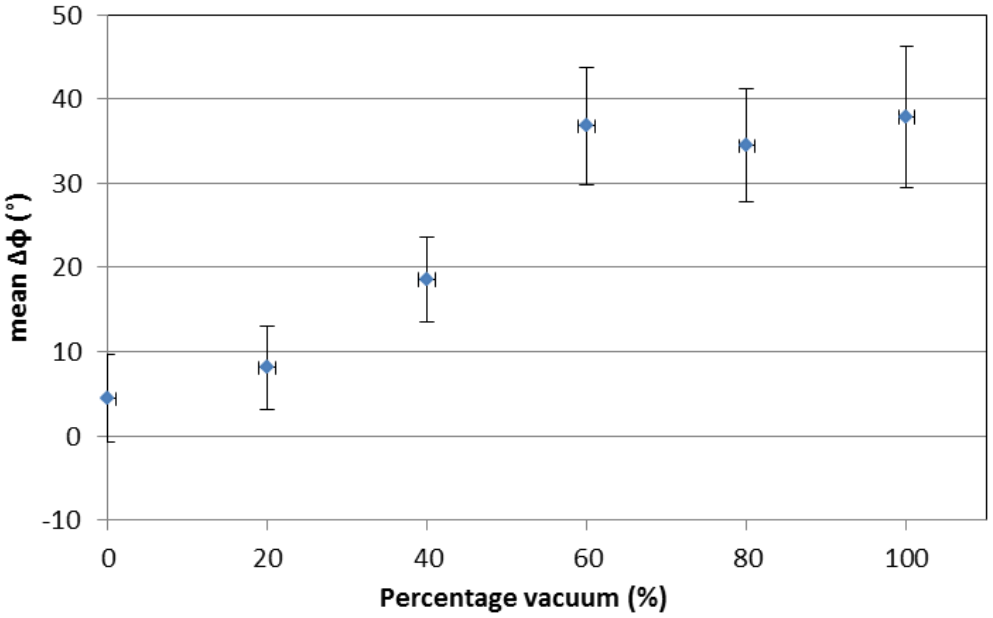

Figure 62 a) Phase contrast profiles taken across the defect location as shown in Figure 61 for vacuum pressures between 0 and 100% and b) the mean $\Delta\phi$ created by the defect at variable vacuum pressures.

A structural FEM was developed using Ansys 14.0 to investigate the amount of displacement likely to occur for the Al sheet adhered to the CFRP plate. The model assumed no adhesion at the kissing defect location. The edges of the original defect were given a boundary condition of zero displacement, i.e. no propagation of the defect was allowed. The vacuum pressure applied to the aluminium was varied between 0 and 100% vacuum and the displacement was recorded. A note should be made that the displacement was of the aluminium

and the adhesive as in the experiment the simulated kissing defect was introduced between the CFRP and the adhesive. Figure 63a shows the displacement of the aluminium between the central point of the defect and the fixed edge under the application of various levels of vacuum loading. These results confirm that for this thin aluminium sheet the defect is being opened under very little applied vacuum pressure thus enabling defect detection as thermal contrast is created, as found in the experiments. The mean displacement for the defect opening has also been found, see Figure 63b. As the maximum opening will occur at the centre of the defect is may be that only the centre point may be detected, causing an underestimation of defect size and so may not be classed as a defect of concern. The use of the mean displacement created, for the purposes of modelling, allows defect detection and classification to be more accurately predicted. This approach highlights where defects may fall below lateral size thresholds dictated by industry due to insufficient contrast created across the full extent of a defect.

a

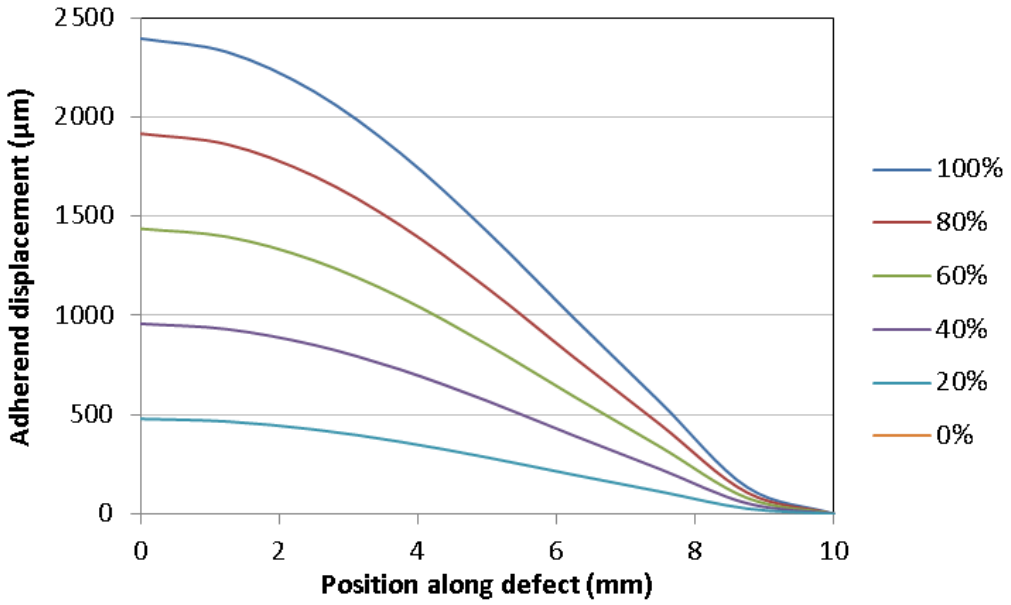

b

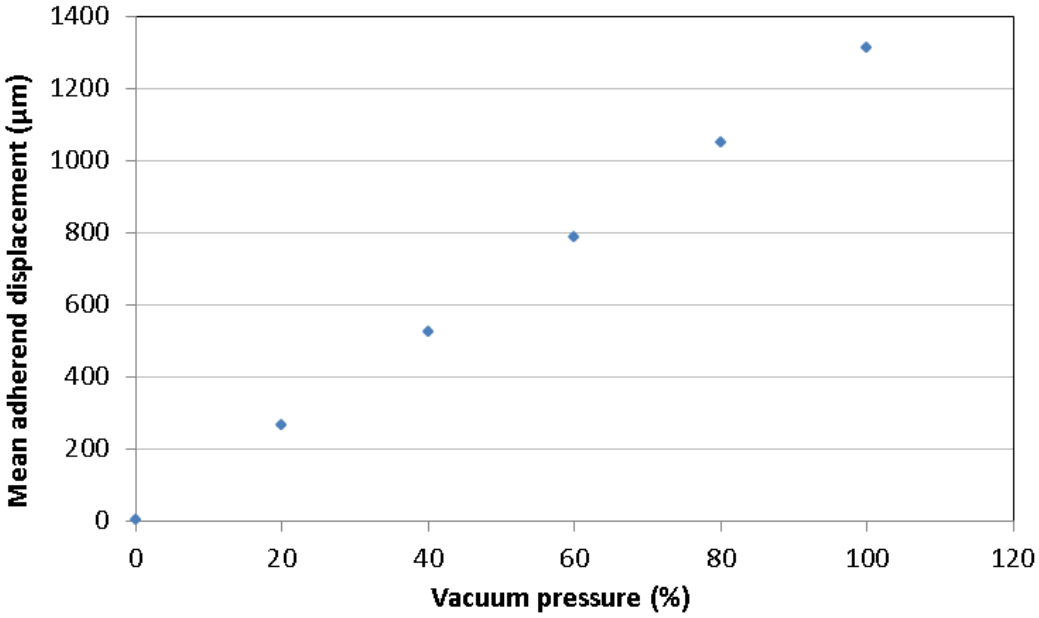

Figure 63 a) displacement across defect from defect centre (0 mm) to defect edge (10 mm) and b) mean adherend displacement for varied applied vacuum pressure.

8.3 Low cost PPT

Preliminary experiments have been carried out using a low cost micro bolometer (Tau 320 from Flir) which is an uncooled system with a maximum frame rate of 25 Hz. The data is acquired using third party software called PC-DVR-4-Net. This type of system, costing below £1000, is aimed at the security and surveillance market. The software is only able to export video image files and does not export the corresponding calibration files. The data presented in

this section is taken from video files and no calibration to temperature has been carried out, as such results are presented in grey level. The aim of this section is to explore the potential of using such a low cost device for NDE applications. A CFRP panel containing a shallow 20 mm diameter PTFE insert at 0.375 mm was used. Figure 64b shows a frame from the bolometer video with PT setup labelled in Figure 64a, for clarity. It is noted that it was necessary to use a large stand-off distance between the detector and the specimen as the detector is designed to look at more distant objects during surveillance tasks and it had a fixed focus. A balance had to be made between focus on the sample and the defect size to be detected which is why the specimen is out of focus in the image. As the detector was moved further away it was also necessary to increase the angle at which the flash was incident on the sample to avoid the flash housing being positioned between the detector and specimen. A line plot of data taken across the defect was extracted from the image, see Figure 65a, which shows a strong thermal gradient created by the non-uniform heating. Line plots extracted from above and below the defect were averaged and subtracted from the defect profile data to show the defect more clearly see Figure 65b. This method of removing the influence of uneven surface heating only works where a defect is already clearly visible in the image and so cannot be used to enhance low contrast defects, such as kissing defects, as it requires reference non-defect regions.

a b

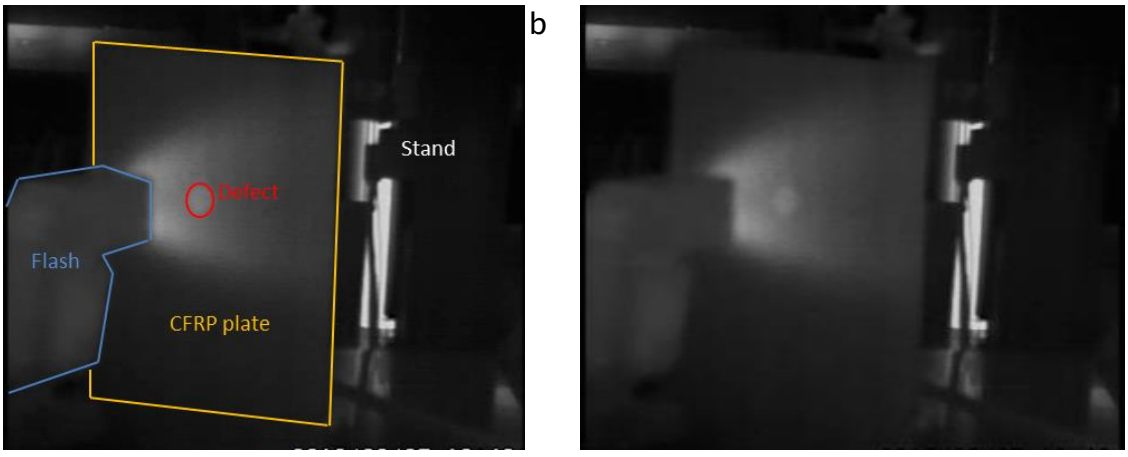

Figure 64 a) labelled diagram identifying PT setup and b) bolometer raw data.

a b

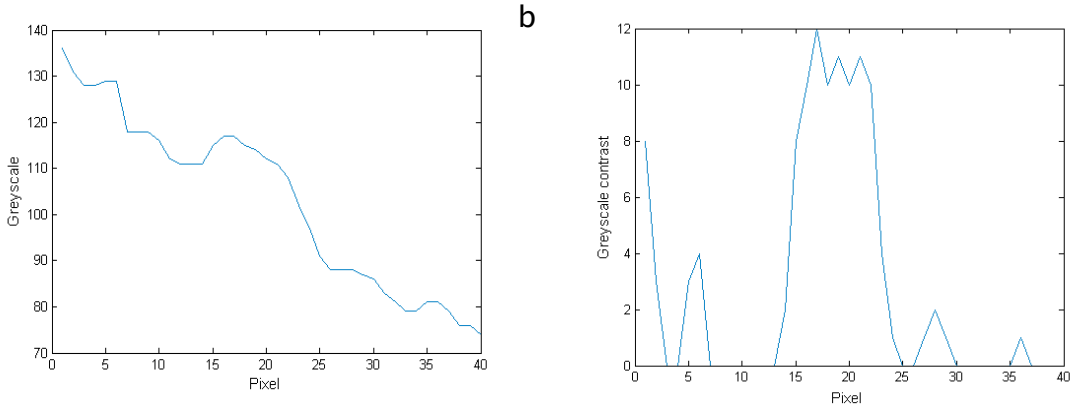

Figure 65 Bolometer profile data taken across the defect showing a) the raw profile data and b) profile with thermal gradient removed.

The data collected demonstrates that the use of a lower cost uncooled bolometer may be well suited to the application of PPT in a more accessible manner. The use of such a device would decrease the cost of the original set up by up to one hundred times. The current study has been undertaken using a low specification micro bolometer to identify a highly contrasting shallow defect. Bolometers able to collect data at higher frame rates and with increased thermal resolution are available and it would be suggested that these would be more suitable for a wider range of defect types and application of PPT.

8.4 Summary

A FEM of the CFRP lap joint of interest has been used to identify the thickness of gap required to create enough thermal contrast in surface temperatures over DC and ND regions to allow a defect to be detected using the current IR photon detector. The manufacturers have quoted a detector sensitivity of 20 mK. The modelled data predict that 10 mm wide air gaps with more than 75 µm thickness would create sufficient thermal contrast for successful identification. The duration for which sufficient contrast is observed is also related to the thickness of the air gap as a thicker gap would have an increased effect on the overall heat flow through that region compared to a thinner gap.

Vacuum loading has been successfully used to identify an experimentally simulated kissing defect in a CFRP/aluminium bond. A partial vacuum of only 40% was found to be necessary to begin to open the silicon grease defect and

create phase contrast for identification. Further work should focus on the application of this approach to reveal defects in bonded joints with adherend of increased stiffness. It is acknowledged that the application of the vacuum to the rear of the sample while applying PPT to the front removes the practical single sided nature from the procedure. Future work should focus on the integration of the PPT set up into a vacuum hood to produce a highly practical on site tool.

A feasibility study was undertaken to investigate the potential of using a cheaper bolometer style IR detector for PT. It was shown that an uncooled bolometer may be used for the application of PT and therefore PPT. The use of such a device as a replacement for the cooled photon detector typically used in PT and PPT would enable the camera cost to decrease to approximately a tenth, clearly making the technique far more appealing and accessible for industrial application. The use of an uncooled device may also simplify the integration of the detector into a vacuum.

9. Industrial applications

9.1 Introduction

The goal of the project was to develop PT/PPT in a manner that made it suitable for the identification of kissing defect in adhesive bonds, with particular reference to application on the Triplex bonded joints in MkIII LNG carriers. It was also important to establish the robustness of PPT when applied to a wider range of industrial applications. The current chapter covers the application of PPT to Triplex bonds as well as introducing three other case studies that have been carried out. These involve the application of PPT to different materials and in different environments to give information about bonded joints.

9.2 GTT MkIII LNG carriers

The construction of Triplex joints within the MkIII LNG carrier is discussed in detail in Section 2.3. The current section combines a series of results that have been obtained using laboratory created Triplex joints containing experimentally simulated defects, detailed in Table 16. PPT has been used to identify such defects. Initial work focused on PTFE insert style defects before moving on to the kissing defects of interest which were simulated using silicon grease.

9.2.1 Test specimens

A Triplex sample was constructed using the rigid and flexible Triplex and the film epoxy adhesive. Initially PTFE inserts and silicon grease were added to a joint between flexible and rigid triplex for investigation using PT and PPT. A second bond was constructed between CFRP and flexible Triplex which contained experimentally simulated kissing defects to enable investigation into the feasibility of vacuum loading. Spreadable epoxy adhesive was used for this CFRP/Triplex bond with a bond area of 250 x 150 mm. MkIII bond involves the adhesion of the RT to thick insulation blocks that are adhered to the inner hull, see Figure 4. However, the adhesion of the RT to the insulation results in the FT being adhered to a fixed structure. As the adhesion of the RT to the

insulation is not under investigation it was reasonable to assume that the FT should be adhered to a more rigid structure to create a more realistic response to the applied vacuum. At this stage it was necessary to maintain two sided access to the bond for PPT inspection and vacuum loading of the bond, so adhering the FT to a thick structure was not possible. Rather the FT was adhered to a CFRP panel, which provided a stiffer adherend suitable for the PPT to be carried out on the bond while the vacuum was applied to the FT. The Triplex and CFRP were selected due to their stiffness mismatch, ensuring the defect was being opened and the whole plate was not deformed. This stiffness mismatch was well suited to be akin to the application of the Triplex material, which is adhered to a very stiff fixed structure in service.

Table 16 Description of Triplex bonded joint sample configurations.

Bulk material	**Configuration**	**Defect material**	**Defect size**	**Defect depths**	**Total sample thickness**
RT – FT, film adhesive	FT and RT panels adhered using epoxy film adhesive (SA80)	PTFE and Silicon grease	5, 10 & 20 mm squares	0.7 mm	1.4 mm
CFRP (Gurit HSC -SE84LV) – FT, epoxy	CFRP and FT panels adhered using spreadable epoxy adhesive	Silicon grease	20 mm square	0.6 mm	1.4 mm

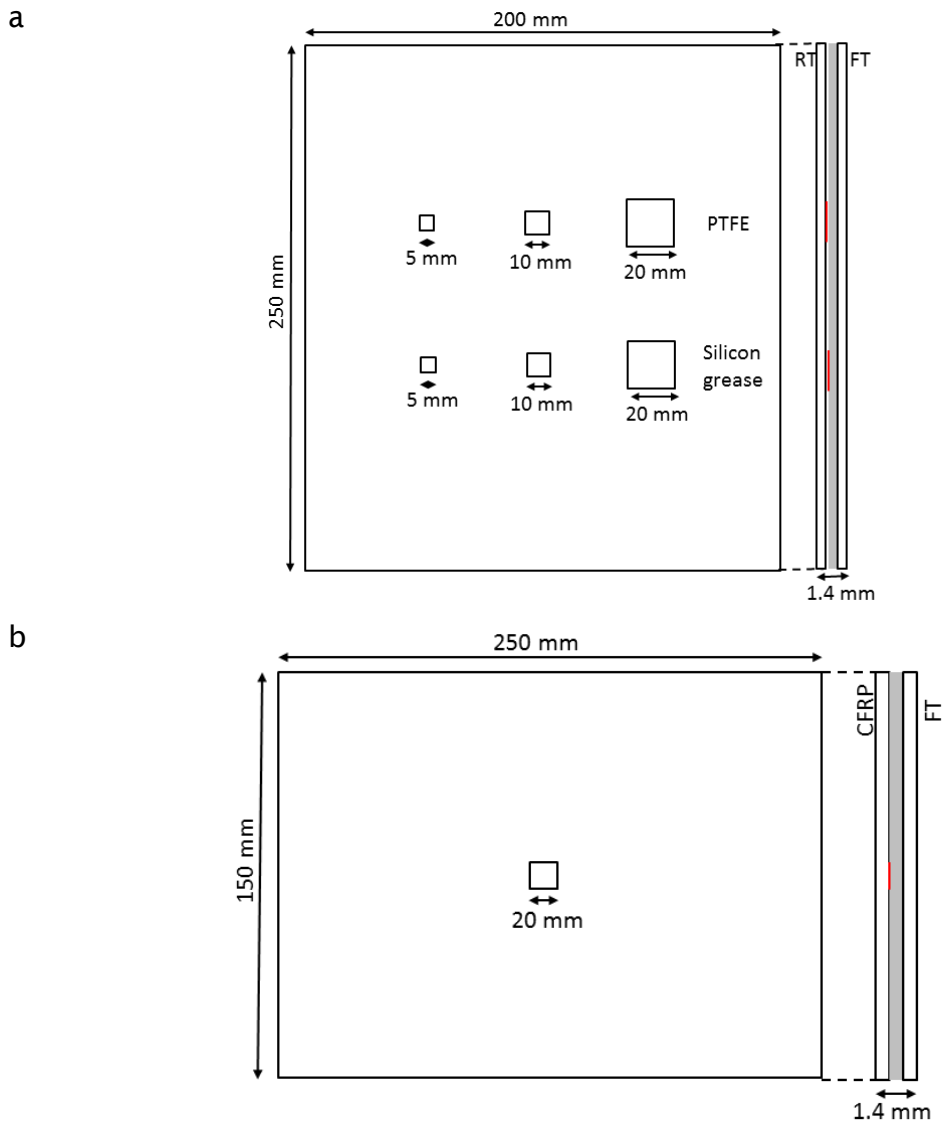

Figure 66 a) Rigid Triplex and flexible Triplex adhesive bond containing PTFE and silicon grease and b) flexible Triplex adhered to CFRP panel containing a single silicon grease simulated kissing defect.

9.2.2 Test arrangements

As Triplex is a layered material of glass and aluminium it required a stronger heating pulse than the single Nikon flash to allow more energy to be added to the system. The increased energy could have been delivered by either the IR heat lamp using the manual shutter or the Bowens 1000W Gemini Pro flash lamps. Both were used successfully on the Triplex material, however, all data presented is taken using the Bowens flashes as they gave more repeatable results due to the more controlled delivery of heat. Data was collected at 383 Hz for a duration of 6 seconds. The vacuum was applied to the rear of the

CFRP sample, on the Triplex, while inspection was carried out on the CFRP side of the bond, as illustrated in Figure 67. A circular vacuum chamber of 120 mm diameter was applied to the Triplex side of the bond and the bond inspected from the CFRP surface. The vacuum pressure was varied between ambient pressure, i.e. 0% vacuum, and full vacuum, 100%, using a vacuum pump. Pressure was varied using a manual valve and a pressure gauge.

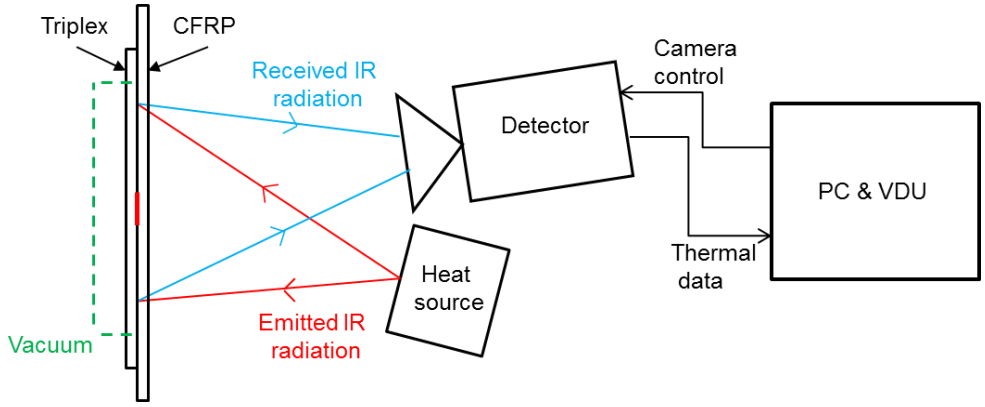

Figure 67 Vacuum loading on CFRP-Triplex bond with simulated kissing defect.

9.2.3 Results

The PTFE inserts were able to be faintly detected using PT but the image of the defect is greatly enhanced using the PPT phase data, see Figure 68. This is highlighted when looking at the profile data taken across the defect area from both the PT thermal and PPT phase images, see Figure 69. In the thermal image the range of temperature between the background level and the defect is reduced due to uneven surface heating, whereas in the PPT phase data the defect peak is maximised as the effect of uneven surface heating is reduced.

a b

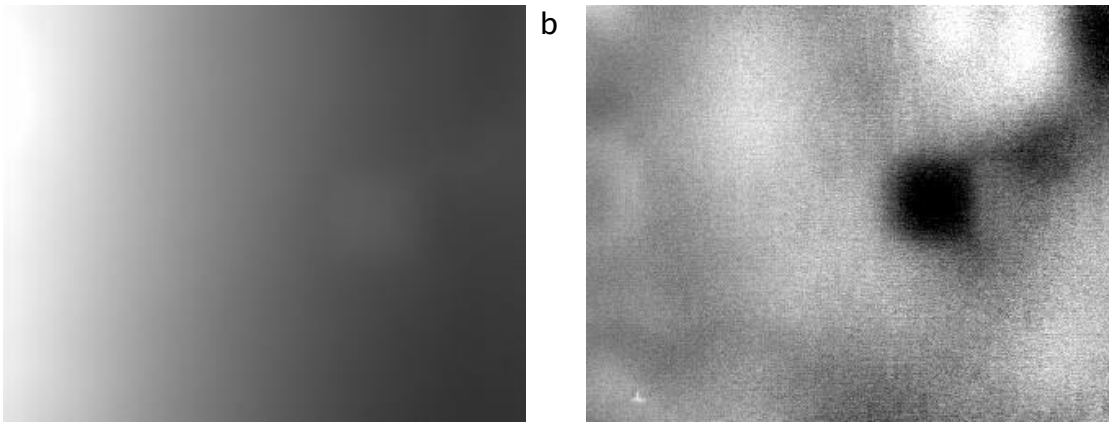

Figure 68 a) PT thermal and b) PPT phase for Triplex bonded joint using epoxy film adhesive with PTFE insert.

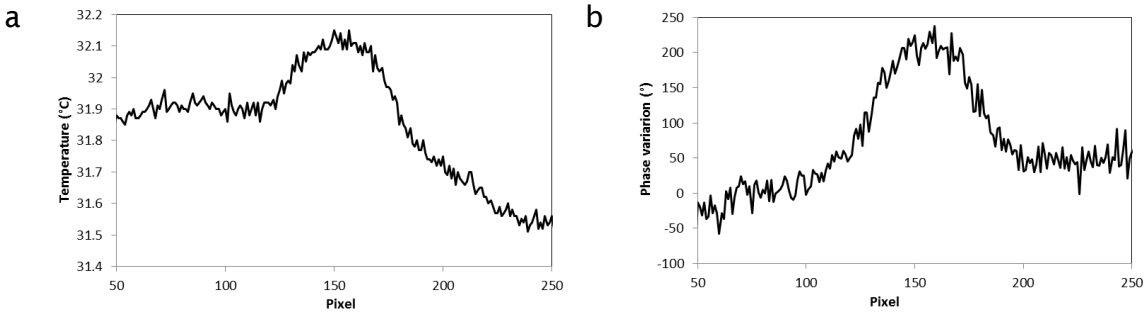

Figure 69 Left: Temperature (left) and PPT phase (right) profiles taken across PTFE defect in the Triplex joint with epoxy film adhesive.

The Triplex joint constructed using the film adhesive also contained silicon grease defects. The PPT phase data was unable to conclusively reveal the silicon grease, see Figure 70. The surface of the flexible Triplex in this case contains dimples or creases from the way in which it has been rolled. These local variations in surface height also produce PPT phase variations that can be seen in the image which may detract from defect detectability and increases the phase variation required to positively identify a defect. As with the previous silicon defect in the CFRP joint, the technique must be developed to enhance the detectability of this type of defect.

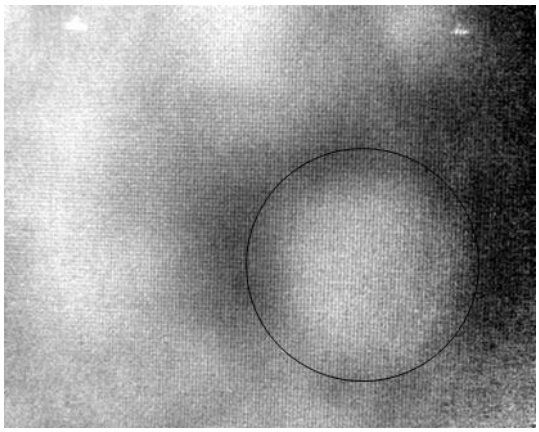

Figure 70 PPT phase data for silicon grease defect indicated by the circle in a Triplex bonded joint using epoxy film adhesive.

Vacuum loading

A structural FEM was developed, similar to that discussed in Section 8.2, to investigate the effect of vacuum loading on the deflection of the FT. Vacuum pressure was varied between 0 and 100 % vacuum. The edges of the defect were allowed zero displacement, i.e. the defect was unable to propagate. A 20

mm defect was modelled, the same as that in the experimental specimen. The results shown in Figure 71a demonstrate that a low level of vacuum loading enables such a defect to open and thus creates thermal contrast to enable defect identification. The centre of the defect will open further than the edges of the defect thus the maximum opening will only occur in a very localised region. To ensure defects may be detected the mean displacement across the width of the defect, rather than just the central point, should be considered as this will be more likely to ensure a more accurate size representation of the defect is found, see Figure 71b.

a

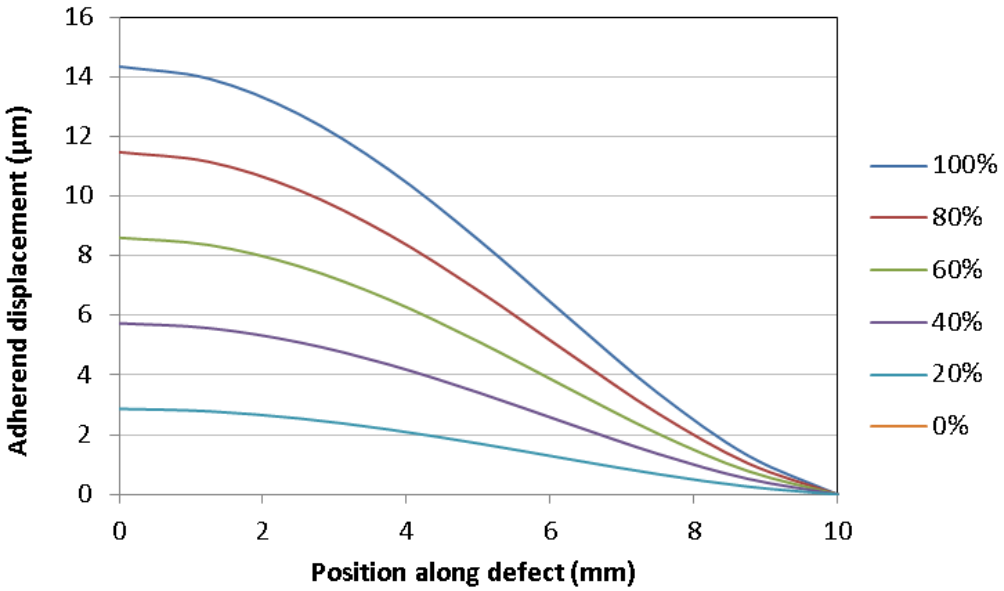

b

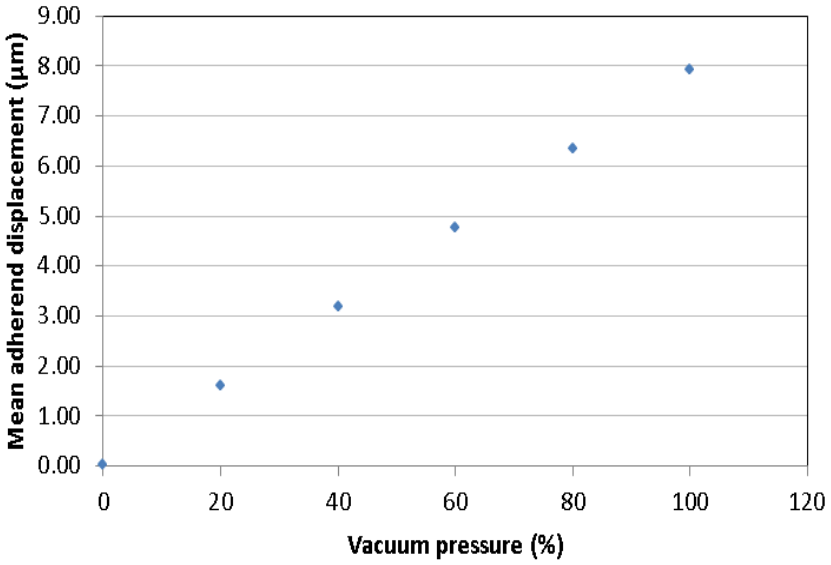

Figure 71 a) displacement across defect from defect centre (0 mm) to defect edge (10 mm) and b) mean adherend displacement for varied applied vacuum pressure.

Creating a sample using only rigid and flexible Triplex for the purposes of vacuum loading was not possible as it was deformed upon application of the vacuum load. A bond using only the FT and RT is not representative of the nature of the bonds created in the MkIII LNG carrier. The construction in the

Figure 72a and b show the PPT phase results of the same region with no load applied and 100% vacuum loading. The lighter circular ring visible in the edges of the images was due to the presence of the aluminium vacuum chamber attached to the rear of the sample. It is clear that without the addition of load the silicon grease contamination was not visible in the phase data, however with the addition of the vacuum it was easily identifiable in the centre of the image. This was emphasised in the profile data taken horizontally across the centre of the defect position for the fully loaded and unloaded conditions, as shown in Figure 72a. The profile plot, in Figure 73a, also demonstrated that the regions away from the defect, i.e. the well bonded regions, were unaffected by the application of the vacuum, hence the defect was not propagated by the loading and the technique remained non-destructive. It should be noted that an unloaded image was taken after the full vacuum was applied showing that permanent deformation had not been caused to the defect or surrounding region by the vacuum loading. Figure 73b shows the mean phase contrast between the defective and non-defective regions for each vacuum partial pressure applied. The defect becomes identifiable in the mean phase contrast data at just 60% of vacuum pressure.

a b

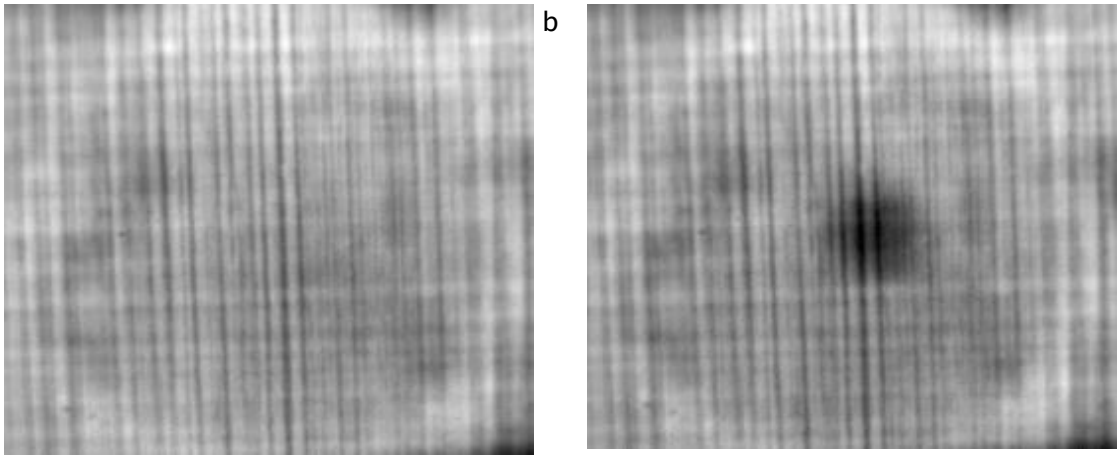

Figure 72 PPT phase data for the CFRP/Triplex bonded sample a) unloaded and b) full vacuum applied to the rear of the sample.

a

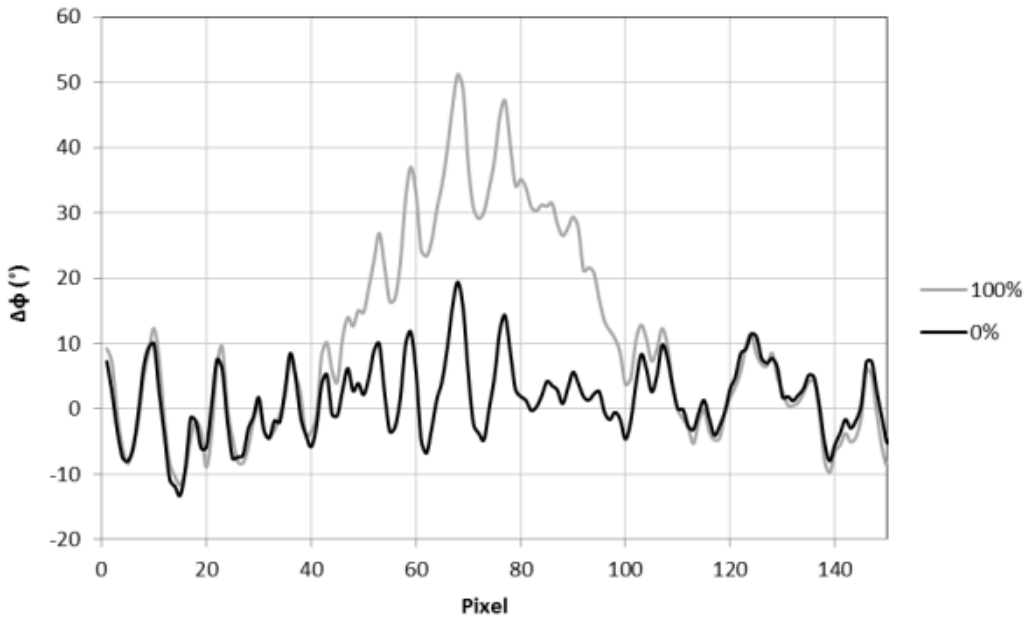

b

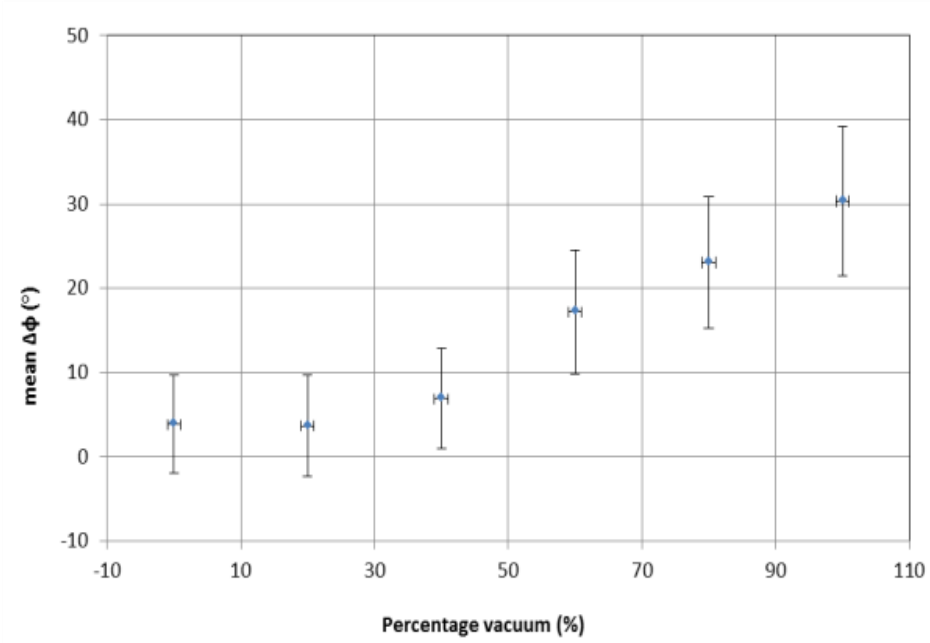

Figure 73 a) phase contrast profiles taken across the defect region under vacuum loading conditions of 100% vacuum and 0% vacuum and b) the mean phase contrast between defect and non-defect regions taken across the width of the defect related to partial vacuum percentage applied.

9.2.4 Summary

Triplex joints were studied using PPT. Kissing defects, which were of specific interest, were simulated using silicon grease. A vacuum load was introduced to apply a load to open defects. To provide sufficient stiffness to simulate a

real Triplex bond the FT was adhered to a CFRP panel. The vacuum was applied to the FT side of the bond and PPT was carried out on the CFRP surface. Sufficient load was applied to the sample to begin to open the 20 mm defect at just 60% of full vacuum. Even under the application of full vacuum loading the profile data demonstrated that the defect was not growing and after removal of the load the defect closed, thus no plastic deformation was caused. To allow the Triplex joints on the vessels to be inspected it would be necessary to combine the PPT setup with the vacuum chamber to regain the single sided access required.

9.3 CFRP repair patches

The National Physical Laboratory (NPL), Teddington, UK, coordinated a project involving a wide range of technologies for the structural health monitoring of a decommissioned concrete footbridge. The footbridge was moved to the NPL site and the stair access to the bridge was removed, forming a cantilever beam. The footbridge was subject to a range of fatigue and static loading cycles in an attempt to propagate damage within the structure. Approximately half way through the three year project, CFRP reinforcement panels were applied to the top surface of the bridge. Patches were applied directly over the root of the beam by a civil engineering company, in the same manner as they have been to structures in service. A second round of companies and universities were then invited to inspect the repair patches using their respective specialist NDE technique. Overall more than 30 partners were invited to participate in the study and the University of Southampton was invited to undertake thermographic inspection. The current work focuses on the application of PPT to an onsite, civil engineering challenge.

9.3.1 Test specimens and arrangements

The thermal stimulation in these tests was provided using the 1500W Quartz heat lamp with the pulse duration controlled manually with a shutter. A 5 second pulse was applied, as this provided the thermal stimulation needed, without overheating. The onsite PPT setup is shown in Figure 74a.

This joint was constructed by industrial users on site using their own materials. The CFRP panel is a 1mm thick UD panel and a specialist epoxy adhesive was used. Details of surface preparation to either the CFRP or the concrete beyond removal of debris are unknown. The epoxy was applied to both adherends and then slid together to minimise trapped air. The adhesive in this case is approximately 1.5 mm thick, adhering to industry standards for the application of CFRP patches for concrete repairs. Two control samples were also made in the same was using the concrete from two of the footbridge steps, shown in Figure 74b. PTFE patches were positioned between the two adhesive layers at a depth of approximately 1.75 mm. Sample A was known to contain four circular PTFE patches and sample B contained only one patch. Diameters of defects were known to vary between 10 mm and 40 mm but their exact location was unknown. A schematic of the construction of the sample pieces and the reinforcement as applied to the bridge are included in Figure 75a and b.

a  b 

Figure 74 a) CFRP reinforcement installed on bridge with the onsite set up of PPT also shown on the decommissioned bridge and b) samples A and B.

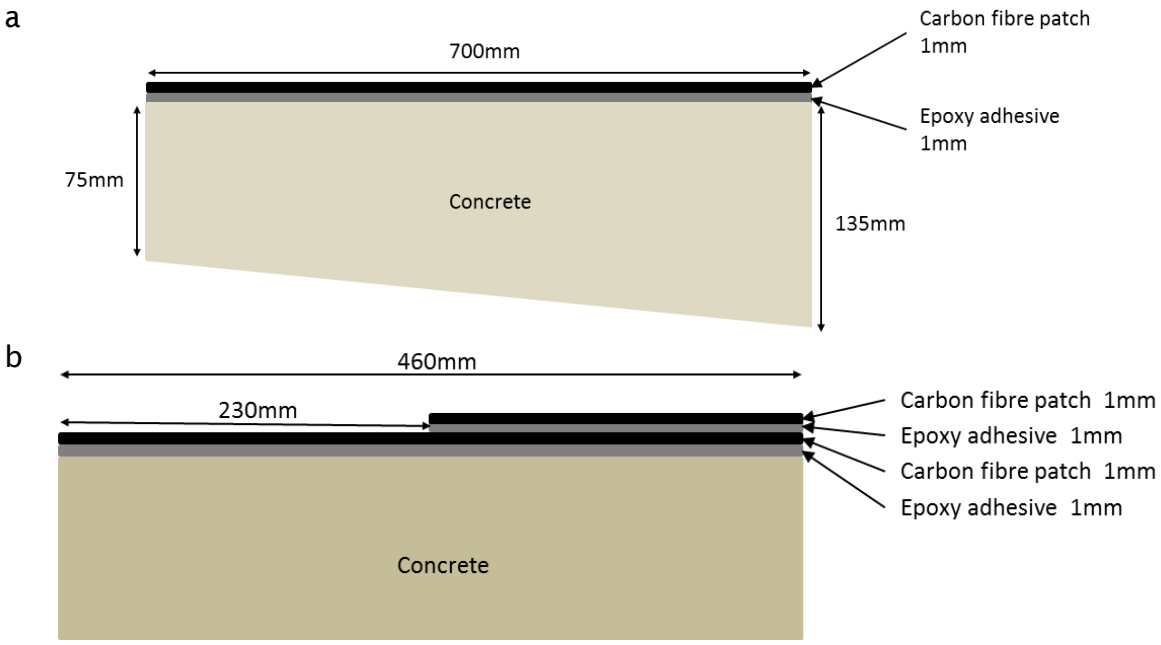

Figure 75 a) Sample schematic and b) bridge composite repair schematic.

9.3.2 Results

Control samples

The PT and PPT data taken for control sample A is presented in Figure 76. The PTFE defect of interest is the crescent shape found to the right of both the thermal PT and PPT phase images, see Figure 76a and b. The PPT phase image has removed the surface effects and reflections that are present in the PT image, which allows clearer identification of defects.

ΔT and $\Delta\phi$ profile plots are presented in Figure 77. The thermal contrast between defect and non-defect is 0.4 K and the phase contrast across the defect is approximately 40°. The shape of the profiles across the defect is quite different to previous cases where profiles are found to be much squarer. This square profile is common for shallow defects where the defect is visible soon after the pulse has been generated. In the current case the defect was much deeper than many previous examples at 1.75 mm deep so the maximum contrast PT image occurs after more time has passed. This additional time allows for an increased amount of lateral diffusion of the heat while the maximum thermal contrast is found over the centre of the defect hence creating a more sloped profile.

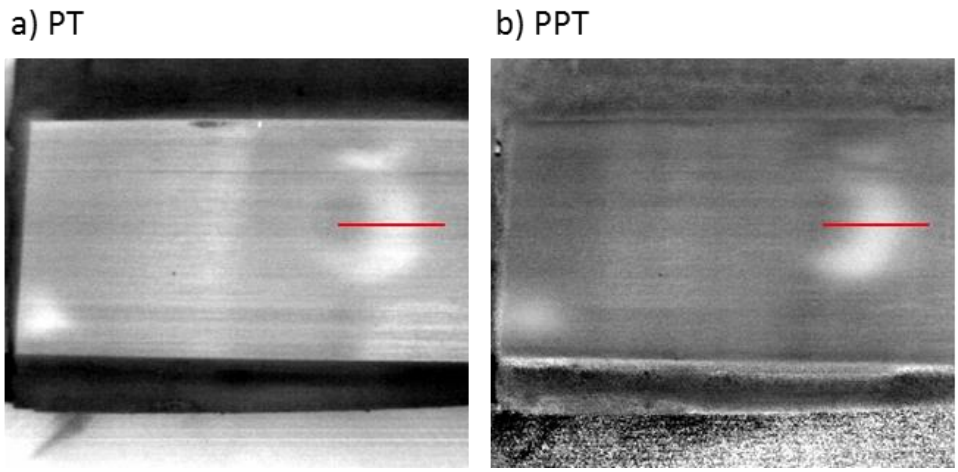

Figure 76 PT and PPT data for the largest defect in sample A to compare PT and PPT techniques a) PT thermal image at 12.5 s, b) PPT phase image at 0.84 Hz.

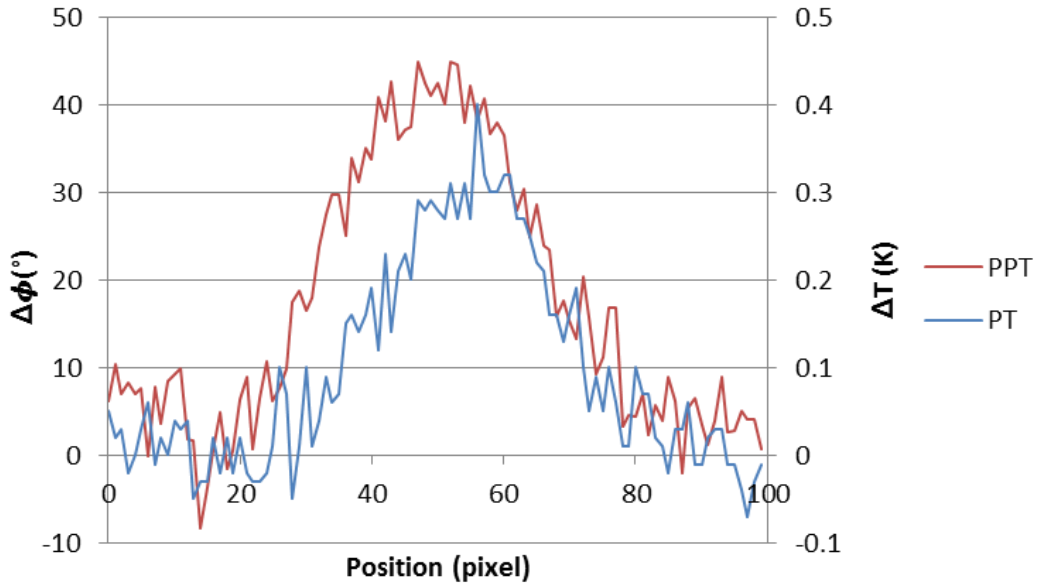

Figure 77 Profile plots taken across the width of the defect visible in the PT and PPT data shown in Figure 76a and b.

Sample A was designed to contain 4 PTFE inserts of different sizes distributed along the length of the bond. PPT data for the whole bond is presented in Figure 78. PPT was only able to identify 2 of the 4 PTFE inserts, indicated with the red arrows. The PPT is also able to identify several real defects, assumed to be voids, in the adhesive layer, indicated by yellow arrows. A UT C-scan was taken using a 35 MHz probe, Figure 79. The UT image clearly shows all 4 of the PTFE defects as well as showing variations in the adhesive. Whilst in this case the defect remains clear amongst the adhesive variations, when smaller

defects were studied they were found to be harder to distinguish from this adhesive information. This was not the case for PPT phase data. It is unclear why the PPT was unable to identify the central 2 PTFE inserts however it was not possible to revisit this case.

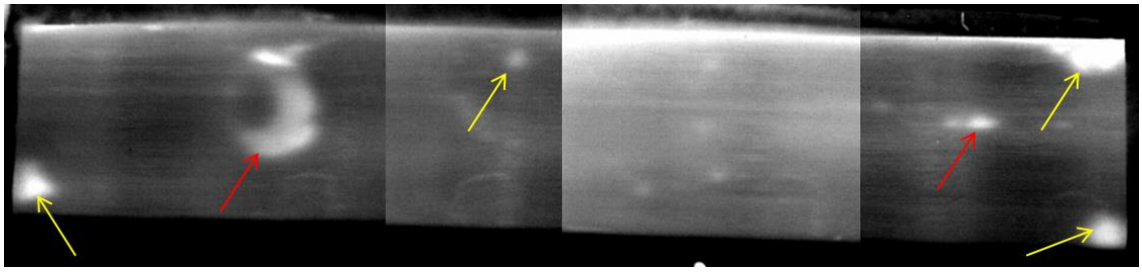

Figure 78 Sample A PPT data with red arrows indicating detected PTFE inserts and yellow arrows indicating manufacturing defects.

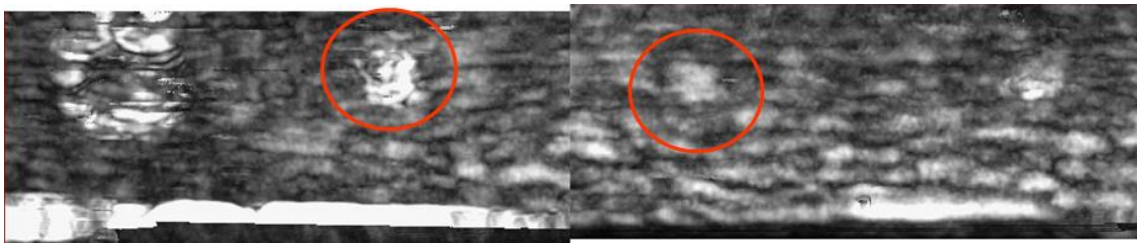

Figure 79 Sample A UT data taken using a 30 MHz transducer using the double through thickness method with a step size of 0.5 mm.

Sample B contained only one PTFE insert that was successfully identified in the PPT data, see Figure 80. Several real defects were also identified in sample B highlighted with yellow arrows.

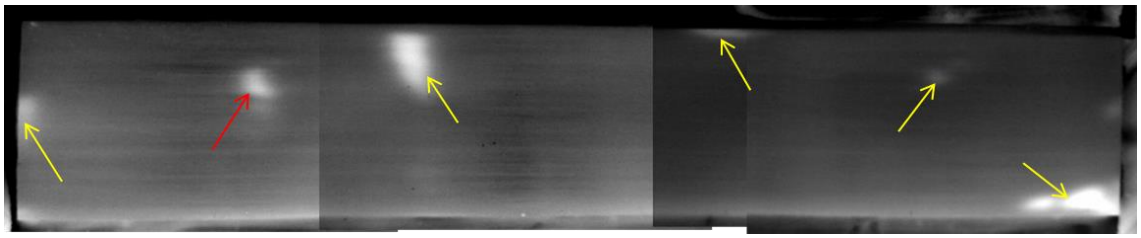

Figure 80 Sample B PPT data with red arrows indicating detected PTFE inserts and yellow arrows indicating manufacturing defects.

FEA

The same FEA model introduced in Section 6.2 has been applied to the current CFRP-Concrete bond to ensure that appropriate experimental parameters such as recording rate were selected when carrying out bridge inspection. In the

current case study there is a discrepancy between the modelled and experimental data, as the decay of the model surface temperature is faster than that in the experiment, see Figure 81a-d. The range in temperatures between the three points is also reduced to only approximately 0.07 K for the modelled data at 20 s compared to 0.3 K for the PT thermal data. This is likely to be caused by inaccuracies in the material properties in the model. For less common materials, such as the adhesive used in this case, as the sample was not manufactured by the author, exact material properties were not available. Therefore estimated values taken from literature were used, which may be reflected in the accuracy of the model. The CFRP-concrete model data decay in the same manner as the experimental data with the DC staying at an elevated temperature for longest and the ND cooling fastest, although the temperature range between them is reduced. The model has a weaker correlation with the experimental data of $\pm$ 0.5 K.

The thermal contrast data presented in Figure 82 highlights the discrepancies between the model and experimental data thought to be caused by the inaccuracies in the thermal properties used in the model. The magnitude of ΔT_{peak} is slightly over predicted by the model at 0.29 K compared to 0.24 K, however the shape of the plot is quite different. It appears that the heat transfer within the model material is much faster than in the real materials leading to this much sharper peak. The modelled case studies in Section 6.2.3 demonstrate that when the exact material is known a good estimate of material properties may be obtained from the literature, however when materials are unknown, as in the current case which was manufactured by a third party, estimated properties of the materials used can cause discrepancies between modelled and experimental results. This indicates there is a requirement to carry out a sensitivity study to establish the effect of the accuracy of material properties used in the model. This could be especially important when considering components containing multiple materials.

a

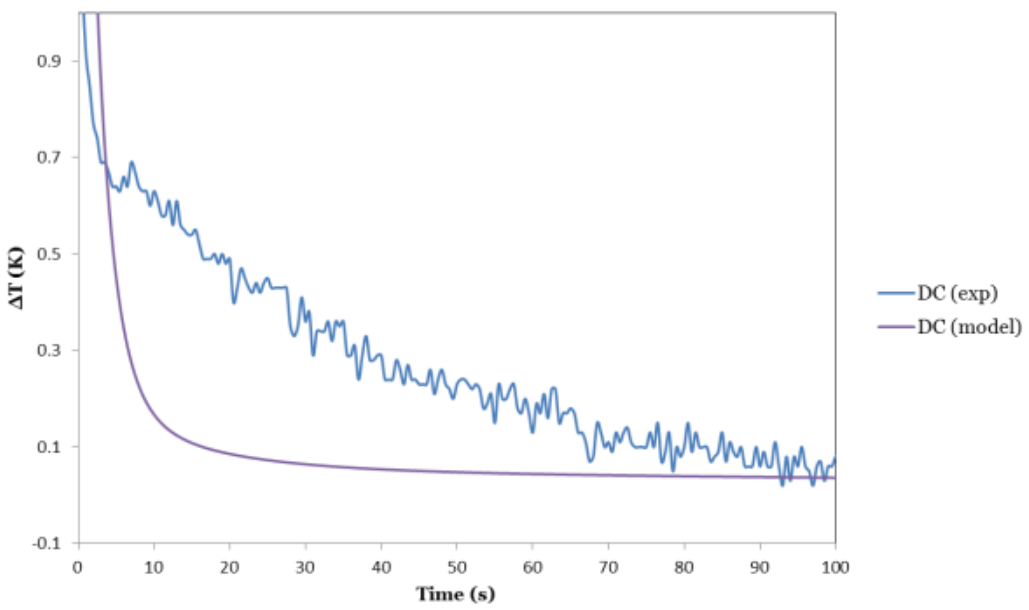
ΔT (K)
0.9
0.7
0.5
0.3
0.1
-0.1
0
10
20
30
40
50
60
70
80
90
100
Time (s)
DC (exp)
DC (model)

b

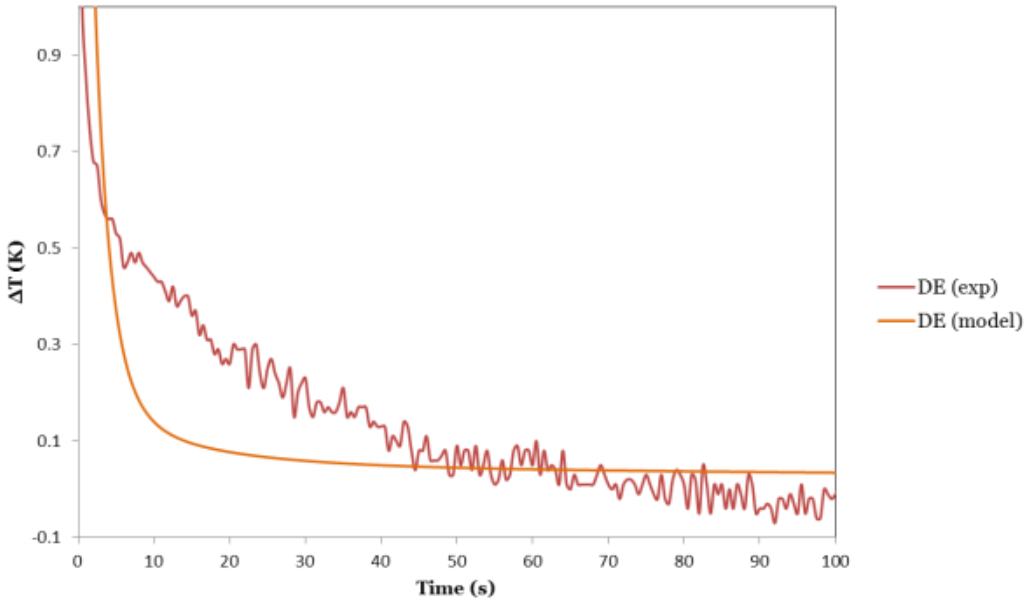
ΔT (K)
0.9
0.7
0.5
0.3
0.1
-0.1
0
10
20
30
40
50
60
70
80
90
100
Time (s)
DE (exp)
DE (model)

c

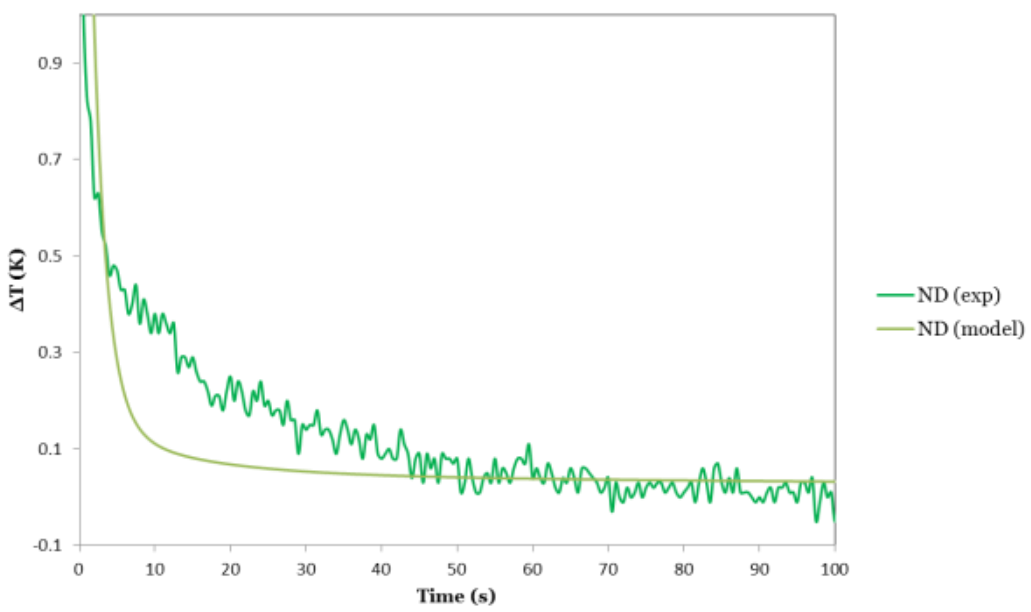

d

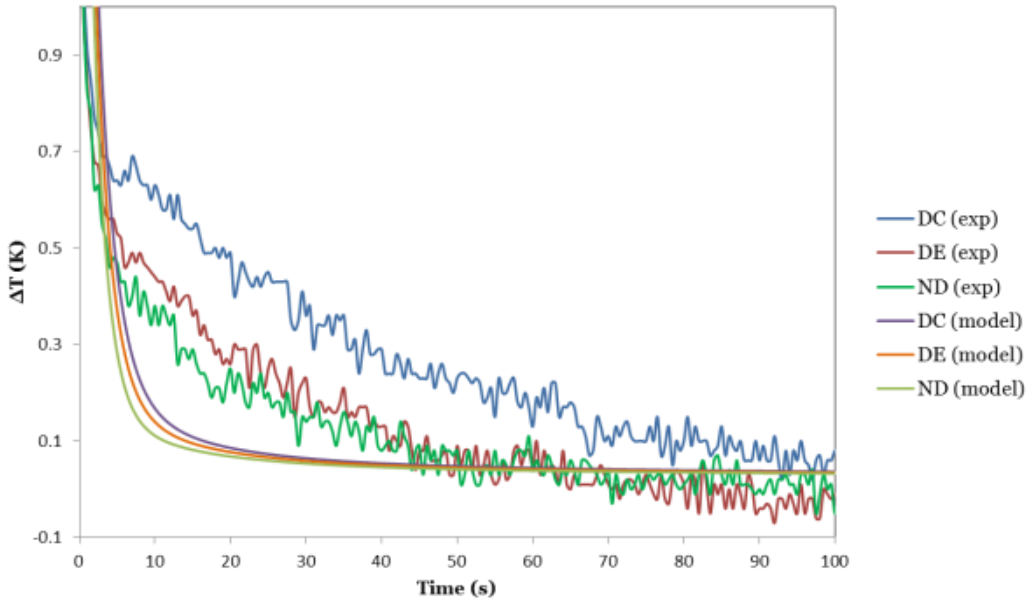

Figure 81 Surface temperature data comparison of PT data for CFRP-Concrete showing modelled and experimental data for a) DC, b) DE, c) ND and d) all three data points.

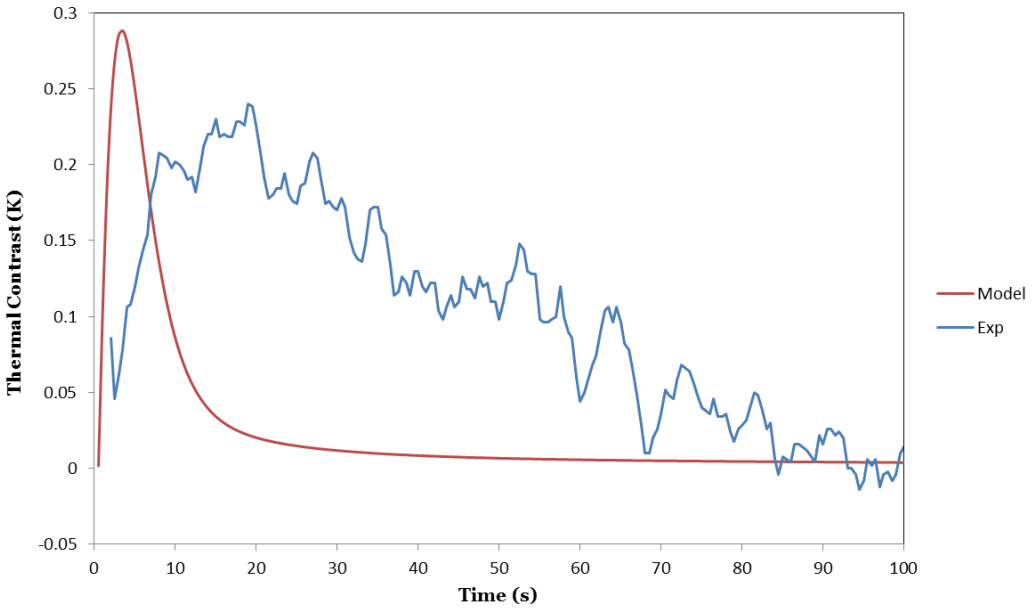

Figure 82 Modelled and experimental surface thermal contrast data between defect and non-defect regions.

The FFT frequency at which the maximum $\Delta\phi$ occurs is accurately predicted for the current concrete case study, shown in Figure 83.

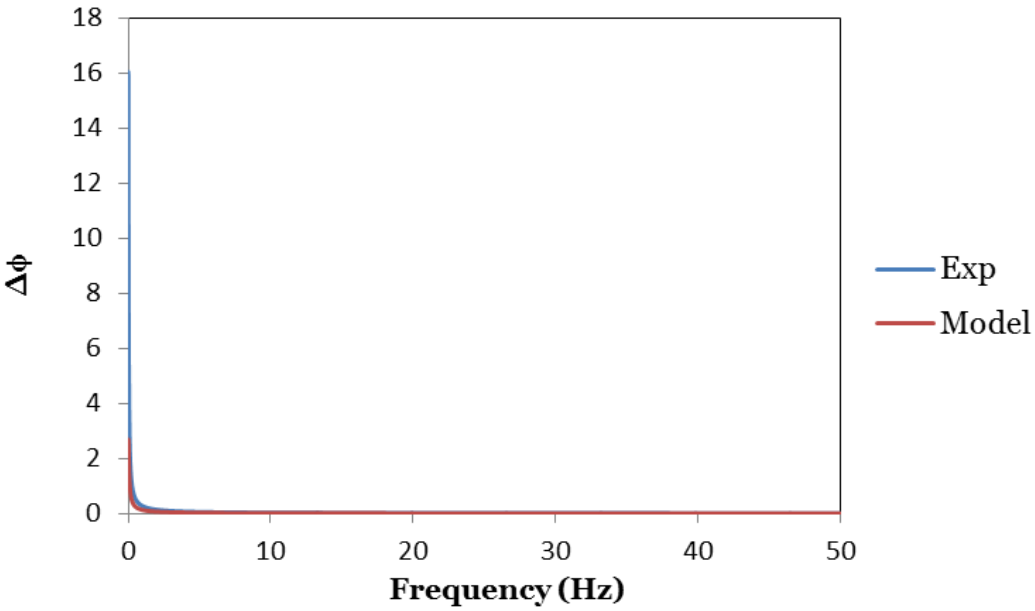

Figure 83 Phase contrast between DC and ND for experimental and modelled data CFRP-Concrete joint with PTFE insert.

The FFT sampled frequency at which the maximum $\Delta\phi$ occurs and the magnitude of this peak are recorded and the ratio between the modelled and experimental results was found, see Table 17.

Table 17 Ratio of modelled and experimental frequency at which the peak phase contrast occurs and ratio of magnitude of maximum phase contrast peak.

	Frequency Ratio	Phase Contrast Ratio
CFRP-Concrete	1.00	0.17

Bridge reinforcement

Once initial tests had been carried out on the control samples the equipment was setup on the bridge to inspect the CFRP patches directly over the root of the cantilever beam. Minimal loading had taken place at the time of first PPT inspection. Figure 84 and Figure 85 show the PPT data collected for the two bridge reinforcement patches. The main defects identified are highlighted with yellow arrows which were all attributed to manufacturing defects.

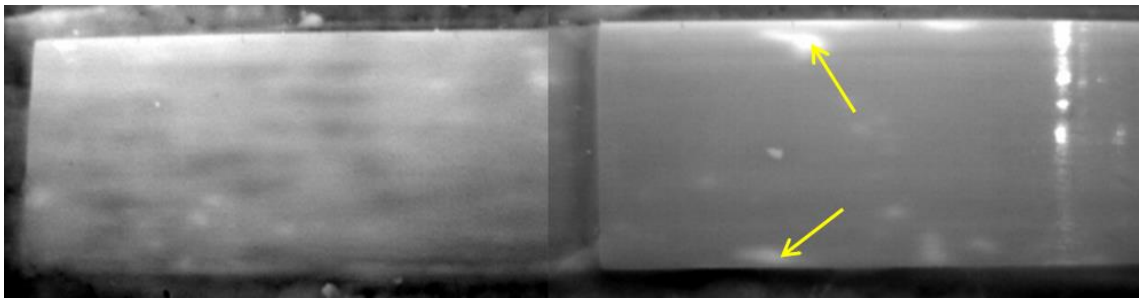

Figure 84 PPT data of bridge reinforcement side 1 with yellow arrows indicating detected manufacturing defects.

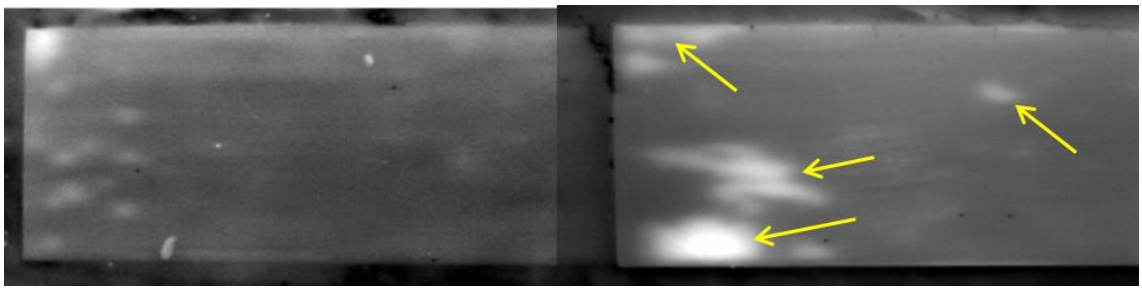

Figure 85 PPT data of bridge reinforcement side 2 with yellow arrows indicating detected manufacturing defects.

Subsequent visits were carried out after significant loading events had been carried out including fatigue cycles and creep studies. The PPT data taken on each visit are presented for the two reinforcement patches in Figure 86a-d and Figure 87a-d. No propagation of the original manufacturing defects was

identified using PPT. However, it should be stated that no propagation of damage was identified by any of the other NDE approaches invited to participate presented at the concluding conference of the project [136]. What was successful in this study was the verification of the robustness of the PT/PPT technique to obtain very similar results for four separate visits in various environmental conditions. The installation of strain gauges by other partners in the observation areas over the duration of the project proved a challenge as the heat path to inspect under the surface was altered, however it was still possible to identify the manufacturing defects.

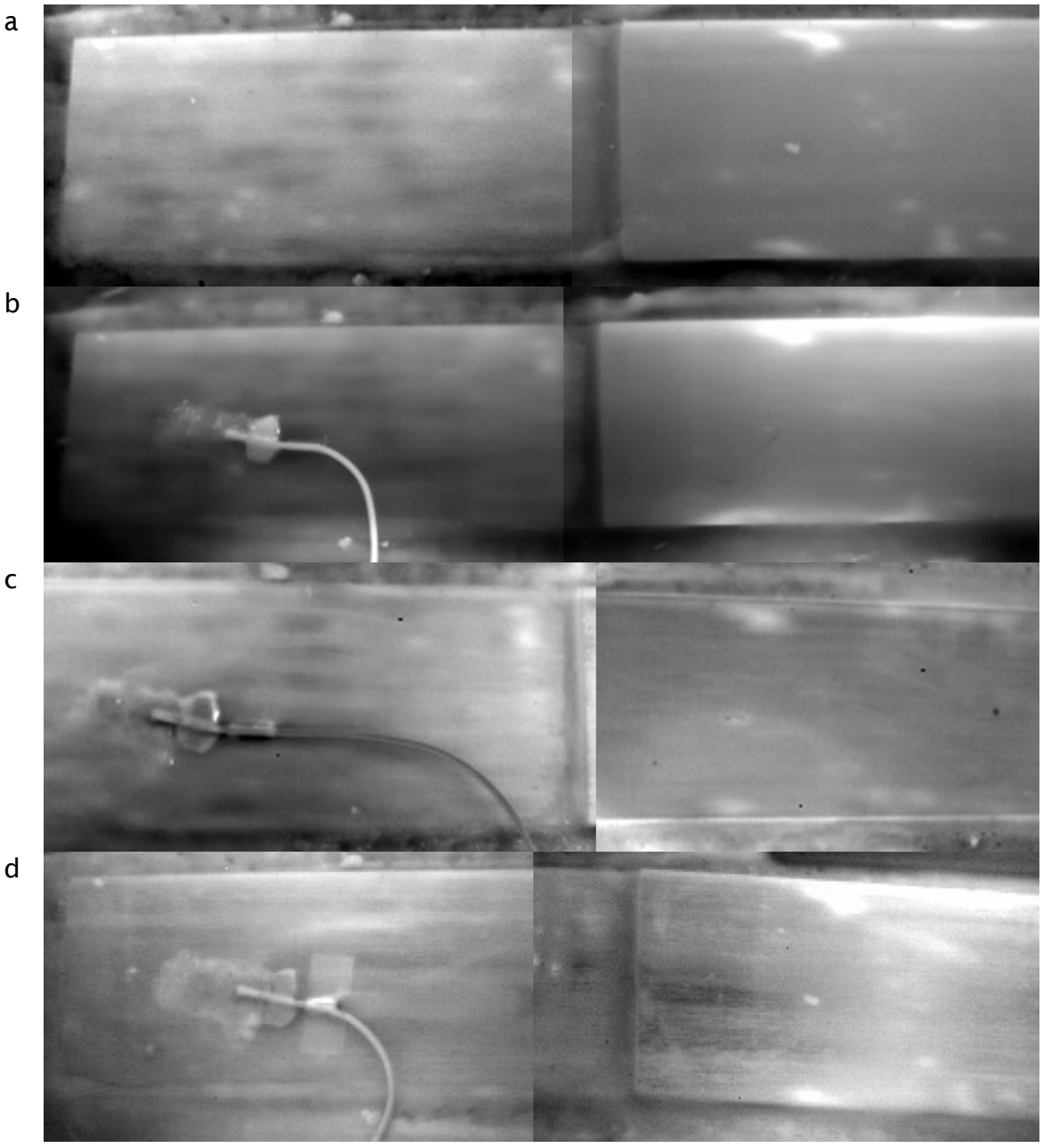

Figure 86 Bridge reinforcement side 1 – repeated visits a-d.

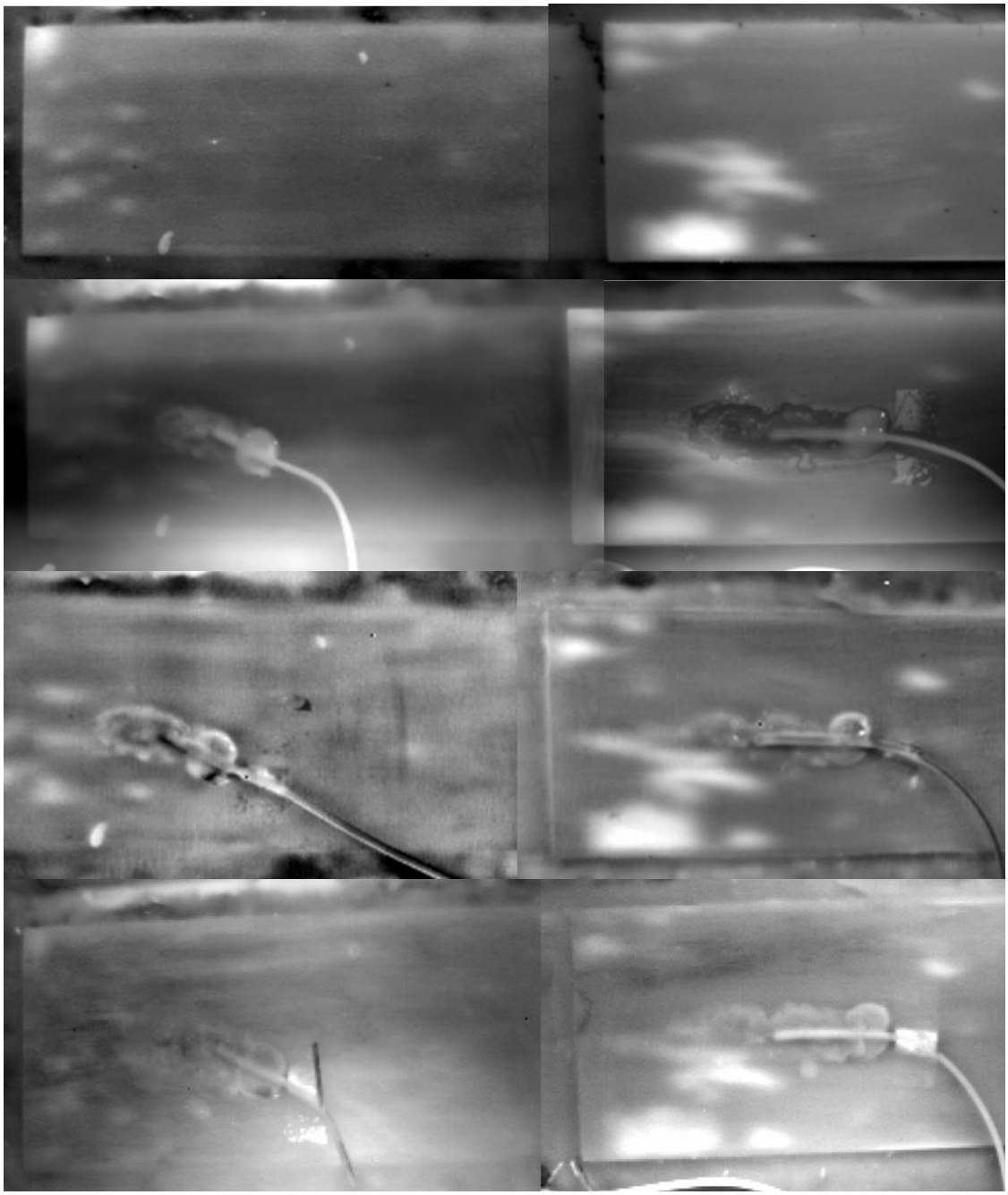

Figure 87 Bridge reinforcement side 2 – repeated visits a-d.

9.3.3 Summary

The UT data consistently revealed the defects in each case, however, the scan taken was far more time consuming than the thermography methods, taking approximately an hour to scan at this resolution. The fact that UT scanning is a point by point process is the main drawback of UT techniques. The current UT scan was taken in an immersion tank using water as the coupling medium; while a gel may be used the requirement to couple the transducer to the

component is a disadvantage of UT. The PT data presented does reveal the defect of interest but there was some reflection on the surface which may detract from defect identification. The reflections are greatly reduced in the PPT phase images, enabling more reliable defect identification.

The main difference between the application of the model to the current study and previous studies was the ability to obtain reliable material properties for the specific materials in components. Whereas in previous applications of the FEA model a common epoxy adhesive was used however the adhesive used to join the concrete and CFRP was much less common and so the thermal material properties were less well documented. It is believed the less reliable properties used in this case led to the errors found in the spread of the decay curves although their relative positions are correct. The model of the CFRP/concrete bond is not able to predict the thermal contrast evolution observed.

9.4 Porosity investigation

Three adhesively bonded samples were provided by an advanced materials manufacturing company which had been manufactured to contain various levels of porosity. The aim of the current investigation was to carry out a feasibility study demonstrating whether different levels of porosity in adhesive bonds may be detected using PT.

9.4.1 Test specimens

Samples were made of two 1.2 mm thick sheets of galvanised steel bonded together with an adhesive layer of 400 μm, photographed in Figure 88. Sample 1 was a control sample where the adhesive layer was pure adhesive. Sample F was a worst case scenario in terms of porosity that included dry chopped strand mat in the bond. The final case was an intermediate porosity which was introduced via the addition of chopped strand mat that was pre impregnated with adhesive. Some surface damage caused by sample preparation was present on samples 1 and D and adhesive was present on the surface of sample F.

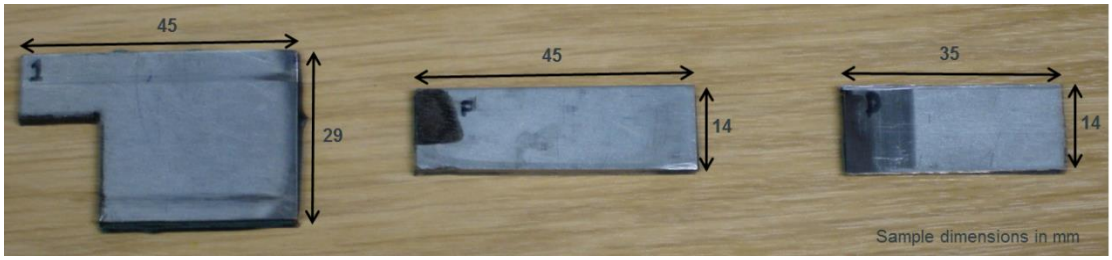

Figure 88 Samples provided containing various levels of porosity. Samples are labelled 1, F and D, left to right.

9.4.2 Testing arrangements

The heat source used in this work was the Nikon Speedlight SB600 external photographic flash unit. Investigations were carried out in transmission and reflection mode as well as painted and unpainted, to give the full range of possible operating conditions. Results are given in terms of ΔT which represents the change in temperature from the original ambient temperature prior to heating.

9.4.3 Results

Transmission mode

The initial test is carried out in transmission mode with the sample painted black to give a high and uniform emissivity to optimum for thermography. The variation in levels of porosity affects the rate heat is able to conduct through the samples as the amount of air trapped in the bond line is varied. Figure 89 shows that as porosity is increased the surface ΔT in transmission mode is decreased. The diffusion of the heat through the thickness of the sample is increased with increased porosity, where sample F has the highest porosity and sample 1 is the control sample. Figure 89 contains repeated tests for the three samples and thus illustrates that these findings are consistent. Figure 90 shows thermal data for each sample at the same time during the thermal evolution. This data illustrates the relative temperatures of each sample when subjected to the same heating and experimental conditions visualising the apparent decrease in temperature with an increase in porosity as a reduced amount of heat is able to diffuse through the samples.

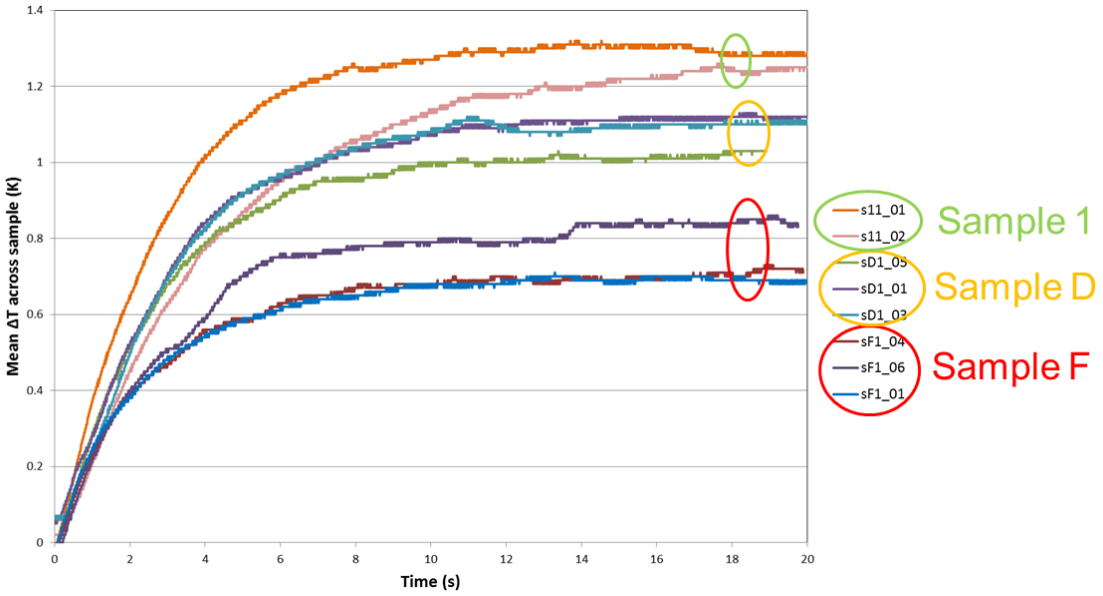

Figure 89 Surface temperature evolution when heated in transmission mode for the three samples.

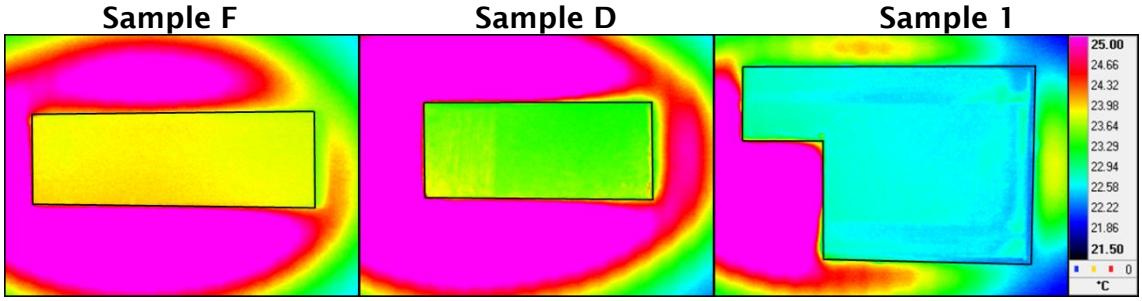

Figure 90 PT transmission thermal data taken at 10 s for the three samples.

Reflection mode

Reflection mode is often preferable to transmission mode in industrial applications due to its requirement for only single sided access, so the experiments were repeated in reflection mode. Figure 91 shows the surface decay data for the three samples, with repeated runs, with the reflection setup maintained throughout. A kink in the decay is noted at 0.02 s for all samples. This is caused by a change in the rate of decay as the heat front passes from the steel adherend into the adhesive. The effect of porosity on the adhesive bond is evident in the PT reflection mode thermal data. As the pulse is applied to the front surface of the samples it is evident that an increase in porosity causes an increase in the ΔT obtained as it hinders the propagation of the heat front through the bond. Figure 92 shows the PT thermal data for the three levels of porosity in reflection mode for the same time during the decay giving

a measure of the relative temperatures as the heat is able to diffuse through the samples at different rates found to be inversely proportional to the level of porosity.

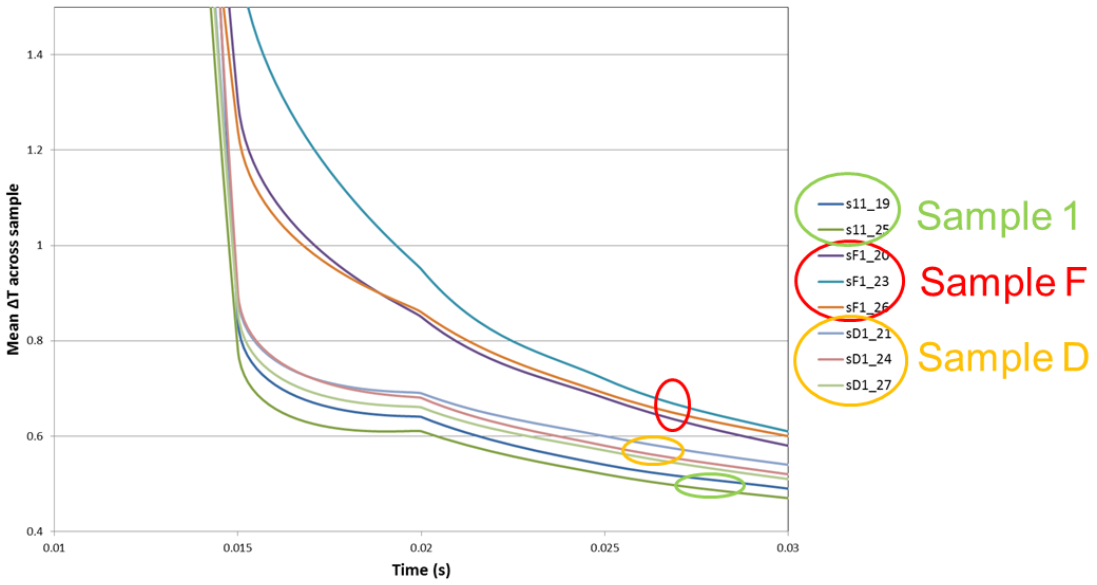

Figure 91 Surface temperature evolution when heated in reflection mode for the three samples.

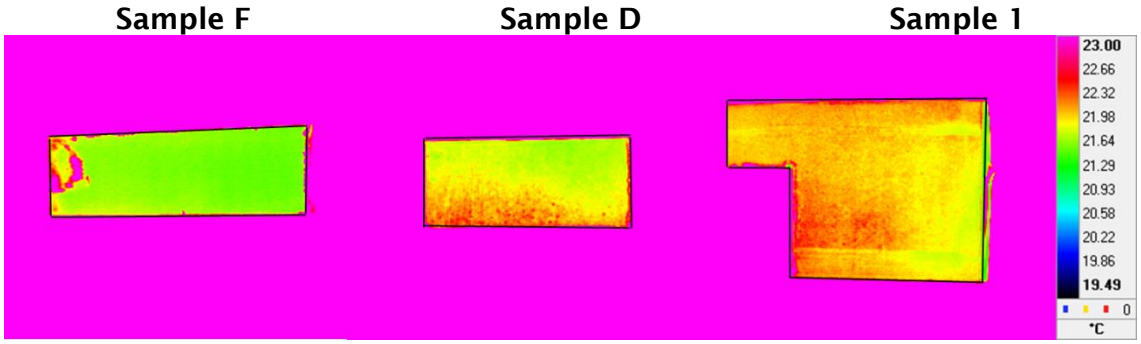

Figure 92 PT reflection thermal data taken at 0.175 s for the three samples.

Unpainted

Finally PT was carried out in transmission and reflection mode without any applied paint coating. If a variation in thermal signal was apparent without the application of matt black paint this would eliminate any preparation time for the porosity inspection of these bonds thus allowing a highly efficient inspection technique. The IR results from reflection mode were heavily saturated due to the strong reflections from the surface of the metallic sample when the pulse was applied and no relationship between porosity and the IR

data was found. Figure 93 shows that in transmission it was still possible to detect the ΔT dependence on porosity. However, the magnitude of ΔT is decreased by a factor of 10 due to the increased reflection of the heat input as well as the decreased emissivity of the front surface for IR detection. This reduced range of ΔT values will impact upon the sensitivity of the experiment to different levels of porosity.

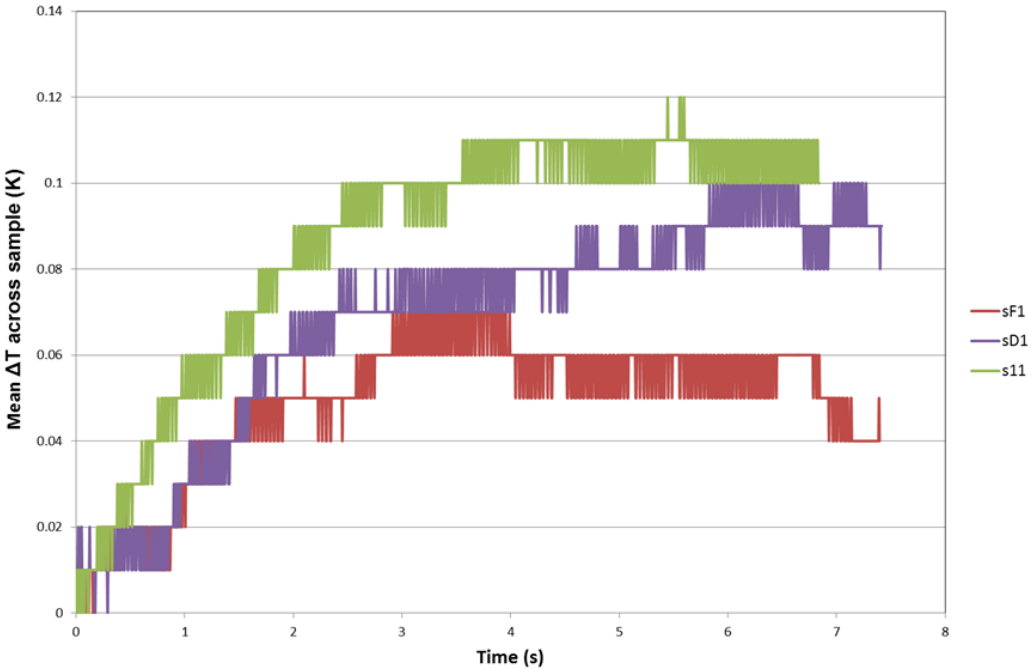

Figure 93 PT transmission data for the three samples unpainted.

9.4.4 Summary

During the porosity feasibility study it was found that direct analysis of the IR PT data revealed a thermal dependence on the porosity of the galvanised steel bonded joints. It was found that when the samples were given a uniform and high emissivity coating porosity detection was possible using PT in both transmission and refection modes. However, when samples were unpainted the low emissivity and large amounts of reflection resulted in only transmission mode giving useful results. The largest variations in ΔT between the high and low level porosities were produced when transmission mode was used on the painted samples. Overall the study showed detection of variations in levels of porosity was feasible using PT and that it would be possible to make the technique very efficient if considering applying it in a high volume role, such as on a production line.

9.5 Thick GFRP panels investigation

It has been identified by a third party that current methods of NDE inspection of certain thick composite structures are not suitable. A round robin exercise of various NDE approaches was arranged to be undertaken on panels with experimentally simulated defects. A total of 10 panels were supplied of two types, 8 sandwich panels and 2 bonded skin panels. Sandwich panels comprised of 5 mm thick GFRP composite skin and 50 mm core while bonded panels were two GFRP plates of 10 mm and 15 mm thickness adhered together using a 2 mm adhesive layer. More specific details of the materials are confidential and unknown to the author.

Due to the size of the panels and the heating sources available, it was necessary to inspect each panel in several sections. The work was carried out using two Bowens Gemini Pro1000 professional photographic flashes as the heat sources and a FLIR SC5000 infrared detector.

Panels were tested by laying them on a trolley to allow manoeuvrability during tests, as the mass of the panels ranged from ~40 kg to 90 kg. The layout of the experimental setup used in the current work is schematically presented in Figure 94. An initial inspection area of 200 x 160 mm was used for the preliminary tests on a sandwich panel, panel 5, making a total of 15 tests per panel, however, due to the desire to reduce the inspection time; this was increased to 245 x 200 mm for the remainder of the sandwich panels, enabling the inspection of the these panels to be completed within 10 tests. An observation area of 245 x 230 mm (with greater overlap) was deployed for the bonded panels. In addition, the distance between the detector and the panel surface was also increased to 830 mm for bonded panel tests. The flash to panel surface distance was maintained at 300 mm for all tests. This provided a change in surface temperature of 20 K, which was sufficiently low to ensure the panels were not damaged by excessive heating.

The panel inspection was carried out blind with no knowledge of specific material properties and no knowledge of the location, geometry and type of defects. Since the heat transfer properties of the materials were not known, the recording duration of 5 minutes and frame fate of 2 Hz were

selected after assessing the results obtained from a GFRP block modelled by the FEM developed in Section 6.2.

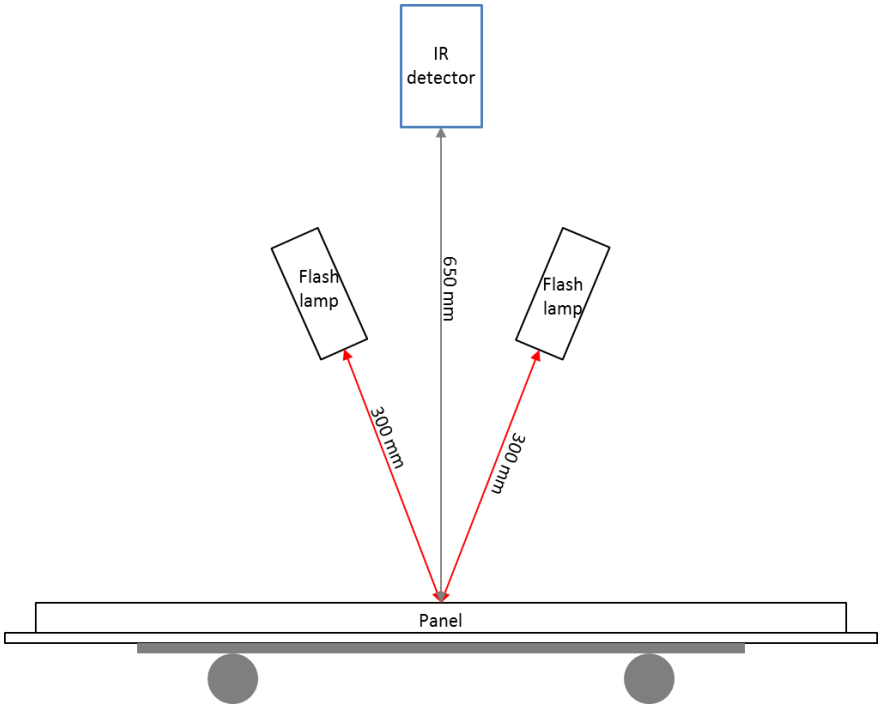

Figure 94 PPT setup with two higher powered flash lamps for the large panels.

9.5.1 Results

Examples of PPT data collected for the panels are presented in Figure 95 and Figure 96 for panels 5 and 6, a sandwich and a bonded panel.

Key features of the PPT data are labelled on the images, however, the current experimental setup deployed and data processing parameters used were unable to reveal any simulated defects in the panels. It has been presumed that no defects were revealed on any of the panels because the parameters for experimental conditions and data collection and processing could not be tailored accurately to the materials and thicknesses of the panels. The thermal diffusivity of GFRP is low and the thermal contrast created by a defect is dependent upon the contrast of the material properties of the defect to the surrounding material. The thickness of the panels also posed a challenge for PPT and it may be the case that more heat is required to enable defect detection. The experiments carried out are unlikely to be the best results possible using PPT, however there will be

limitations on the detectability of defects in such panels. The following work therefore focuses on modelling the experimental procedure to validate the feasibility of this technique on such materials.

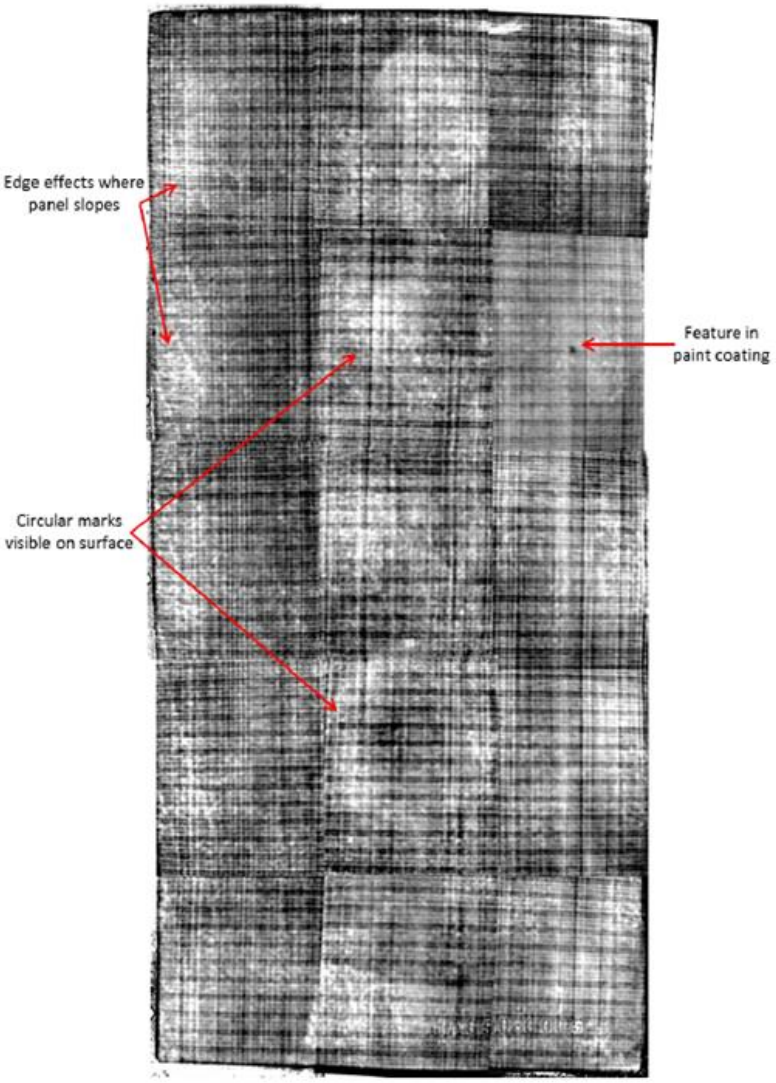

Figure 95 PPT phase images of panel 5 – sandwich construction.

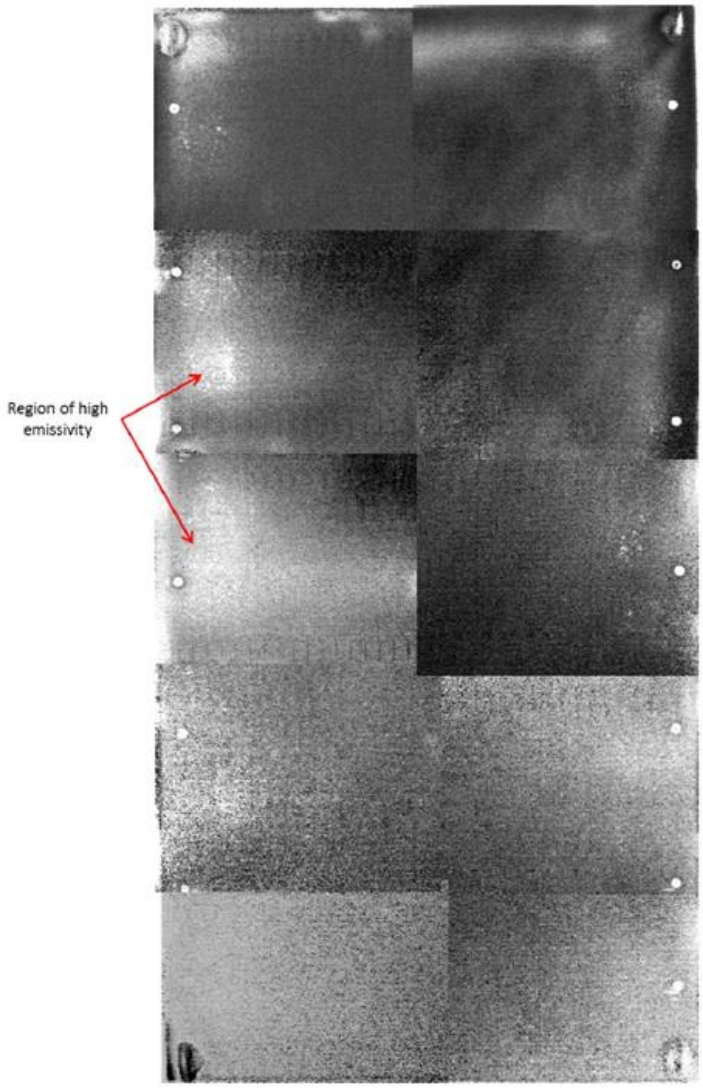

Figure 96 PPT phase images of Panel 6 – bonded skin construction.

9.5.2 Finite Element Analysis (FEA)

A series of 2D transient thermal models were constructed to establish an increased understanding of the requirements of the experimental conditions including pulse strength and recording duration in order to ascertain whether it was possible to identify typical defects at the depths of interest. The thermal conductivity, specific heat and density of each material estimated from literature values are presented in Table 18. Core material properties have been omitted from this table as the information is confidential. The convection of heat from all free surfaces of the sample was considered and used the appropriate heat transfer coefficients found in the literature [116, 132]. The duration of heating was set to 0.5 ms, equal to the experimental value used for

the current flash lamps. Two materials have been considered as defect materials in all models, namely air and PTFE.

Table 18 Material data taken from literature [116].

Material	Thermal conductivity ($Wm^{-2}K^{-1}$)	Specific heat ($Jkg^{-1}K^{-1}$)	Density (kgm^{-3})
GFRP	0.3 / 0.38	1200	1900
PTFE	0.42	1000	2200
Air	0.0257	1.005	1.205
Adhesive	0.14	500	460

Data extracted from the models is presented as change in temperature (ΔT) data, which is the maximum thermal contrast between the surface directly over the centre of the defect and a defect free area. The detector sensitivity is 20 mK, therefore if the surface contrast created was found to be less than this threshold then it was classed as unidentifiable.

GFRP block FEA model

Initially a GFRP block model was produced with a 10 mm diameter defect at 5 mm and 15 mm depths with a total block thickness of 20 mm, shown in Figure 97a. The idea behind this initial model was to estimate how long after the application of heat it would take for a thermal response to be visible in the surface thermal data from defects at these depths to provide the duration of data collection for the experiments. The model was also to investigate the temperature that the front surface must reach during the heating stage in order to reveal the defect. The defect depths were selected according to the skin face sheet thickness of the sandwich panels provided and the thickness of the upper adherend of the bonded panels. The defect material was selected initially as air and then as PTFE. The results obtained from the block model are presented in Figure 97b where each data point represents a different model run.

From these results it is clear that detection of a PTFE insert within a GFRP composite is relatively difficult when compared with the detection of an air gap of the same geometry. Figure 97b shows that a 0.2 mm thick, 10 mm

wide air defect present at 5 mm deep in the GFRP should be visible, above the detector sensitivity, if a pulse of heat above 320 K is used. As the air defect is located deeper (15 mm) in the GFRP, more heat is required (approximately 450 K), for sufficient heat to propagate to that depth and reveal such a defect. The PTFE material properties are relatively close to those of the GFRP and so the thermal contrast and hence variation in thermal flow through the material produced between the defect and bulk regions is far less than for the air defect. As such it is necessary to introduce a far stronger pulse of approximately 460 K to reveal the 5 mm deep PTFE defect. A 15 mm deep defect remains undetectable using the current heating parameters.

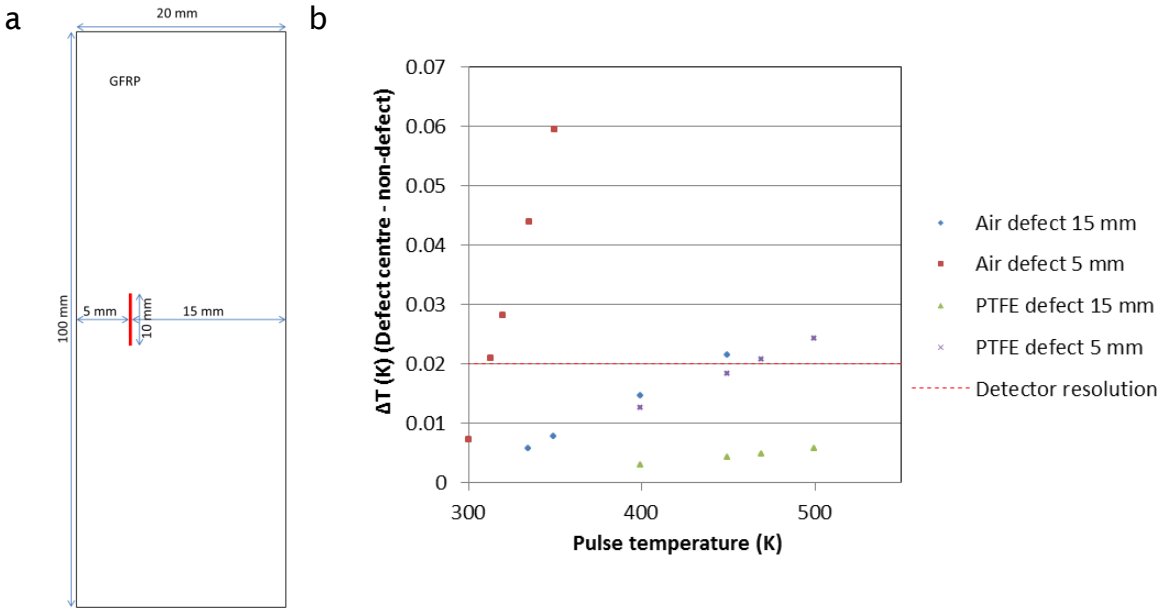

Figure 97 GFRP block model a) schematic of geometry and b) FEA results for air and PTFE insert at 5 and 15 mm.

Sandwich panel FEA model

Using the geometries provided in the general panel information supplied; an FE model was created of the sandwich panel type through a 200 mm wide area, as shown in Figure 98a. A 0.2 mm thick defect was added between the GFRP face sheet and the core material. The defect material was varied between air and PTFE and two defect diameters, 20 mm and 100 mm, were investigated to give an indication of the effect of defect size on the thermal contract produced. Simulations were run varying the pulse surface temperature between 320 K

and 500 K to demonstrate the effect of pulse temperature on the identification of such defects. Results of these models are shown in Figure 98b.

Figure 98b shows the relative thermal contrasts produced between air and PTFE defects. The difference in the slopes of the curves plotted for both defect types is due to the difference in the thermal properties of air and PTFE with the surrounding material and strongly governs the detectability of the defect. Defects of larger diameters create a larger thermal contrast, and it is likely that defect thickness also has an effect on the thermal contrast produced. The thickness of defects has not been investigated in the scope of the current study.

Defects present in the back face sheet, behind the core material would not be identified using this approach due to the inability to transfer sufficient heat through the core material.

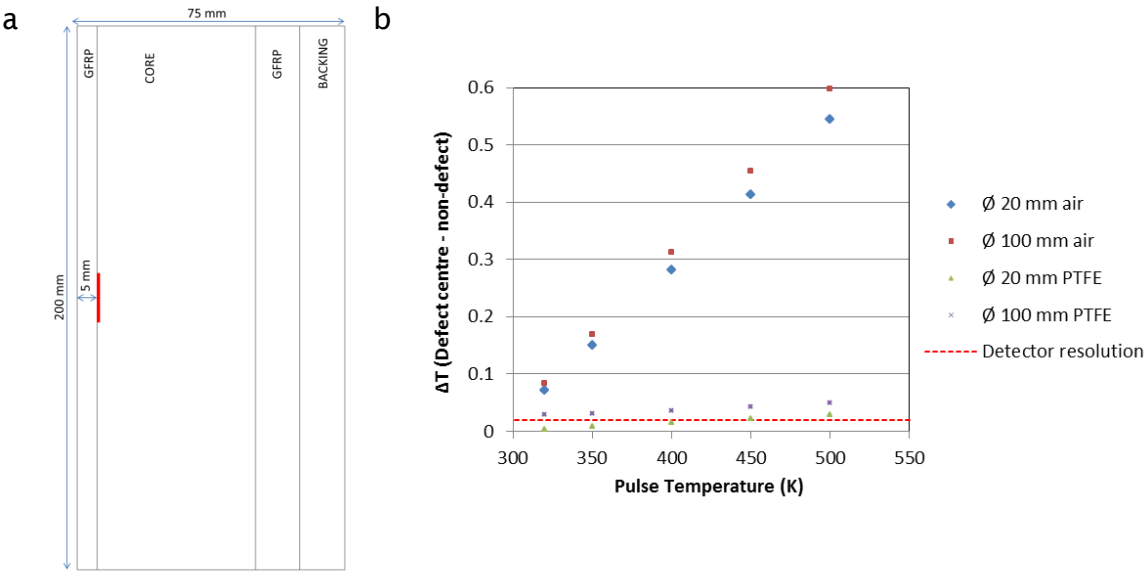

Figure 98 Sandwich panel model a) schematic of geometry and b) FEA results for 20 and 100 mm diameter air and PTFE inserts under the 5 mm thick front face sheet.

Bonded skin panel FEA model

For completeness, a final FE model of the bonded skin panel design has been created. Once again the estimated geometries given in the supplied information were used to create the geometry, see Figure 99a. The defect material was varied between air and PTFE and the heating pulse temperature was also varied. A defect with geometry of 20 mm diameter

and 0.2 mm thickness was considered between the front GFRP plate and the adhesive layer. Results are given in Figure 99b. Once again it is shown that an air gap defect has a stronger thermal contrast compared to the PTFE insert of the same geometry. A weak thermal contrast for both types of defect material is observed when the defect is positioned below a thickness of 15 mm in GFRP. More energy is required to create a thermal contrast in surface temperature over defect and non -defect regions as the depth of the defect is increased. For the heat pulse temperatures tested, the thermal contrast created by the PTFE gap defect remains below the detector threshold. The air gap defect becomes visible when the heat pulse temperature exceeds 400 K. While there is a positive correlation between the detectability of defects and the temperature of the heat pulse applied, the practicalities of heating the surface of a sample uniformly to higher temperatures should be considered as well as the potential to damage the surface by overheating.

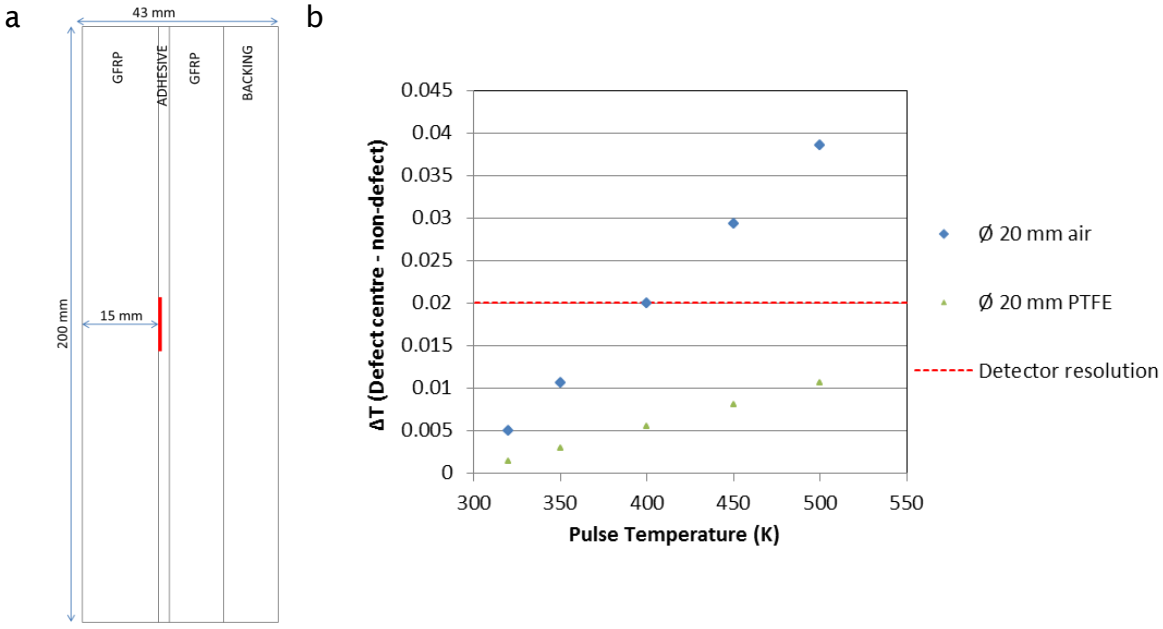

Figure 99 Bonded panel model a) schematic of the geometry and b) FEA results for 20 and diameter air and PTFE inserts under the 15 mm thick front adherend.

9.5.3 Summary

Initial PPT inspection was unable to identify the defects in the panels provided. FEA modelling has been carried out to investigate what defect materials may or

may not be visible via improved tailoring of experimental parameters. Increased heating would improve defect detection, although care should be taken to avoid damage of the composite materials and paint coatings by applying too much heat. Detection of defects is dependent upon the nature of the defect and the difference in the thermal properties between the experimentally simulated defect and the surrounding materials. Defect size may also affect the thermal contrast required to enable detection; however this is secondary to the difference in thermal properties between the experimentally simulated defect and the surrounding material. Data processing of the experimental results could be improved and refined if a known defect test sample were provided to enable frequency parameters to be refined.

Post-round robin analysis

After the results of this round robin exercise were collected, which are presented previously, the nature of some of the defects added to the panels was revealed. It was found that the circular marks indicated in Figure 95, were actually the defects of interest and were water blister defects inserted below the face sheet of sandwich panel 5. These were identified in the PPT data but were also visible when the surface of the panel was visibly inspected. Defects that had not caused a slight alteration in the surface emissivity via distortion of the surface remained undetected due to the thickness of the GFRP as demonstrated by the FEA.

10. Conclusions and future work

10.1 Conclusions

In Chapter 1 a series of objectives are laid out to achieve the aim of exploring the potential of using thermographic methods to develop a reliable method of identifying kissing defects in adhesive bonds. The objectives and how they have been achieved are detailed below. By fulfilling these objectives PPT has been shown to have strong potential as a technology that could be implemented as a practical and portable device for NDE of adhesive bonds in a variety of applications, including the MkIII LNG carrier. The list below provides the objective and the conclusion that was drawn in investigating the objective.

1. **Define the underlying physics of thermographic techniques with particular reference to pulsed and pulse phase thermography (PT/PPT).**

- The underlying physics of thermography is covered in Chapter 4 where the heat transfer mechanisms are established.
- Methods for sizing defects are determined from the literature.
- The influence of experimental and data processing parameters are established.

2. **Identify the potential and limitations of PT/PPT applied to a range of metallic and polymer materials.**

- In Chapter 5 PT and PPT were used to inspect samples of various materials and the practicalities of application of the techniques were defined.
- PPT was found to be advantageous over PT as it reduced the effect of uneven surface heating and enabled deeper probing into materials.
- For shallow, strongly contrasting defects PT may be well suited however it was noted that for more challenging defect detection the additional computational expense of PPT processing into phase data was worthwhile.
- The effect of material diffusivity has been demonstrated where highly diffusive materials, such as metals, results in a blurred image of a

defect. The amount of blurring, caused by the lateral diffusion of the heat across the sample, is dependent on the depth of the defect.

3. **Define the nature of a kissing defect and establish a method of accurately experimentally simulating and introducing kissing defects into structures.**

- A definition of a kissing defect was established via assessment of current literature on the subject.
- A reliable means of experimentally simulating kissing defects in adhesive bonds was shown to be via the addition of silicon grease to one of the adherends.
- Silicon grease was found to maintain its position during bond assembly and reduce the strength of adhesive bonds, giving repeatable defects to interrogate.

4. **Apply PPT to the experimentally simulated kissing defects and assess if they are detectable using the thermographic techniques.**

- PPT was applied to the experimentally simulated defects and it was necessary to enhance thermal contrast to allow kissing defects to be detected.
- CFRP single lap joints were used to investigate the effect of loading on the visibility of defects in adhesive joints.
- Loading created sufficient bending in the single lap joints to cause the defect to open.
- The opening enhanced the kissing defect's effect on the heat front propagation through the bond, enabling defect detection.
- Finite element models were developed to identify the degree to which a kissing defect must be opened to create sufficient contrast for defect detection.

5. **Compare and validate PPT with other NDE methods such as water coupled ultrasound.**

- UT C-scans were taken across a range of samples and were demonstrated to be highly capable for the identification of thin defects, particularly when using very high frequency probes.

- The main disadvantages of C-scanning are the time a scan can take and the coupling of the transducer to the component.
- Comparisons with PPT generally showed that for the time taken to assess a component using PPT compared to UT, PPT provided a more efficient means of defect identification.

6. Develop a numerical model of the heat interactions in a structure to understand the physics of PT/PPT and tailor experiments to particular component configurations.

- A FE model was developed to establish the defect detection limitations of PT and PPT which was validated using three case studies.
- The model predicted PT data well for the case studies used.
    - It was demonstrated that the model was capturing the heat transfer and hence the thermal contrast produced in the experiments well.
- PPT phase contrast data was calculated for the modelled and experimental results.
    - The processing routine used under predicted the magnitude of the phase contrast but had some success the frequency at which the peak $\Delta\phi$ occurred.
    - The *arc*tan used in phase calculations was found to emphasise small differences between the modelled and experimental PT data.
- The developed model was then used to carry out a defect detectability study relating the defect detectability to bulk material properties.
    - Plateaus were found where thermal properties were close between defect and bulk material properties in both the PT and PPT data. In this region defects were found to be undetectable. It was found that the extent of these plateaus was reduced when the thermal data was processed into phase data.
    - Kissing defects were suggested to be found within these plateau regions as they create insufficient thermal contrast to be detected using standard thermography methods.

7. **Assess how the technique may need to be adapted from the laboratory set-up to become a practical, portable tool for use in the field.**

- To identify kissing defects using PPT a load must be applied. To enable a more practical tool to be found a method of loading suitable for application in the field was required.
- The feasibility of vacuum loading was demonstrated using a CFRP plate adhered to a thin aluminium sheet.
- The vacuum was applied to the aluminium adherend and the bond was inspected using PPT on the CFRP side of the bond.
    - A vacuum of only 20% was required to open a bond to create sufficient phase contrast for defect detection.
    - The use of such a portable method of loading joints may be the key to a practical onsite inspection tool suitable for the inspection of adhesive joints.
- A lower cost bolometer detector was successfully used in PT for the identification of shallow and highly contrasting defects.

8. **Consider the practicalities of applying PPT as a tool for use in a shipyard environment.**

- Initial experiments aimed to identify the correct setup to detect strongly contrasting defects in the Triplex adhesive bonds found in the MkIII LNG carrier.
- The following work demonstrated that kissing defects would insufficiently affect thermal propagation to reveal a defect.
- The concept of the application of a vacuum to open previously undetected kissing defects has been demonstrated to be possible.
    - A vacuum of 60% was found to be sufficient to reveal an experimentally simulated kissing defect when the FT was adhered to a CFRP panel.

Through the achievement of the aim of the thesis and the completion of the above objectives, two main areas of novelty have been developed, specifically:

1. The development of a thermographic technique to enable kissing defect identification via the addition of a small load to enhance thermal contrast, as detailed in objectives 4 and 7.
2. The development of a numerical model able to accurately simulate PT and PPT to establish the limits of defect detectability and investigate experimental parameters, as detailed in objective 6.

10.2 Recommendations for future work

A series of recommendations for future work are suggested. These may be divided into development of the PPT technique into a tool suitable for use in industry, the automation of the process and the development and use of the FEM.

10.2.1 Development of PPT and vacuum loading

The current IR detector used in the preceding work uses a Stirling pump to cool the detectors sensor array. This would cause problems when attempting to combine the PPT setup and the vacuum load to allow single sided access. This problem may be simplified via the use of an uncooled bolometer device. The use of a bolometer for the application of PT has been shown to be feasible. The use of such a device would also lower the cost of the setup substantially. While the removal of the cooling system will simplify the incorporation of the IR detector, careful consideration should be given to the full or partial enclosure of devices within a vacuum. Devices may be fully enclosed within a vacuum chamber or only the heating elements and lenses may be included. Care must be taken to consider distortion of lenses if there is a pressure gradient across them. Another factor to consider would be the heat application and the resultant ambient heating within an enclosed space.

10.2.2 Automation

PPT data collection parameters can be tailored to specific applications. If the same components are to be investigated repeatedly then such parameters will remain constant throughout tests. However, if a range of components are to

be investigated it would be advisable to automate the parameter selection procedure in order to make setup less user dependent.

When considering the application of the combined PPT and vacuum tool to the Triplex bonds found in the MkIII carrier then due to the length of bonds involved robotic automation would be very advantageous. To be able to leave the experiments to run unmanned along the length of the bonds would reduce the labour required for inspection significantly. The technology to move a device along the bond line already exists in the welding industry.

Automatic defect recognition has not been covered in the thesis however there are several edge recognition softwares that exist, e.g. [137]. The use of such an approach would remove the time consuming role of assessing all the data and be used to highlight areas required for closer inspection be trained personnel.

10.2.3 Numerical modelling

In this thesis two numerical models have been developed, a structural model and a transient thermal model. The combination of these models would be akin to the incorporation of the PPT and vacuum application in the experiments and would result in a very powerful predictive tool to be used in conjunction with the experiments. Once the exact experimental setup has been defined and incorporated with the vacuum application the model could be used to create a database of detectable defect parameters tailored to a specific application or material of interest using the developed PPT tool.

List of References

1. Flom, Y. and Arsenault, R.J., *Interfacial bond strength in an aluminium alloy 6061 - SiC composite.* Materials Science and Engineering, **77**: p. 191-197. 1986.
2. da Costa Mattos, H.S., Sampaio, E.M., and Monteiro, A.H., *Static failure analysis of adhesive single lap joints.* International Journal of Adhesion & Adhesives, **31**: p. 446-454. 2011.
3. Ehrhart, B., Valeske, B., Muller, C.-D., and Bockenheimer, C. *Methods for the quality assessment of adhesive bonded CFRP structures - a resume.* in *2nd International Symposium on NDT in Aerospace 2010*. Hamburg, Germany. 2010.
4. Kapadia, A., *National Composites Network: Best Practice Guide - Non-destructive testing of composite materials*. 2007.
5. Yan, D., Drinkwater, B.W., and Neild, S.A. *Experimental and theoretical characterisation of kissing bonds in adhesive joint using non-linear ultrasonic measurement*. in *AIP Conference Proceedings*. Rhode Island, USA. 2010.
6. Yan, D., Drinkwater, B.W., and Neild, S.A., *Measurement of the ultrasonic nonlinearity of kissing bonds in adhesive joints.* NDT&E International, **42**: p. 459-466. 2009.
7. Nagy, P.B., *Ultrasonic detection of kissing bonds at adhesive interfaces.* Journal of Adhesion Science and Technology, **5**(8): p. 619-630. 1991.
8. Jiao, D. and Rose, J.L., *An ultrasonic interface layer model for bond evaluation.* Journal of Adhesion Science and Technology, **5**(8): p. 631-646. 1991.
9. Maldague, X., *Introduction to NDT by active infrared thermography*, in *Materials Evaluation*. p. 1060-1073. 2002.
10. Maldague, X., Galmiche, F., and Ziadi, A., *Advances in pulsed phase thermography.* Infrared Physics and Technology, **43**: p. 175-181. 2002.
11. Thevenet, D., Creac'hcadec, L., and Sohier, J.Y., *Experimental analysis of the behaviour of adhesively bonded joints under tensile/compression-shear cyclic loadings.* Journal of Adhesion and Adhesives, **44**: p. 15 - 25. 2013.
12. Vijaya Kumar, R.L., Bhat, M.R., and Murthy, C.R.L., *Evaluation of kissing bond in composite adhesive lap joints using digital image correlation: Preliminary studies.* Journal of Adhesion and Adhesives, **42**: p. 60-68. 2013.
13. Omar, M., Hassan, M., Donohue, K., Saito, K., and Alloo, R., *Infrared thermography for inspecting the adhesion integrity of plastic welded joints.* NDT&E International, **39**: p. 1-7. 2006.
14. Shepard, S.M., *Method and apparatus for detecting kissing unbond defects*, Google Patents. 2006.
15. Chu, T., Mahajan, A., DiGregorio, A., and Russell, S.S., *Determination of optimal experimental parameters for transient thermography imaging using finite-element models.* The Imaging Science Journal, **53**: p. 20-26. 2005.
16. Krishnapillai, M., Jones, R., Marshall, I.H., Bannister, M., and Rajic, N., *NDTE using pulse thermography: Numerical modeling of composite subsurface defects.* Composite Structures, **75**: p. 241-249. 2006.
17. Krishnapillai, M., Jones, R., Marshall, I.H., Bannister, M., and Rajic, N., *Thermography as a tool for damage assessment.* Composite Structures, **67**: p. 149-155. 2005.

18. Dumoulin, J., Ibarra-Castanedo, C., Quiertant, M., Taillade, F., Bendada, A., and Maldague, X. *Evaluation of FRP gluing on concrete structures by active infrared thermography*. in *10th International Conference on Quantitative Infrared Thermography*. Quebec, Canada. 2010.
19. Baldan, A., *Adhesion phenomena in bonded joints.* International Journal of Adhesion & Adhesives, **38**: p. 95-116. 2012.
20. Pocius, A.V., *Adhesives*, in *Physical properties of polymers handbook*, J.E. Mark, Editor Springer Science+Business Media, LLC: New York, USA. 2007.
21. Tajima, Y., Matsuura, T., Numata, Y., Yamazaki, D., Kawamura, H., and Osedo, H., *Surface free energy and wettability determination of various fullerene derivative films on amorphous carbon wafer.* Journal of Applied Physics, **47**: p. 5730. 2008.
22. Mattox, D.M., *Handbook of physical vapor deposition (PVD) processing*. 2nd Edition Oxford, UK: William Andrew Applied Science Publishers. 54-56. 2010.
23. Brockmann, W., Geiss, P.L., Klingen, J., and Schroder, B., *Adhesive Bonding: Adhesives, Applications and Processes* Germany: Wiley-Vch. 2009.
24. Adams, R.D. and Cawley, P., *A review of defect types and nondestructive testing techniques for composites and bonded joints.* NDT International, **21**(4): p. 208-222. 1988.
25. Yang, S., Gu, L., and Gibson, R.F., *Nondestructive detection of weak joints in adhesively bonded composite structures.* Composite Structures, **51**: p. 63-71. 2001.
26. Jeenjitkaew, C., Luklinska, Z., and Guild, F., *Morphology and surface chemistry of kissing bonds in adhesive joints produced by surface contamination.* International Journal of Adhesion & Adhesives, **30**: p. 643-653. 2010.
27. *Characterisation of Composite Materials*. Materials Characterization Series, C.R. Brundle and J.C.A. Evans: Momentum Press. 2010.
28. Davis, M.J. and Bond, D.A. *The importance of failure mode identification in adhesive bonded aircraft structures and repairs*. in *ICCM 12*. Paris, France. 1999.
29. Marty, P.N., Desai, N., and Andersson, J. *NDT of kissing bond in aeronautical structures*. in *16th World Conference on NDT*. Montreal, Canada. 2004.
30. Sakagami, T. and Kubo, S., *Applications of pulse heating thermography and lock-in thermography to quatitative nondestructive evaluation.* Infrared Physics and Technology, **43**: p. 211-218. 2002.
31. Pickering, S.G., Chatterjee, K., Almond, D.P., and Tuli, S., *LED optical excitation for the long pulse and lock-in thermographic techniques.* NDT&E International, **58**: p. 72-77. 2013.
32. Benitez, H.D., Ibarra-Castanedo, C., Bendada, A., Maldague, X., Loaiza, H., and Caicedo, E., *Definintion of a new thermal contrast and pulse correction for defect quantification in pulsed thermography.* Infrared Physics and Technology, **51**: p. 160-167. 2008.
33. Ibarra-Castanedo, C., Piau, J.-M., Guilbert, S., Avdelidis, N.P., Genest, M., Bendada, A., and Maldague, X., *Comparative study of active thermography techniques for the nondestructive evaluation of honeycomb structures.* Research in Nondestructive Evaluation, **20**: p. 1-31. 2009.

34. Feuillet, V., Ibos, L., Fois, M., Dumoulin, J., and Candau, Y., *Defect detection and characterization in composite materials using square pulse thermography coupled with singular value decomposition analysis and thermal quadrupole modeling.* NDT&E International, **51**: p. 58-67. 2012.
35. Sfarra, S., Ibarra-Castanedo, C., Santulli, C., Paoletti, A., Paoletti, D., Sarasini, F., Bendada, A., and Maldague, X., *Falling weight impacted glass and basalt fibre woven composites inspected using non-destructive techniques.* Composites: Part B, **45**: p. 601-608. 2013.
36. Sfarra, S., Ibarra-Castanedo, C., Santulli, C., Sarasini, F., Ambrosini, D., Paoletti, D., and Maldague, X., *Eco-friendly laminates: From the indentation to non-destructive evaluation by optical and infrared monitoring techniques.* Strain, **49**: p. 175-189. 2013.
37. Genest, M., Martinez, M., Mrad, N., Renaud, G., and Fahr, A., *Pulsed thermography for non-destructive evaluation and damage growth monitoring of bonded repairs.* Composite Structures, **88**(1): p. 112-120. 2009.
38. Roach, D., Rackow, K., and Duvall, R. *Innovative use of adhesive interface characteristics to nondestructively quantify the strength of bonded joints*. in *10th European Conference on Non-Destructive Testing*. Moscow, Russia. 2010.
39. Brotherhood, C.J., Drinkwater, B.W., and Guild, F.J., *The effect of compressive loading on the ultrasonic detectability of kissing bonds in adhesive joints.* Journal of Nondestructive Evaluation, **21**(3): p. 95-104. 2002.
40. Howarth, D., *Adhesive bonding in LNG ship construction*, Lloyd's Register.
41. Kuo, J.F., Campbell, R.B., Ding, Z., Hoie, S.M., Rinehart, A.J., Sanstrom, R.E., Yung, T.W., Greener, M.N., and Danaczko, M.A., *LNG tank sloshing assessment methodology - the new generation.* International Journal of Offshore and Polar Engineering, **19**(4): p. 241-253. 2009.
42. Grieve, P., *GST, A new generation of LNG membrane-type land storage tank*: www.gtt.fr.
43. Kim, K.H., Yoon, S.H., and Lee, D.G., *Vibration isolation of LNG containment systems due to sloshing with glass fibre composite.* Composite Structures, **94**: p. 469-476. 2012.
44. Wang, B. and Shin, Y. *Full-scale test and FE analysis of LNG MkIII containment system under sloshing loads*. in *The 21st International Offshore and Polar Engineering Conference*. Hawaii, USA. 2011.
45. de Lauzon, J., Diebold, L., and Malenica, S. *Sloshel project - strength assessment of LNG cargo containment systems under sloshing loads*. in *International Offshore and Polar Engineering Conference*. Maui, Hawaii. 2011.
46. Han, S., Cho, H., Lee, J., Rim, C.W., Suh, Y., and Lee, T.K. *Experimental study on the structural behaviour of secondary barrier of Mark-III LNG CCS*. in *Proceedings of the ASME 2009 28th International Conference on Ocean, Offshore and Arctic Engineering*. Honolulu, Hawaii, USA. 2009.
47. Choe, J., Kim, K.H., Lee, D., Bang, C.S., and Lee, D.G., *Glass composite vibration isolating structure for the LNG cargo containment system.* Composite Structures, **107**: p. 469-475. 2014.
48. Yu, H.Y., Kim, B.G., and Lee, D.G., *Cryogenic reliability of composite insulation panels for liquefied natural gas (LNG) ships.* Composite Structures, **94**: p. 462-468. 2012.

49. Kim, B.G. and Lee, D.G., *Leakage characteristics of the glass fabric composite barriers of LNG ships.* Composite structures, **86**: p. 27-36. 2008.
50. Maguire, J.R. *Acoustic emission monitoring of composite containment systems*. in *9th International Conference on Damage Assessment of Structures*. Oxford, UK. 2011.
51. Teti, R. and Alberti, N., *Ultrasonic identification and measurement of defects in composite material laminates.* CIRP Annals - Manufacturing Technology, **39**(1): p. 527-530. 1990.
52. Hsu, D.K. and Hughes, M.S., *Simultaneous ultrasonic velocity and sample thickness measurement and application in composites.* Journal of the Acoustical Society of America, **92**(2): p. 669-675. 1992.
53. Diamanti, K. and Soutis, C., *Structural health monitoring techniques for aircraft composite structures.* Progress in Aerospace Sciences, **46**: p. 342-352. 2010.
54. Gachagan, A., Hayward, G., Kelly, S.P., and Galbraith, W., *Characterization of air-coupled transducers.* IEEE Transactions on Ultrasonics, Ferroelectrics, and Frequency Control, **43**(4): p. 678-689. 1996.
55. Jolma, P., Segercrantz, S., and Berggreen, C., *Ultimate failure of debond damaged sandwich panels loaded with lateral pressure - an experimental and fracture mechanics study.* Journal of Sandwich Structures and Materials, **9**: p. 167-196. 2007.
56. Pastor, M.-L., Pescay, C., and Garnier, C. *Comparison of two nondestructive tests in carbon/epoxy composites*. in *ICCM 17*. Edinburgh, UK. 2009.
57. Garnier, C., Pastor, M.-L., Eyma, F., and Lorrain, B., *The detection of aeronautical defects in situ on composite stuctures using non destructive testing.* Composite Structures, **93**: p. 1328-1336. 2011.
58. Buonsanti, M., Cacciola, M., Calcagno, S., Megali, G., Morabito, F.C., Pellicano, D., and Versaci, M., *Evaluation of defects in multilayer carbon fibre epoxy for aeronautics applications.* Advances in Acoustics and Vibration, **2009**. 2009.
59. Karmazin, A., Kirillova, E., Seemanm, W., and Syromyatnikov, P. *On the solution of crack identification problems in composite materials*. in *2nd International Symposium on NDT in Aerospace 2010*. Hamburg, Germany. 2010.
60. Kortschot, M.T. and Beaumont, P.W.R., *Damage mechanisms of composite materials: I - measurement of damage and strength.* Composite Science and Technology, **39**: p. 289-301. 1990.
61. Schilling, P.J., Karedla, B.P.R., Tatiparthi, A.K., Verges, M.A., and Herrington, P.D., *X-ray computed microtomography of internal damage in fiber reinforced polymer matrix composites.* Composite Science and Technology, **65**: p. 2071-2078. 2005.
62. Howarth, D. and Durkin, J. *Shipyard fabrication and its quality control: Some problems and solutions*. in *Technology Days 2010, Lloyd's Register*. 2010.
63. Sheppard, P.J., Phillips, H.J., and Cooper, I. *The practical use of NDE methods for the assessment of damaged marine composite structures*. in *ICCM 17*. Edinburgh, UK. 2009.
64. Zoughi, R., *Microwave non-destructive testing and evaluation*. Non-destructive evaluation series The Netherlands: Kluwer Academic Publishers. 2000.

65. Green, G.A., Campbell, P., and Zoughi, R. *An investigation into the potential of microwave NDE for maritime application*. in *16th World Conference on Nondestructive Testing*. Montreal. 2004.
66. *Non-destructive evaluation (NDE) of polymer matrix composites - techniques and applications*. Composite Science and Engineering: Woodhead Publishing. 2013.
67. Mook, G., Lange, R., and Koeser, O., *Non-destructive characterisation of carbon-fibre-reinforced plastics by means of eddy-currents.* Composites Science and Technology, **61**(6): p. 865-873. 2001.
68. Lange, R. and Mook, G., *Structural analysis of CFRP using eddy current methods.* NDT&E International, **27**(5): p. 241-248. 1994.
69. Heuer, H., Schulze, M.H., and Meyendorf, N. *High resolution inspection of carbon fiber materials by eddy current techniques*. in *2nd International Symposium on NDT in Aerospace 2010*. Hamburg, Germany. 2010.
70. Hung, Y.Y., *Shearography for Non-destructive Evaluation of Composite Structures.* Optics and Lasers in Engineering, **24**: p. 161-182. 1996.
71. Hung, Y.Y. and Ho, H.P., *Shearography: An optical measurement technique and applications.* Materials Science and Engineering, **R 49**. 2005.
72. Huke, P., Focke, O., Falldorf, C., von Kopylow, C., and Bergmann, R.B. *Contactless defect detection using optical methods for non destructive testing*. in *2nd International Symposium on NDT in Aerospace 2010*. Hamburg, Germany. 2010.
73. Ganesan, A.R. *Holographic and laser speckle methods in non-destructive testing*. in *National Seminar and Exhibition on Non-Destructive Evaluation*. Trichy, India. 2009.
74. Schuth, M., Vossing, F., and Yang, L. *Shearographic NDT - measuring systems in theory and application (endoscope for nondestructive test)*. in *2nd International Symposium on NDT in Aerospace*. Hamburg, Germany. 2010.
75. Halmshaw, R., *Non-destructive testing*. Metallugy and Materials Science Series, P.H. R.W.K.Honeycombe London: Edward Arnold. 320. 1987.
76. Vavilov, V.P., *Pulsed thermal NDT of materials: back to basics.* Nondestructive Testing and Evaluation, **22**(2): p. 177-197. 2007.
77. Ibarra-Castanedo, C. and Maldague, X., *Interactive methodology for optimized defect characterisation by quantitative pulsed phase thermography.* Research in Nondestructive Evaluation, **16**: p. 175-193. 2005.
78. Sun, J.G., *Analysis of pulsed thermography methods for defect depth prediction.* Journal of Heat Transfer, **128**: p. 329-338. 2006.
79. Shepard, S.M., *Introduction to active thermography for non-destructive evaluation.* Anti-Corrosion Methods and Materials, **44**(4): p. 236-239. 1997.
80. Chapman, G.B. *Infrared monitoring of friction welds and adhesive bond curing in automotive manufacturing*. in *16th World Conference on NDT*. Montreal, Canada. 2004.
81. Harizi, W., Chaki, S., Bourse, G., and Ourak, M., *Mechanical damage assessment of glass fibre-reinforced polymer composites using passive infrared thermography.* Composites: Part B, **59**: p. 74-79. 2014.
82. Libonati, F. and Vergani, L., *Damage assessment of composite materials by means of thermographic analysis.* Composites: Part B, **50**: p. 82-90. 2013.

83. Renshaw, J., Chen, J.C., Holland, S.D., and Thompson, R.B., *The sources of heat generation in vibrothermography.* NDT&E International, **44**: p. 736-739. 2011.
84. Keo, S.A., Brachelet, F., Breaban, F., and Defer, D., *Steel detection in reinforced concrete wall by microwave infrared thermography.* NDT&E International, **62**: p. 172-177. 2014.
85. Ren, W., Liu, J., Tian, G.Y., Gao, B., Cheng, L., and Yang, H., *Quantitative Non-destructive Evaluation Method for Impact Damage Using Eddy Current Pulsed Thermography.* Composites: Part B, **54**: p. 169-179. 2013.
86. Liu, J., Tian, G.Y., Gao, B., Ren, W., and Meng, J.S., *Investigation of thermal imaging sampling frequency for eddy current pulsed thermography.* NDT&E International, **62**: p. 85-92. 2014.
87. Avdelidis, N.P., Ibarra-Castanedo, C., Maldague, X., Marioli-Riga, N.P., and Almond, D.P., *A thermographic comparison study for the assessment of composite patches.* Infrared Physics and Technology, **45**: p. 291-299. 2004.
88. Quinn, S. and Dulieu-Barton, J.M., *Identification of the sources of non-adiabatic behaviour for practical thermoelastic stress analysis.* Journal of Strain Analysis, **37**(1): p. 59-71. 2002.
89. Dulieu-Barton, J.M. and Stanley, P., *Development and applications of thermoelastic stress analysis.* Journal of Strain Analysis, **33**(2): p. 93-104. 1998.
90. Diaz, F.A., Patterson, E.A., Tomlinson, R.A., and Yates, J.R., *Measuring stress intensity factors during fatigue crack growth using thermoelasticity.* Fatigue & Fracture of Engineering Materials & Structures, **27**: p. 571-583. 2004.
91. Tomlinson, R.A. and Olden, E.J., *Thermoelasticity for the analysis of crack tip stress fields - a review.* Strain, **35**(2): p. 49-55. 1999.
92. Plum, R., Medgenberg, J., Merzbacher, M., and Ummenhofer, T. *Extended thermoelastic stress analysis applied to carbon steel and CFRP*. in *2nd International Symposium on NDT in Aerospace*. 2010.
93. Boyd, S.W., Dulieu-Barton, J.M., and Rumsey, L., *Stress analysis of finger joints in pultruded GRP materials.* International Journal of Adhesion & Adhesives, **26**: p. 498-510. 2005.
94. Johnson, S., *Thermoelastic stress analysis for detection and characterizing static damage initiation in composite lap shear joints.* Composites: Part B, **56**: p. 740-748. 2014.
95. Bolduc, M. and Roy, C. *Evaluation of impact damage in composite materials using acoustic emission*. in *Composite materials: fatigue and fracture*. Philadelphia, USA. 1993.
96. Asokan, R., Arumugam, V., Santullli, C., and Stanley, A.J., *Acoustic emission monitoring of repaired composite laminates.* Journal of Reinforced Plastics and Composites, **31**(18): p. 1226-1235. 2012.
97. Karhnak, S.J. and Duke, J.C. *Predicting performance of adhesively bonded joints on acousto-ultrasonic evaluation*. in *Composite Bonding ASTM STP 1227*. Philadelphia, USA. 1994.
98. Cuc, A. and Guiurgiutiu, V. *Disbond detection in adhesively-bonded structures using piezoelectric wafer active sensors*. in *SPIE*. 2004.
99. Heller, K., Jacobs, L.J., and Qu, J., *Characterization of adhesive bond properties using Lamb waves.* NDT&E International, **33**(8): p. 555-563. 2000.

100. Hung, M.Y.Y., Chen, Y.S., and Ng, S.P., *Review and comparison of shearography and pulsed thermography for adhesive bond evaluation.* Optical Engineering, **46**(5). 2007.
101. Hung, Y.Y., Chen, Y.S., Ng, S.P., Liu, L., Huang, Y.H., Luk, B.L., Ip, R.W.L., Wu, C.M.L., and Chung, P.S., *Review and comparison of shearography and active thermography for nondestructive evaluation.* Materials Science and Engineering: Reports, **64**(5-6): p. 73-112. 2009.
102. Hung, Y.Y. *Automated shearography for nondestructive evaluation and strain measurement*. in *SPIE 2455 - Nondestructive evaluation of aging aircrafts, aerospace hardware and materials*. Oakland, USA. 1995.
103. Schliekelmann, R.J., *Non-destructive testing of bonded joints, recent developments in testing systems.* Non-Destructive Testing, **8**: p. 100-110. 1975.
104. Rhee, S.-H. and Hwang, T.-K. *Use of acoustic emission to identify the bonding status of a rocket motor case*. in *ICCM 17*. Edinburgh, UK. 2009.
105. Schroeder, J.A., Ahmed, T., Chaudhry, B., and Shepard, S., *Non-destructive tesing of structural composites and adhesively bonded composite joints: pulsed thermography.* Composites : Part A, **33**: p. 1511-1517. 2002.
106. Tashan, J. and Al-Mahadi, R., *Bond defect detection using PPT IRT in concrete structures strengthened with different CFRP systems.* Composite Structures, **111**: p. 13-19. 2014.
107. Huth, S., Breitenstein, O., Huber, A., Dantz, D., Lambert, U., and Altmann, F., *Lock-in IR-Thermography - a novel tool for material and device characterization.* Diffusion and defect Data. B, Solid State Phenomena, **82/84**: p. 741-746. 2002.
108. Junyan, L., Yang, W., and Jingmin, D., *Research on thermal wave processing of lock-in thermography based on analyzing image sequences for NDT.* Infrared Physics and Technology, **53**: p. 348-357. 2010.
109. Rajic, N., *Principal component thermography for flaw contrast enhancement and flaw depth characterisation in composite structures.* Composite Structures, **58**: p. 521-528. 2002.
110. Rajic, N., *Principle component thermography*, in *DSTO Technical Report TR-1298*. 2002.
111. Junyan, L., Qingju, T., and Yang, W., *The study of inspection on SiC coated carbon-carbon composite with subsurface defects by lock-in thermography.* Composite Science and Technology, **72**: p. 1240-1250. 2012.
112. Ibarra-Castanedo, C., Susa, M., Klein, M., Grenier, M., Piau, J.-M., Ben Larby, W., Bendada, A., and Maldague, X. *Infrared thermography: principle and applications to aircraft materials*. in *International Symposium on NDT in Aerospace*. Furth, Germany. 2008.
113. Ibarra-Castanedo, C., Avdelidis, N.P., and Maldague, X., *Quantitative pulsed phase thermography applied to steel plates.* Proceedings of SPIE, **5782**(342). 2005.
114. Dereniak, E.L. and Boreman, G.D., *Infrared detectors and systems* New York: John Wiley and Sons, Inc. 1996.
115. Haller, E.E., *Physics and design of advanced IR bolometers and photoconductors.* Infrared Phys, **25**(1/2): p. 257-266. 1985.

116. Maldague, X., *Theory and practice of infrared technology for nondestructive testing*. Wiley series in microwave and optical engineering, K. Chang Chichester: John Wiley & Sons, Inc. 2001.
117. Carslaw, H.S., Jaeger, J.C., *Heat Conduction in Solids*. Second Edition, O.S. Publications Oxford: Oxford University Press. 1961.
118. Parker, W.J., Jenkins, R.J., Butler, C.P., and Abbott, G.L., *Flash method of determining thermal diffusivity, heat capacity, and thermal conductivity.* Journal of Applied Physics, **32**(9): p. 1679-1685. 1961.
119. Mulholland, G.P. and Cobble, M.H., *Diffusion through composite media.* International Journal of Heat and Mass Transfer, **15**: p. 147-160. 1972.
120. Riley, K.F., *Mathematical methods for the physical sciences* Cambridge: Cambridge University Press. 1974.
121. Busse, G., Wu, D., and Karpen, W., *Thermal wave imaging with phase sensitive modulated thermography.* Journal of Applied Physics, **71**(8): p. 3962-3965. 1992.
122. Avdelidis, N.P. and Almond, D.P., *Through skin assessment of aircraft structures using pulsed thermography.* NDT&E International, **37**: p. 353-359. 2004.
123. Meola, C., Calomagno, G.M., and Giorleo, L., *Geometrical limitations to detection of defects in composites by means of infrared thermography.* Journal of Nondestructive Evaluation, **23**: p. 125-132. 2004.
124. Zeng, Z., Li, C., Tao, N., Feng, L., and Zhang, C., *Depth prediction of non-air interface defect using pulsed thermography.* NDT&E International, **48**: p. 39-45. 2012.
125. Ibarra-Castanedo, C., Gonzalaz, D., Klein, M., Pilla, M., Vallerand, S., and Maldague, X., *Infrared image processing and data analysis.* Infrared Physics and Technology, **46**: p. 75-83. 2004.
126. Wysocka-Fotek, O., Oliferuk, W., and Maj, M., *Reconstruction of size and depth of simulated defects in austenitic steel plate using pulsed infrared thermography.* Infrared Physics and Technology, **55**: p. 363-367. 2012.
127. Omar, M., Hassan, M., Saito, K., and Alloo, R., *IR self-referencing thermography for detection of in-depth defects.* Infrared Physics and Technology, **46**: p. 283-289. 2005.
128. *The data conversion handbook* Oxford, UK: Newnes. 2005.
129. Robinson, A.F., Dulieu-Barton, J.M., Quinn, S., and Burguete, R.L., *Paint coating characterization for thermoelastic stress analysis of metallic materials.* Measurement Science and Technology, **21**: p. 1-11. 2010.
130. Waugh, R.C., Dulieu-Barton, J.M., and Quinn, S., *Modelling and evaluation of pulsed and pulse phase thermography through application of composite and metallic case studies.* NDT&E International, **66**: p. 52-66. 2014.
131. Maldague, X. and Marinetti, S., *Pulse phase infrared thermography.* Journal of Applied Physics, **79**(5): p. 2694 - 2698. 1996.
132. MatWeb, L. *MatWeb, Material property data*. [cited 2012 6th May]; Data base of materials data sheets].
133. Manohar, A. and Lanza di Scalea, F., *Determination of defect depth and size using virtual heat sources in pulsed infrared thermography.* Experimental Mechanics, **53**: p. 661-671. 2013.
134. Ibarra-Castanedo, C. and Maldague, X., *Pulsed phase thermography reviewed.* Quantitative Infrared Thermography Journal, **1**(1): p. 47-70. 2004.
135. Kaviany, M., *Essentials of heat transfer* Cambridge, UK: Cambridge University Press. 2011.

136. *NPL Footbridge Project: Advanced data analysis and sensor networks*. Teddington, UK. 7th December 2012.
137. Kovesi, P., *Phase congruency: A low-level image invariant.* Psychological Research, **64**: p. 136-148. 2000.